

Modelling Precipitation of Carbides in Martensitic Steels

Shingo Yamasaki
Darwin College

*This dissertation is submitted
for the degree of Doctor of Philosophy
at the University of Cambridge*

PREFACE

This dissertation is submitted for the degree of Doctor of Philosophy at the University of Cambridge. The research described herein was conducted under the supervision of Professor H. K. D. H. Bhadeshia in the Department of Materials Science and Metallurgy, University of Cambridge, between October 2000 and November 2003.

Except where acknowledgement and reference are made to previous work, this work is, to the best of my knowledge, original. This dissertation is the result of my own work and includes nothing which is the outcome of work done in collaboration except where specifically indicated in the text. Neither this, nor any substantially similar dissertation has been, or is being, submitted for any other degree, diploma, or other qualification at any other university. This dissertation does not exceed 60,000 words in length.

Shingo Yamasaki

February 2004

ACKNOWLEDGEMENTS

I am grateful to Professor D. J. Fray for the provision of laboratory facilities in the Department of Materials Science and Metallurgy at the University of Cambridge. I would like to express my sincere thanks to my academic supervisor Professor H. K. D. H. Bhadeshia for his great encouragement, and all members of the Phase Transformations group for their advice and help.

I gratefully appreciate Dr S. Aihara and Mr T. Tarui at Nippon Steel Corporation for giving me the opportunity to study at the University of Cambridge. I would like also to thank Mr D. Hirakami for his kind help with experimental work at Nippon Steel Corporation. I am indebted to grants from the Personnel Division of Nippon Steel Corporation and would like to acknowledge the generosity of the organization for their financial support.

I would like to express my appreciation to all the members of the PT-Group in the Materials Science Department for their help and friendship, in particular, Dr T. Sourmail, Dr C. G. Mateo, Dr V. Yardley, Dr M. Gonzales (now at Corus) and Dr N. Fujita (now at Nippon Steel Corporation) . Many thanks also to my other friends.

I wish to express my thanks to Michiko, my wife, for her dedicated support to my life in Cambridge. I am also grateful my son, Hiroki for his encouragement.

ABSTRACT

The purpose of this work was to model carbide precipitation in steels of a quaternary system which includes two substitutional elements. The work focuses on secondary hardening steels which are used for high-strength components, where hydrogen embrittlement is one of the major factors responsible for failure. It is believed that carbide particles can act as hydrogen trapping sites, thus reducing the risk of embrittlement. The thesis begins with a review of the physical metallurgy of secondary hardening steels and the phenomena of hydrogen embrittlement and hydrogen trapping.

The basic theory for the precipitation processes, including the nucleation and diffusion-controlled growth of particles, is reviewed in Chapter 2. Significant progress has recently been made in modelling the overall kinetics of transformations which occur simultaneously. The new theory, also reviewed, adopts classical nucleation and diffusion-controlled growth concepts and takes into account the capillarity effect.

In the present work, a modified model has been developed for the precipitation of needle-shaped carbides, and a new model for plate-shaped carbides. The models are then verified experimentally, using five steels designed specifically for this purpose. Using the chemical compositions of the steels and thermodynamic data, the carbide precipitation, dissolution and coarsening kinetics at 600 °C were estimated. It is found that reasonable agreement can be obtained between experiment and theory for ternary steels, when multicomponent diffusion and capillarity effects are taken into account. This applies to both needle and plate-shaped particles. The same approach was then used successfully for quaternary steels.

For the specific steels studied, M_2C - and M_4C_3 -type carbides are expected to be hydrogen trapping sites which improve the hydrogen embrittlement properties. Experimental results on the hydrogen trapping capacity of the steels confirm this expectation and the relationships between the hydrogen trapping capacity and the features of M_4C_3 carbide particles are discussed.

Finally, conclusions are drawn and suggestions are made for future work.

Contents

1	Introduction	1
1.1	Overview	1
1.2	High-strength steel parts in automobiles	2
1.3	Physical metallurgy of tempered martensitic steels	4
1.3.1	Tempering of martensite	4
1.3.2	Carbides in alloy steels	5
1.3.3	Precipitation behaviour in Mo- and V-containing steels	6
1.4	Hydrogen embrittlement	10
1.4.1	Introduction	10
1.4.2	Examples of hydrogen embrittlement phenomena	10
1.4.3	Fracture modes	12
1.4.4	Hydrogen trapping in steels	13
1.5	Summary	13
2	Theories for isothermal precipitation kinetics	14
2.1	Classical nucleation theory	14
2.1.1	Misfit strain energy	14
2.1.2	Interfacial energy	15
2.1.3	Activation energy for nucleation	16
2.1.4	Nucleation rate	16
2.1.5	Chemical driving force	17
2.2	Diffusion-controlled growth theory (binary system)	19
2.2.1	One-dimensional growth	19
2.2.2	Growth of spherical particles	21
2.2.3	Growth of particles with the capillarity effect	22

2.3	Diffusion-controlled growth theory (ternary systems)	30
2.3.1	Growth of spherical particles	30
2.3.2	Growth of particles with the capillarity effect	35
2.4	Diffusion-controlled growth theory (higher order systems)	35
2.5	Ostwald ripening	36
2.6	Summary	36
3	Modelling of carbide precipitation during tempering	37
3.1	Models for precipitation of a single phase	37
3.2	Models for precipitation of several phases in multicomponent systems	38
3.2.1	Robson and Bhadeshia model	38
3.2.2	Fujita and Bhadeshia model	46
3.3	Summary	51
4	Thermodynamic calculations	52
4.1	Introduction	52
4.2	Application of MTDATA	52
4.2.1	General description of MTDATA	52
4.2.2	Experimental steels	53
4.2.3	Possible phases in the experimental alloys	53
4.3	Relative phase stabilities	54
4.3.1	Steel <i>A</i>	54
4.3.2	Steel <i>B</i>	54
4.3.3	Steel <i>C</i>	56
4.3.4	Steel <i>D</i>	56
4.3.5	Steel <i>E</i>	56
4.3.6	Prospective precipitation sequence	56
4.4	Equilibrium chemical composition of the stable phases	58
4.5	Paraequilibrium and equilibrium cementite composition	61
4.6	Effect of Mn on carbide precipitation	61
4.7	Summary	62

5	Experimental procedures	64
5.1	Introduction	64
5.2	Materials and processing conditions	64
5.3	Optical microscopy	65
5.4	Hardness measurements	66
5.5	Transmission electron microscopy (TEM)	66
5.5.1	Sample preparation	66
5.5.2	Selected area diffraction	67
5.5.3	Measurement of particle size	68
5.5.4	Measurement of the thickness of a thin foil sample	69
5.5.5	X-ray energy-dispersed spectroscopy (XEDS) measurement	70
5.6	Hydrogen trapping capacity measurements	70
6	Experimental results	73
6.1	Optical microstructure	73
6.2	Hardness	73
6.3	TEM observation	73
6.4	Hydrogen trapping capacity measurement	73
7	Modelling Mo₂C in a Fe-C-Mo ternary system	79
7.1	Experimental work	79
7.1.1	Material	79
7.1.2	Transmission electron microscopy	79
7.2	Precipitation of alloy carbide with local equilibrium	94
7.3	Growth of particles: capillarity	95
7.4	Modelling of needle-shaped carbide growth	97
7.4.1	Chemical composition and equilibrium phases	97
7.4.2	Capillarity effect in multicomponent systems	98
7.4.3	Overall transformation kinetics	98
7.4.4	Inputs and calculations	102
7.5	Results and discussion	103
7.6	Summary and conclusions	106

8	Modelling V_4C_3 in a Fe-C-V ternary system	108
8.1	Experimental work	108
8.1.1	Material	108
8.1.2	Transmission electron microscopy	108
8.2	Modelling of plate-shaped carbide growth	120
8.2.1	Chemical composition and equilibrium phases	120
8.2.2	Local equilibrium, multicomponent systems	120
8.2.3	Capillarity effect, multicomponent systems	120
8.2.4	Growth of the particles with capillarity effect	122
8.2.5	Overall transformation kinetics	123
8.2.6	Inputs and calculations	126
8.3	Results and discussion	126
8.4	Summary and conclusions	131
9	Modelling M_4C_3 in a Fe-C-Mo-V quaternary system	132
9.1	Experimental work	132
9.1.1	Material	132
9.1.2	TEM observations	132
9.2	Modelling of plate-shaped carbide growth	152
9.2.1	Chemical composition and equilibrium phases	152
9.2.2	Capillarity effect in multicomponent systems	152
9.2.3	Precipitation of the alloy carbide with local equilibrium and capillarity effect	154
9.2.4	Overall transformation kinetics	157
9.2.5	Inputs and calculations	159
9.3	Results and discussion	160
9.4	Summary and conclusions	167
10	Hydrogen trapping behaviour	168
10.1	Introduction	168
10.2	Discussion	168
11	Conclusions and suggestions for further work	171

12 Appendix - Computer program	173
12.1 Program for nucleation and growth of needle-shaped precipitate : Mo_2C . . .	173
12.1.1 Provenance of Source Code	173
12.1.2 Purpose	173
12.1.3 Specification	173
12.1.4 Description	173
12.1.5 References	173
12.1.6 Parameters	174
12.1.7 Error Indicators	175
12.1.8 Accuracy	175
12.1.9 Further Comments	175
12.1.10 Examples	175
12.2 Program for nucleation and growth of needle-shaped precipitate : V_4C_3 . . .	178
12.2.1 Provenance of Source Code	178
12.2.2 Purpose	178
12.2.3 Specification	178
12.2.4 Description	178
12.2.5 References	178
12.2.6 Parameters	178
12.2.7 Error Indicators	180
12.2.8 Accuracy	180
12.2.9 Further Comments	180
12.2.10 Examples	180
12.3 Program for nucleation and growth of plate-shaped precipitate : M_4C_3 . . .	183
12.3.1 Provenance of Source Code	183
12.3.2 Purpose	183
12.3.3 Specification	183
12.3.4 Description	183
12.3.5 References	183
12.3.6 Parameters	184
12.3.7 Error Indicators	185
12.3.8 Accuracy	185

12.3.9 Further Comments	185
12.3.10 Examples	186

Nomenclature and Abbreviations

a	Activity
b	Burgers vector of dislocation at the interface
b_t	Transient compositions of matrix
C_0^H	Constant defining hydrogen solubility in metals
C_1	Coefficient related to dislocation energy
C_2	Coefficient of three-dimensional parabolic rate constant
C_3	Coefficient of diffusion distance
C^H	Hydrogen solubility in metals
C_l	Speed of light in vacuum
c_X	Atomic fraction of the diffusing species X
\bar{c}	Atomic fraction of solute in the alloy
\bar{c}'	Mean atomic fraction of solute in the matrix
\bar{c}_X	Atomic fraction of component X in the alloy
c_X^θ	Atomic fraction of component X in θ
$c_X^{\alpha\beta}$	Atomic fraction of component X in α in equilibrium with β
$c_X^{\beta\alpha}$	Atomic fraction of component X in β in equilibrium with α
$c^{\alpha\beta}$	Atomic fraction of solute in α in equilibrium with β
$c^{\beta\alpha}$	Atomic fraction of solute in β in equilibrium with α
$c_{X,r}^{\alpha\beta}$	Atomic fraction of component X in α in equilibrium with a curved β interface
$c_{X,r}^{\beta\alpha}$	Atomic fraction of component X in a curved β particle in equilibrium with α
$c_r^{\alpha\beta}$	Atomic fraction of solute in α in equilibrium with a curved β interface
$c_r^{\beta\alpha}$	Atomic fraction of solute in curved β particle in equilibrium with α
D	Diffusion coefficient of the solute
D_{ij}	Inter-diffusion coefficient of element i and j
D_X	Diffusion coefficient of element X
\bar{d}	Mean diffusion distance between precipitates
d	Inter-atomic spacings
d_e	Inter-atomic spacings of the embryo
d_{hkl}	Spacing of hkl planes
d_m	Inter-atomic spacings of the matrix
d_t	Thickness of the cementite plate
$E_1(p)$	Exponential integral
e	Charge of an electron
F	Structure factor for Bragg angle
f	Atomic scattering amplitude
G^*	Activation energy for nucleation

G^α	Molar Gibbs free energy of α
$G^{T,P}$	Molar Gibbs free energy at (T, P)
G_r^β	Free energy of β phase precipitate which has curved interface
ΔG	Free energy change
ΔG_V	Chemical driving force for nucleation per unit volume of nucleus
ΔG_ϵ	Volume strain energy
ΔG_0	Free energy change of the system
ΔG_m	Maximum energy change per unit mole of equilibrium precipitate for nucleation
ΔG_n	Free energy change per unit mole of equilibrium precipitate
H	Curvature of a particle
H^{SER}	Enthalpy of the element or substance in the reference state at 298.15 K
ΔH	Enthalpy of solution of hydrogen in metal
h	Planck constant
I	Nucleation rate
I_β	Nucleation rate of β phase
J	Flux of the solute
K	Stress intensity factor
K_C	Critical stress intensity factor
k	Boltzmann constant
L	Diffusion distance
L_{cam}	Camera length
\bar{l}	Mean radius of needle-shaped precipitates
m	Constant in Zener - Hillert equation
m_c	Constant in Zener - Hillert equation
m_e	Electron mass
N_A	Avogadro's number
N_V	Number of nucleation sites per unit volume
N^β	Number density of β precipitates
N_0^β	Initial number density of β precipitates of Ostwald ripening stage
N_n	Number density of critical-sized embryo containing n atoms
O	Surface area
P	Pressure
P^H	Gas pressure
\bar{p}	Péclet number
Q^*	Activation energy for the transfer of atoms across the interface
R	Gas constant
R_{hkl}	Distance between the transmitted and diffracted reflections in electron diffraction pattern
r	Radial coordinate
r_0	Initial particle radius

r^I	Radius of spherical precipitate
r^{IC}	Radius of curvature at the tip
r^*	Critical radius of embryo
\bar{r}	Mean radius of precipitate
r_c	Critical tip radius at which growth ceases
T	Absolute temperature
t	Time
V	Volume
V_{ac}	Acceleration voltage
V_β	Real volume of β
dV_β	Increase in real volume of β
V_β^e	Extended volume of β
dV_β^e	Increase in extended volume of β
v	Growth rate
v_c	Growth rate of a flat interface governed by the interface process
v_β	Growth rate of β particles
W	Constant relating the volume fractions of two phases
w_c	Carbon concentration of alloys in wt.%
x^I	Position of the interface
x	Coordinate of precipitate
Z	Varying function of Ω
α	Ferrite
α_3	Three-dimensional parabolic rate constant
α_{3x}	Three-dimensional parabolic rate constant for solute X
β	Precipitate (carbide)
Γ	Capillarity coefficient
γ	Precipitate
γ_B^α	Activity coefficient of B atom in α
Δ	Volume misfit
δ	Misfit between the two lattices
ϵ	Strain
ζ	Volume fraction
ζ^{Max}	Maximum fraction for each phase
ζ_i	Fraction at any instance for the i th phase
ζ_β	Volume fraction of β phase
θ	Precipitate (cementite)
θ_B	Bragg angle
κ	Shear modulus
λ	Wavelength
μ	Chemical potential per atom
μ_X^α	Chemical potential per X atom in α

μ_X^β	Chemical potential per X atom in β
μ_{Xr}	Chemical potential per X atom in a phase with curved interfaces
ν_i^α	Atomic volume of component i in α phase
ν^β	Atomic volume of β phase
$\nu^{P,T}$	Atomic volume at P,T
ξ	Extinction distance
σ	Interfacial energy per unit area
σ_0	Energy of a coherent interface per unit area
τ	Incubation time for nucleation
ϕ	Needle aspect ratio
Ω	Supersaturation
Ω_r	Supersaturation with capillarity effect
Ω_X	Supersaturation of solute X
∇	Laplacian
χ	atomic concentration of solute
HAC	Hydrogen-assisted cracking
HAZ	Heat affected zone
HIC	Hydrogen-induced cracking
HSLA	High-strength low-alloy
IC	Interface-composition
IG	Intergranular fracture
MVC	Microvoid coalescence rupture
MTDATA	Metallurgical and Thermochemical Databank
PC	Pre-stressed concrete
QC	Quasi-cleavage fracture
SSCC	Sulfide stress corrosion cracking
TEM	Transmission electron microscope
TMCP	Thermomechanical control process
TTP	Time - temperature precipitation diagram
XEDS	X-ray energy dispersive spectroscopy

Chapter 1

Introduction

1.1 Overview

Steels are the most important and useful of all materials because of their low price and the wide range of desirable properties which can be controlled easily by changing the chemical composition and processing. The mechanical properties depend to some extent on the microstructure, which is influenced by precipitation reactions. These are therefore important in the design of microstructures for specific applications.

Alloy carbides have played an important role in the development of structural steels, for example in the strengthening and toughening of microalloyed steels and in the exploitation of secondary-hardened steels for service at elevated temperatures. A less well-known application is the introduction of carbides, such as Mo_2C and V_4C_3 , into the steel as hydrogen trapping sites to enhance the resistance to static fracture of components such as springs, bolts and power plant items [1, 2, 3]; it is in this context that the present work was initiated. The mechanical and hydrogen trapping properties depend on many parameters, but the two most significant of these are the carbide size and number density. These parameters have in the past been manipulated on the basis of experience and experimental work. The aim in this research was to develop a model for estimating the kinetics of alloy-carbide microstructures during the tempering of steels, in the hope of accelerating the design process for novel, hydrogen-resistant steels.

As will be discussed in section 3.2, a theory which generalizes the extended volume concept to simultaneous precipitation reactions has been established [4, 5]. Using this, Fujita and Bhadeshia modelled the precipitation of Mo_2C , accounting approximately for the capillarity effect in a ternary system [6]. The carbide particles were assumed to be in the form of thin cylinders with hemispherical ends, as in the Zener treatment [7]. A disadvantage of this method is that the needle aspect ratio had to be chosen arbitrarily. The purposes of the present work were threefold. Firstly, it was intended to improve on that model, with a better representation of the shape of the precipitate, for the simulation of the tempering of a Fe-Mo-C ternary martensitic steel. Secondly, the work was extended to the modelling of M_4C_3 , which is a plate-shaped particle in Fe-C-V ternary and Fe-C-Mo-V quaternary systems. The

‘M’ stands for metal atoms. Account is taken of local equilibrium, the capillarity effect, and simultaneous cementite enrichment and dissolution in a multicomponent system.

The third aspect of the work was to clarify the relationship between the hydrogen trapping capacity of steels which contain Mo_2C or M_4C_3 particles and the properties of these carbides, such as average size, number density, chemical composition and volume fraction.

1.2 High-strength steel parts in automobiles

An automobile consists of outer panels and a platform, which contains the drive system, engine system and exhausting system. High-strength steels are used for these parts to ensure safety. The weight of the platform is around 70 % of the total weight of an automobile. It is therefore necessary to reduce the weight of these parts by strengthening if fuel consumption is to be reduced.

I Bolts and fasteners

In general, bolts are manufactured from hot-rolled medium-carbon alloy steels. These steels are annealed to spheroidize the carbides, then cold-forged to shape the bolt. A typical commercial heat treatment after forging involves austenisation followed by quenching to martensite and subsequent tempering. The typical austenisation treatment is 0.5–1.0 h at 850–920 °C, and the tempering condition is 0.5–1.0 h at 350–600 °C. The tensile strength of bolts for automobiles is between 800 and 1200 MPa; this is determined by the chemical composition of the steel and the tempering temperature. The properties required are high tensile strength and yield ratio (> 0.9). The typical chemical composition for bolts is shown in Table 1.1.

C	Si	Mn	Cr	Mo	Al	N
0.35	0.20	0.35	1.20	0.30	0.01	0.008

Table 1.1: Chemical composition of a bolt steel in wt. %.

II Bearings

Bearings are manufactured from hot-rolled high-carbon alloy steels. These steels are annealed to spheroidize carbides, then cold-forged to produce the bearing shape. A typical commercial heat treatment after forging involves austenisation followed by quenching to martensite and subsequent tempering. The typical austenisation treatment is 0.5–1.0 h at 820–920 °C, and the tempering treatment is 1.0–2.0 h at 170–200 °C. The hardness is about 800 HV. The most important property for bearings is good rolling contact fatigue resistance. The typical chemical composition is shown in Table 1.2.

C	Si	Mn	Cr	Al	N
0.96	0.20	0.35	1.34	0.035	0.008

Table 1.2: Chemical composition of a bearing steel in wt. %.

III Springs

Springs are manufactured from drawn, quenched and tempered high carbon steel wires. The wires are coiled to form the spring shape. A typical commercial heat treatment involves austenisation followed by quenching to martensite followed by tempering. The typical austenisation heat-treatment is 0.5–1.0 h at 900–950 °C, with tempering for 1.0–2.0 h at 180–250 °C. The final hardness is about 500–700 HV. The most important characteristic required of springs is good fatigue resistance. Typical chemical compositions are shown in Table 1.3.

C	Si	Mn	Cr	V	Cu
0.68	0.22	0.76	-	-	0.02
0.53	0.23	0.80	0.96	0.20	0.06

Table 1.3: Chemical compositions of spring steels in wt. %.

These high strength parts use as their basis tempered martensite, because of its good balance of hardness and toughness and ease of heat treatment. In recent years, weight reduction of automobiles for fuel economy improvement, and cost reduction by elimination of some parts or process steps, have called for steels of yet higher strength. However, high-strength steels tend to suffer from hydrogen embrittlement. Hydrogen embrittlement is thus one of the largest factors obstructing the strengthening of steels.

1.3 Physical metallurgy of tempered martensitic steels

1.3.1 Tempering of martensite

The tempering of martensite is usually carried out in the range 150–600 °C. Extensive studies have been carried out on the tempering behaviour of martensitic steels. For a carbon steel, this is divided into three stages:

1. Precipitation of ϵ carbide at 70–150 °C. This has a hexagonal crystal structure ($a = 2.755 \text{ \AA}$, $c = 4.349 \text{ \AA}$ [8]) and a composition $\text{Fe}_{2.4}\text{C}$ [9], and forms as narrow plates with a well-defined orientation relationship.
2. Decomposition of retained austenite at 150–280 °C, possibly to bainite and cementite.
3. Precipitation of cementite above 200 °C. As the cementite grows, ϵ carbide dissolves.

However, the tempering of alloy steel is divided into four stages. The first three of these are the same as those of carbon steels, but the temperature at which each stage occurs depends on the alloy composition. For example, Si and Cr stabilize ϵ carbide so that the third stage occurs at a higher temperature (above 300 °C). Si and Cr also retard the growth of cementite, and steels containing these elements resist softening up to 500 °C [10]. The addition of carbide-forming elements such as Mo, V, and Nb, even in small amounts, gives a pronounced softening resistance. These elements retard the climb of dislocations and keep the dislocation density high even if the steel is tempered above 500 °C [11]. This resulting high dislocation density aids the precipitation of alloy carbides in the subsequent fourth stage.

The fourth stage of tempering of alloy steel martensite is the process during which complex alloy carbides precipitate with the complementary dissolution of cementite. These alloy carbides may themselves dissolve at later times of this stage as different, more stable carbides start to precipitate. The nucleation mechanism of alloy carbides is classified into two categories: (1) in-situ transformation and (2) separate nucleation. In the former case, carbides nucleate at the same place as the existing cementite, and the hardening effect is reduced because the distribution of the nucleating carbides is dominated by that of the existing cementite. In the alternative scenario, carbides nucleate independently of the cementite, and may produce a considerable hardening effect if the precipitates are coherent with the matrix. The initial metastable precipitates are those for which nucleation is easiest. At longer times, other more stable phases may form. Although the nucleation of these phases is more difficult, their formation leads to a reduction in the free energy of the system and is, therefore, thermodynamically favourable. The formation of the more stable precipitates is accompanied by the dissolution of the existing metastable precipitates. However, it is also possible for thermodynamically stable phase to precipitate in the early stage of the tempering sequence (e.g. Nb(C,N)) [12]. Such phases do not dissolve during subsequent tempering. In the following paragraphs, the characteristics of some carbide phases which precipitate during tempering in alloy steels will be summarized.

1.3.2 Carbides in alloy steels

In the following, ‘M’ stands for metallic elements and ‘X’ represents the interstitial elements C or N.

I M_3C

Carbon is an interstitial solute in iron and hence has a much higher mobility than substitutional solutes or iron. It is natural, therefore, that iron carbides are the first to form when virgin martensite is tempered. In low and medium carbon steels containing dislocated martensite, cementite precipitates first in the tempering process. This cementite grows by a paraequilibrium mechanism; paraequilibrium is a state in which carbon achieves a uniform chemical potential across the interface, subject to the constraint that the substitutional-solute to iron atom ratio is maintained constant everywhere [13]. The formation of paraequilibrium cementite during the tempering of martensite is considered to occur by a displacive mechanism [14, 15, 16, 17].

The steps following the rapid precipitation of paraequilibrium cementite are complicated because the chemical composition of the cementite changes as it absorbs or rejects solutes in order to achieve its equilibrium composition. Mn and Cr can dissolve into cementite in large quantities [18]. W, V, and Mo have limited solubility in cementite. The rate of enrichment will be fastest when the cementite particles are small and the ferrite is highly supersaturated in carbide-forming solute atoms [19]. Cementite, although kinetically favoured, is less stable than many alloy carbides; consequently, while the cementite composition changes, alloy carbide precipitation commences and eventually leads to the dissolution of the cementite. These processes must all be considered to occur simultaneously in any model.

II M_2X

In many cases, M_2X is the next phase to precipitate after cementite. It has a hexagonal structure and commonly precipitates as fine needles parallel to $\langle 100 \rangle_\alpha$. The orientation relationship is that of Pitsch and Schrader [20]:

$$\{0001\}_{M_2X} // \{011\}_\alpha \text{ and } \langle 11\bar{2}0 \rangle_{M_2X} // \langle 100 \rangle_\alpha$$

M_2X is generally considered to nucleate on matrix dislocations and martensite lath boundaries. Studies of an Fe-C-Mo alloy have shown that Mo_2C can also nucleate on ferrite/cementite boundaries [21]. The composition can vary widely with Mo, Cr and V soluble in significant quantities. In steels containing Mo, with no nitrogen and a low Cr content, M_2X is often close to the ideal Mo_2C composition [22].

III MX

MX is a V- or W-rich carbide. It has an fcc (face-centred cubic) structure and commonly precipitates as fine disks on $(100)_\alpha$. The orientation relationship is that of Baker and Nutting [23]:

$$\{100\}_{\text{MX}}//\{100\}_{\alpha} \text{ and } \langle 001 \rangle_{\text{MX}}//\langle 011 \rangle_{\alpha}$$

MX particles form in a fine dispersion within the martensite laths, and it is therefore believed that they contribute significantly to hardening.

IV M_7C_3

M_7C_3 is a Cr-rich carbide with a trigonal crystal structure. Typical lattice parameters are $a = 14.0 \text{ \AA}$ and $c = 4.5 \text{ \AA}$. Fe and Mn are also soluble in this phase. It usually occurs after M_2C formation [22], or after cementite formation if there has not been any intermediate M_2X precipitation [24]. It is considered that M_7C_3 will only precipitate if the Cr content is sufficiently high compared to other alloying elements [25]. If Mo is present, it is possible that M_{23}C_6 , rather than M_7C_3 , will form after M_2C . Nucleation can occur either on fresh sites or in-situ at the ferrite/cementite interface.

V M_{23}C_6

M_{23}C_6 is also a Cr-rich carbide which may, in addition, contain W, Mo, V and Ni [25]. It has a fcc crystal structure of which the typical lattice parameter is $a = 10.7 \text{ \AA}$ [26]. It forms after either M_7C_3 or M_2C and is often the equilibrium carbide in high-Cr (9–12 wt. %) steel. Nucleation occurs predominantly on prior austenite grain boundaries and lath boundaries [27].

VI M_6C

In steels containing Mo and relatively low levels of Cr, M_6C is the equilibrium carbide. It has an fcc crystal structure with a lattice parameter $a = 11.0 \text{ \AA}$ and is Mo-rich but may also contain Cr and V [26]. M_6C precipitates on the grain boundaries; therefore, it is thought that it nucleates separately from M_2X , which precipitates in the laths [28]. However, it is also reported that M_6C nucleation can occur on M_2X or M_{23}C_6 interphase boundaries [29]. In addition, nucleation is possible on prior austenite grain and lath boundaries.

1.3.3 Precipitation behaviour in Mo- and V-containing steels

I Carbide precipitation in Fe-C-Mo steels

A great deal of effort has been made to clarify the carbide precipitation behaviour in Mo steels [10, 21, 28, 30, 31, 32, 33, 34]. In alloys containing a large amount (more than 3 wt. %) of Mo, precipitation of fine Mo_2C is observed just after the onset of secondary hardening [21]. On the other hand, in normal high-strength low-alloy (HSLA) steels, in which the Mo content does not exceed 1 wt. %, it was generally difficult to observe the precipitation of alloy carbides before or at the peak hardening stage. When the steels were overaged, needle-shaped Mo_2C is observed [33]. However, using field ion microscopy (FIM), the existence of Mo_2C particles, which have a near-stoichiometric composition, was confirmed in a 0.15C-1.0Mo (wt. %) steel in an early stage of tempering [34]. Figure 1.1 shows the structure of Mo_2C [35, 36].

There is a well-defined orientation relationship between Mo_2C and the matrix [21, 31, 33]. The preferred growth direction of Mo_2C is parallel to $\langle 11\bar{2}0 \rangle_{\text{Mo}_2\text{C}} // \langle 100 \rangle_\alpha$. The spacing between the Mo atoms in Mo_2C and Fe atoms in the α phase along this direction is very similar with only a 4.5 % mismatch, as shown in Fig. 1.2.

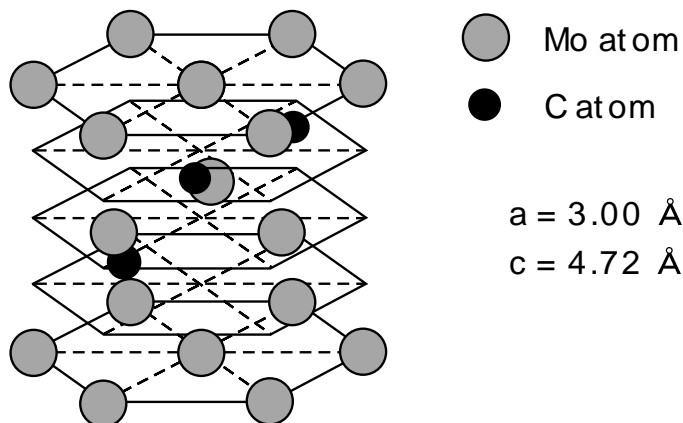


Figure 1.1: Schematic diagram of the structure of Mo_2C [35, 36].

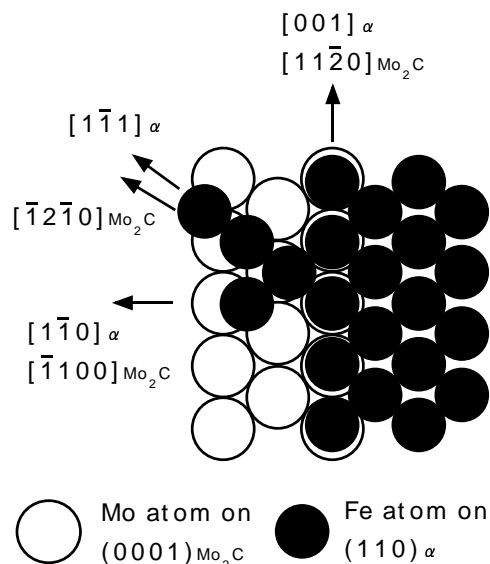


Figure 1.2: Configuration of Fe and Mo atoms on $(110)_\alpha$ which is parallel to $(0001)_{\text{Mo}_2\text{C}}$ [12].

It is reported that the phases which precipitate after Mo_2C are M_{23}C_6 and/or M_aC_b . In ternary steels, M_{23}C_6 has a composition $\text{Fe}_{21}\text{Mo}_2\text{C}_6$ and precipitates in ferrite or prior austenite grain boundaries [28]. M_aC_b is orthorhombic with composition Fe_2MoC [37]. The equilibrium carbide is thought to be M_6C , which has a composition between $\text{Fe}_3\text{Mo}_3\text{C}$ and $\text{Fe}_4\text{Mo}_2\text{C}$. It precipitates on the grain boundaries.

II Carbide precipitation in Fe-C-V steels

Only a small amount of V (0.2 wt. %) is necessary to give remarkable secondary hardening, introduced by the precipitation of V carbide in which the metal atoms adopt an fcc structure and the interstitial atoms occupy octahedral sites. Figure 1.3 shows the structure of V_4C_3 . Although the stoichiometric composition is VC, the carbide is usually depleted in C and is denoted V_4C_3 . An orientation relationship between V_4C_3 and the ferrite matrix has been reported [23, 38]. V_4C_3 forms as platelets lying on $\{100\}_\alpha$ planes. Figure 1.4 shows the configuration of V and Fe atoms in a (100) plane, indicating excellent coherency between both lattices in this plane (about 2.1 % mismatch) [12]. On the other hand, the lattice misfit is about 47 % in planes perpendicular to this plane. This is the primary reason why V_4C_3 grows in the form of thin plates. Above 500 °C, V_4C_3 precipitates as very fine particles, of length less than 20–30 Å. In this stage, because of the coherency strains, the phase of the particles cannot easily be identified in thin foil samples. However, their existence can be confirmed using X-ray diffraction and dark-field imaging. It is thought that the nucleation sites for V_4C_3 are generally dislocations. V_4C_3 is the stable phase in the Fe-C-V system.

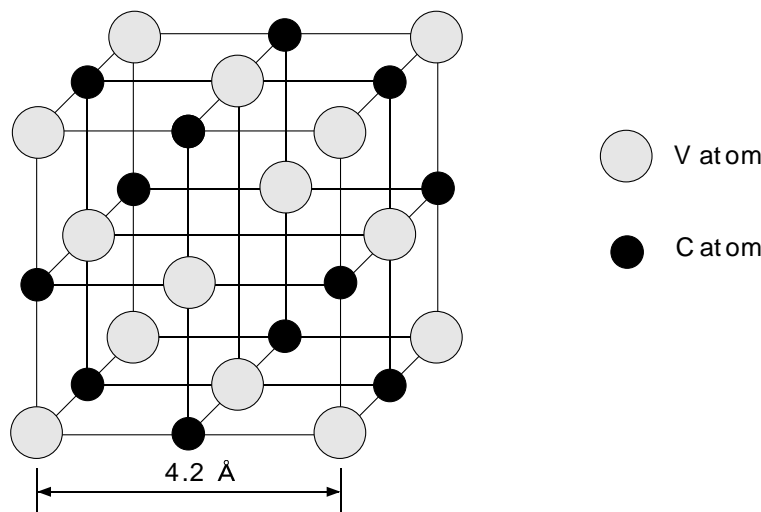


Figure 1.3: Schematic diagram of the structure of V_4C_3 .

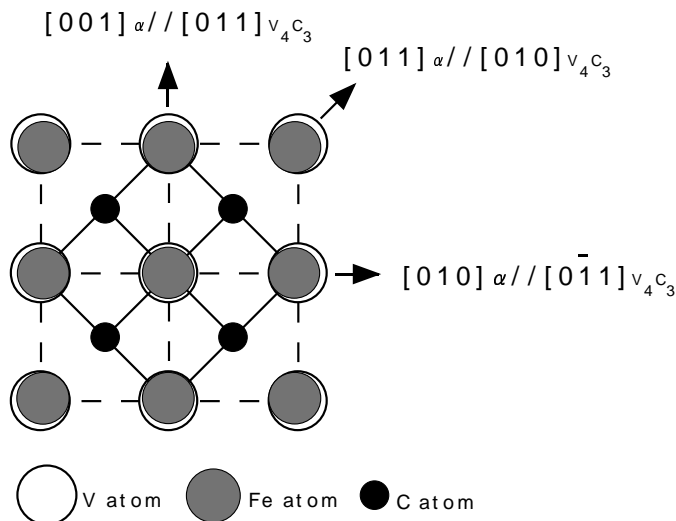


Figure 1.4: Configuration of Fe and V atoms on $(100)_\alpha$ which is parallel to $(100)_{V_4C_3}$ [12].

III Carbide precipitation in quaternary Fe-C-Mo-V steels

It is reported that the sequence of carbide precipitation in Fe-C-Mo-V steel is [39]:

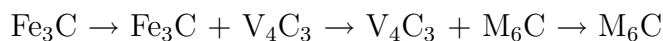


Table 1.4 contains some details of typical alloy carbides in secondary hardening steels.

System	Precipitate	Structure	Lattice parameter / Å
Fe-C-Mo	Fe_3C	Orthorhombic	$a = 4.5241, b = 5.0883, c = 6.7416$
	Mo_2C	Hexagonal	$a = 3.002, b = 4.724$
	$Fe_{21}Mo_2C_6$ ($M_{23}C_6$)	Cubic-F	$a = 10.7$
	Fe_2MoC (M_aC_b)	Orthorhombic	$a = 16.3, b = 10.0, c = 11.3$
Fe-C-V	Fe_3C	Orthorhombic	$a = 4.5241, b = 5.0883, c = 6.7416$
	V_4C_3	Cubic-F	$a = 4.2$
Fe-C-Mo-V	Fe_3C	Orthorhombic	$a = 4.5241, b = 5.0883, c = 6.7416$
	V_4C_3	Cubic-F	$a = 4.2$
	M_6C	Cubic-F	$a = 11.0$

Table 1.4: Data for alloy carbides considered in present work [37, 40]

1.4 Hydrogen embrittlement

1.4.1 Introduction

Hydrogen introduced into steels by, for example, corrosion or electroplating, causes unpredictable fracture and a deterioration in mechanical properties. The time to fracture depends on the hydrogen concentration in the steel, the tensile strength of the steel and the applied stress. It is noticeable that the hydrogen embrittlement susceptibility of steels rises significantly as the tensile strength increases, as shown in Fig. 1.5 [41].

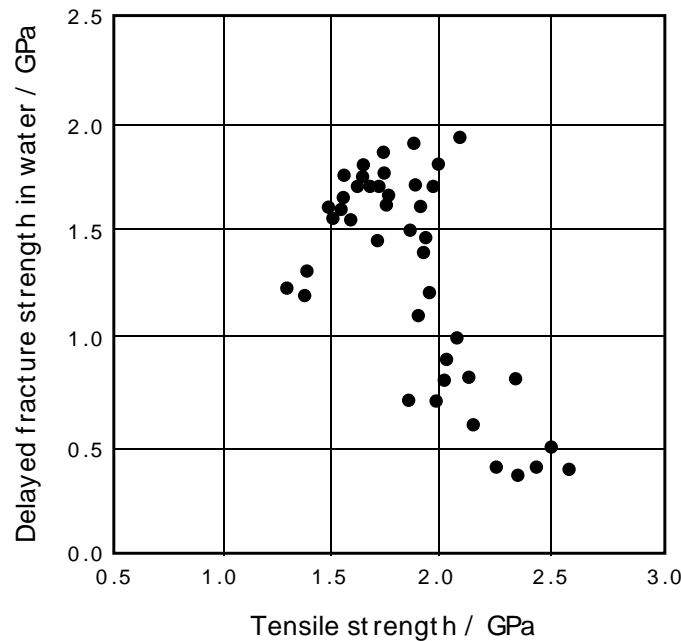


Figure 1.5: Relationship between tensile strength and delayed fracture strength in water for quenched and tempered steels [41].

1.4.2 Examples of hydrogen embrittlement phenomena

I Flake (fish eye)

The flake is sometimes called a hair-line-crack or fish-eye. Bennek *et al.* [42] advocated that flaking, which was a serious problem in high strength steel for gunnery, was caused by the pressure of gaseous hydrogen, and this problem came to be recognised as a hydrogen embrittlement phenomenon. As will be shown later, the solubility of hydrogen in the austenite phase is larger than that in ferrite. Supersaturated hydrogen in α due to the $\gamma \rightarrow \alpha$ transformation therefore segregates as gaseous hydrogen at nonmetallic inclusion/matrix interfaces and causes cracks. The gas pressure can be estimated by Sieverts' law [43, 44]:

$$C^H = C_0^H \sqrt{P^H} \exp(-\Delta H/RT) \quad (1.1)$$

where C^H is the hydrogen solubility in the metal, C_0^H is a constant, P^H is the hydrogen gas pressure (atm), ΔH is the enthalpy of solution of hydrogen in the metal, T is the absolute temperature and R is the gas constant ($\text{J K}^{-1}\text{mol}^{-1}$). In the case where $C^H=0.1$ ppm, P^H will be 1400 MPa, which is greater than the yield stress of many commercial steels.

II Sulfide stress corrosion cracking (SSCC)

There were cases in which joints of pipes used in oil wells ruptured only a few days after the commencement of operation [45, 46]. These accidents were caused by so-called sulfide stress corrosion cracking (SSCC) which was considered to be a kind of stress corrosion cracking; however, it was later clarified that SSCC was caused by hydrogen, which was absorbed into the steel from the H_2S -containing environment.

III Cold cracking in the heat affected zone of weldments

When a steel is welded, the heat affected zone (HAZ) of the parent steel is hardened and becomes susceptible to hydrogen embrittlement cracking. There are two types of hydrogen cracking in a HAZ or the weld metal: (a) that occurring during welding and (b) that occurring during service. The latter is called ‘stress corrosion cracking of the hydrogen embrittlement type’, and is caused by hydrogen entering into a weldment from moist hydrogen sulfide gas or other hydrogenous environments in service. Names for the former type include ‘cold cracking’, ‘delayed cracking’ and ‘HAZ hydrogen cracking’ [47].

IV Hydrogen induced cracking (HIC)

HIC, which is caused by the pressure of gaseous hydrogen segregating at the interfaces between nonmetallic inclusions and the matrix, is a serious problem for line pipes. It occurs in environments in which H_2S exists in high concentrations, and is known as blister. It is noticeable that HIC occurs even when steels are not stressed. HIC is a typical hydrogen embrittlement phenomenon for low tensile strength steels.

V Delayed fracture

Delayed fracture is a phenomenon in which bolts or pre-stressed concrete (PC) steel bars with tensile strengths of over 1000 MPa suddenly fail some time after loading. It is caused by hydrogen introduced into the steel by, for example, corrosion or electroplating. The fracture is dominated by intergranular cracking. The critical hydrogen concentration for delayed fracture strongly depends on the tensile strength of the steel and the applied stress; for example, it is below 0.1 wt. ppm for a 1500 MPa martensitic steel [3], and therefore can be provided even by atmospheric corrosion. Delayed fracture is a typical hydrogen embrittlement phenomenon in high tensile strength steel.

1.4.3 Fracture modes

The fracture modes of hydrogen embrittlement include microvoid coalescence (MVC), quasi-cleavage fracture (QC) and intergranular fracture (IG) [48].

The QC mode is particularly characteristic of hydrogen embrittlement. The crystallographic orientation of a hydrogen-embrittlement fracture is on the $\{110\}$ plane, the same as in ordinary cleavage fracture or brittle fracture. Gerberich *et al.* suggested, from SEM observations which clarified that there were striations on the hydrogen embrittlement fracture surface, that hydrogen embrittlement cracks progressed by $\{100\}$ discontinuous cleavage [49].

The IG mode is predominant in higher-carbon martensitic steels. It was considered that IG-mode fracture was explained by the decohesion model [50]. However, Lynch observed that even on the IG mode fracture surface, there were traces of plastic deformation such as small dimples [51]. Robertson *et al.* have shown, using environmental cell transmission electron microscopy, that the fracture occurs in the vicinity of, but not at, grain boundaries in stainless alloys [52].

Beachem has shown the interrelationship between the stress intensity factor, the hydrogen concentration and the hydrogen-assisted fracture mode at crack tips, using pre-cracked samples [48]. The MVC mode is predominant when the stress intensity factor (K) is high, and the QC mode at intermediate K . IG predominates when K is low (Fig. 1.6).

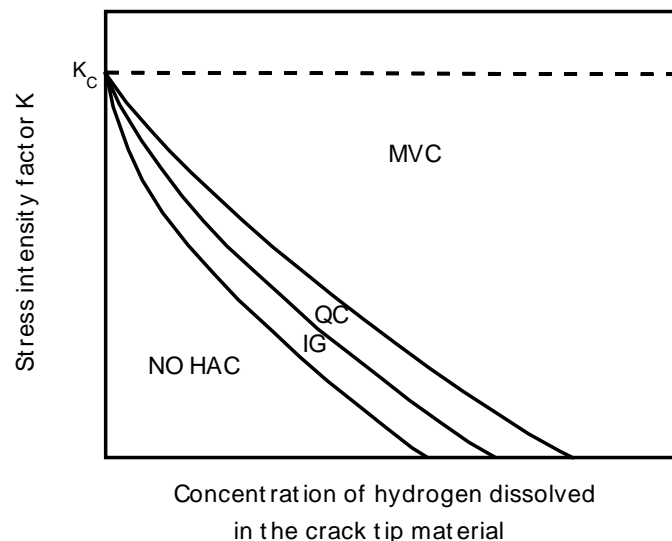


Figure 1.6: Effects on fracture modes of hydrogen concentration at crack tip and stress intensity factor [48]. HAC denotes hydrogen-assisted cracking and IG, QC and MVC denote intergranular, quasi-cleavage and microvoid coalescence fracture modes, respectively. K_C is the critical stress intensity factor at which cracks propagate without hydrogen.

1.4.4 Hydrogen trapping in steels

According to Sieverts' law, the solubility of hydrogen in ferrite should be very low at room temperature, e.g. 7×10^{-4} wt. ppm at 1 atm H_2 gas. However, practical steels can absorb 0.1 wt. ppm hydrogen in an atmospheric environment because of the existence of many kinds of trapping sites for hydrogen. The hydrogen trapping energy depends on the type of trapping site. Some kinds of sites show a high trapping energy [53]; in other words, hydrogen is fixed at these sites and should be harmless. The hydrogen trapping phenomenon is, therefore, considered to be practical method of improving the hydrogen embrittlement resistance of steels. There has been much research on hydrogen trapping; the following are considered to be hydrogen trapping sites:

1. dislocations [54, 55, 56, 57, 58];
2. prior austenite grain boundaries [55, 57, 58];
3. microvoids [55];
4. MnS/ α interfaces [56];
5. cementite/ α interfaces [55, 59, 60];
6. boron [61];
7. TiC [53];
8. V_4C_3 [2, 3, 62, 63];
9. Mo_2C [3].

Amongst these, V_4C_3 and Mo_2C have been used in some steels for bolts and springs [2, 3, 63]. The hydrogen trapping behaviour of carbides was studied using tritium autoradiography. It was observed that hydrogen was trapped at incoherent interfaces between carbides and the matrix [64]. However, the relationship between the volume fraction or surface area of carbide and the amount of trapped hydrogen has not yet been studied systematically. It is therefore difficult to design an optimal microstructure for the purpose of hydrogen trapping with an appropriate chemical composition and heat treatment condition.

1.5 Summary

Alloy carbides are of great importance in obtaining reliable mechanical properties and hydrogen embrittlement resistance in a variety of steels. Especially in tempered martensitic steels for automobile parts, they play a very important role in controlling the microstructure and obtaining the required strength. Although a great deal of experimental work has been carried out to characterise the precipitation process, this is still not fully understood. There is therefore a demand for the physical modelling of carbide precipitation kinetics.

Chapter 2

Theories for isothermal precipitation kinetics

2.1 Classical nucleation theory

Heterophase fluctuations, which are small, local fluctuations of phase structure and concentration in systems of two or more components, cause the nucleation of phase transformations. The free energy change associated with the nucleation process is dominated by volume free energy, surface free energy and misfit strain energy terms. When a spherical embryo with a radius r^I is created by heterophase fluctuation, the total free energy change can be represented by summing all of these contributions:

$$\Delta G = \frac{4}{3}\pi(r^I)^3\Delta G_V + 4\pi(r^I)^2\sigma + \frac{4}{3}\pi(r^I)^3\Delta G_\epsilon \quad (2.1)$$

where ΔG_V is the chemical free energy change per unit volume and has a negative value. σ is the interfacial energy per unit area and ΔG_ϵ is the misfit strain energy per unit volume.

2.1.1 Misfit strain energy

Nabarro gave the elastic strain energy for an ellipsoidal nucleus of β phase having semi-axes a, a, c in an isotropic α matrix as:

$$\Delta G_\epsilon = \frac{2}{3}\kappa\Delta^2\nu^\beta f(c/a) \quad (2.2)$$

where Δ is the volume misfit and κ is the shear modulus of the matrix [65]. Δ is defined as:

$$\frac{\nu^\beta - \nu^\alpha}{\nu^\beta} \quad (2.3)$$

where ν^α and ν^β are the specific volumes of atoms in the α matrix and the β precipitate phase, respectively. Thus the elastic strain energy is proportional to the square of the volume misfit, Δ^2 . The function $f(c/a)$ is a factor that takes into account the shape effect and is shown in Fig. 2.1.

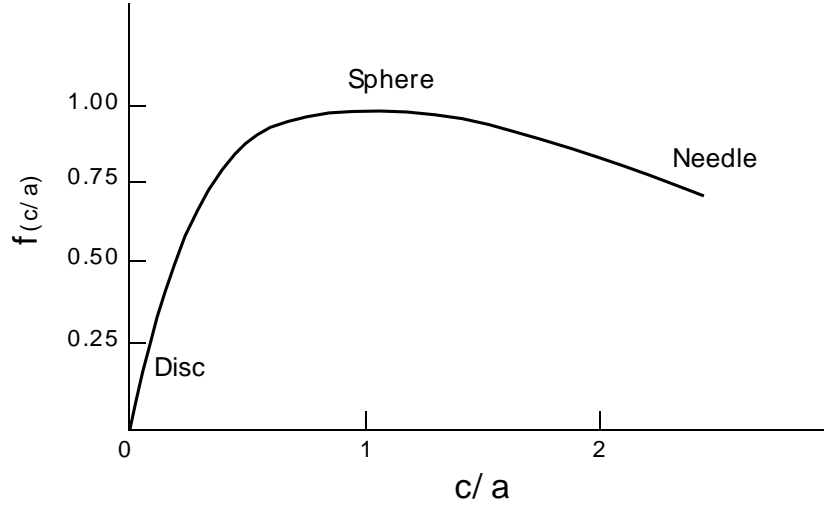


Figure 2.1: An illustration of the variation of the function $f(c/a)$ of an incoherent nucleus with its shape [65].

2.1.2 Interfacial energy

Boundaries between different solid phases can be classified into coherent, semi-coherent and incoherent interfaces. For nucleation in crystalline solids, σ can vary widely from very low values for a coherent interface to high values for an incoherent interface. A coherent interface arises when all the lattice planes of the two phases are continuous across the interface. The strain associated with a coherent interface raises the total energy of the system, and for sufficiently large atomic misfit, it would be energetically more favourable to replace the coherent interface with a semi-coherent interface in which the misfit is periodically taken up by misfit dislocations. When the interfacial plane has a very different atomic configuration in the two adjoining phases, or even if it is similar but the inter-atomic distances of the two phases differ by more than 25 %, there will not be good matching across the interface and the interface will be incoherent [66].

If d_e and d_m are the unstressed inter-atomic spacings of the embryo and the matrix respectively, the misfit between the two lattices, δ , is defined by:

$$\delta = \left| \frac{d_e - d_m}{d_e} \right| \quad (2.4)$$

If the lattice of the embryo is distorted at the interface with the matrix lattice such that the inter-atomic spacing of the embryo becomes d , the strain can be expressed as follows:

$$\epsilon = \left| \frac{d_e - d}{d_e} \right| \quad (2.5)$$

Thus, $\epsilon = 0$ for an incoherent interface and $\epsilon = \delta$ for a coherent interface.

For a semi-coherent interface on which the magnitude of the Burgers vector of the dislocation at the interface is b , for small values of δ , $(\delta - \epsilon)/b$ is the approximate number density of edge dislocations which are introduced in the interface to accommodate the misfit between two phases.

The interfacial energy can be considered approximately to be the sum of two parts: (a) a chemical contribution, for a fully coherent interface, and (b) a structural term which is the extra energy caused by the misfit dislocations. The interfacial energy, accordingly, can in general be expressed as follows:

$$\sigma = \sigma_0 + C_1(\delta - \epsilon) \quad (2.6)$$

where σ_0 is the surface energy of a coherent interface and C_1 is a coefficient related to dislocation energy. Therefore, σ will vary from low values for coherent interfaces to high values for incoherent interfaces. In general, σ_0 may be up to 200 mJ m⁻² and σ ranges between 200 and 500 mJ m⁻² for a semi-coherent interface and may be up to 1000 mJ m⁻² for an incoherent interface. Therefore, nuclei with coherent interfaces precipitate preferentially [66].

2.1.3 Activation energy for nucleation

Figure 2.2 shows the relationship between ΔG and r^I which is derived from equation 2.1. The maximum free energy occurs at a critical radius, r^* , when the net free energy change has a value G^* , known as the activation energy for nucleation. r^* is represented as:

$$r^* = \frac{-2\sigma}{(\Delta G_V + \Delta G_\epsilon)} \quad (2.7)$$

The activation energy is:

$$G^* = \frac{16\pi}{3} \frac{\sigma^3}{(\Delta G_V + \Delta G_\epsilon)^2} \quad (2.8)$$

2.1.4 Nucleation rate

The number density of critical-sized embryos N_n is represented as follows [67]:

$$N_n = N_V \exp\left(\frac{-G^*}{kT}\right) \quad (2.9)$$

where N_n is the number of critical-sized embryos containing n atoms per unit volume of the system, N_V is the number of nucleation sites per unit volume of the system and k is the Boltzmann constant. Each critical-sized embryo can be made supercritical and become a

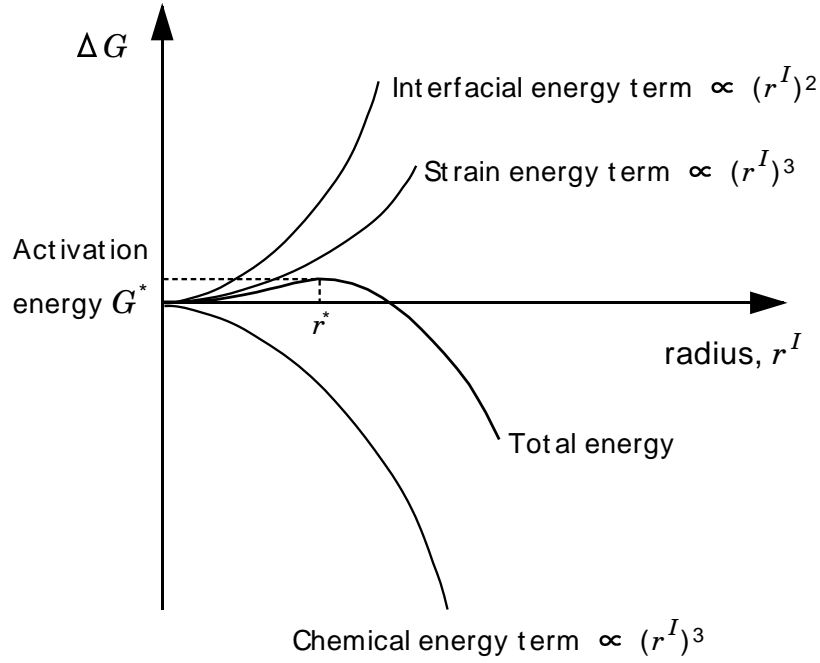


Figure 2.2: The free energy change associated with the formation of a nucleus as a function of radius r^I .

nucleus by transferring an atom in contact with the embryo into it. The formulation of this is complicated, but to a good approximation, the nucleation rate is given by:

$$I = N_V \frac{kT}{h} \exp \left\{ \frac{-(G^* + Q^*)}{kT} \right\} \quad (2.10)$$

where Q^* is the free energy of activation for the transfer of atoms across the interface (approximately equal to the activation energy for diffusion when the nucleus is coherent) and h is the Planck constant [68].

2.1.5 Chemical driving force

In order to evaluate equation 2.10, it is necessary to determine G^* , i.e. ΔG_V . Figure 2.3 shows schematically the free energy curves of the matrix α and the precipitate β in a Fe-C binary system. Equilibrium precipitation causes the free energy of the system to decrease by ΔG_0 as shown in Fig. 2.3 (a). The corresponding free energy change per unit mole of equilibrium precipitate is, to a good approximation, given by:

$$\Delta G_n = \Delta G_0 \frac{(c^{\beta\alpha} - c^{\alpha\beta})}{(\bar{c} - c^{\alpha\beta})} \quad (2.11)$$

where $c^{\beta\alpha}$ is the concentration of the solute in β in equilibrium with α , $c^{\alpha\beta}$ is the concentration of the solute in α in equilibrium with β and \bar{c} is the concentration of the solute in the alloy.

However, equation 2.11 does not describe the free energy change for nucleation, because the volume fraction of nuclei is so small compared with that of the equilibrium precipitate that the matrix composition hardly changes during nucleation. In such a case, the alternative nucleus composition which is determined by the energy gap between two parallel tangents, one of which is a tangent to the free energy curve for α at the point for \bar{c} , leads to the maximum energy change ΔG_m (Fig. 2.3 (b)) [19].

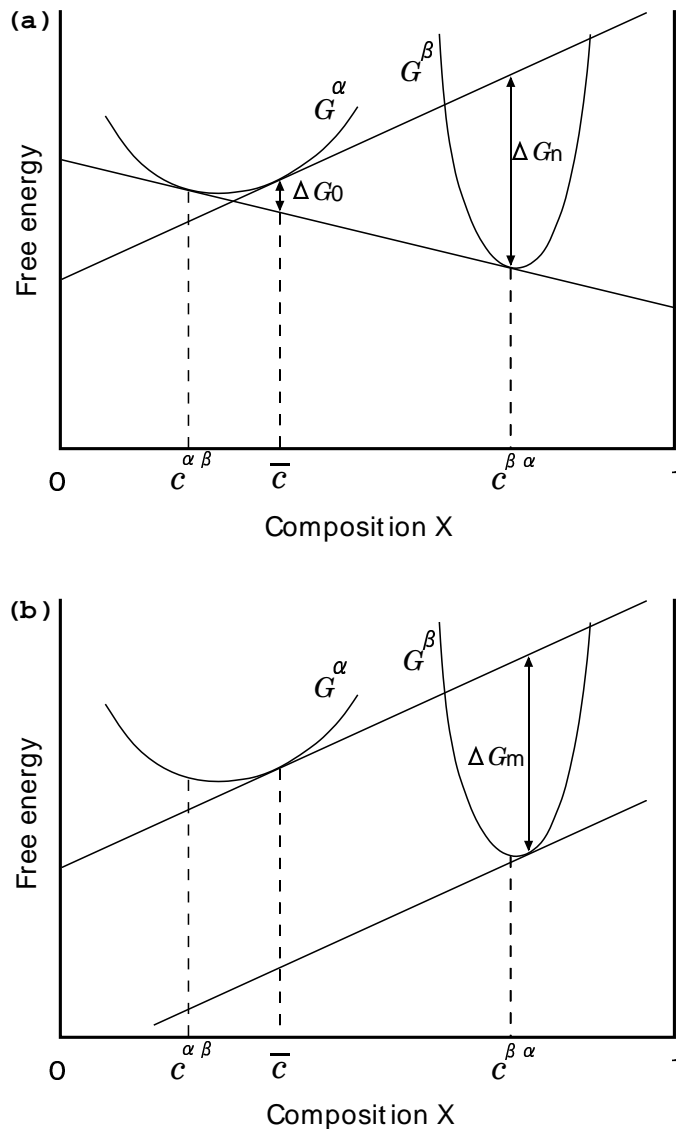


Figure 2.3: An illustration of the construction for finding the driving force for nucleation.

2.2 Diffusion-controlled growth theory (binary system)

At the interface between the matrix and a precipitate phase, the structure, composition, or both, change discontinuously. These discontinuities are maintained during the motion of this interface, which constitutes growth of the precipitate phase.

Some kinds of transformations, such as martensitic transformation, occur without a composition change. However, in many transformations, the product has a different composition from the parent phase. The velocity of interfacial motion then depends on the mobility of the atoms in the matrix and the rate of atomic transfer across the interface.

Consider the precipitation of a β particle which grows in a matrix of α in a multicomponent system. Mass-balance must be satisfied for each element at the β/α interface. Zener presented the classical solution for a binary system using the following assumptions [69]:

- a. growth is isothermal;
- b. it is controlled by diffusion of solute in the matrix, α ;
- c. interface compositions are given by local equilibrium;
- d. the diffusion coefficient in α is independent of composition;
- e. the growth is shape-preserving;
- f. the growth occurs in a semi-infinite medium.

At first, for simplicity, one-dimensional growth will be considered.

2.2.1 One-dimensional growth

Figure 2.4 shows the solute concentration profile adjacent to the moving interface in a two-component system. $\chi^{\beta\alpha}$ is the solute concentration in the precipitate β which is in equilibrium with α , $\chi^{\alpha\beta}$ is the solute concentration in the matrix which is in equilibrium with β , and $\bar{\chi}$ is the mean solute concentration in the alloy. From Fick's first law, the flux at the interface is given by

$$J_{x=x^I} = -D \left(\frac{d\chi}{dx} \right)_{x=x^I} \quad (2.12)$$

where x is the coordinate normal to the interface, D is the diffusion coefficient of the solute and x^I is the position of the interface. In order to maintain the concentrations $\chi^{\beta\alpha}$ and $\chi^{\alpha\beta}$ at the interface, this flux must be equal to the rate at which the solute is partitioned:

$$v(\chi^{\beta\alpha} - \chi^{\alpha\beta}) = J_{x=x^I} \quad (2.13)$$

where v is the interface velocity. Using Zener's approximation which is shown in Fig. 2.5,

$$\left(\frac{d\chi}{dx} \right)_{x=x^I} = \frac{(\chi^{\alpha\beta} - \bar{\chi})}{L} \quad (2.14)$$

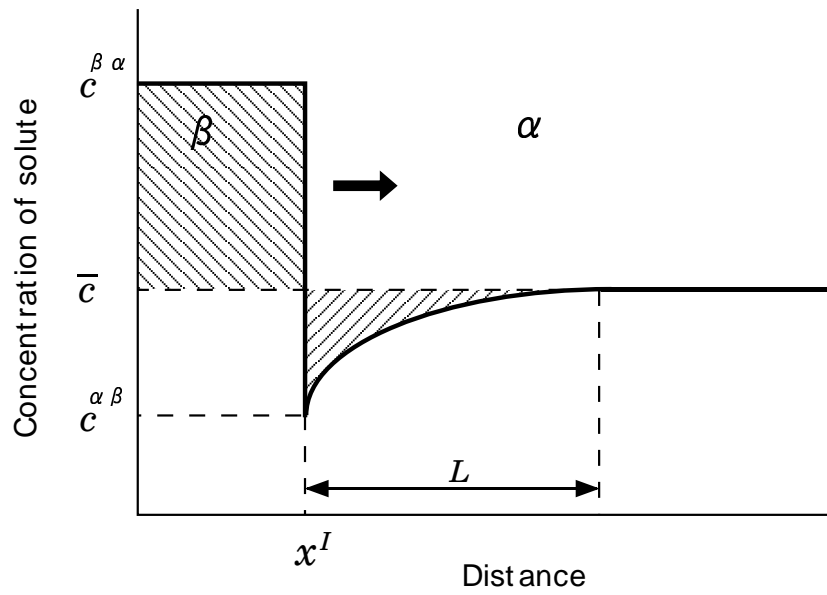


Figure 2.4: Schematic illustration of the solute mole fraction profile at the interface between matrix α and growing precipitate β . L is a nominal diffusion distance and x^I is the position of the interface.

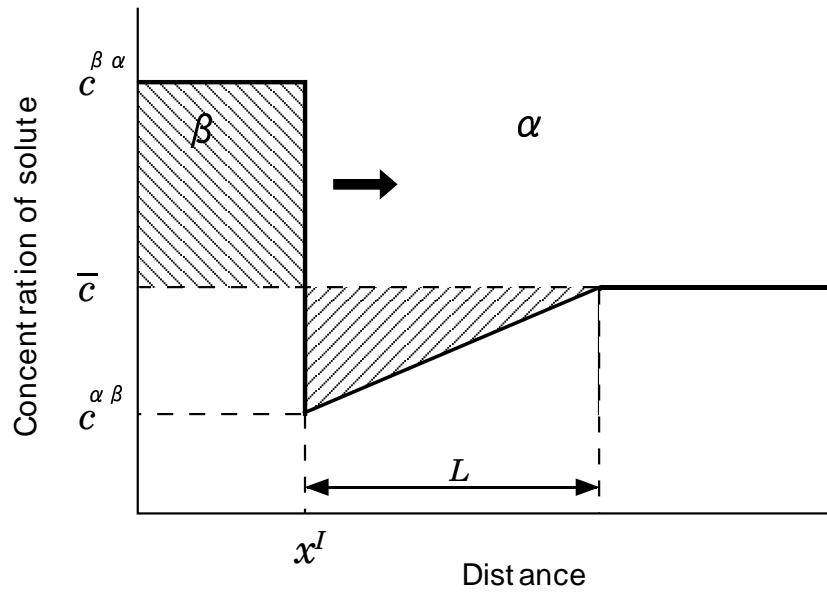


Figure 2.5: The constant mole fraction gradient approximation profile of solute atoms [7].

where L is the diffusion distance. From conservation of mass, L can be calculated as:

$$L = 2x^I \frac{(\chi^{\beta\alpha} - \bar{\chi})}{(\bar{\chi} - \chi^{\alpha\beta})} \quad (2.15)$$

Hence, from equations 2.12-2.15, the interface velocity can be written as:

$$v = \frac{D}{2x^I} \frac{(\bar{\chi} - \chi^{\alpha\beta})^2}{(\chi^{\beta\alpha} - \chi^{\alpha\beta})(\chi^{\beta\alpha} - \bar{\chi})} \quad (2.16)$$

For the case of alloy carbide precipitation, in which the solute elements are typically Cr, Mo, or V, $\chi^{\beta\alpha}$ is much larger than $\chi^{\alpha\beta}$ and $\bar{\chi}$. Therefore, it may be assumed that $(\chi^{\beta\alpha} - \chi^{\alpha\beta})$ is nearly equal to $(\chi^{\beta\alpha} - \bar{\chi})$. Equation 2.16 is then approximated as follows:

$$2x^I v = D\Omega^2 \quad (2.17)$$

where Ω is the supersaturation of the solute which can be represented as:

$$\Omega = \frac{(\bar{\chi} - \chi^{\alpha\beta})}{(\chi^{\beta\alpha} - \chi^{\alpha\beta})} \quad (2.18)$$

Considering that $v = \frac{dx^I}{dt}$, equation 2.18 can be integrated to give the profile dimension as:

$$x^I = \Omega\sqrt{Dt} \quad (2.19)$$

This is the parabolic growth law. The precipitate dimension is found to be proportional to \sqrt{Dt} and growth is parabolic with a velocity varying as $\sqrt{D/t}$. In fact, parabolic growth is expected in all circumstances where the diffusion distance increases as the particle grows.

2.2.2 Growth of spherical particles

Parabolic growth is expected during the diffusion-controlled growth of spheres:

$$r^I = \alpha_3\sqrt{Dt} \quad (2.20)$$

where r^I is the radius of the particle and α_3 is a proportionality constant analogous to Ω in equation 2.19. In general, the growth velocity can be described as:

$$v = \frac{dr^I}{dt} = \frac{D}{(c^{\beta\alpha} - c^{\alpha\beta})} \left(\frac{\partial c}{\partial r} \right)_{r=r^I} \quad (2.21)$$

where r is the radial coordinate. To determine α_3 in equation 2.20, it is necessary to solve Fick's second law:

$$\frac{\partial c}{\partial t} = \frac{D}{r^2} \frac{\partial}{\partial r} \left(r^2 \frac{\partial c}{\partial r} \right) \quad (2.22)$$

The boundary conditions for the solution of this equation are $c(r, 0) = \bar{c}$ and $c(r^I, t) = c^{\alpha\beta}$. Zener showed that if $c^{\alpha\beta}$ is constant, the distribution of solute is given by:

$$c(r, t) = \bar{c} + (c^{\alpha\beta} - \bar{c}) \frac{\phi(r/\sqrt{Dt})}{\phi(r^I/\sqrt{Dt})} \quad (2.23)$$

where

$$\phi(x) = \int_x^\infty \eta^{-2} \exp\left(\frac{-\eta^2}{4}\right) d\eta \quad (2.24)$$

The term r^I/\sqrt{Dt} is a dimensionless function of the concentration and determines the growth velocity. This term is α_3 in equation 2.20 and for three-dimensional growth, this will be:

$$\alpha_3 = C_2 \sqrt{2} \sqrt{\frac{(\bar{c} - c^{\alpha\beta})}{(c^{\beta\alpha} - \bar{c})}} \quad (2.25)$$

where C_2 varies from 1 to $\sqrt{3}$ as \bar{c} changes from $c^{\alpha\beta}$ to $c^{\beta\alpha}$. This parabolic growth law can be applied for the growth of spherical particles in which the particle radius is large enough so that the capillarity effect on the equilibrium concentration is small.

2.2.3 Growth of particles with the capillarity effect

Capillarity effect in a binary system

When interfaces are curved, there are additional energy terms which cannot be neglected. Consider an assembly in a binary system consisting of elements A and B in which a β precipitate of surface area O and surface free energy per unit area σ is in equilibrium with the α matrix. Equilibrium at a planar interface is expressed by:

$$\begin{aligned} \mu_A^\alpha(c^{\alpha\beta}) &= \mu_A^\beta(c^{\beta\alpha}) \\ \mu_B^\alpha(c^{\alpha\beta}) &= \mu_B^\beta(c^{\beta\alpha}) \end{aligned} \quad (2.26)$$

where μ_A^α is the chemical potential per atom of A in the α phase, and $c^{\alpha\beta}$ and $c^{\beta\alpha}$ are the equilibrium compositions of the matrix and the precipitate, respectively, for infinite planar interfaces. Brackets are used to denote that the chemical potential is a function of the composition. Curved interfaces contribute an additional thermodynamic potential so that both the solubility limit $c^{\alpha\beta}$ and the equilibrium composition $c^{\beta\alpha}$ vary with the particle size. These quantities are then denoted as $c_r^{\alpha\beta}$ and $c_r^{\beta\alpha}$ [70].

When a curved interface moves during particle growth, in which dn atoms are transferred from the α matrix to the β phase, there is an additional energy term σdO due to the

increase in surface area of the β particle. As shown in Fig. 2.6, this term is $\sigma \frac{dO}{dn}$ represented as a displacement of G^β to G_r^β and the new equilibrium compositions are given by the points of contact of the common tangent on the curves of G^α and G_r^β . The new equilibrium conditions are therefore:

$$\begin{aligned}\mu_A^\alpha(c_r^{\alpha\beta}) &= \mu_A^\beta(c_r^{\beta\alpha}) = \mu_{Ar} \\ \mu_B^\alpha(c_r^{\alpha\beta}) &= \mu_B^\beta(c_r^{\beta\alpha}) = \mu_{Br}\end{aligned}\tag{2.27}$$

From the geometry of Fig. 2.6, the following equation can be obtained to a good approximation:

$$\mu_{Br} - \mu_B = \frac{(1 - c^{\alpha\beta})}{(c^{\beta\alpha} - c^{\alpha\beta})} \sigma \frac{dO}{dn}\tag{2.28}$$

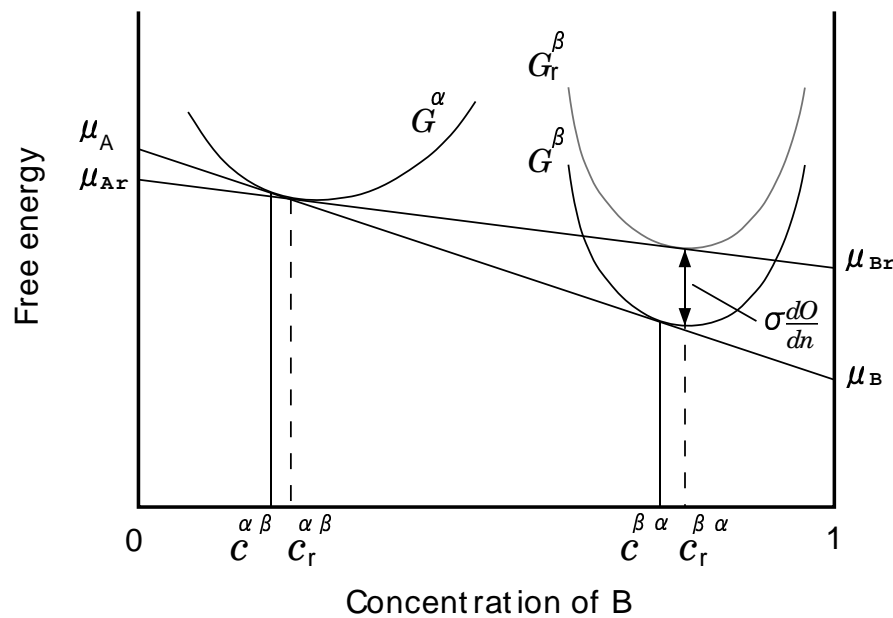


Figure 2.6: Schematic illustration of free energy and interface concentration changes due to the capillarity effect in an A-B binary system [70].

On the other hand, in terms of activity coefficients, the following relation is obtained:

$$\mu_{Br} - \mu_B = kT \ln \left(\frac{\gamma_{Br}^\alpha c_r^{\alpha\beta}}{\gamma_B^\alpha c^{\alpha\beta}} \right)\tag{2.29}$$

where γ_B^α is the activity coefficient of B atoms in the α phase. For dilute solutions or those which obey Henry's law, γ_B^α is a constant. Equations 2.28 and 2.29 then give [70]:

$$\ln\left(\frac{c_r^{\alpha\beta}}{c^{\alpha\beta}}\right) \simeq \frac{(c_r^{\alpha\beta} - c^{\alpha\beta})}{c^{\alpha\beta}} = \frac{\sigma}{kT} \frac{dO}{dn} \frac{(1 - c^{\alpha\beta})}{(c^{\beta\alpha} - c^{\alpha\beta})} \quad (2.30)$$

For spherical particles or the tips of needles,

$$\frac{dO}{dn} = \frac{2\nu^\beta}{r^{IC}} \quad (2.31)$$

For edges of plate-shaped particles,

$$\frac{dO}{dn} = \frac{\nu^\beta}{r^{IC}} \quad (2.32)$$

where ν^β is the volume per atom in the β phase, and r^{IC} is the radius of curvature at the interface.

Therefore, $c_r^{\alpha\beta}$ for a spherical particle and the hemispherical tip of a needle is given by:

$$c_r^{\alpha\beta} = \left(1 + \frac{2\Gamma}{r^{IC}}\right)c^{\alpha\beta} \quad (2.33)$$

and $c_r^{\alpha\beta}$ for a plate edge is given by:

$$c_r^{\alpha\beta} = \left(1 + \frac{\Gamma}{r^{IC}}\right)c^{\alpha\beta} \quad (2.34)$$

where Γ is the capillarity coefficient, given by:

$$\Gamma = \frac{\sigma\nu^\beta}{kT} \frac{(1 - c^{\alpha\beta})}{(c^{\beta\alpha} - c^{\alpha\beta})} \quad (2.35)$$

Zener model

For the case of lengthening of plates or needles, the growth is greatly affected by the capillarity effect because of the small radius of curvature at the interface. Zener assumed that the tip of a needle was hemispherical and that the edge of a plate was hemicylindrical so that the composition of the α phase at the interface, $c_r^{\alpha\beta}$, was constant over the curved surface [7]. Figure 2.7 shows the mole fraction profile across the curved interface, in which the equilibrium mole fraction in the matrix at the tip or edge, $c_r^{\alpha\beta}$, is increased relative to that for a planar interface, $c^{\alpha\beta}$, due to the Gibbs-Thomson effect. The mole fraction gradient of the solute element is $(\bar{c} - c_r^{\alpha\beta})/L$, where L is a characteristic diffusion distance which can be expressed as $L = C_3 r^{IC}$, where C_3 is a constant. Therefore, diffusion occurs rapidly. Assuming that the curvature of the interface is constant during growth then, by analogy with equation 2.16, the lengthening rate is given by:

$$v = \frac{D}{C_3 r^{IC}} \frac{(\bar{c} - c_r^{\alpha\beta})}{(c_r^{\beta\alpha} - c_r^{\alpha\beta})} \quad (2.36)$$

The supersaturation due to the capillarity effect is given by:

$$\Omega_r = \frac{(\bar{c} - c_r^{\alpha\beta})}{(c_r^{\beta\alpha} - c_r^{\alpha\beta})} \quad (2.37)$$

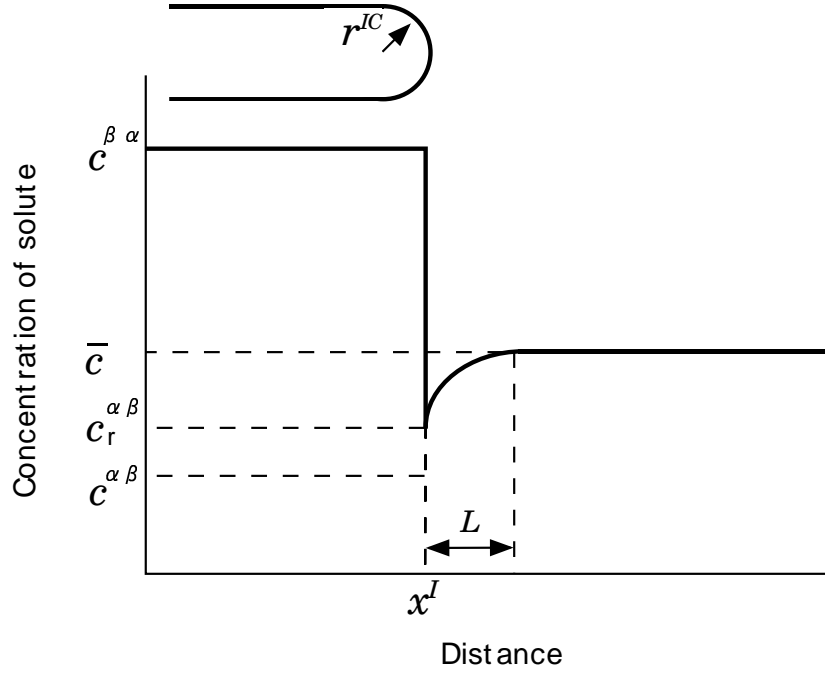


Figure 2.7: Schematic illustration of the solute mole fraction profile at the interface between the matrix α and the growing needle-shaped precipitate β which has a curved interface. r^{IC} is the radius of curvature at the needle tip, L is the nominal diffusion distance and x^I is the position of the interface.

Assuming that the value of $(c_r^{\beta\alpha} - c_r^{\alpha\beta})$ is nearly equal to that of $(c^{\beta\alpha} - c^{\alpha\beta})$, equation 2.37 can be simplified as follows:

$$\Omega_r = \left(1 - \frac{r_c}{r^{IC}}\right) \Omega \quad (2.38)$$

where r_c is the critical tip radius at which Ω_r is reduced to zero and growth ceases, and is given as follows, by combining equation 2.33, 2.34 and 2.37:

$$r_c = \frac{2c^{\alpha\beta}\Gamma}{(\bar{c} - c^{\alpha\beta})} \quad (\text{for a needle})$$

$$r_c = \frac{c^{\alpha\beta}\Gamma}{(\bar{c} - c^{\alpha\beta})} \quad (\text{for a plate})$$
(2.39)

Therefore, the growth rate v is given by:

$$v = \frac{D\Omega}{C_3 r^{IC}} \left(1 - \frac{r_c}{r^{IC}}\right)$$
(2.40)

It is not possible to give a reliable estimate of C_3 , but if it is assumed that Zener's approximation represented in Fig. 2.4 remains valid, $C_3 \simeq 1$. According to equation 2.40, in the absence of soft-impingement, the lengthening rate should be constant for a given plate thickness or a radius of curvature (linear growth).

Equation 2.40 expresses the relationship between the growth rate and the tip radius but does not predict either uniquely. To calculate the growth rate, it is necessary to evaluate the value of r^{IC} . Zener assumed that the growth rate would be the maximum possible velocity given by equation 2.40, and in this case, $r^{IC} = 2r_c$. Therefore, from equation 2.40, the growth rate is given by:

$$v = \frac{D\Omega}{2r^{IC}}$$
(2.41)

In the theory of diffusion, it is convenient to introduce a dimensionless velocity parameter known as the Péclet number \bar{p} which is defined as:

$$\bar{p} = \frac{vr^{IC}}{2D}$$
(2.42)

The Zener theory thus gives:

$$\Omega_r = \Omega \left(1 - \frac{r_c}{r^{IC}}\right) = 2C_3 \bar{p}$$
(2.43)

Zener-Hillert model

Hillert attempted to give a more rigorous treatment of the diffusion problem for plate growth, by considering the mole fraction at the interface in terms of two co-ordinates: the direction of growth and the normal to the plane of the plate [71]. The steady-state growth rate is given by:

$$v = \frac{D\Omega}{2} \frac{(c^{\beta\alpha} - c_r^{\alpha\beta})}{(c^{\beta\alpha} - \bar{c})} \frac{1}{m} \left(1 - \frac{m_c}{m}\right)$$
(2.44)

where m and m_c are arbitrary constants, approximately equal to r^{IC} and r_c , respectively. This corresponds to Zener's equation 2.40 with [72]:

$$C_3 = 2 \frac{(c^{\beta\alpha} - \bar{c})}{(c^{\beta\alpha} - c_r^{\alpha\beta})} \quad (2.45)$$

and Ω_r can be represented as:

$$\Omega_r = \frac{4\bar{p}}{1 + 4\bar{p}} \quad (2.46)$$

Ivantsov model

An exact solution of the diffusion problem for a particle growing with constant velocity in one direction was obtained by Horvay and Cahn [73] based on the analysis due to Ivantsov [74]. This shows that, for the case in which the particle shape is a elliptical paraboloid of revolution, the Ivantsov theory gives:

$$\Omega = \bar{p} \exp(\bar{p}) \int_p^\infty \frac{1}{\eta} \exp(-\eta) d\eta \equiv \bar{p} \exp(\bar{p}) E_1(\bar{p}) \quad (2.47)$$

where $E_1(\bar{p})$ represents the exponential integral [75]. For the case in which the particle shape is a paraboloid plate of revolution, the Ivantsov theory gives:

$$\Omega = \sqrt{\pi\bar{p}} \exp(\bar{p}) \operatorname{erfc}\sqrt{\bar{p}} \quad (2.48)$$

Figure 2.8 shows the shapes used to represent needle- and plate-shaped precipitates.

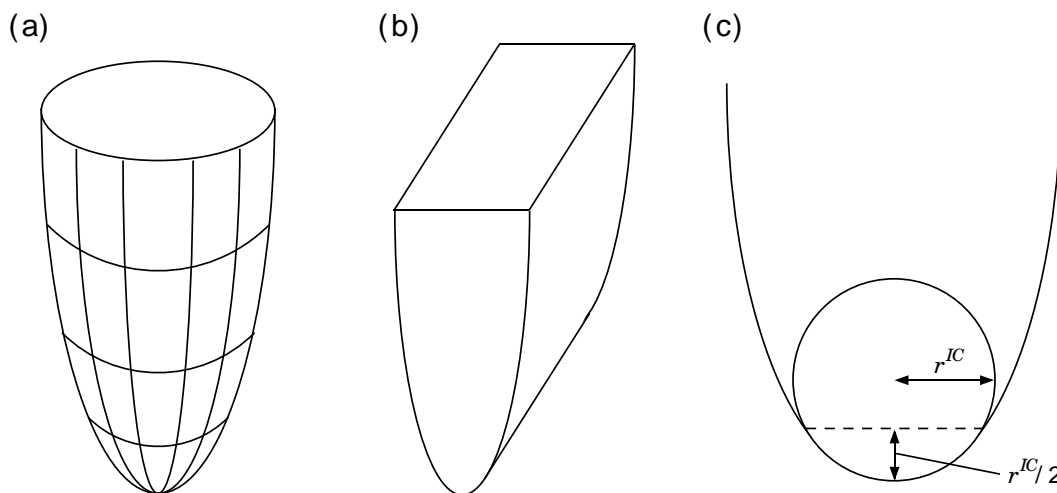


Figure 2.8: (a) paraboloid of revolution; (b) parabolic cylinder; (c) radius of the paraboloid tip.

In contrast to equation 2.40, Horvay and Cahn expressed the general results for elliptical paraboloids in the form:

$$vr^{IC} \propto \Omega^Z \quad (2.49)$$

where Z is a slowly varying function of Ω . The Zener theory gives $Z = 1$, whilst the Ivantsov theory gives $Z = 1.1$ to 1.4 , for a needle-shaped particle. For a parabolic plate, the Ivantsov theory gives $Z = 2$.

Trivedi model

The most comprehensive theory is due to Trivedi [76], based on the analysis due to Ivantsov [74]. In this, a needle is assumed to be in the form of a shape-preserving paraboloid of revolution and a plate is assumed to be in the form of a shape-preserving parabolic cylinder of revolution, as shown in Fig. 2.8. The capillarity effect and interface kinetics effect are accounted for.

According to Trivedi, the supersaturation for a parabolic needle can be represented as:

$$\Omega = \bar{p} \exp(\bar{p}) E_1(\bar{p}) \left(1 + \frac{v}{v_c} \Omega R_1(\bar{p}) + \frac{r_c}{r^{IC}} \Omega R_2(\bar{p}) \right) \quad (2.50)$$

where v_c is the velocity of a flat interface which is completely governed by interface processes. $R_1(\bar{p})$ and $R_2(\bar{p})$ are:

$$\begin{aligned} R_1(\bar{p}) &= \frac{1}{2\bar{p}} N_1(\bar{p}) - 1 \\ R_2(\bar{p}) &= \frac{1}{4\bar{p}} N_2(\bar{p}) - 1 \end{aligned} \quad (2.51)$$

The values of $N_1(\bar{p})$ and $N_2(\bar{p})$ are [76]:

$$N_1(\bar{p}) = 2\bar{p}^{3/2} \exp(\bar{p}) \sum_{n=0}^{\infty} \frac{\Gamma(n+0.5)}{\Gamma(n+1)} I_{2n} \operatorname{erfc}(\sqrt{\bar{p}}) \frac{\psi(n+1, 2, \bar{p})}{\psi(n+1, 1, \bar{p})} L_n^0(\bar{p}) \quad (2.52)$$

$$N_2(\bar{p}) = 2\bar{p}^{3/2} \exp(\bar{p}) \sum_{n=0}^{\infty} 2\sqrt{\bar{p}} I_{2n+1} \operatorname{erfc}(\sqrt{\bar{p}}) + N_1(\bar{p}) \quad (2.53)$$

where $I_n \operatorname{erfc}(x)$, $\Gamma(x)$, $L_n^0(x)$ and $\psi(x)$ are the normalized integral error function, gamma function, Laguerre polynomial and confluent hypergeometric function of the second type, respectively. The values of the functions $N_1(\bar{p})$ and $N_2(\bar{p})$ were obtained numerically by Trivedi; they become 1.4050 and 3.8410 respectively for small values of supersaturation

($\Omega \ll 1$) [76]. Equation 2.50 gives the general solution for the growth of precipitate needles. The right-hand side is a sum of three terms of which the first is the result obtained by Ivantsov [74] for the case of an iso-concentration boundary. The second and the third terms are corrections to that solution due to the interface kinetics and capillarity effects respectively.

For a parabolic plate, the supersaturation can be represented by:

$$\Omega = \sqrt{\pi\bar{p}} \exp(\bar{p}) \operatorname{erfc}\sqrt{\bar{p}} \left(1 + \frac{v}{v_c} \Omega S_1(\bar{p}) + \frac{r_c}{r^{IC}} \Omega S_2(\bar{p}) \right) \quad (2.54)$$

where $S_1(\bar{p})$, $S_2(\bar{p})$ are:

$$S_1(\bar{p}) = \frac{1}{2\bar{p}} M_1(\bar{p}) - 1 \quad (2.55)$$

$$S_2(\bar{p}) = \frac{1}{4\bar{p}} M_2(\bar{p}) - 1$$

The values of $M_1(\bar{p})$ and $M_2(\bar{p})$ are [77]:

$$M_1(\bar{p}) = \frac{2\bar{p}}{\pi} \sum_{m=0}^{\infty} \Gamma\left(m + \frac{1}{2}\right) \frac{I_{2m-1} \operatorname{erfc}(\sqrt{\bar{p}})}{I_{2m} \operatorname{erfc}(\sqrt{\bar{p}})} \psi\left(m + \frac{1}{2}, 1, \bar{p}\right) \quad (2.56)$$

$$M_2(\bar{p}) = \frac{4\bar{p}^2}{\pi} \sum_{m=0}^{\infty} \Gamma\left(m + \frac{3}{2}\right) \frac{I_{2m-1} \operatorname{erfc}(\sqrt{\bar{p}})}{I_{2m} \operatorname{erfc}(\sqrt{\bar{p}})} \psi\left(m + \frac{3}{2}, 2, \bar{p}\right) \quad (2.57)$$

where $I_m \operatorname{erfc}(x)$ and $\Gamma(x)$ are the normalized integral error function [75] and the gamma function [14], respectively. The values of the functions $M_1(\bar{p})$ and $M_2(\bar{p})$ were obtained numerically by Trivedi and become $2/\pi$ and $4/\pi$ respectively for small values of supersaturation ($\Omega \ll 1$) [77]. Equation 2.54 gives the general solution for the growth of precipitate plates. The right-hand side is a sum of three terms of which the first is the result obtained by Ivantsov [74] for the case of an iso-concentration boundary. The second and the third terms are corrections to that solution due to the interface kinetics and capillarity effects respectively.

However, equations 2.50 and 2.54 give only the value of \bar{p} for the given values of Ω and the values of r_c/r^{IC} and v/v_c . It has been suggested by Zener that this solution corresponds to the radius of curvature which gives rise to the maximum growth rate [7].

For a needle (paraboloid of revolution), this maximum growth rate can be obtained by differentiating equation 2.50 with respect to r^{IC} and setting $\frac{\partial v}{\partial r^{IC}} = 0$, which gives [78]:

$$0 = (g(\bar{p}))^2 \frac{r_c}{r^{IC}} \left(2 \frac{\bar{p}}{q} R'_1(\bar{p}) - \frac{1}{\bar{p}} R_2(\bar{p}) + R'_2(\bar{p}) \right) + \frac{g(\bar{p})}{\bar{p}} + g(\bar{p}) - 1 \quad (2.58)$$

where $g(\bar{p}) = \bar{p} \exp(\bar{p}) E_1(\bar{p})$ and q , a parameter which indicates the relative magnitudes of the interface kinetics and diffusion effects, is given by $q = v_c/(2D/r_c)$.

For a plate (parabolic cylinder), the maximum growth rate can be obtained by differentiating equation 2.54 with respect to r^{IC} and setting $\frac{\partial v}{\partial r^{IC}} = 0$, which gives :

$$0 = (g^*(\bar{p}))^2 \frac{r_c}{r^{IC}} \left(\frac{\bar{p}}{q^*} S_1'(\bar{p}) - \frac{1}{\bar{p}} S_2(\bar{p}) + S_2'(\bar{p}) \right) + \frac{g^*(\bar{p})}{2\bar{p}} + g^*(\bar{p}) - 1 \quad (2.59)$$

where $g^*(\bar{p}) = (\pi\bar{p})^2 \exp(\bar{p}) \operatorname{erfc}(\bar{p})$ and $q^* = v_c/(D/r_c)$.

The solution of equations 2.58 and 2.59 has been obtained for large values of Ω ($\Omega \geq 0.2$) [77] and for small values of Ω ($\Omega \leq 1.0$) [78].

2.3 Diffusion-controlled growth theory (ternary systems)

2.3.1 Growth of spherical particles

For a ternary system, it is necessary to deal with two independent flow equations, one for each diffusible component, with four interdiffusion coefficients:

$$J_1 = -D_{11} \nabla \chi_1 - D_{12} \nabla \chi_2 \quad (2.60)$$

$$J_2 = -D_{21} \nabla \chi_1 - D_{22} \nabla \chi_2$$

where χ_1 and χ_2 represent the concentrations of solutes 1 and 2, respectively, and ∇ is a Laplacian. Coates suggested that, if it is assumed that the cross terms D_{12} and D_{21} can be neglected, i.e., compositional atoms diffuse independently, growth behaviour in a ternary system obeying Zener's model (described in section 2.2.2) can be deduced by a straightforward extension from binary to ternary systems [79]. Coates also inspected the effect of this simplification and demonstrated that, while there are observable changes in behaviour, the overall behaviour is not affected qualitatively. With this assumption, the flow equations can be written:

$$\begin{aligned} \frac{\partial \chi_1}{\partial t} &\simeq D_{11} \nabla^2 \chi_1 = \frac{D}{r^2} \frac{\partial}{\partial r} \left(r^2 \frac{\partial \chi_1}{\partial r} \right) \\ \frac{\partial \chi_2}{\partial t} &\simeq D_{22} \nabla^2 \chi_2 = \frac{D}{r^2} \frac{\partial}{\partial r} \left(r^2 \frac{\partial \chi_2}{\partial r} \right) \end{aligned} \quad (2.61)$$

Each equation involves only one kind of composition variable and is identical in form to equation 2.22 for binary systems. Therefore, in the same way, equations 2.23 to 2.25, which are identical to the result obtained for a binary system, can be derived for solutes 1 and 2.

In a ternary system, the position of the moving interface must be identical for compositions 1 and 2. Accordingly, equation 2.20 becomes:

$$r^I = \alpha_{3_1} \sqrt{D_1 t}$$

$$r^I = \alpha_{3_2} \sqrt{D_2 t}$$
(2.62)

where α_{3_1} and α_{3_2} are the parabolic rate constants for solutes 1 and 2 respectively. Since $D_1 \neq D_2$, α_{3_1} cannot in general be equal to α_{3_2} . α_{3_1} and α_{3_2} are functions of their respective supersaturations, so:

$$\alpha_{3_2}(\Omega_2) = \sqrt{\frac{D_1}{D_2}} \alpha_{3_1}(\Omega_1)$$
(2.63)

Figure 2.9 is a schematic diagram of a two-phase field in a ternary system. The tie-lines, e.g. MP , connect compositions of the two phases which are in equilibrium. An alloy whose nominal composition A lies in the two-phase field consists of two phases whose equilibrium compositions are M' and P' given by the ends of the tie-line passing through the point A .

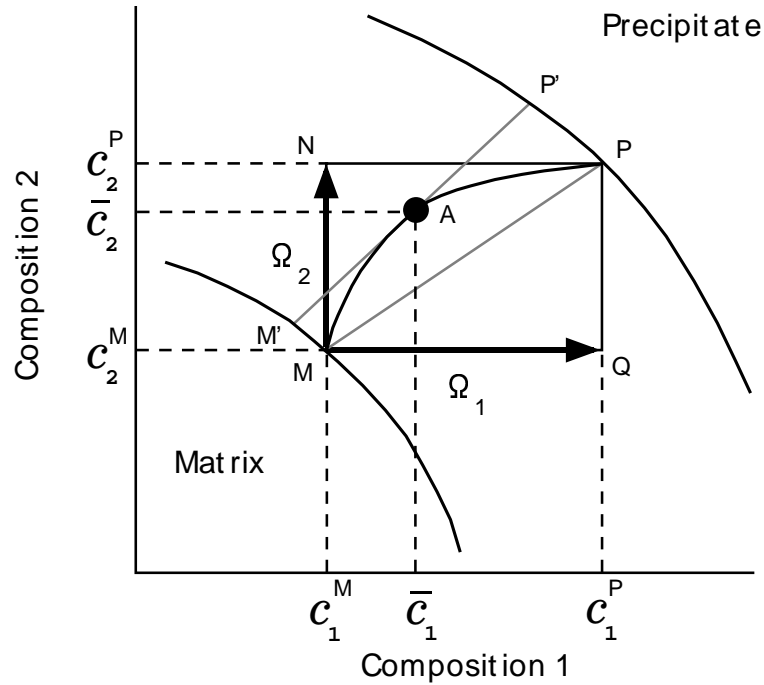


Figure 2.9: Schematic diagram of a two-phase field in a ternary system. An alloy A may grow with interface compositions M and P , and exhibit different supersaturations Ω_1 and Ω_2 for each component.

During the growth of the precipitate into the matrix for alloy A , the system chooses tie-lines giving a combination of supersaturations for components 1 and 2 that will satisfy equation 2.63, to ensure that the fluxes of both components are appropriate to give the same

interface velocity $\frac{dr^I}{dt}$ for both components. Accordingly, the tie-line that represents the compositions at the M/P interface need not pass through the point A .

In Fig. 2.9, the supersaturation is zero at the point M and unity at the point P , and therefore the sides MN and MQ may be taken to be coordinate axes which represent the supersaturations Ω_1 and Ω_2 . Here, by definition:

$$\begin{aligned}\Omega_1 &= \frac{(\bar{c}_1 - c_1^M)}{(c_1^P - c_1^M)} \\ \Omega_2 &= \frac{(\bar{c}_2 - c_2^M)}{(c_2^P - c_2^M)}\end{aligned}\tag{2.64}$$

Thus, an alloy composition A , (\bar{c}_1, \bar{c}_2) anywhere inside rectangle $MNPQ$ may be associated with the tie-line MP permitting corresponding combinations of the (Ω_1, Ω_2) pair.

For a given value of the ratio D_1/D_2 , equation 2.63 represents a relation between the supersaturations of composition 1 and 2. Figure 2.10 is a plot of the resulting relations for a range of values of the ratio D_1/D_2 . A curve for a given value of D_1/D_2 gives the alloy compositions which will select the same tie-line in order to satisfy equation 2.63 during the growth stage. Application of this calculation for each tie-line in the two-phase region yields an envelope of curves which covers this field, and accordingly permits any nominal alloy composition to associate with the interface compositions M and P satisfying equation 2.63. These curves are called interface composition contours or, briefly, IC contours.

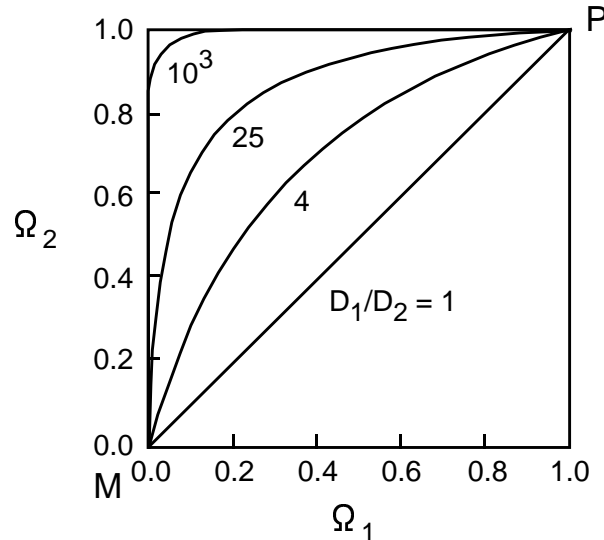


Figure 2.10: Relation between the interface-composition (IC) contour and the ratio of diffusion coefficients D_1/D_2 . $\Omega_1 = \frac{(\bar{c}_1 - c_1^M)}{(c_1^P - c_1^M)}$, $\Omega_2 = \frac{(\bar{c}_2 - c_2^M)}{(c_2^P - c_2^M)}$ where 1 and 2 represent elements.

When $D_1/D_2 = 1$, the IC contour coincides with the tie-line MP . If $D_1/D_2 \gg 1$, the IC contour lies adjacent to the sides of rectangle for each tie-line in Fig. 2.10. Figure 2.11 shows IC contours for the latter case, which is characterized by the condition $D_1/D_2 \equiv D_C/D_X \gg 1$ for a Fe-C-X ternary system. This pattern divides the $M+P$ two-phase field into two regions, labelled I and II in Fig. 2.11. Region I is the low supersaturation region in which IC contour segments lie adjacent to the lines of constant c_C . Region II at high supersaturations has IC contour segments at nearly constant c_X .

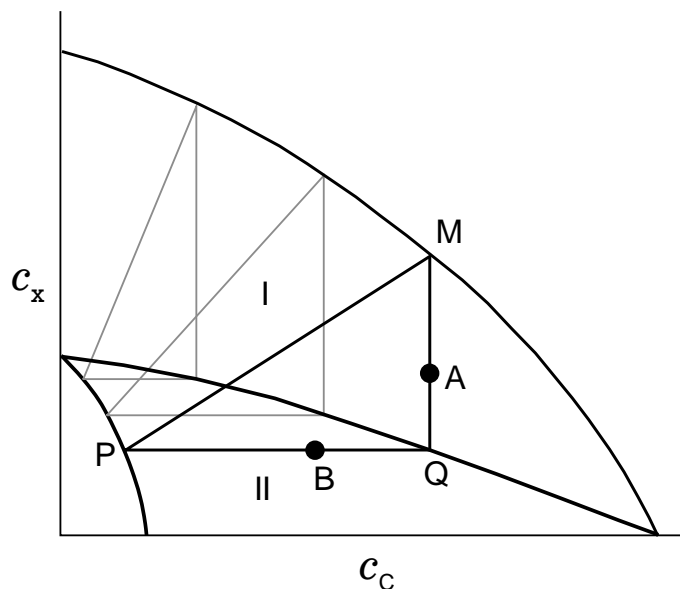


Figure 2.11: Interface-composition (IC) contour M-Q-P for a Fe-C-X alloy system.

An alloy composition A in region I would choose the interface composition MP and establish the concentration profile shown in Fig. 2.12 (a) with a small carbon concentration gradient satisfying local equilibrium. An alloy B in region II would also choose MP for its interface composition and yield the profile shown in Fig. 2.12 (b) with a concentration spike of alloy element X. In region I, growth is accompanied by the partitioning of X. In contrast, in region II, the system solves the problem caused by the condition $D_C/D_X \gg 1$ by choosing a precipitate composition c_X which is not significantly different from the gross composition of B , \bar{c}_X ; thus, the growth will proceed without partitioning.

Coates later extended his analysis to take into account the influence of the ternary diffusional interaction [80]. The result of this was consistent with the thermodynamic concepts proposed by Hillert [81].

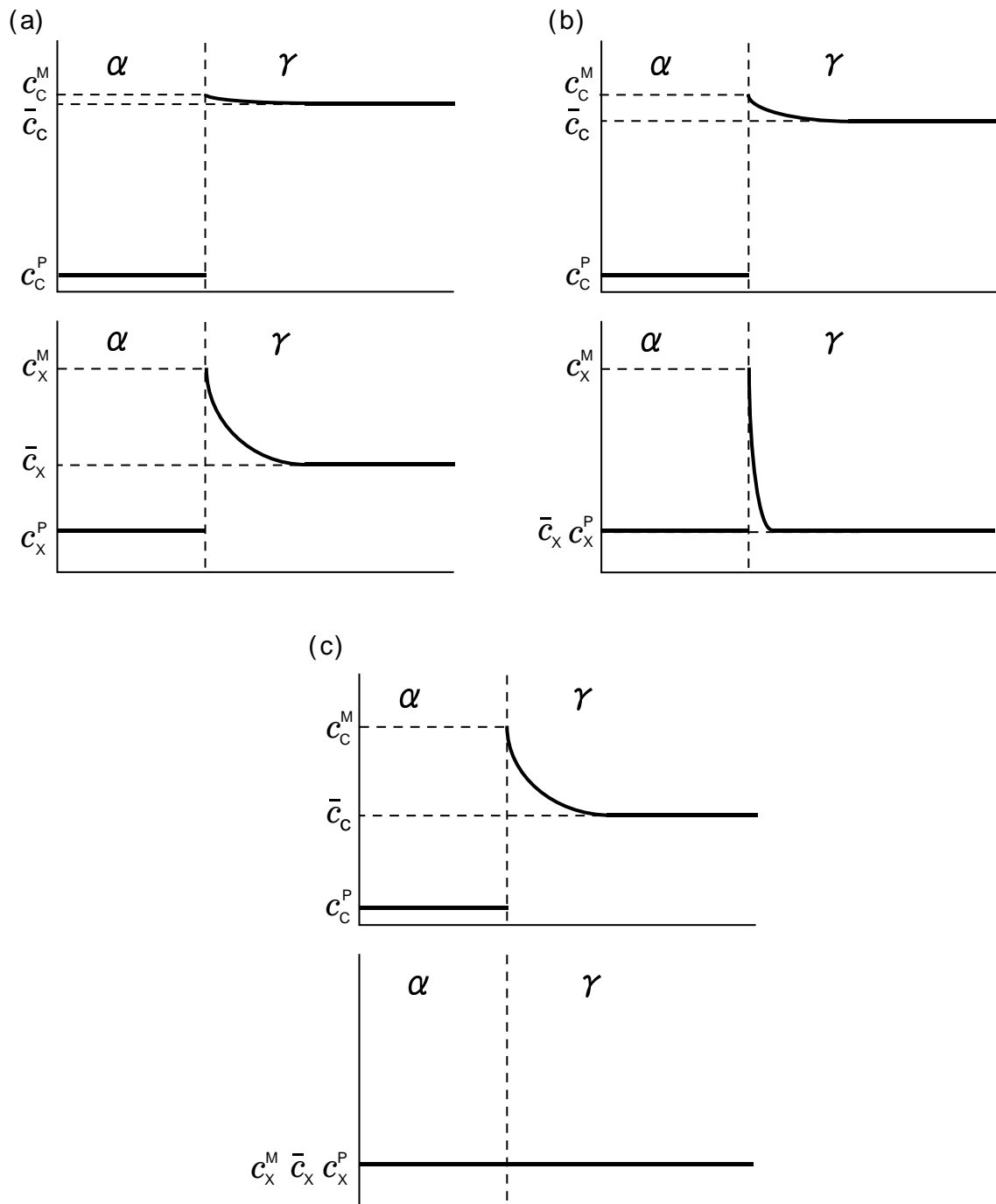


Figure 2.12: Schematic composition profiles for alloy compositions A (in region I) and B (in region II) in Fig. 2.11 according to Coates' equilibrium model, (a) and (b). (c) represents composition profiles for the case of paraequilibrium. The vertical axes represent solute concentration and the horizontal axes represent distance.

2.3.2 Growth of particles with the capillarity effect

Fujita and Bhadeshia [5, 6] modelled the precipitation of carbides in multicomponent systems, taking account of the capillarity effect. This model was based on Coates' local equilibrium theory for a ternary system. The capillarity effect was evaluated using equation 2.33 which is for a binary system. This model plays an important role in the present work and will therefore be discussed in detail in section 3.2.

2.4 Diffusion-controlled growth theory (higher order systems)

If all the cross terms of the diffusion coefficient are assumed to be negligible, then the $(n - 1)$ flux equations system can be derived independently in an n -component system, in the same manner as in equation 2.61.

Figure 2.13 describes the relation between the tie-line MP and IC contour M-Q-P in a Fe-C-X-Y quaternary system [82]. The resulting IC contour is a space curve constructed so that its projection on each ij plane matches the appropriate mapping of the contour curve for components i and j in Fig. 2.10.

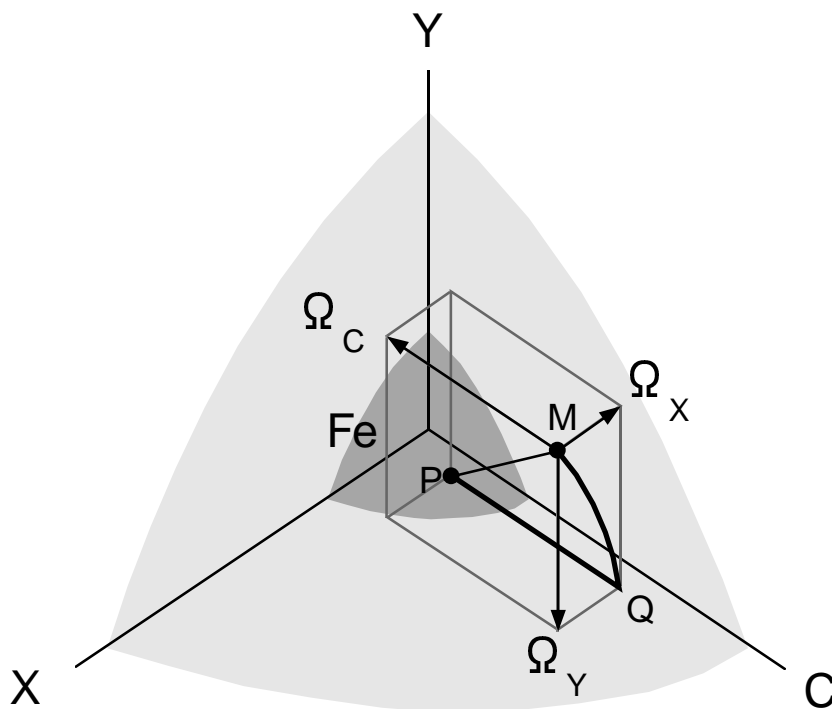


Figure 2.13: Mapping of Coates' construction on tie-line MP and IC contour M-Q-P in quaternary system.

2.5 Ostwald ripening

Coarsening occurs because the total energy of the system is reduced by eliminating interfaces; in practice, large particles grow more rapidly than small particles during precipitation, and large particles grow at the expense of smaller ones during classical coarsening. The average particle size therefore increases with time. Classical coarsening occurs slowly because of the small energies associated with the interfaces compared with the free energy change accompanying precipitation. Ostwald ripening can therefore be assumed to occur after the ‘completion’ of the precipitation. Coarsening theory for spheres leads to the following relationship [83, 84]:

$$\bar{r}^3 - r_0^3 = \left(\frac{8\sigma\nu^\beta D c^{\alpha\beta}}{9kT} \right) t \quad (2.65)$$

where \bar{r} is the average particle radius, r_0 is the initial average particle radius, ν^β is the atomic volume of the β phase, D is the solute diffusion coefficient, σ is the interfacial energy, $c^{\alpha\beta}$ is the equilibrium solute concentration in the matrix at the infinite plane, k is the Boltzmann constant and t is time. This equation is valid when the equilibrium volume fraction of β phase is small.

2.6 Summary

As shown in this chapter, diffusion-controlled growth theories for binary systems which take account of the capillarity effect have been well developed. Because of the difficulties in the evaluation of the capillarity effect and the mass balance of elements at the interfaces in multicomponent systems, theories or models taking account of capillarity have not yet been developed to such an extent in these systems. However, for needle-shaped or plate-shaped precipitates, the capillarity effect must be taken into account, since they have a small tip radius at the moving front of the interface. In the following chapter, existing models for carbide precipitation in multicomponent systems will be summarised.

Chapter 3

Modelling of carbide precipitation during tempering

3.1 Models for precipitation of a single phase

Many attempts have been made to predict precipitation kinetics. Liu and Jonas analyzed data on Ti(CN) precipitation in austenite, as determined by stress relaxation using the classical theory of nucleation, and predicted the start time for the strain-induced precipitation of Ti(CN) in austenite [85].

Akamatsu *et al.* predicted the kinetics of Nb(C,N) precipitation in austenite by introducing local equilibrium at the austenite/Nb(C,N) interface into the classical nucleation and spherical-growth theory [86]. This model properly accounted for the diffusion of both Nb and C. The carbide was modelled as $\text{Nb}(\text{C}_x, \text{N}_{1-x})$, and the results showed that the rate of MC-type carbide precipitation was influenced by the concentration ratio $\bar{c}_{\text{Nb}}/\bar{c}_{\text{C}}$. Akamatsu *et al.* adopted the methods used by Liu and Jonas [85], but the chemical driving force for nucleation was evaluated not for the equilibrium composition, which was defined by the tie-line passing through the alloy composition, but for the calculated initial nucleus composition. It was assumed that nucleation took place on dislocations. However, Akamatsu *et al.* did not take into account the capillarity effect in their calculations, and did not allow for the destruction of nucleation sites as precipitation proceeded.

Okaguchi *et al.* developed a model for predicting carbonitride precipitation during the hot working of Nb-Ti HSLA steels [87]. The solubility and composition of the precipitates, and the chemical driving force for the precipitation from supersaturated austenite, were estimated using a regular solution model composed of four binary compounds. The carbide was modelled as $(\text{Nb}_x, \text{Ti}_{1-x})(\text{C}_y, \text{N}_{1-y})$. The effect of the elastic energy of a dislocation (the nucleation site) on the free energy change was taken into account and the change in the density of dislocations which acted as nucleation sites during hot working was calculated using plasticity theory. The time dependence of the volume fraction and the particle radii were also calculated on the basis of classical nucleation theory. According to the experiments, the Nb/(Nb+Ti) concentration ratio in the carbide varies from 0.1 to 0.3. The calculations

showed much better agreement with this observation than the independent precipitation (NbC+TiC+TiN) model of Keown and Wilson [88].

The precipitation of NbC during deformation at high temperatures has also been simulated by Bon *et al.* and Saito *et al.* [89, 90].

All of these models deal with only one precipitation reaction occurring at any instant. In practice, there are cases where many reactions may occur simultaneously.

3.2 Models for precipitation of several phases in multicomponent systems

Robson and Bhadeshia developed a simultaneous precipitation model by extending the classical Kolmogorov-Johnson-Mehl-Avrami concept of extended space [91, 92, 93] to many phases [4, 94, 95]. Fujita and Bhadeshia improved that model to deal with carbide size and to account for the capillarity effect [5].

3.2.1 Robson and Bhadeshia model

I Simple simultaneous reaction

When precipitates β and θ form at the same time, the increase in real volumes of β and θ , dV_β and dV_θ respectively, are given in terms of their extended volumes, dV_β^e and dV_θ^e , as follows:

$$dV_\beta = \left(1 - \frac{V_\beta + V_\theta}{V}\right) dV_\beta^e \quad (3.1)$$

$$dV_\theta = \left(1 - \frac{V_\beta + V_\theta}{V}\right) dV_\theta^e \quad (3.2)$$

where V is the total volume of the system and V_β and V_θ are the real volumes of β and θ respectively. In general, V_β is a complicated function of V_θ and it is not possible to analytically integrate these equations to find the relationship between the actual and extended volumes. However, in certain simple cases, it is possible to relate V_θ to V_β by multiplication with a suitable constant W :

$$\frac{V_\theta}{V_\beta} = W \quad (3.3)$$

Equations 3.1 and 3.2 can then be written as:

$$dV_\beta = \left\{1 - \frac{(1+W)V_\beta}{V}\right\} dV_\beta^e \quad (3.4)$$

$$dV_\theta = \left\{1 - \frac{(1+W)V_\theta}{WV}\right\} dV_\theta^e \quad (3.5)$$

Accordingly, the volume fractions ζ_β and ζ_θ are given by:

$$\zeta_\beta = \frac{1}{1+W} \left[1 - \exp \left\{ -\frac{(1+W)}{3} \pi v_\beta^3 I_\beta t^4 \right\} \right] \quad (3.6)$$

$$\zeta_\theta = \frac{1}{1+W} \left[1 - \exp \left\{ -\frac{(1+W)}{3W} \pi v_\theta^3 I_\theta t^4 \right\} \right] \quad (3.7)$$

where v_β , v_θ and I_β , I_θ are the growth rates and the nucleation rates of β and θ , respectively, and t is time.

II Complex simultaneous reactions

In practice, the multiple reactions found in most industrial steels are not as simple as described above. Precipitation reactions may affect each other by removing solute atoms from the matrix. Any change in the matrix composition must alter the growth and nucleation rates. To illustrate the methodology, a calculation for secondary hardening steels, due to Robson and Bhadeshia, is described below [4].

The precipitates which are dealt with in the model are M_3C , M_2C , $M_{23}C_6$, M_6C and Laves phase; the relevant parameters are listed in Table 3.1.

Precipitate	Nucleation and growth condition
M_3C	No nucleation but paraequilibrium growth of a number of particles followed by change in chemical composition
M_2C	Finite nucleation rate and diffusion-controlled linear growth of needles.
$M_{23}C_6$	Finite nucleation rate and diffusion-controlled parabolic growth of spheroids.
M_6C	Finite nucleation rate and diffusion-controlled parabolic growth of spheroids.
Laves phase	Finite nucleation rate and diffusion-controlled parabolic growth of spheroids.

Table 3.1: The calculation parameters of isothermal precipitation in a secondary hardening steel [4].

All phases except M_3C form with the equilibrium composition. The shape of M_2C is assumed to be that of needles, so the growth should follow the Zener equation described in section 2.2.3. For $M_{23}C_6$ and Laves phase, the shapes are assumed to be spherical, so the growth should follow the parabolic law described in section 2.2.2. M_3C can precipitate rapidly since it forms with paraequilibrium composition, i.e. only carbon atoms diffuse.

Model for M_3C enrichment

The M_3C which is formed in paraequilibrium will, during heat treatment, change its composition toward equilibrium. The principal change in this process involves enrichment

in substitutional solutes and a complementary rejection of iron into the ferrite. The rate of enrichment is given approximately by [96]:

$$c_X = \bar{c}_X + 4\sqrt{D_X t} \frac{(\bar{c}_X - c_X^{\alpha\theta})}{d_t \sqrt{\pi}} \quad (3.8)$$

where c_X represents the concentration of the diffusing species X , t is the time since M_3C formation, d_t is the thickness of the cementite plate, D_X is the diffusion coefficient for the solute X in the matrix (it is assumed that the corresponding diffusivity in the cementite is identical to that in the ferrite), $c_X^{\alpha\theta}$ is the concentration of the substitutional solute X in the ferrite which is in equilibrium with the cementite, and \bar{c}_X is the mean concentration of the substitutional solute X in the alloy. This equation is valid only in the absence of soft impingement.

The typical size of M_3C investigated experimentally for 10CrMoV and 2.25Cr1Mo steels is 30 nm [95, 97]. Using this value of the thickness in equation 3.8, the relationship between time and concentration of substitutional solute in M_3C can be obtained.

The number of nucleation sites for M_3C has been characterised by Takahashi and Bhadeshia [98]. The M_3C volume fraction can be calculated using the lever rule and the approximation that any carbon dissolved in the ferrite can be neglected. The volume fraction ζ_θ of M_3C is then given by:

$$\zeta_\theta = \frac{\bar{c}_C}{c_C^{\theta\alpha}} \quad \text{with} \quad c_C^{\theta\alpha} \simeq 0.25 \quad (3.9)$$

where \bar{c}_C is the atomic fraction of C in the alloy. Venugopalan and Kirkaldy suggested that the average size of the cementite before any Ostwald ripening is indicated empirically by the following equation [99]:

$$\bar{r}^3 = (2.26 - 6.4 \times 10^{-3}T + 4.6 \times 10^{-6}T^2)\zeta_\theta \times 10^{-3} \quad (3.10)$$

where \bar{r} is the average size in μm and T is the tempering temperature in $^\circ\text{C}$. Therefore, the number of M_3C particles per unit volume is given by:

$$N^\theta = \frac{\zeta_\theta}{\frac{4}{3}\pi\bar{r}^3} \quad (3.11)$$

Model for M_2C , $M_{23}C_6$, and Laves phase

M_2C is a needle-shaped carbide; therefore, M_2C particles were modelled as cylinders growing at a constant rate with a constant aspect ratio. The volume of a needle which nucleated at a time τ , at a later time t is therefore given by:

$$V_\tau = \frac{\pi v^3 (t - \tau)^3}{\phi^2} \quad (3.12)$$

where v is the linear growth rate represented by equation 2.40 and ϕ is the needle aspect ratio; measurement showed this value to be ~ 15 .

$M_{23}C_6$ and Laves phase are represented as spheres, the radius of each of which is given by:

$$r_\tau^I = \alpha_3 \sqrt{D(t - \tau)} \quad (3.13)$$

where α_3 is the three-dimensional parabolic rate constant given by equation 2.25. The volume of an individual particle at a time $t - \tau$ is given by:

$$V_\tau = \left(\frac{4}{3}\right) \pi \alpha_3^3 (D(t - \tau))^{\frac{3}{2}} \quad (3.14)$$

From classical theory, the nucleation rate per unit volume is given by:

$$I = N_V \frac{kT}{h} \exp \left\{ \frac{-(G^* + Q^*)}{kT} \right\} \quad (3.15)$$

$$G^* = \frac{16\pi\sigma^3}{3\Delta G_V^2} \quad (3.16)$$

where h is the Planck constant, N_V is the number of nucleation sites per unit volume, Q^* is the energy required to transfer atoms across the ferrite/carbide interface (assumed to be the activation energy for volume diffusion [68]). σ is the surface energy per unit area and ΔG_V is the chemical driving force for nucleation per unit volume of nucleus. Here, the misfit strain energy ΔG_ϵ is neglected. ΔG_V for each precipitate was calculated using the Metallurgical and Thermochemical Databank (MTDATA) [100]. N_V and σ are unknown and difficult to predict and therefore the values of N_V and σ were found by fitting the model to experimental data.

Solute partitioning effects (soft impingement)

Alloy carbide formation is controlled by the diffusion of substitutional solute atoms. The change of the matrix composition during precipitation can affect the subsequent nucleation and growth process. In the mean field approximation, such changes are averaged over the remaining matrix phase as a method for dealing with soft impingement. The maximum fraction of each phase designated as ζ^{Max} is given by a lever rule:

$$\zeta_\beta^{Max} = \frac{(\bar{c} - c^{\alpha\beta})}{(c^{\beta\alpha} - c^{\alpha\beta})} \quad (3.17)$$

The effect of soft impingement in the mean field approximation may be expressed in terms of an extent-of-reaction parameter, defined as:

$$\Phi = \frac{\zeta}{\zeta^{Max}} \quad (3.18)$$

where ζ is the phase fraction. Therefore, Φ changes from 0 to 1 during precipitation and can be defined for each phase. For simultaneous precipitation, Φ can be generalised to account for concentration changes caused by each new phase. If there are n phases forming simultaneously, Φ for the i th phase is given by:

$$\Phi_i = \frac{\sum_{i=0}^n \zeta_i (c^{i\alpha} - c^{\alpha i})}{(\bar{c} - c^{\alpha i})} \quad (3.19)$$

where ζ_i is the fraction at any instance for the i th phase.

Physically, Φ represents the fraction of excess solute remaining in the matrix with respect to the phase in question. Therefore, it is possible to make the approximation that the chemical driving force ΔG for the formation of each phase should be related linearly to $(1 - \Phi_i)$ as indicated in following equation:

$$\Delta G_i \{ \Phi_i \} = (1 - \Phi_i) \Delta G_i \{ \Phi_i = 0 \} \quad (3.20)$$

where the braces are used to identify functional dependence. For M_3C , it is necessary to calculate the value of Φ_{M_3C} differently. This is because M_3C nucleates with the paraequilibrium composition. Therefore, the value should include the composition change of diffusing solute element:

$$\Phi_{M_3C} = \frac{\bar{c} - \bar{c}'}{c^{M_3C\alpha} - \bar{c}'} \quad (3.21)$$

where $c^{M_3C\alpha}$ is the mole fraction of the solute in M_3C in equilibrium with α . \bar{c}' is the mean mole fraction in the matrix at any time, which is:

$$\bar{c}' = \frac{\bar{c} - \sum_{i=1}^n \zeta_i c^{i\alpha}}{1 - \sum_{i=1}^n \zeta_i} \quad (3.22)$$

Schematic composition profiles are shown in Fig. 3.1 (a) at a certain time when both β and γ are precipitating in matrix α and Fig. 3.1 (b) when the solute concentration in matrix reaches equilibrium with β and precipitation of β is complete. As γ precipitates further, removing solute, β will start to dissolve.

Dissolution of metastable phase

Figure 3.2 shows a schematic drawing of the concentration profile for a case where β and γ are precipitating in matrix α . When the solute concentration in the matrix, \bar{c}' , falls below $c^{\alpha\beta}$ due to the effect of soft impingement, the metastable phase β will start to dissolve. Considering the mass-balance between β and the matrix, the following equation can be obtained:

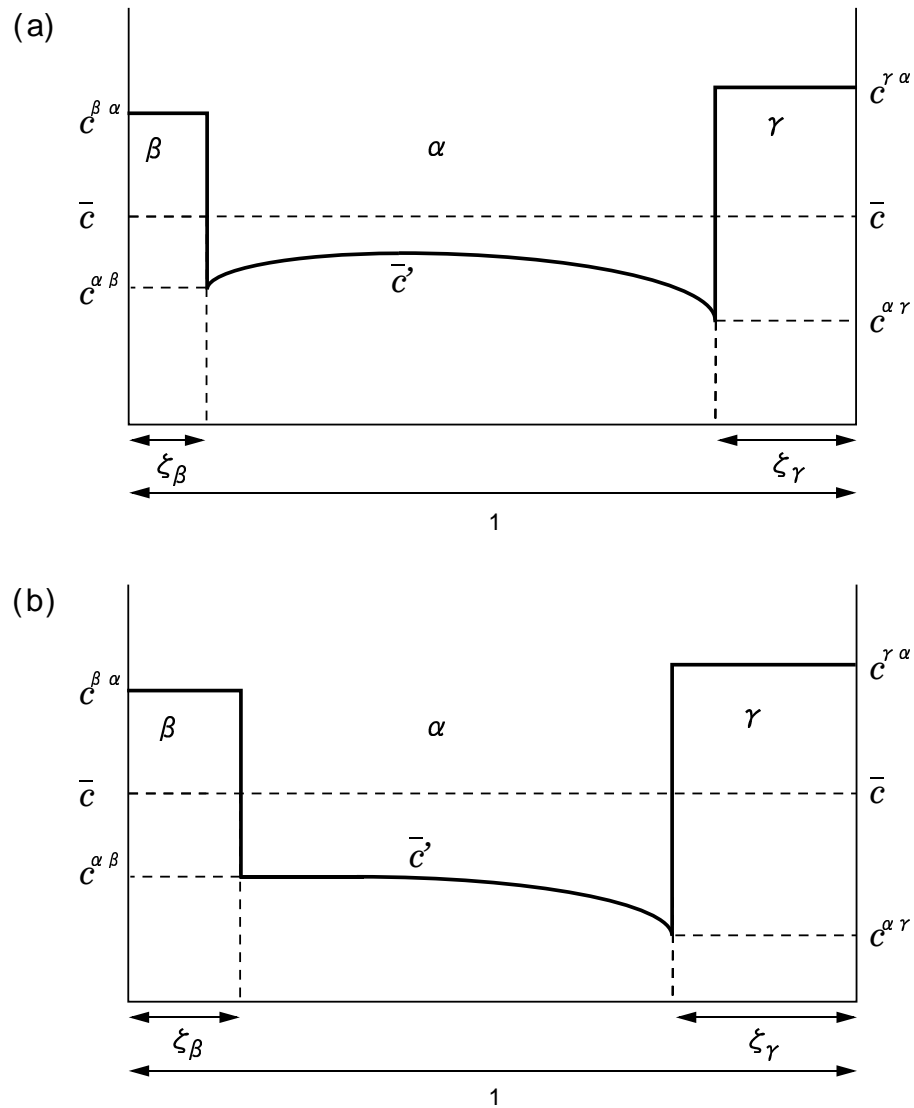


Figure 3.1: Distribution of solute when (a) both β and γ are precipitating, and (b) the precipitation of β has been completed [4]. Note that \bar{c} is the solute mole fraction in the matrix α and that ξ_β and ξ_γ are phase volume fractions for β and γ respectively.

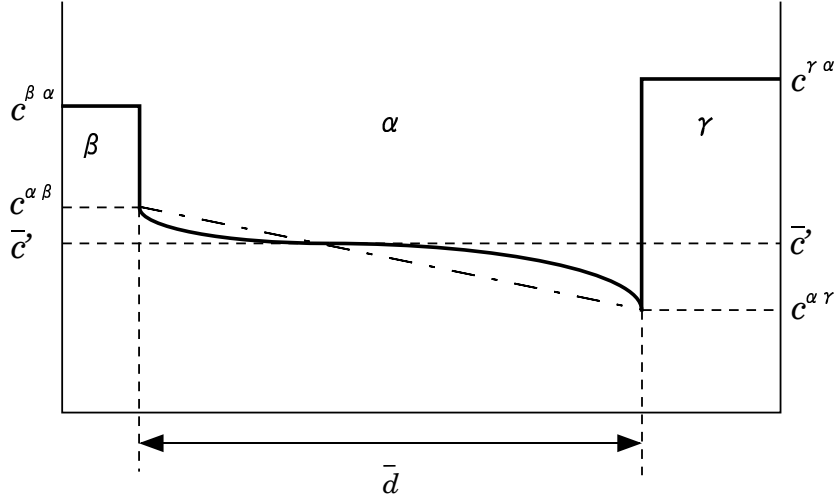


Figure 3.2: Illustration of solute distribution when β is dissolving and γ is precipitating in matrix α [4]. The dotted line represents the linearized mole fraction gradient approximation for dissolution. \bar{c} is the mean mole fraction in the matrix at any time.

$$\frac{dr^I}{dt}(c^{\beta\alpha} - c^{\alpha\beta}) = -D\left(\frac{\partial c}{\partial r}\right)_{r=r^I} \quad (3.23)$$

where D is the diffusion coefficient of the solute element in the matrix. If the mole fraction gradient is assumed to be constant (the Zener linearized gradient approximation), it may be assumed that:

$$\left(\frac{\partial c}{\partial r}\right)_{r=r^I} = \frac{(c^{\alpha\beta} - c^{\alpha\gamma})}{\bar{d}} \quad (3.24)$$

where \bar{d} is the mean diffusion distance between β and γ precipitates, given by:

$$\bar{d} = (N^\beta + N^\gamma)^{-\frac{1}{3}} \quad (3.25)$$

where $N^\beta + N^\gamma$ are the number densities of β and γ precipitation, which are assumed to be constant during dissolution. It is assumed that the whole process can be represented by a mean radius \bar{r} for a spherical particle and \bar{l} for a needle. With this assumption, the change of volume for the dissolving phase V_β with time can be described as follows for spherical particles and needles, respectively:

$$\frac{dV_\beta}{dt} = 4\pi\bar{r}^2 D \frac{(c^{\alpha\beta} - c^{\alpha\gamma})}{\bar{d}(c^{\beta\alpha} - c^{\alpha\beta})} \quad (3.26)$$

$$\frac{dV_\beta}{dt} = 3\pi\bar{l}^3 D \frac{(c^{\alpha\beta} - c^{\alpha\gamma})}{\phi\bar{d}(c^{\beta\alpha} - c^{\alpha\beta})} \quad (3.27)$$

In the case of M_3C in paraequilibrium, the composition changes with time from paraequilibrium to equilibrium. When the value of Φ_{M_3C} is equal to 1, dissolution starts, and then it is dealt with in the same way as for other metastable phases.

III Some example calculations

The model described above is for isothermal heat treatment. The parameters for the calculation have been listed in Table 3.1. There have been some experimental investigations for 2.25Cr1Mo steel so the sequence of precipitation is known [22]. The predicted time-temperature precipitation diagram (TTP) for 2.25Cr-1Mo steel is shown in Fig. 3.3 (a), with Baker and Nutting's experimental data [4]. For a high-chromium heat-resistant steel, which has excellent creep resistance, similar data are shown in Fig. 3.3 (b) together with the predictions due to [4]. There is remarkable agreement between experimental data and the theory. Using the same model, Robson and Bhadeshia predicted correctly that the precipitation process for 3Cr1.5Mo steel would be quite different from that of 2.25Cr1Mo steel, and more similar to that of 10CrMoV steel.

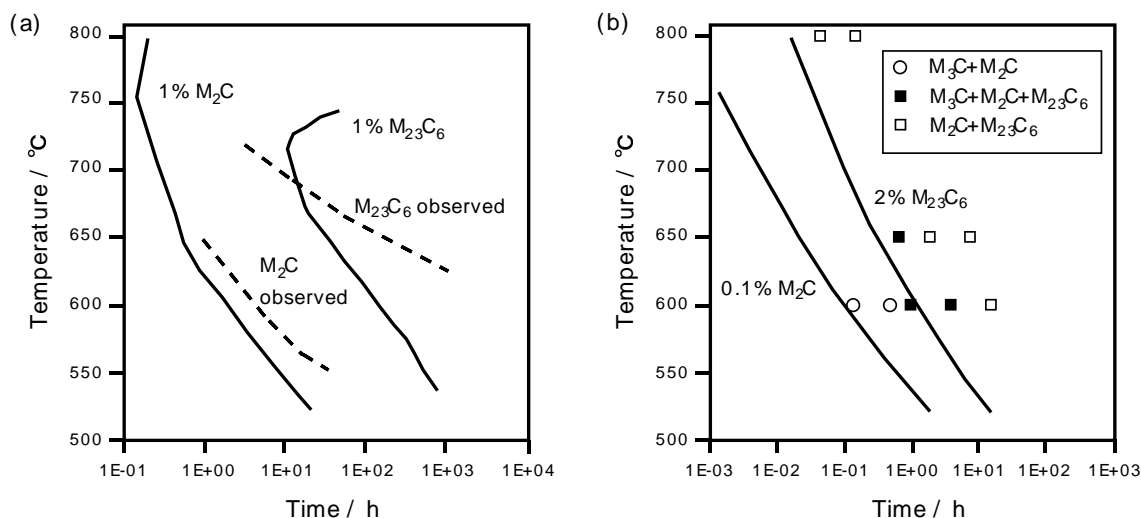


Figure 3.3: Predicted time-temperature-precipitation diagrams for precipitates in (a) 2.25Cr1Mo steel and (b) 10CrMoV steel, together with experimental data on 2.25Cr1Mo steel from [22] and [4].

3.2.2 Fujita and Bhadeshia model

The Robson and Bhadeshia model can be used to estimate the volume fraction of carbides but it would be useful also to treat particle sizes and coarsening. This has been achieved by Fujita and Bhadeshia, who attempted to take better account of multicomponent diffusion and capillarity [5]. Given the small equilibrium volume fractions of carbides, they also relaxed the extended volume concept to permit particle sizes to be approximately calculated.

I Modifications to Robson and Bhadeshia model by Fujita and Bhadeshia

Cementite precipitation

M_3C particles were assumed by Robson and Bhadeshia to be uniform in size for the calculation. However, the measured thickness of M_3C on ferrite lath boundaries (50 nm) was about twice that of those within the laths (20 nm). These values hardly change in the early stages of tempering. Considering that the total volume fraction must be a function of the carbon concentration, and the thickness is approximately constant before the dissolution of M_3C , the initial number density of M_3C particles N_0^θ (m^{-3}) must be a function of the carbon concentration. From measurements, N_0^θ was expressed as:

$$N_0^\theta = 2.23 \times 10^{22} w_c - 1.0 \times 10^{21} \quad (3.28)$$

where w_c is the carbon concentration of alloys in wt. %. This equation was obtained empirically and is valid for steels with w_c from 0.1 to 0.15 wt. %.

Avrami theory

In the application of Avrami theory, the conversion of extended space into real space, which is necessary to account for impingement, prevents the calculation of anything but the volume fraction. Given that the total fraction of precipitation is small, the effect of hard impingement can be neglected, in which case it becomes possible to follow the evolution of each particle.

Diffusion-controlled growth in a multicomponent system

The original model of Robson and Bhadeshia treated the growth of all precipitates other than M_3C in terms of the diffusion of Cr alone. For a binary system, the compositions at the interface are given by a tie-line on the equilibrium phase diagram. There is a unique tie-line, the one which passes through the average composition. The mole fraction profile which develops during the precipitation of the solute-rich phase β from the matrix α is illustrated in Fig. 2.4. The analysis involves one mass-balance at the interface which is moving with a velocity v :

$$v(c_{Cr}^{\beta\alpha} - c_{Cr}^{\alpha\beta}) = -D_{Cr} \left(\frac{\partial c_{Cr}}{\partial x} \right)_{x=x^I} \quad (3.29)$$

Practical steels, however, contain many solute elements. In a multicomponent system, mass-balance equations must be satisfied simultaneously for each element if equilibrium is to be maintained at the moving interface. Therefore, for an alloy carbide in a Fe-C-X system, at least two mass conservation equations, one for the substitutional element X and the other for the interstitial carbon C, must be satisfied simultaneously:

$$\begin{aligned} v(c_X^{\beta\alpha} - c_X^{\alpha\beta}) &= -D_X \left(\frac{\partial c_X}{\partial x} \right)_{x=x^I} \\ v(c_C^{\beta\alpha} - c_C^{\alpha\beta}) &= -D_C \left(\frac{\partial c_C}{\partial x} \right)_{x=x^I} \end{aligned} \quad (3.30)$$

This causes difficulties since the interstitial and substitutional elements have vastly different diffusion coefficients.

Fujita applied Coates' theory, described in section 2.3, to the precipitation of alloy carbides (M_2C , M_7C_3 and $M_{23}C_6$) at low supersaturation after the completion of paraequilibrium M_3C precipitation. In Fig. 3.4, the point *a* designates the alloy composition and the point *b* represents the matrix composition after the completion of paraequilibrium M_3C precipitation. Because of the low supersaturation, β precipitation commences with the governing tie-line *c* – *f*. Then, due to the depletion of solute X, the matrix composition changes along the direction *b* → *e*. The controlling tie-line thus shifts towards that passing through the bulk composition *b*, and accordingly, the ferrite and carbide compositions shift along *c* → *e* and *f* → *d*, respectively.

Capillarity effect

The state of equilibrium between two phases changes with the curvature of the interface separating them. This capillarity effect scales with the interface energy because additional work has to be done to create new interfacial area as a curved interface moves. The equilibrium composition of the ferrite changes as follows [70].

For a spherical particle and hemispherical tip of a needle,

$$c_r^{\alpha\beta} = \left(1 + \frac{2\Gamma}{r^{IC}} \right) c^{\alpha\beta} \quad (3.31)$$

For a plate edge and a cylinder,

$$c_r^{\alpha\beta} = \left(1 + \frac{\Gamma}{r^{IC}} \right) c^{\alpha\beta} \quad (3.32)$$

where r^{IC} is the radius of curvature at the tip and Γ is a capillarity coefficient given by:

$$\Gamma = \frac{\sigma\nu^\beta (1 - c^{\alpha\beta})}{kT (c^{\beta\alpha} - c^{\alpha\beta})} \quad (3.33)$$

where ν^β is the atomic volume of the β phase.

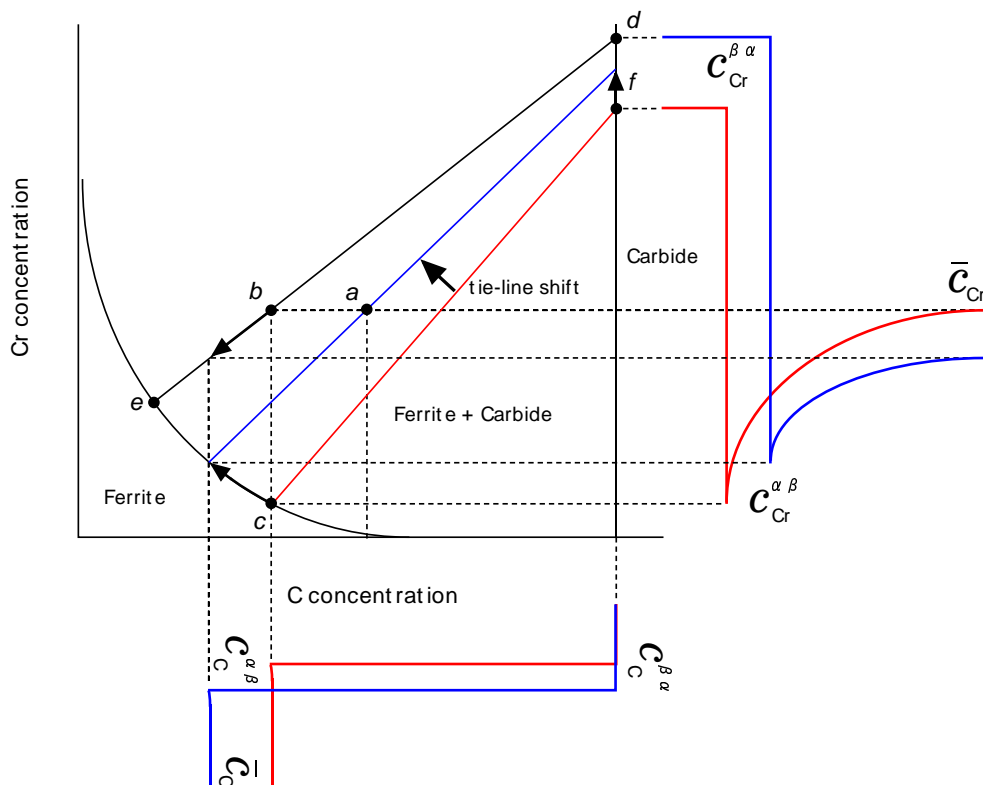


Figure 3.4: Schematic isothermal section through the Fe-C-Cr phase diagram. The alloy composition is plotted as the point a whereas the composition of the ferrite after the precipitation of paraequilibrium cementite is represented by the point b .

The tip radius of a needle-shaped carbide should be identical for each element. However, according to the method used by Robson and Bhadeshia [4], the tip radii for M_2C have different values depending on the element M . Therefore, the critical radius was fixed at a constant value which was chosen to give the best agreement between the predicted and measured growth rate. Fujita introduced the capillarity corrected concentration of each solute, which gives the same tip radius when inserted into equation 3.31, into the model. Figure 3.5 shows the calculation for the $\alpha/\alpha+M_2C$ phase boundary at each given tip radius in the isothermal section at 700 °C for a Fe-C-Mo system when the interfacial energy $\sigma = 0.20 \text{ J m}^{-2}$.

Coarsening

Coarsening may occur during or after precipitation. According to the classical theory of Ostwald ripening, the following equation can be obtained [83, 84]:

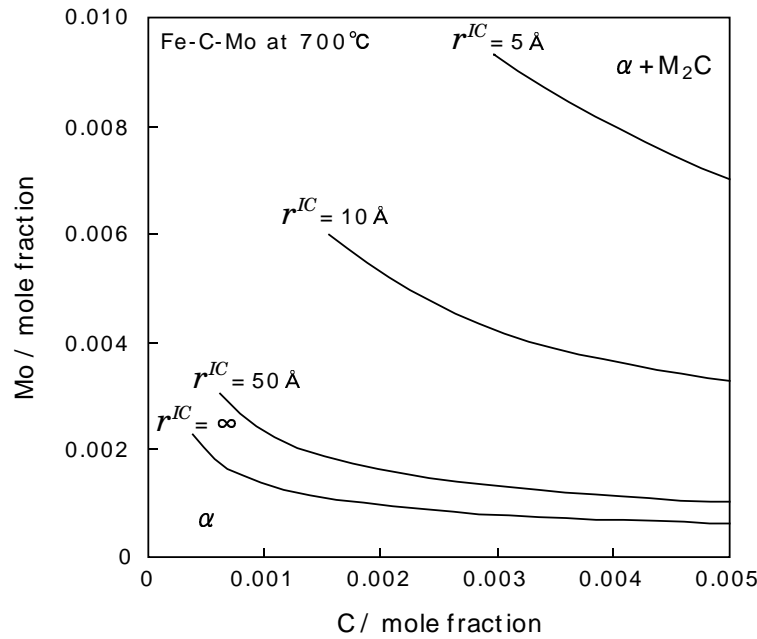


Figure 3.5: Calculation results of $\alpha/\alpha+M_2C$ phase boundary at each given tip radius in the isothermal section at 700 °C for a Fe-C-Mo system when the interfacial energy $\sigma = 0.20 \text{ J m}^{-2}$.

$$\bar{r}^3 - r_0^3 = \left(\frac{8\sigma\nu^\beta Dc^{\alpha\beta}}{9kT} \right) t \quad (3.34)$$

where \bar{r} is the average particle radius, r_0 is the initial particle radius, σ is the interfacial energy, ν^β is the volume of an atom of the β phase, D is the solute diffusion coefficient, $c^{\alpha\beta}$ is the equilibrium solute concentration in the matrix α at which $r \rightarrow \infty$, k is the Boltzmann constant, T is absolute temperature and t is time. This equation is valid when the equilibrium volume fraction is small.

The theories applied for the enrichment of cementite, soft impingement and dissolution of metastable phases are the same as those used in the Robson and Bhadeshia model [4]. The parameters for each precipitate is the same as those used in the Robson and Bhadeshia model. M_7C_3 (spheroid) is considered and Laves phase is removed since Laves phase was not observed experimentally. Table 3.2 shows a comparison of the assumptions in the two models.

Robson and Bhadeshia model	Fujita and Bhadeshia model
Based on Avrami theory	Nucleation and growth but no treatment of impingement Nucleation site consumption
Using mean particle size	Particle size distribution due to different nucleation times and growth rates
Cr diffusion-controlled growth	Diffusion-controlled growth in a multicomponent system Mass-balances of Cr and C are considered.
No treatment of capillarity effect	Capillarity effect in a multicomponent system

Table 3.2: Comparison of assumptions in the two models.

II Some example calculations and experiments

The model described above is for isothermal heat treatment and is suitable for power plant steels. Calculations are illustrated in Fig. 3.6 together with experimental data. The Fujita and Bhadeshia model correctly predicts the carbide precipitation sequence.

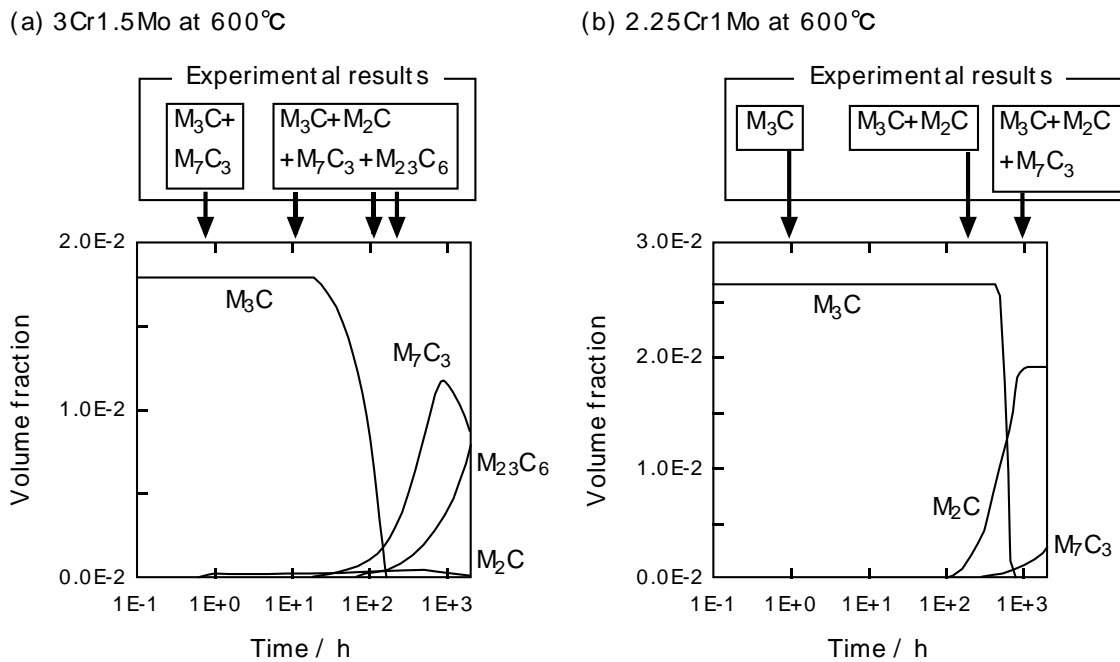


Figure 3.6: Calculations of multiple precipitation reactions for (a) 3Cr1.5Mo and (b) 2.25Cr1Mo steels for 600 °C using Fujita and Bhadeshia model.

3.3 Summary

As shown in this chapter, there have been several attempts to model the precipitation of carbides in multicomponent systems. In Fujita and Bhadeshia's model, the precipitation of Mo_2C was modelled taking account of the capillarity effect in a ternary system [6]. The carbide particles were assumed to be in the form of thin cylinders with hemispherical ends, as in the Zener treatment [7]. A disadvantage of their method is that the needle-aspect ratio had to be chosen arbitrarily. In addition, there is a problem in the evaluation of the capillarity effect in multicomponent systems, since this model mistakenly treats the different solutes as independent. As shown in Chapter 7, the simplest exact method to evaluate the influence of capillarity on the interface composition is to modify the Gibbs energy value of the carbide phase in the database used by thermodynamic calculation software such as MTDATA.

Chapter 4

Thermodynamic calculations

4.1 Introduction

Modelling precipitation in secondary hardening steels requires knowledge of both thermodynamic and the kinetic parameters for a variety of possible phases. To obtain these parameters, experimental data are required. The prerequisite thermodynamical information for modelling consists of:

1. the stable phases corresponding to the temperature;
2. the phase fractions corresponding to the temperature;
3. the relative phase stability;
4. the equilibrium chemical compositions of possible phases;
5. the iso-activity curves in the carbide-ferrite two-phase field.

The use of the computer package Metallurgical and Thermodynamic Data Bank (MTDATA) [100] makes these thermodynamic calculations possible.

4.2 Application of MTDATA

4.2.1 General description of MTDATA

Recently, the advent of thermochemical data banks has made the calculation of phase equilibria relatively straightforward. In the present work, the National Physical Laboratory's MTDATA has been used. This package is capable of calculating phase equilibria for multi-component systems in which many phases may coexist. It works by combining experimentally determined data to estimate the Gibbs free energy of each phase. In MTDATA, the free energy of phases such as ferrite, austenite, cementite and other carbides such as M_7C_3 are calculated using a sublattice model which involves terms called unaries. Commonly, the temperature and pressure dependencies of unaries are described using the G-HSER format:

$$G^{T,P} - H^{SER} = a + bT + cT \ln T + eT^2 + fT^3 + i/T + \int_0^P \nu^{P,T} N_A dP \quad (4.1)$$

where $G^{T,P}$ is the molar Gibbs energy at (T, P) , $\nu^{P,T}$ is the atomic volume at (T, P) , N_A is Avogadro's number and H^{SER} is the enthalpy of the element or substance in the reference state at 298.15 K. However, Mo_2C , V_4C_3 and other carbides are calculated using a pure substance model which has fixed chemical compositions.

For any system, the reliability of the predictions will depend on the available data for all the components and their interactions. For any given system, MTDATA calculates the compositions and mass fractions of the phases at which the Gibbs energy of the system is a minimum. It is possible to calculate the phase equilibria of a system which includes arbitrary phases as long as data exists, and it is therefore possible to deduce the relative stabilities of the phases and to determine precipitation sequences. Although it cannot predict the time dependence of the microstructure, which requires kinetic modelling, MTDATA is useful tool in the design of alloys.

4.2.2 Experimental steels

Steels with the chemical compositions listed in Table 4.1 were manufactured. The purpose of the research was to model the carbide precipitation behaviour in ternary and quaternary systems, and Fe-C-Mo, Fe-C-V and Fe-C-Mo-V systems were therefore chosen. However, the alloys also contain manganese to ensure hardenability, and small quantities of aluminium and nitrogen to simulate practical steels. Commercial steels contain about 50 ppm of nitrogen and in many cases, aluminium to fix nitrogen as AlN.

Steel	C	Si	Mn	Mo	V	Al	N
Steel A	0.10	<0.005	1.99	1.60	0.00	0.03	0.0049
Steel B	0.10	<0.005	1.95	0.00	0.57	0.03	0.0043
Steel C	0.10	<0.005	2.00	1.59	0.57	0.03	0.0044
Steel D	0.10	<0.005	2.00	0.40	0.57	0.03	0.0044
Steel E	0.10	<0.005	2.00	0.40	0.30	0.03	0.0044

Table 4.1: Chemical compositions of experimental steels in wt. %.

4.2.3 Possible phases in the experimental alloys

Calculations using MTDATA begin with a choice of possible phases. The steels in Table 4.1 contain carbon, aluminium and nitrogen as common elements, therefore cementite and AlN can, in principle, form.

In Steels A and C, containing molybdenum, it is expected that the stable phase will be M_6C , in which 'M' stands for metallic elements. M_2C and M_{23}C_6 are included since these

are likely transient precipitates. In a Fe-C-Mo ternary system, M_2C -type carbide is actually Mo_2C , in which molybdenum atoms form a hexagonal closed-packed lattice (hcp) [12]. In higher-order systems, other alloying elements can dissolve into Mo_2C .

In Steels *B* to *E*, containing vanadium, it is considered that M_4C_3 -type carbide exists as the stable phase. In a Fe-C-V ternary system, the M_4C_3 -type carbide is actually V_4C_3 , in which vanadium atoms form a face-centred cubic lattice (fcc) [12]. In higher-order systems, other alloying elements can dissolve into V_4C_3 . Therefore, M_2C and M_4C_3 were represented as hcp and fcc phase, respectively.

The phases allowed in the calculations are listed in Table 4.2. The calculations were performed for the temperature range of 400 – 1200 °C. It is therefore necessary to consider the existence of the austenite (fcc) phase. To allow both austenite and M_4C_3 to exist as separate phases, a miscibility gap was introduced for the fcc phase.

Steel	Phase
Steel <i>A</i>	bcc (α), fcc (γ), cementite, hcp (M_2C), fcc (M_4C_3), M_6C , M_7C_3 , $M_{23}C_6$, AlN
Steel <i>B</i>	bcc (α), fcc (γ), cementite, hcp (M_2C), fcc (M_4C_3), M_6C , M_7C_3 , $M_{23}C_6$, AlN
Steel <i>C</i>	bcc (α), fcc (γ), cementite, hcp (M_2C), fcc (M_4C_3), M_6C , M_7C_3 , $M_{23}C_6$, AlN
Steel <i>D</i>	bcc (α), fcc (γ), cementite, hcp (M_2C), fcc (M_4C_3), M_6C , M_7C_3 , $M_{23}C_6$, AlN
Steel <i>E</i>	bcc (α), fcc (γ), cementite, hcp (M_2C), fcc (M_4C_3), M_6C , M_7C_3 , $M_{23}C_6$, AlN

Table 4.2: Prospective phases for equilibrium calculations using MTDATA for steels for the present research. α and γ represent ferrite and austenite, respectively.

4.3 Relative phase stabilities

4.3.1 Steel *A*

The relative stability of a phase can be deduced by removing existing phases one by one in the equilibrium calculation. Figure 4.1 shows the relationship between phase fraction (wt. fraction) and temperature in Steel *A*: (a) is the result of all phases in Table 4.2, (b) is obtained by removing hcp from (a). From these results, it can be deduced that the stable carbides at 600 °C are M_2C and M_6C , and the second most stable carbide is M_7C_3 .

4.3.2 Steel *B*

Figure 4.2 shows the relationship between phase fraction (wt. fraction) and temperature in Steel *B*: (a) is the result of all phases in Table 4.2, and (b) is obtained by removing M_4C_3 from (a). From this results, the stable carbide at 600 °C is M_4C_3 , and the second most stable carbide is cementite.

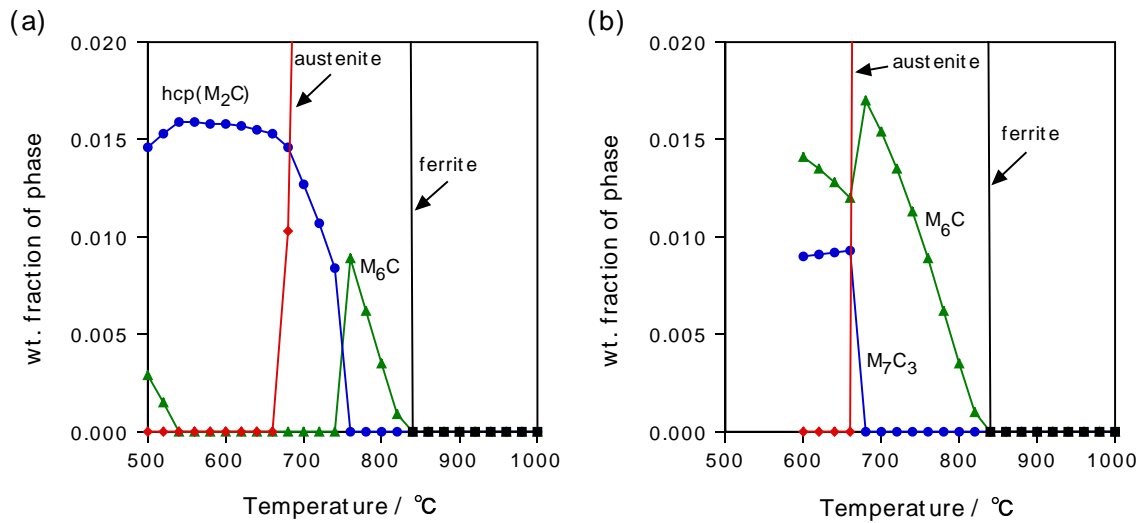


Figure 4.1: Relationship between wt. fraction of each phase and temperature in Steel A obtained by MTDATA. (a) is the result containing all phases in Table 4.2, (b) is obtained by removing hcp from (a).

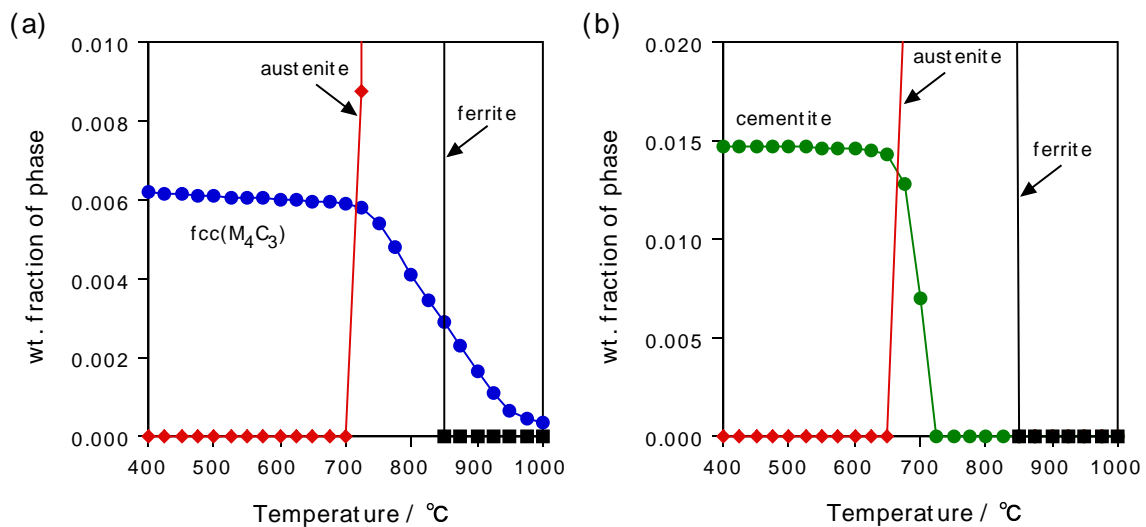


Figure 4.2: Relationship between wt. fraction of each phase and temperature in Steel B obtained by MTDATA. (a) is the result containing all phases in Table 4.2, and (b) is obtained by removing M₄C₃ from (a).

4.3.3 Steel *C*

Figure 4.3 shows the relationship between phase fraction (wt. fraction) and temperature in Steel *C*: (a) is the result of all phases in Table 4.2, (b) is obtained by removing M_6C from (a). From these results, the stable carbides at 600 °C are M_4C_3 and M_6C , and the second most stable carbide is M_2C .

4.3.4 Steel *D*

Figure 4.4 shows the relationship between phase fraction (wt. fraction) and temperature in Steel *D*: (a) is the result of all phases in Table 4.2, and (b) is obtained by removing M_4C_3 from (a). From these results, the stable carbide at 600 °C is M_4C_3 , and the second most stable carbide is M_2C .

4.3.5 Steel *E*

Figure 4.5 shows the relationship between phase fraction (wt. fraction) and temperature in Steel *E*: (a) is the result of all phases in Table 4.2, and (b) is obtained by removing M_4C_3 from (a). From these results, the stable carbide at 600 °C is M_4C_3 , and the second most stable carbides are M_2C and cementite.

4.3.6 Prospective precipitation sequence

According to the results above, the stable phases and fractions of those phases depend on temperature. In many cases, secondary hardening occurs at around 600 °C [12], and therefore, the tempering treatment which follows quenching is in practice carried out at around 600 °C. Accordingly, the present research focuses on this temperature.

The precipitation sequence of carbides is complicated to predict. In general, M_2C - and M_4C_3 -type carbides precipitate in the early stages of tempering after the completion of paraequilibrium cementite precipitation. The complex carbides such as $M_{23}C_6$ and M_6C start to precipitate after this. It is therefore considered that if M_2C is more stable than M_6C , M_6C will not exist even as a transient phase. Accordingly, the possible sequence of precipitation at 600 °C is summarized in Table 4.3.

Steel	Stable phase	Second most stable phase	Precipitation sequence
Steel <i>A</i>	hcp (M_2C)	M_6C	cementite \rightarrow M_2C
Steel <i>B</i>	fcc (M_4C_3)	cementite	cementite \rightarrow M_4C_3
Steel <i>C</i>	fcc (M_4C_3), M_6C	hcp (M_2C)	cementite \rightarrow M_2C + M_4C_3 \rightarrow M_4C_3 + M_6C
Steel <i>D</i>	fcc (M_4C_3)	hcp (M_2C)	cementite \rightarrow M_4C_3
Steel <i>E</i>	fcc (M_4C_3)	hcp (M_2C), cementite	cementite \rightarrow M_4C_3

Table 4.3: Most stable and second most stable phases and possible carbide precipitation sequences for each steel at 600 °C.

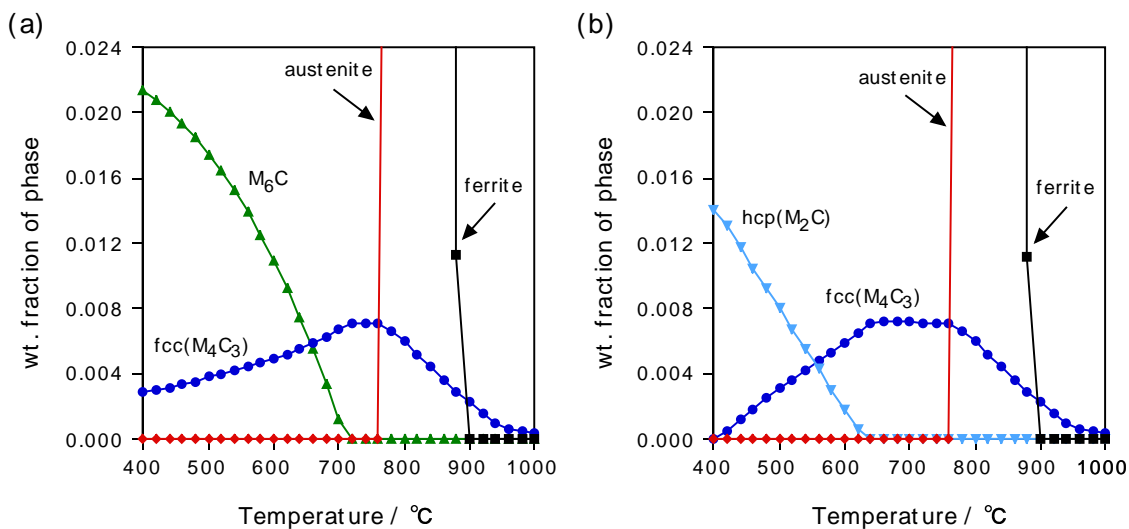


Figure 4.3: Relationship between wt. fraction of each phase and temperature in Steel *C* obtained by MTDATA. (a) is the result containing all phases in Table 4.2, (b) is obtained by removing M_6C from (a).

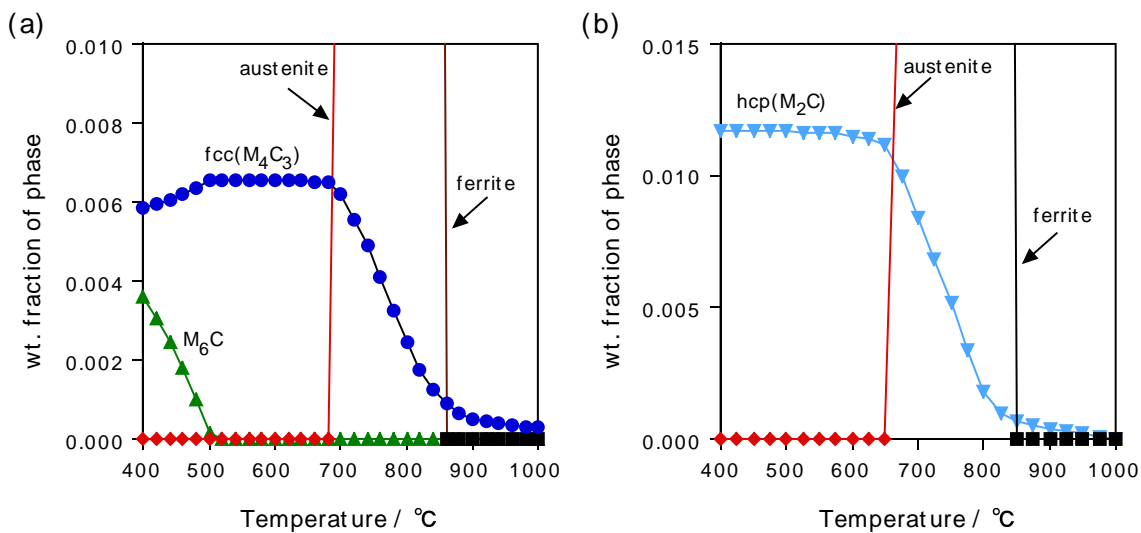


Figure 4.4: Relationship between wt. fraction of each phase and temperature in Steel *D* obtained by MTDATA. (a) is the result containing all phases in Table 4.2, and (b) is obtained by removing M_4C_3 from (a).

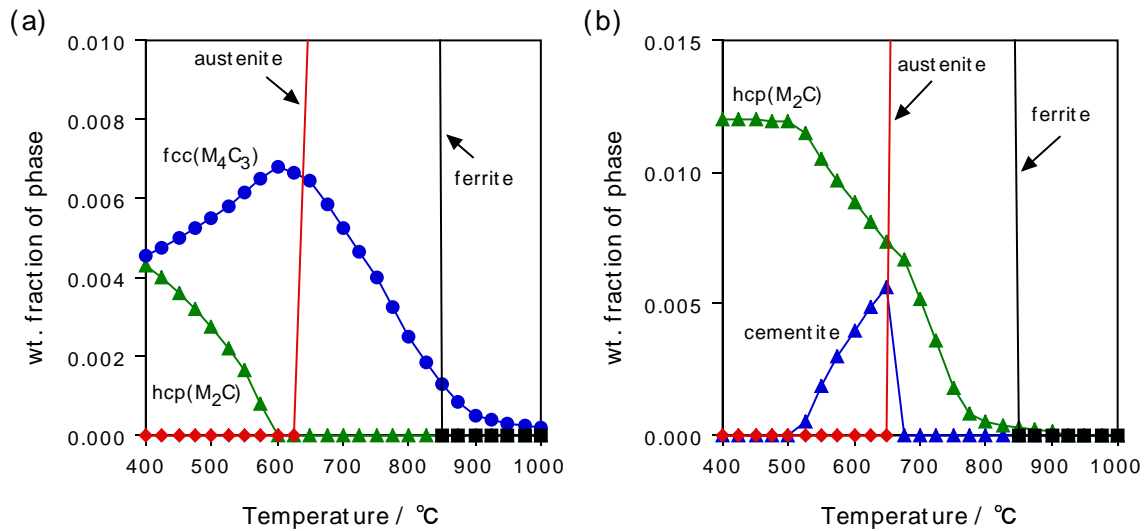


Figure 4.5: Relationship between wt. fraction of each phase and temperature in Steel *E* obtained by MTDATA. (a) is the result containing all phases in Table 4.2, (b) is obtained by removing M₄C₃ from (a).

4.4 Equilibrium chemical composition of the stable phases

The chemical composition of a precipitate shifts toward the equilibrium composition during growth in which local equilibrium is maintained at the interface. Growth ceases when the composition of the precipitates reaches equilibrium. Ostwald ripening may then occur at a slower rate.

The chemical compositions of the equilibrium carbides as a function of temperature are shown in Fig. 4.6 - 4.10. In Steel *A*, the equilibrium carbide at 600 °C is M₂C. Mn can dissolve into M₂C up to 10 at. %. In Steel *B*, the equilibrium carbide at 600 °C is M₄C₃. Nitrogen can dissolve into this carbide in large quantities at higher temperatures, and thus the chemical composition can be represented as V₄(C,N)₃. Mn is virtually insoluble in M₄C₃. In Steel *C*, the equilibrium carbides for 600 °C are M₆C and M₄C₃. Mn is insoluble in both of these phases. M₄C₃ is a V-rich carbide and Mo can dissolve into it up to 11 at. %. M₆C is a Mo-rich carbide and V can dissolve into it up to 7 at. %. Nitrogen also has a high solubility at high temperatures in M₄C₃, which can be represented as (V,Mo)₄(C,N)₃. In Steel *D* and *E*, the equilibrium carbide for 600 °C is M₄C₃. Steels *C* - *E* were designed to give different Mo:V ratios in M₄C₃.

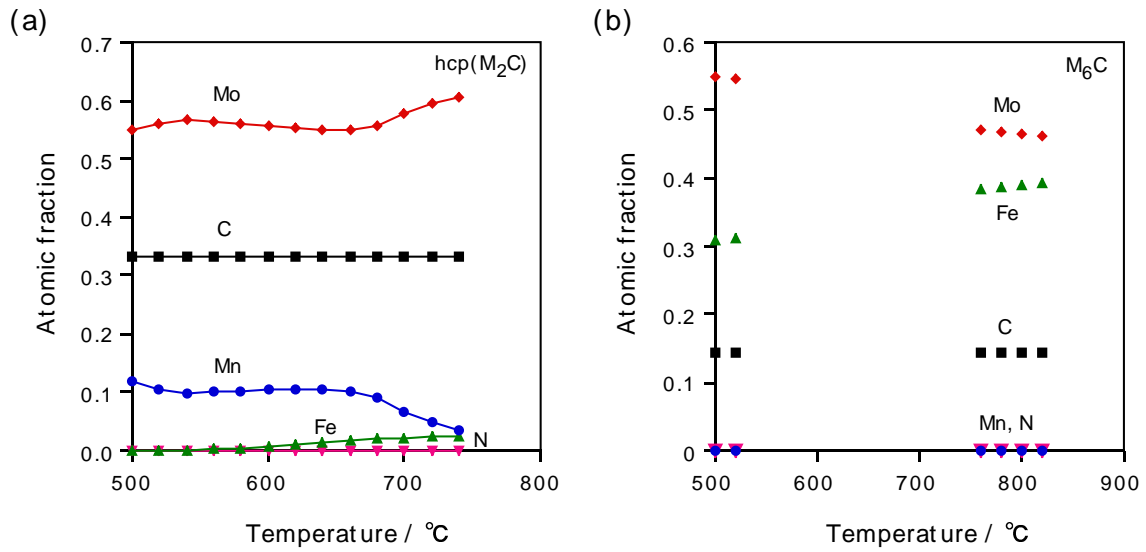


Figure 4.6: Relationship between the equilibrium chemical composition of stable carbides and temperature in Steel A: (a) is for hcp (M_2C), and (b) is for M_6C .

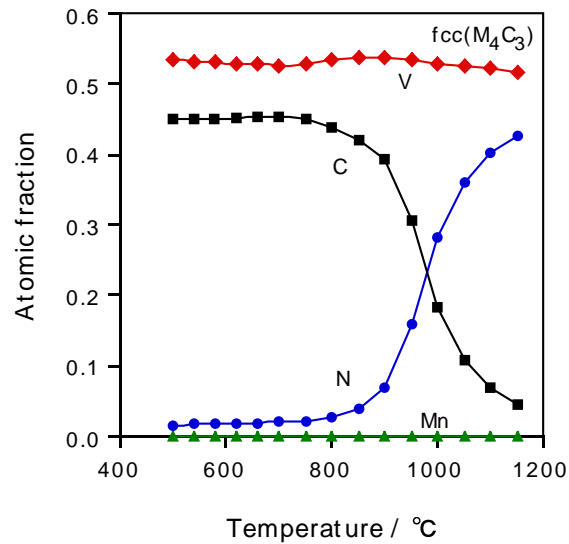


Figure 4.7: Relationship between the equilibrium chemical composition of stable carbide of fcc structure (M_4C_3) and temperature in Steel B.

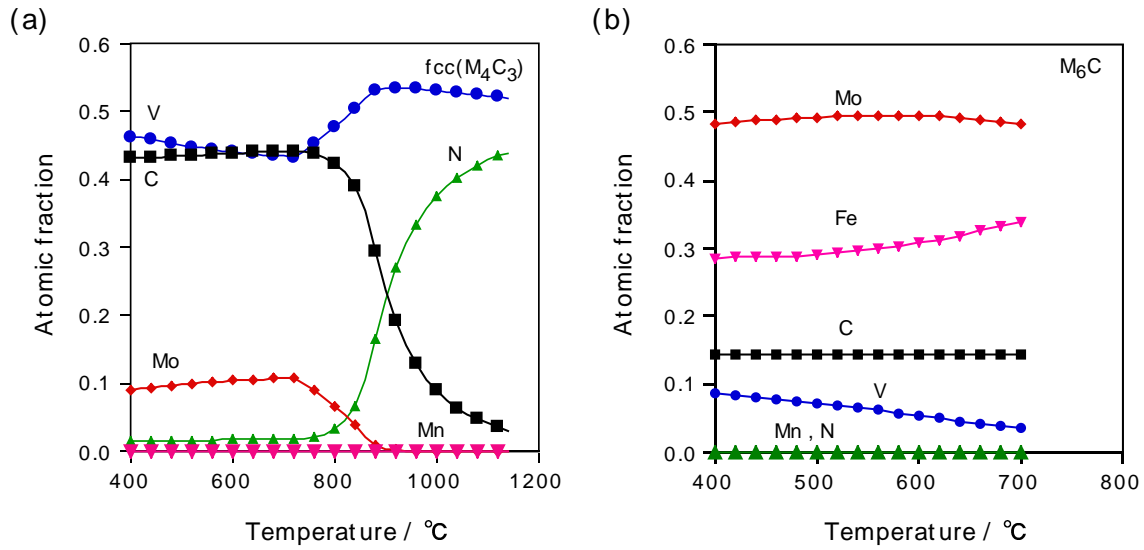


Figure 4.8: Relationship between the equilibrium chemical composition of stable carbides and temperature in Steel C: (a) is for $fcc(M_4C_3)$, and (b) is for M_6C .

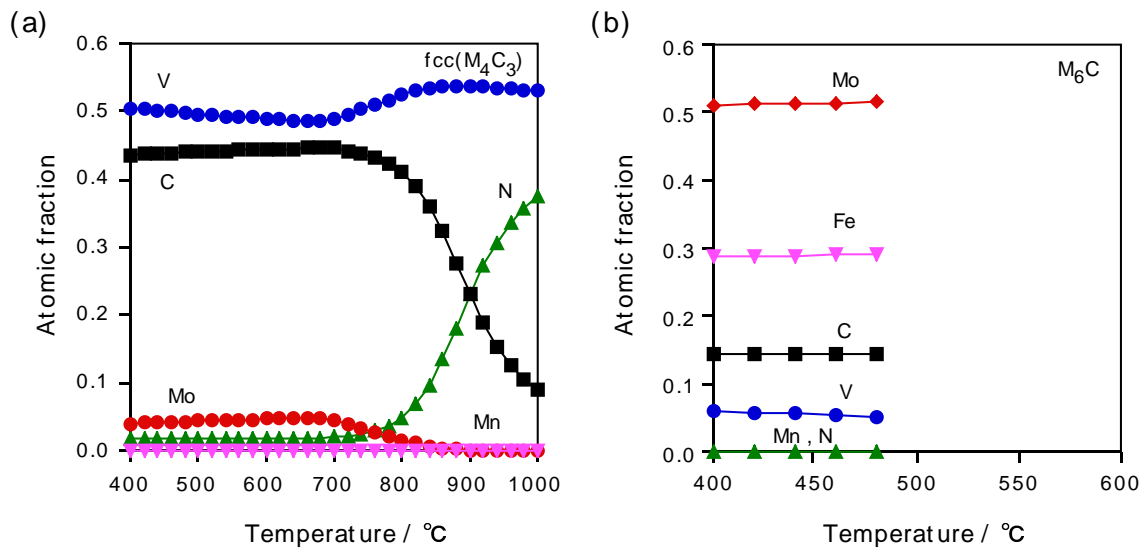


Figure 4.9: Relationship between the equilibrium chemical composition of stable carbides and temperature in Steel D: (a) is for $fcc(M_4C_3)$, and (b) is for M_6C .

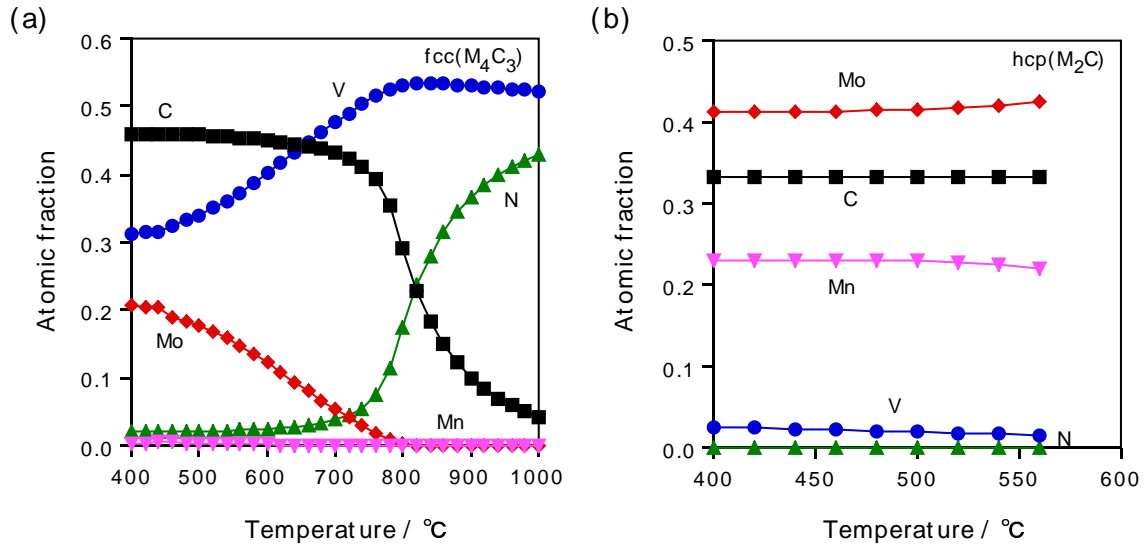


Figure 4.10: Relationship between the equilibrium chemical composition of stable carbides and temperature in Steel *E*: (a) is for fcc (M_4C_3), and (b) is for M_2C .

4.5 Paraequilibrium and equilibrium cementite composition

Cementite is not the equilibrium phase in Steels *A* - *E*. However, paraequilibrium cementite precipitates in the early stages of tempering and then is enriched toward equilibrium during tempering, until it starts to dissolve. It is therefore necessary to calculate the paraequilibrium and equilibrium compositions of cementite to model the enrichment process. Table 4.4 shows the compositions of cementite for 600 °C. Mn has a solubility in cementite of up to 15 – 20 at. %. In MTDATA, there are no data for the solubility of Al and N in cementite.

4.6 Effect of Mn on carbide precipitation

The steels for the present research contain about 2 wt. % Mn. Mn is known to be soluble in cementite, M_7C_3 and $M_{23}C_6$. In 2.25Cr-1Mo steel, Mn accelerates M_7C_3 precipitation [101]. The effects of Mn on the equilibrium phases therefore have to be confirmed. Figure 4.11 shows the weight fractions of the equilibrium phases as a function of temperature for Steels *A* – *E* without Mn.

Steel		Fe	C	Mn	Mo	V	Al	N
Steel A	paraequilibrium	0.728	0.250	0.015	0.007	-	-	-
	equilibrium	0.506	0.250	0.201	0.043	-	-	-
Steel B	paraequilibrium	0.730	0.250	0.015	-	0.005	-	-
	equilibrium	0.498	0.250	0.147	-	0.105	-	-
Steel C	paraequilibrium	0.723	0.250	0.015	0.007	0.005	-	-
	equilibrium	0.478	0.250	0.143	0.030	0.099	-	-
Steel D	paraequilibrium	0.728	0.250	0.015	0.002	0.005	-	-
	equilibrium	0.492	0.250	0.147	0.007	0.104	-	-
Steel E	paraequilibrium	0.730	0.250	0.015	0.002	0.002	-	-
	equilibrium	0.508	0.250	0.169	0.009	0.064	-	-

Table 4.4: Chemical compositions of the paraequilibrium and equilibrium cementite for 600 °C (in atomic fraction).

Compared with Fig. 4.1 – 4.5, the equilibrium phases are not affected significantly by the presence of Mn. However, according to Table 4.4, the equilibrium chemical composition of cementite contains a significant amount of Mn, and therefore the enrichment or precipitation behaviour of cementite could be influenced by Mn.

4.7 Summary

The thermodynamic calculations necessary for the experimental work and modelling of carbide precipitation were performed. In Steel A, the equilibrium carbide for 600 °C is M_2C , which is virtually pure Mo_2C . In Steel B, the equilibrium carbide for 600 °C is M_4C_3 , which is virtually pure V_4C_3 . In Steel C, the equilibrium carbides for 600 °C are M_4C_3 and M_6C , both of which contain significant amounts of Mo and V. In Steel D and E, the equilibrium carbide for 600 °C is M_4C_3 , which contains significant amounts of Mo and V. Mn does not seem to affect the equilibrium phase and does not dissolve into M_2C , M_4C_3 or M_6C to any significant extent. M_2C in Steel A therefore can be modelled as Mo_2C in a Fe-C-Mo ternary system. M_4C_3 in Steel B can be modelled as V_4C_3 in a Fe-C-V ternary system as well. On the other hand, M_4C_3 in Steel C – E must be modelled as $(V,Mo)_4C_3$ in a Fe-C-Mo-V quaternary system.

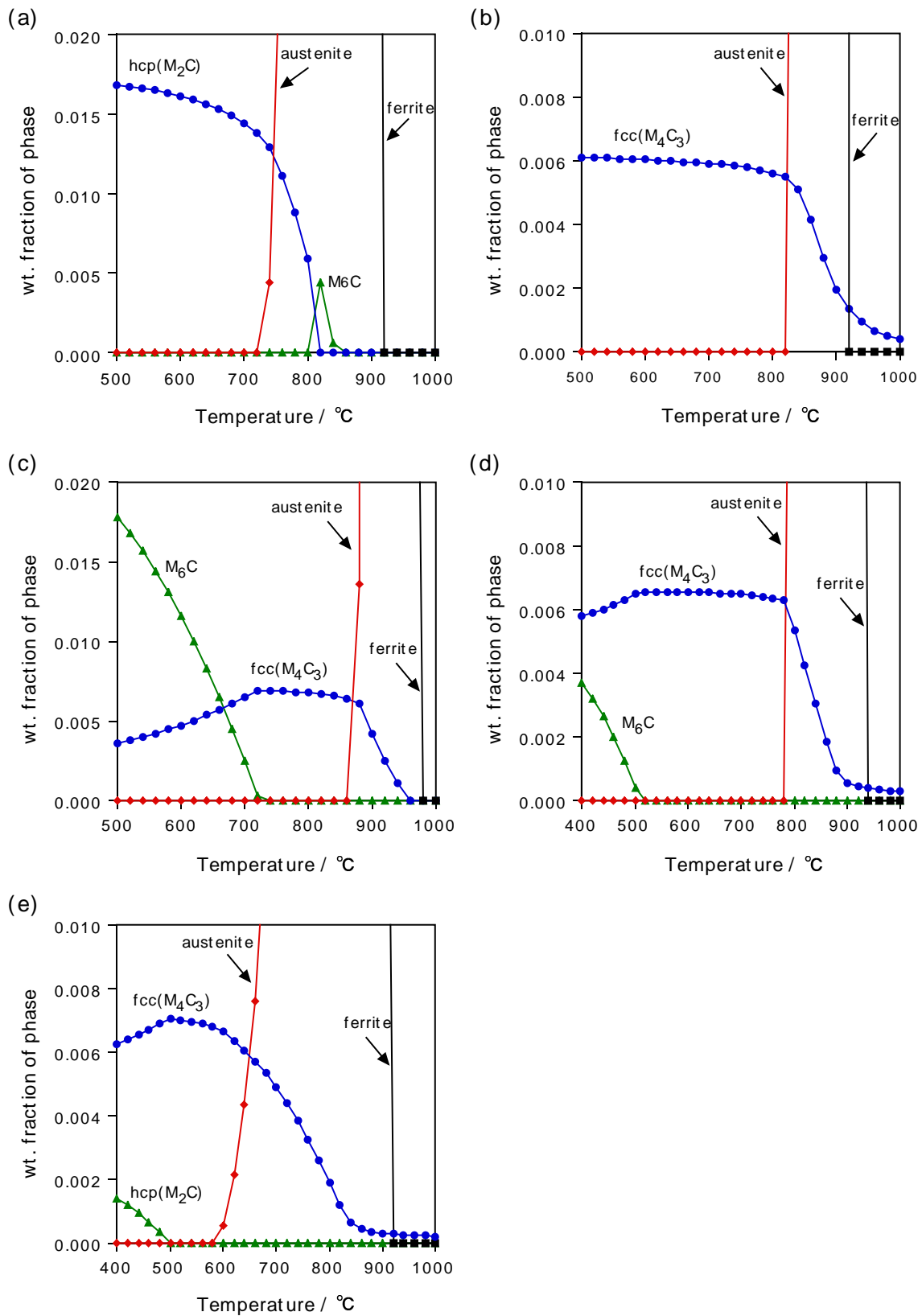


Figure 4.11: Weight fractions of equilibrium phases as a function of temperature in each steel without Mn. (a), (b), (c), (d), (e) are for Steel A, B, C, D, E respectively.

Chapter 5

Experimental procedures

5.1 Introduction

As mentioned in the previous chapter, progress has been made in the modelling of precipitation for multicomponent and multiphase systems. However, there are some factors in the model which must be determined experimentally. For example, the number density of nucleation sites and the interfacial energies are deduced by fitting. By transmission electron microscope (TEM) observation, it is possible to measure the number of sites with great accuracy. Precipitation reactions are at any moment controlled by diffusion of the substitutional solutes in which a mass-balance is maintained. From the calculations for quaternary systems in the previous chapter, it is predicted that the carbide compositions will change as precipitation progresses to maintain mass-balance. To verify the model for a quaternary system, it is necessary to make quantitative measurements. The energy dispersive X-ray (EDX) analysis is useful in determining the solute concentrations in precipitates. Figure 5.1 shows a flow chart of research to verify and improve the model.

There are two main purposes for the experiments: firstly, verification of the theory for simultaneous precipitation reactions in a quaternary system, and obtaining data on the particle sizes, matrix/carbide interface areas, carbide volume fractions and carbide compositions. Secondly, it is necessary to obtain data on hydrogen trapping by alloy carbides, and from these data, to deduce the relationship between the hydrogen trapping capacity and carbide properties such as the volume fraction, the interfacial area and the particle size.

5.2 Materials and processing conditions

Table 5.1 shows the chemical compositions of the materials designed for the present work. Steels *A - C* each contain 0.1 wt. % carbon. Steels *A* and *B* contain stoichiometric quantities of Mo for Mo₂C and V for V₄C₃, respectively. Steels *C*, *D* and *E* contain both molybdenum and vanadium.

Steels *A - E*, described in Table 5.1 were vacuum-melted as 10 kg ingots, heated at 1250 °C for 30 min in an argon atmosphere, hot-rolled to 12 mm thickness plate and air-

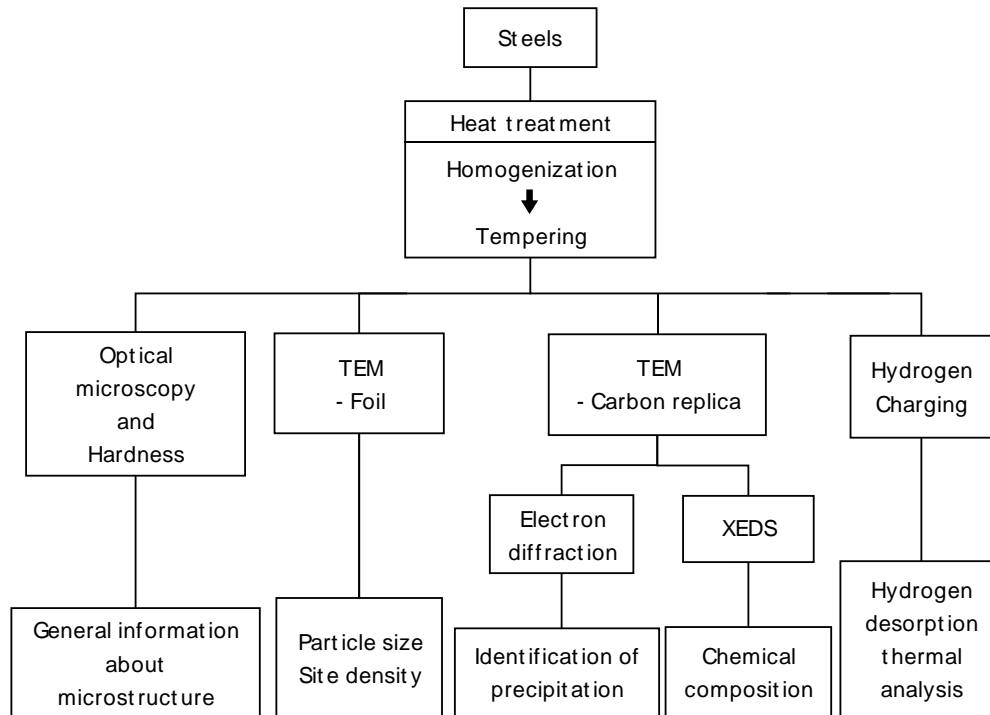


Figure 5.1: Experimental procedure.

cooled. From these plates, the specimens for heat treatment were machined to 3 mm and 8 mm diameter. The specimens were sealed in silica tubes under a partial pressure of argon (about 150 mm Hg), before normalizing. Using MTDATA, the equilibrium phases for each steel at a variety of temperatures were calculated as shown in Fig. 4.1 - 4.5. According to these results, all the steels become fully austenitic at temperatures above 1000 °C. Therefore, the homogenization temperature was chosen to be 1250 °C, at which the samples were held for 50 h.

After the homogenization treatment, the specimens were quenched into water as the silica tubes were broken. Then, the specimens were sealed again and tempered at 600 °C for 0.5 h, 10 h, 20 h, 30 h, 100 h, 560 h and 1150 h. After tempering, all the specimens were again quenched into water simultaneously breaking the tubes.

5.3 Optical microscopy

Specimens for optical microscopy observation were hot-mounted in Bakelite moulding powder, ground with silicon carbide paper down to 1200 grit and then polished with 6 and 1 μm diamond pastes. The specimens were then etched with 4 vol. % nital (nitric acid in

Steel	C	Si	Mn	Mo	V	Al	N
Steel A	0.10	<0.005	1.99	1.60	0.00	0.03	0.0049
Steel B	0.10	<0.005	1.95	0.00	0.57	0.03	0.0043
Steel C	0.10	<0.005	2.00	1.59	0.57	0.03	0.0044
Steel D	0.10	<0.005	2.00	0.40	0.57	0.03	0.0044
Steel E	0.10	<0.005	2.00	0.40	0.30	0.03	0.0044

Table 5.1: Chemical compositions of experimental steels in wt. %.

methanol). The optical microstructures were observed using an Olympus microscope.

5.4 Hardness measurements

The Vickers hardness of the specimens was measured with a load of 10 kg applied for 10 seconds. Five measurements were taken in each case.

5.5 Transmission electron microscopy (TEM)

TEM was performed using Jeol 2000FX transmission electron microscopes operated at 200 kV.

5.5.1 Sample preparation

Two types of specimens were examined using TEM; thin foils and carbon extraction replicas.

Thin foils were sliced from bulk specimens as 3 mm diameter discs approximately 250 μm in thickness using a silicon carbide blade and cooling lubricant. Great care was taken not to bend the specimens. After slicing, the specimens were ground with silicon carbide paper to around 50 μm thickness. Electropolishing was conducted using a twin jet electropolisher [102]. The solutions for electropolishing were 5 vol. % perchloric acid, 20 vol. % glycerol and 75 vol. % methanol. The electropolishing was performed with the solution at 15 $^{\circ}\text{C}$, the electrical potential being set at 50 V. Thin foil observation is crucial to define the orientation relationship between the precipitates and the matrix.

Carbon replica specimens were also prepared from each sample for TEM examination. Replicas have a number of advantages over thin foil samples. By eliminating effects due to the steel matrix, the size and the chemical composition of the carbides may be measured more accurately. Working with a magnetic specimen in the electron beam, which can cause problems, is also avoided. Furthermore, the area of each sample which may be studied is greater than that of a thin foil, where the electron transmitting region may be rather small. Single stage extraction replicas were prepared. The sample was polished mechanically by the same method as for optical microscopy, and chemically etched with 4 vol. % nital for few

seconds. A carbon coating of 20 ~ 30 nm (brown gold colour) was deposited in a vacuum of 10^5 torr onto the etched surface. This film was then scored with a sharp blade to divide it into several smaller squares (about 1 mm²). Electrolytic etching in a solution of 5 % hydrochloric acid in methanol at 7.5 V was used to remove the carbon film, which was then washed in methanol and floated off in distilled water. Each sample yielded approximately ten smaller squares of film which were mounted on copper grids and dried before examination in the TEM. Figure 5.2 shows a schematic drawing of the sample preparation procedures.

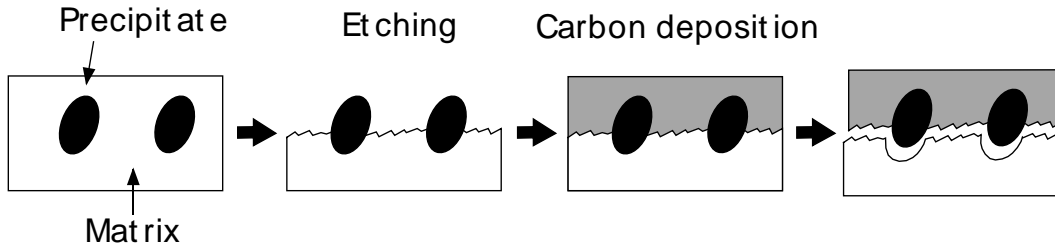


Figure 5.2: Schematic drawing of carbon replica sample preparation.

5.5.2 Selected area diffraction

Selected area electron diffraction using replica specimens is one of the most reliable methods to identify unknown precipitates. The precipitates of interest are chosen using a selected area aperture and a corresponding diffraction pattern is obtained. Figure 5.3 shows a schematic drawing of the geometry of diffraction. The relationship amongst the parameters can be described as follows [103]:

$$R_{hkl}d_{hkl} = L_{cam}\lambda \quad (5.1)$$

where R_{hkl} is the distance between the transmission spot and the diffraction spot from hkl plane, d_{hkl} is the spacing of hkl planes, L_{cam} is the camera length, and λ is the wavelength given by [104]:

$$\lambda = \frac{h}{[2m_e eV_{ac}(1 + \frac{eV_{ac}}{2m_e C_l})]^{0.5}} \quad (5.2)$$

where V_{ac} is the accelerating voltage, C_l is the speed of light in vacuum, h is the Planck constant, e is the charge of an electron and m_e is the electron mass. The camera length was calibrated using a gold film. Figure 5.3 shows a schematic diagram of the geometry of diffraction.

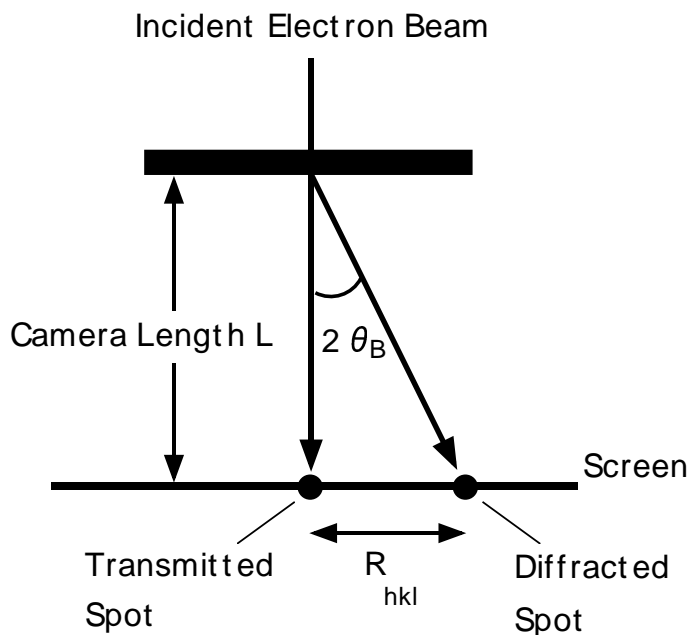


Figure 5.3: Schematic diagram of the geometry of diffraction in transmission electron microscopy. L_{cam} , R_{hkl} and θ_B are the camera length, distance between the transmitted spot and the diffracted spot in the diffraction pattern and Bragg angle, respectively.

5.5.3 Measurement of particle size

M_2C has an hcp structure with a specific orientation relationship with the ferrite matrix [12]:

$$\begin{aligned} \{0001\}_{M_2C} // \{110\}_\alpha \\ \langle 11\bar{2}0 \rangle_{M_2C} // \langle 001 \rangle_\alpha \end{aligned}$$

In the $\langle 001 \rangle_\alpha$ direction, which is parallel to the $\langle 11\bar{2}0 \rangle_{M_2C}$, the matching of both phases is very good, and thus M_2C particles grow in the $\langle 001 \rangle_\alpha$ direction. Therefore, the observation of M_2C particles was performed from $\langle 001 \rangle_\alpha$ direction to measure the particle length and diameter.

M_4C_3 (V_4C_3) has an fcc structure. The orientation relationship between V_4C_3 and the ferrite matrix is reported as [38]:

$$\begin{aligned} \{100\}_{V_4C_3} // \{100\}_\alpha \\ \langle 100 \rangle_{V_4C_3} // \langle 110 \rangle_\alpha \end{aligned}$$

V and Fe atoms have excellent coherency between the lattices along $\{001\}_\alpha$ plane (about 2.1 % mismatch) [12], and thus M_4C_3 particles grow in plate shape on a $\{001\}_\alpha$ plane. The observation of M_4C_3 particles was therefore performed from the $\langle 001 \rangle_\alpha$ direction to measure the particle diameter and thickness.

5.5.4 Measurement of the thickness of a thin foil sample

Consider the case in which the grain boundary or the interface is declined to the incident beam, as shown in Fig. 5.4. It is assumed that one of the lattice planes of one grain (grain A in Fig. 5.4) satisfies the Bragg condition, and no lattice plane satisfies the Bragg condition in another grain (grain B in Fig. 5.4). The incident beam in grain A is then diffracted and the transmitted beam is strong at the depth of $n \times \xi$ from the foil surface, where n is an integer and ξ is the extinction distance, which is represented as:

$$\xi = \frac{\pi V_{cell} \cos \theta_B}{\lambda F} \quad (5.3)$$

where V_{cell} is the volume of a unit cell of the material, θ_B is the Bragg angle, λ is the wavelength and F is the structure factor for the Bragg angle θ_B , which can be represented as $F = 2f$ for the bcc structure where f is atomic scattering amplitude.

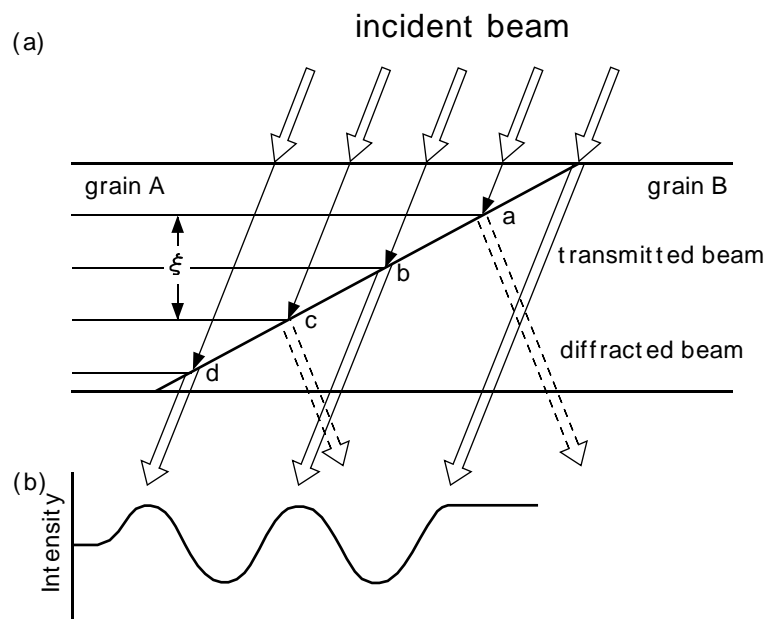


Figure 5.4: (a) Schematic diagram of the geometry of transmitted and diffracted beams at the grain boundary. The transmitted beam from the grain A is strong at the points b and d . (b) Beam contrast on the screen (thickness fringes).

These transmitted beams are not affected by grain B ; they therefore create a type of contrast called thickness fringes on the screen. The foil thickness can therefore be obtained using the number of thickness fringes and the value of the extinction distance for diffraction in grain B . The extinction distances for several $\{hkl\}$ diffraction are known. Table 5.2 shows examples of extinction distance of iron for the two-beam condition at 100 kV.

hkl	110	200	220	400
Extinction distance / nm	28.6	41.2	65.8	116.2

Table 5.2: Examples of extinction distances of iron for two-beam condition at 100 kV [105].

5.5.5 X-ray energy-dispersed spectroscopy (XEDS) measurement

When an electron beam ionizes an atom, the characteristic X-ray energy emitted is unique to the ionized atom. XEDS produces spectra which are plots of X-ray counts versus X-ray energy, which can be used to identify the atom. To perform XEDS analysis in the TEM, the specimen was tilted to 45 °; the live time was 100 s. The dead time was kept below 20 %.

XEDS analysis is particularly useful on carbon replicas, where the precipitates are separated from the matrix. In thin foils, the size of most of the particles is so small that XEDS patterns often contain a large contribution from the matrix. Most of the phases, once characterised by diffraction and composition, can be directly identified from their XEDS pattern.

Results of TEM observations will be presented in chapters on modelling.

5.6 Hydrogen trapping capacity measurements

Specimens of dimensions 8 mm ϕ \times 70 mm L were chosen for the hydrogen trapping measurements. The trapped hydrogen concentration was analyzed through programmed temperature analysis using a gas chromatograph (Yanako GC 1300) [106]. Figure 5.5 shows the schematic diagram of this apparatus. The evolution rate curve of diffusible hydrogen which causes embrittlement of steels shows a peak at 100 °C using this apparatus with a heating rate of 100 °C hour⁻¹. It was investigated that diffusible hydrogen would be fully evaporated using 75 h atmospheric aging with the sample size and hardness for present work, as shown in Fig. 5.6.

Cathodic hydrogen charging was carried out for 48 hours with a current density of 0.2 mA cm⁻² in one litre of 3 wt. % NaCl aqueous solution with 3 g of NH₄SCN (ammonium rhodanate) added as a catalyst. The specimens were then kept at 20 °C atmosphere for 100 h

to evaporate diffusible hydrogen; therefore only trapped hydrogen remained in the specimen. The test specimens were heated from room temperature to 800 °C at a constant programming rate (100 °C hour⁻¹) in Ar carrier gas using gas chromatograph apparatus, and the curves of the hydrogen evolution rate against temperature were obtained. A hydrogen evolution rate curve shows a peak temperature corresponding to the trapping energy of hydrogen [53]. The area-integrated value of this peak was then taken as the trapped hydrogen concentration.

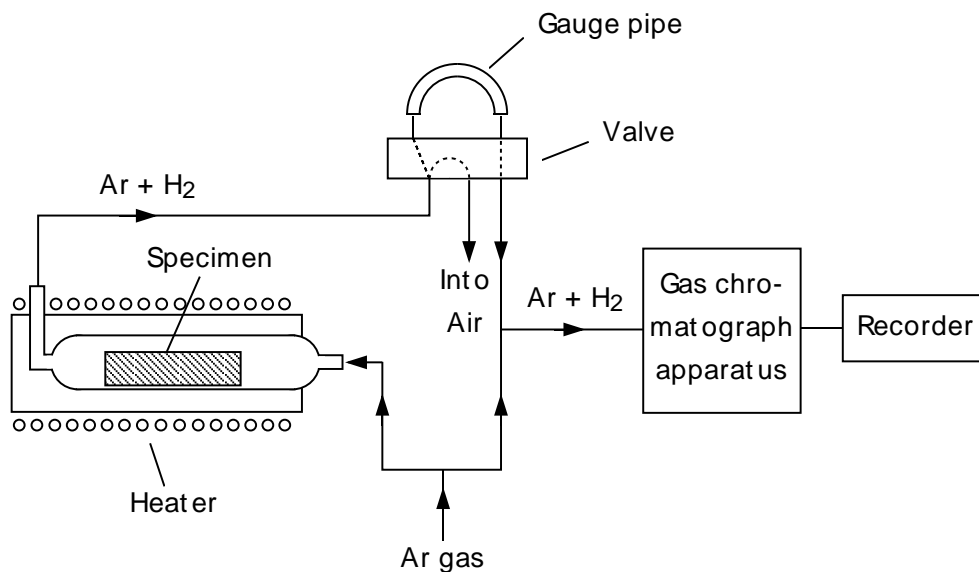


Figure 5.5: Schematic diagram of hydrogen measuring apparatus.

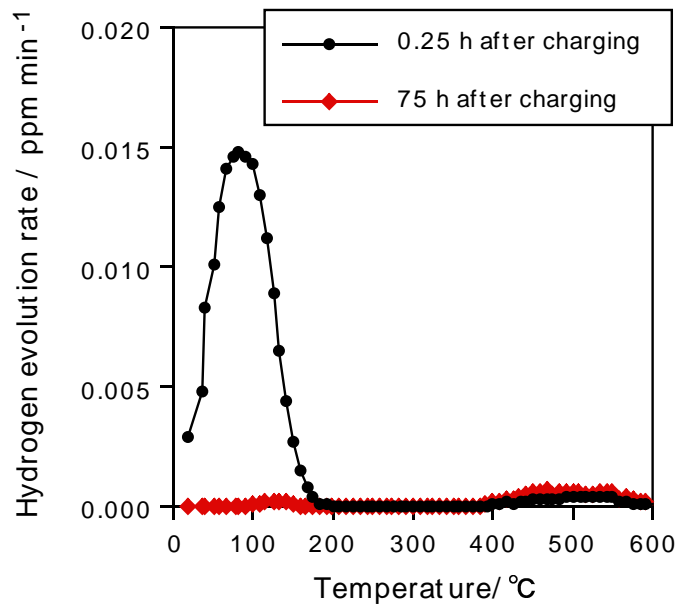


Figure 5.6: Relationship between the hydrogen evolution rate and temperature of samples which were charged with hydrogen and kept for 0.25 h and 75 h at 20 °C atmosphere after hydrogen charging. The chemical composition of the samples was 0.2C-0.2Si-0.5Mn-0.2Cr in wt. % and the Vickers hardness was 350.

Chapter 6

Experimental results

6.1 Optical microstructure

Figures 6.1 and 6.2 show the optical microstructure of (a) Steel *A*, (b) Steel *B*, (c) Steel *C*, (d) Steel *D* and (e) Steel *E* after quenching. Each microstructure was found to be fully martensitic.

6.2 Hardness

Figure 6.3 shows the relationship between the hardness of the steels tested and the tempering time. In the figure, As Q denotes as-quenched.

6.3 TEM observation

Results of TEM observations and EDX measurements will be shown in chapters 7, 8 and 9, as they are relevant to modelling.

6.4 Hydrogen trapping capacity measurement

Figure 6.4 shows the relationships between hydrogen evolution rate and temperature (left), and between amount of hydrogen evolved and temperature (right) for (a) Steel *A*, (b) Steel *B*, (c) Steel *C*, (d) Stees *D* and (e) Steel *E* for various tempering times. The evolved hydrogen amount was obtained by area-integration of the hydrogen evolution rate curve. It is considered that these hydrogen concentrations represent the hydrogen trapping capacities for each tempering condition. The peak temperature in an evolution rate curve corresponds to the hydrogen trapping energy [107, 108]; the trapping energy of hydrogen with 180-200 °C peak temperature is about 30 kJ mol⁻¹ [2, 63]. It was found that steels whose hydrogen trapping capacity was more than 3 wt. ppm showed excellent hydrogen embrittlement resistance [2, 63].

Figure 6.5 shows the relationship between the hydrogen trapping capacity and tempering time for each steel. The hydrogen trapping capacity increases and reaches a maximum,

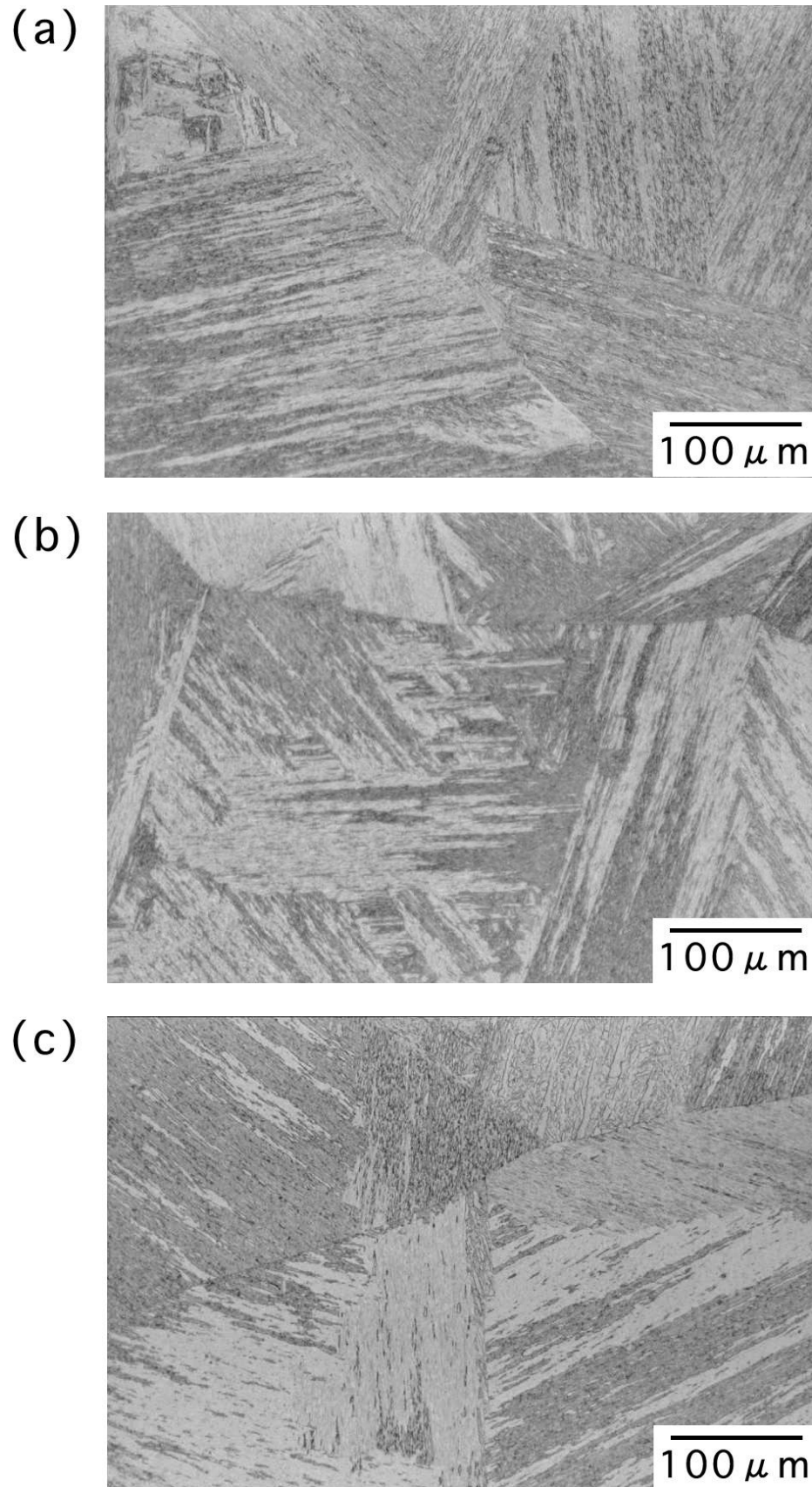


Figure 6.1: Optical microstructure of (a) Steel *A* (b) Steel *B* and (c) Steel *C* after quenching.

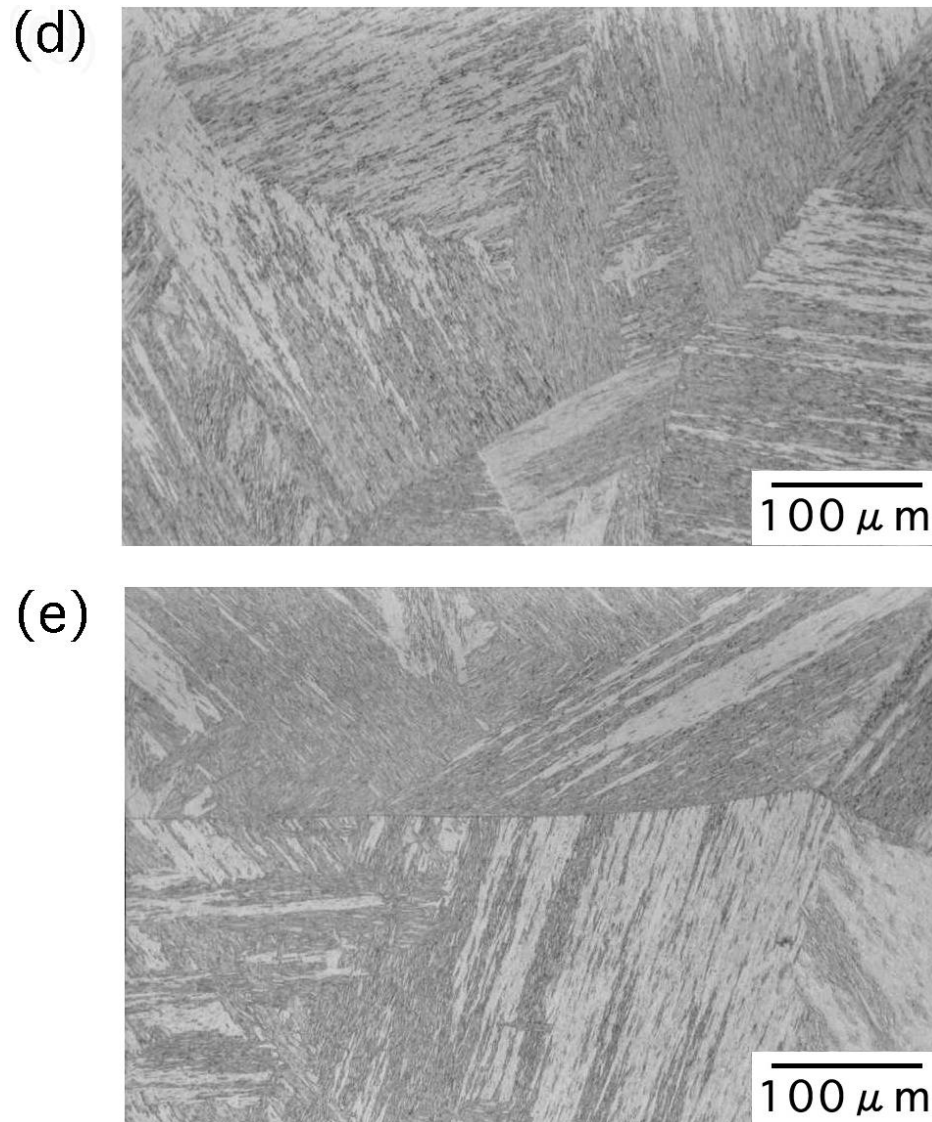


Figure 6.2: Optical microstructure of (d) Steel *D* and (e) Steel *E* after quenching.

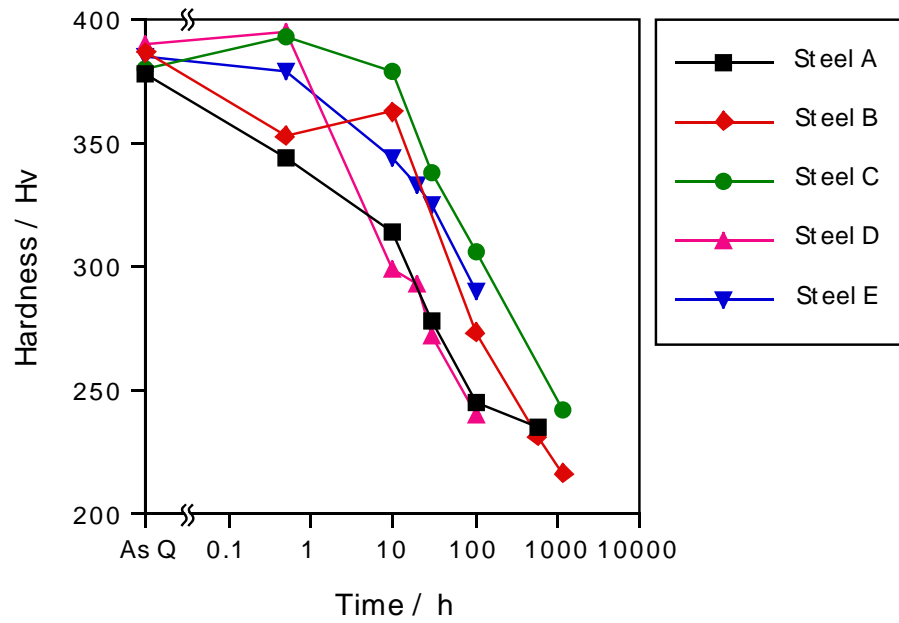


Figure 6.3: Relationship between Vickers hardness of the steels tested and the tempering time. As Q denotes as-quenched.

then decreases, with increasing tempering time. This means that the hydrogen trapping capacity does not merely correspond to the carbide volume and surface area.

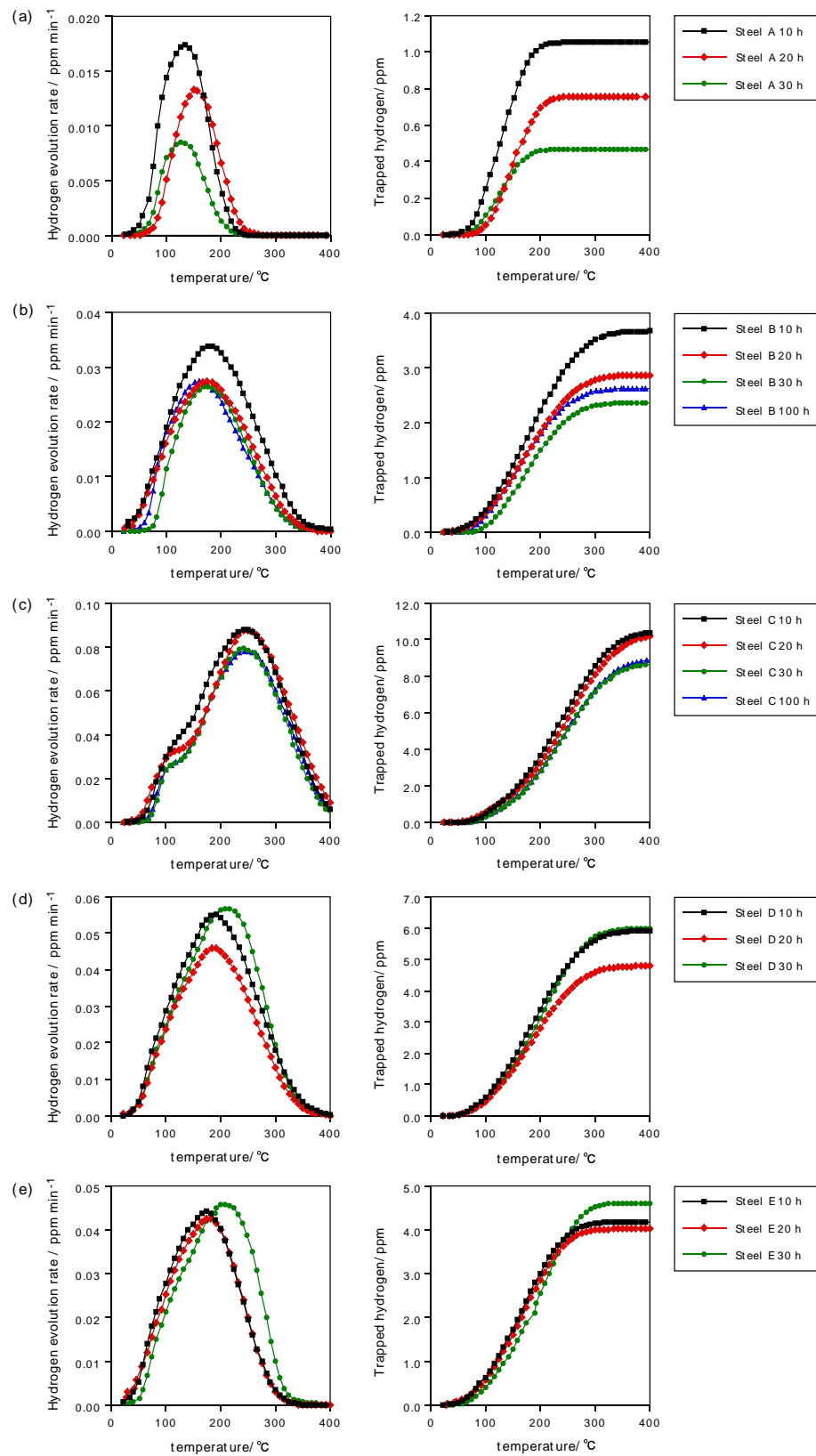


Figure 6.4: The graphs on the left represent the relationship between hydrogen evolution rate and temperature for various tempering times. The right-hand graphs represent the relationship between the evolved hydrogen amount, which is obtained by area-integration of the left graphs, and temperature. (a), (b), (c), (d) and (e) correspond to Steel A, B, C, D and E, respectively.

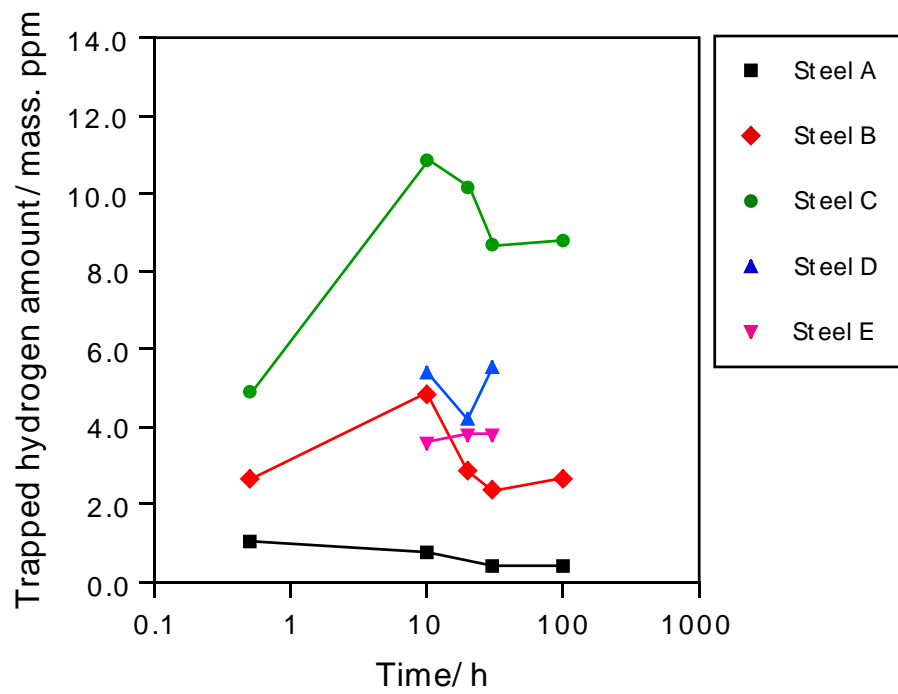


Figure 6.5: Relationship between the hydrogen trapping capacity of each steel and tempering time. Tempering was carried out at 600 °C.

Chapter 7

Modelling Mo_2C in a Fe-C-Mo ternary system

7.1 Experimental work

Experiments were conducted to provide data for model verification. As shown later, the model can predict the average carbide length, volume fraction and number density. It is therefore necessary to obtain these data experimentally to verify the model. Transmission electron microscopy was used to obtain the necessary data.

7.1.1 Material

Table 7.1 shows the chemical composition of the material designed for the present work. The steel contains 0.1 wt. % carbon and a stoichiometric quantity of Mo for Mo_2C . As will be shown later, experimental data and thermodynamic calculations show that in this steel the carbide is virtually pure Mo_2C with negligible quantities of iron or manganese in the metal sites. Therefore, its precipitation can be modelled as if it occurred in a ternary Fe-Mo-C system.

	C	Si	Mn	Mo	Al	N
Steel A	0.10	<0.005	1.99	1.60	0.03	0.0049

Table 7.1: Chemical composition of experimental steel in wt. %.

7.1.2 Transmission electron microscopy

I Molybdenum carbide

Figures 7.1 - 7.6 show thin-foil TEM images of Steel A tempered for a variety of times. These pictures were taken from the [100] orientation of the matrix. Figure 7.7 shows the images of a carbon replica from the specimen which was tempered for 560 h at 600 °C. From

the diffraction patterns in Fig. 7.7, the needle-shaped precipitates have a hexagonal close-packed (hcp) structure and are considered to be M_2C , where ‘M’ stands for metal atoms (Mo, Mn, Fe); the molybdenum-rich carbide is henceforth referred to as M_2C . It is known that M_2C grows along the three equivalent $\langle 001 \rangle$ directions of ferrite, and, for example in Fig. 7.4, precipitates growing in three $\langle 001 \rangle$ directions are observed. In Fig. 7.1 - 7.6, the point-like precipitates are the cross-sectional images of precipitates growing in the $[100]$ direction, which is parallel to the observation direction.

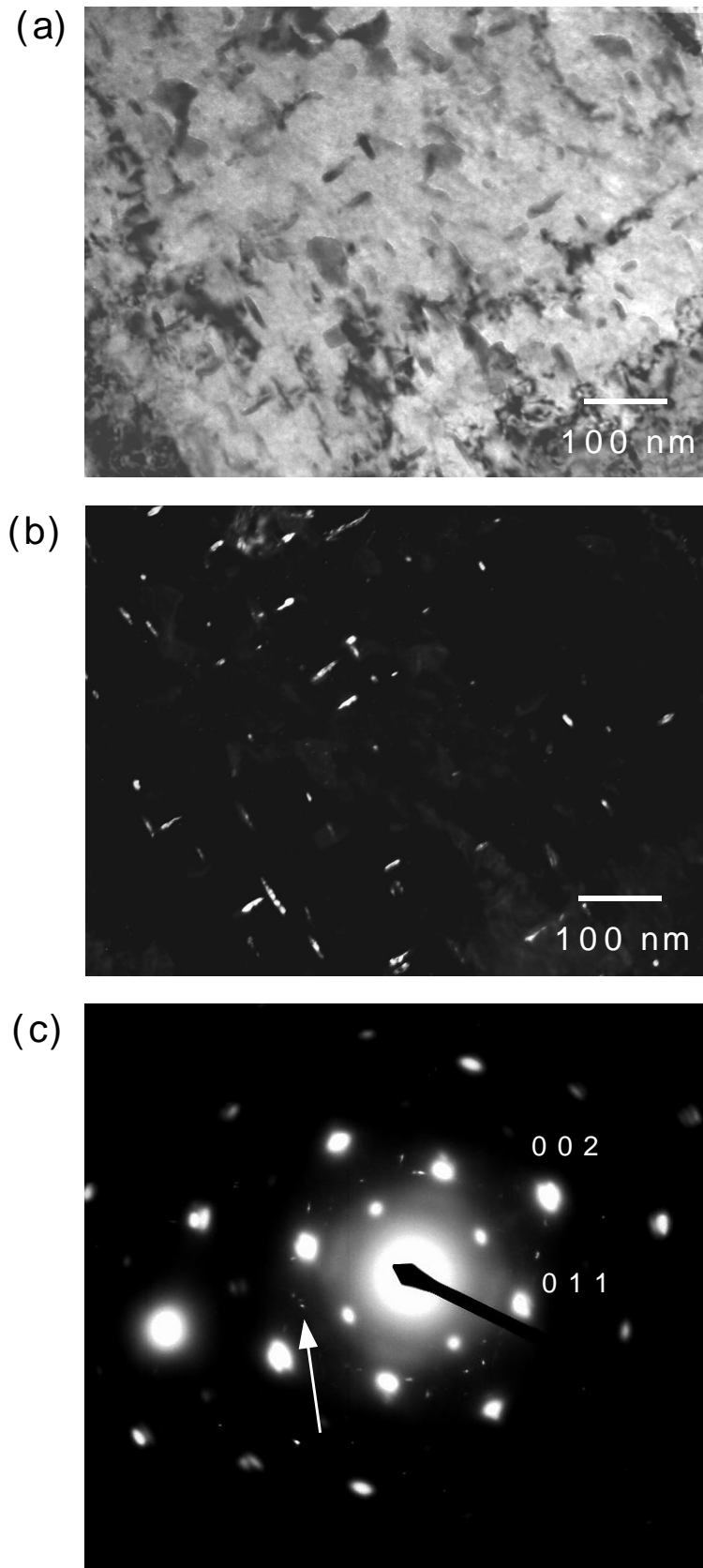


Figure 7.1: TEM observation of a thin-foil from Steel A tempered at 600 °C for 0.5 h. Zone axis is [100] of ferrite matrix. (a) Bright field image. (b) Dark field image using the carbide diffraction spot indicated by the arrow in (c). The 002 and 011 reflections are from the ferrite.

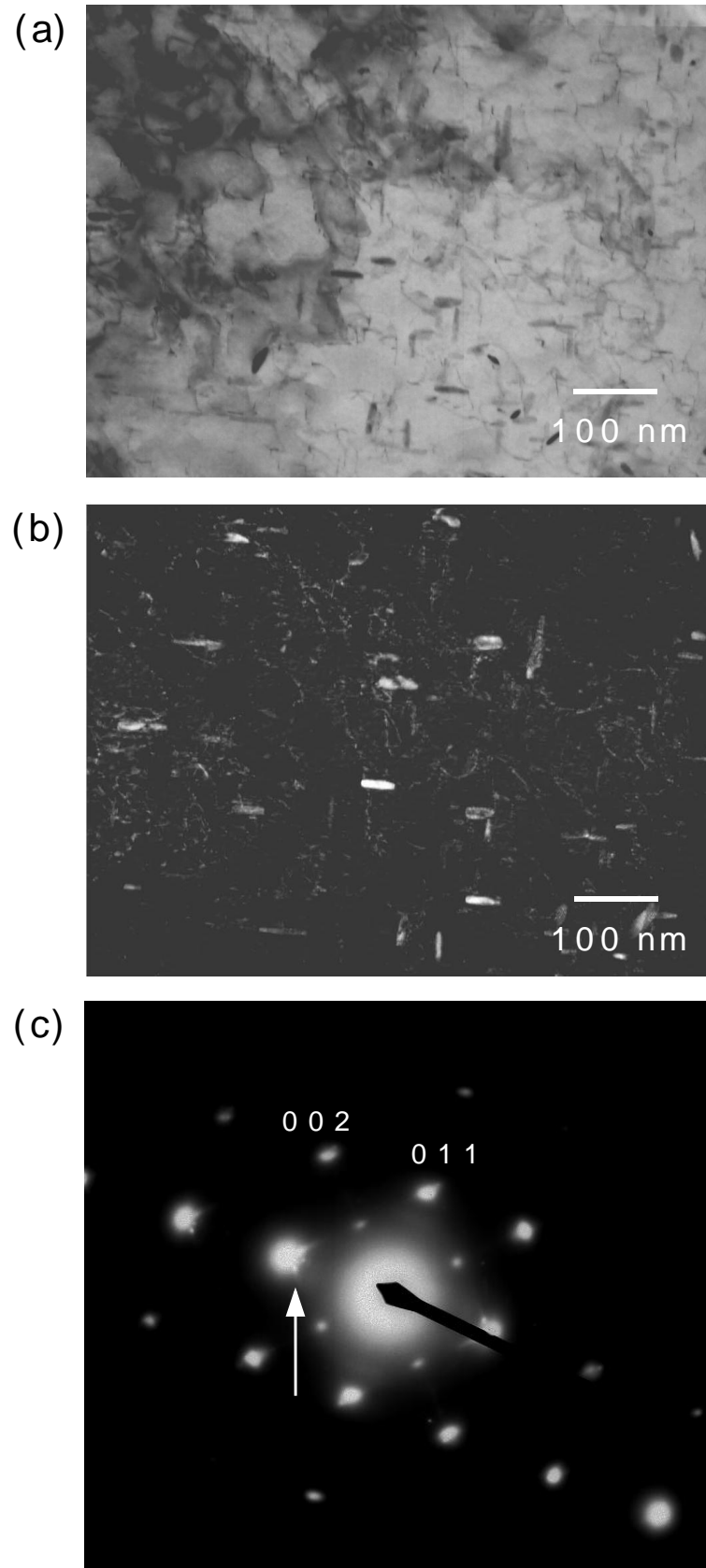


Figure 7.2: TEM observation of a thin-foil from Steel A tempered at 600 °C for 10 h. Zone axis is [100] of ferrite matrix. (a) Bright field image. (b) Dark field image using the carbide diffraction spot indicated by the arrow in (c). The 002 and 011 reflections are from the ferrite.

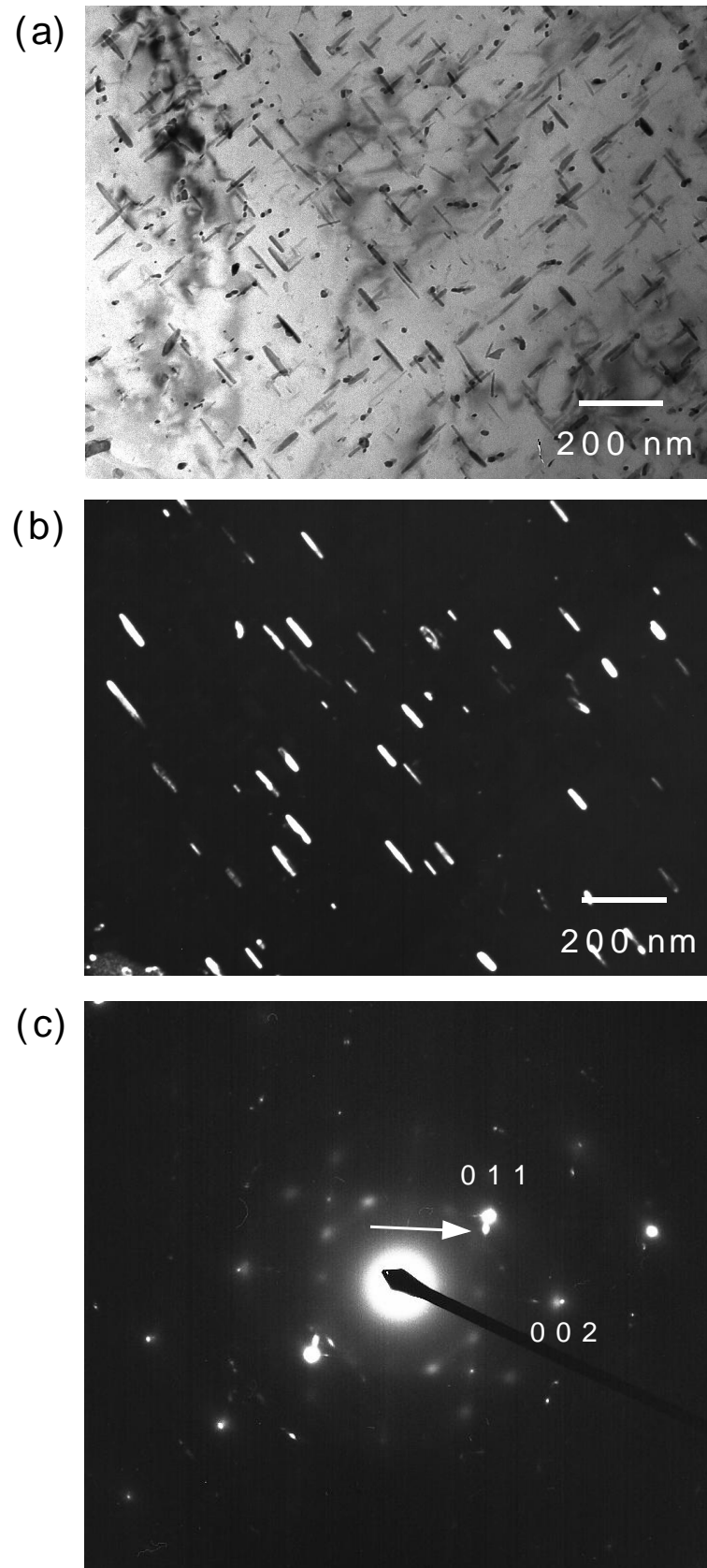


Figure 7.3: TEM observation of a thin-foil from Steel A tempered at 600 °C for 30 h. Zone axis is [100] of ferrite matrix. (a) Bright field image. (b) Dark field image using the carbide diffraction spot indicated by the arrow in (c). The 002 and 011 reflections are from the ferrite.

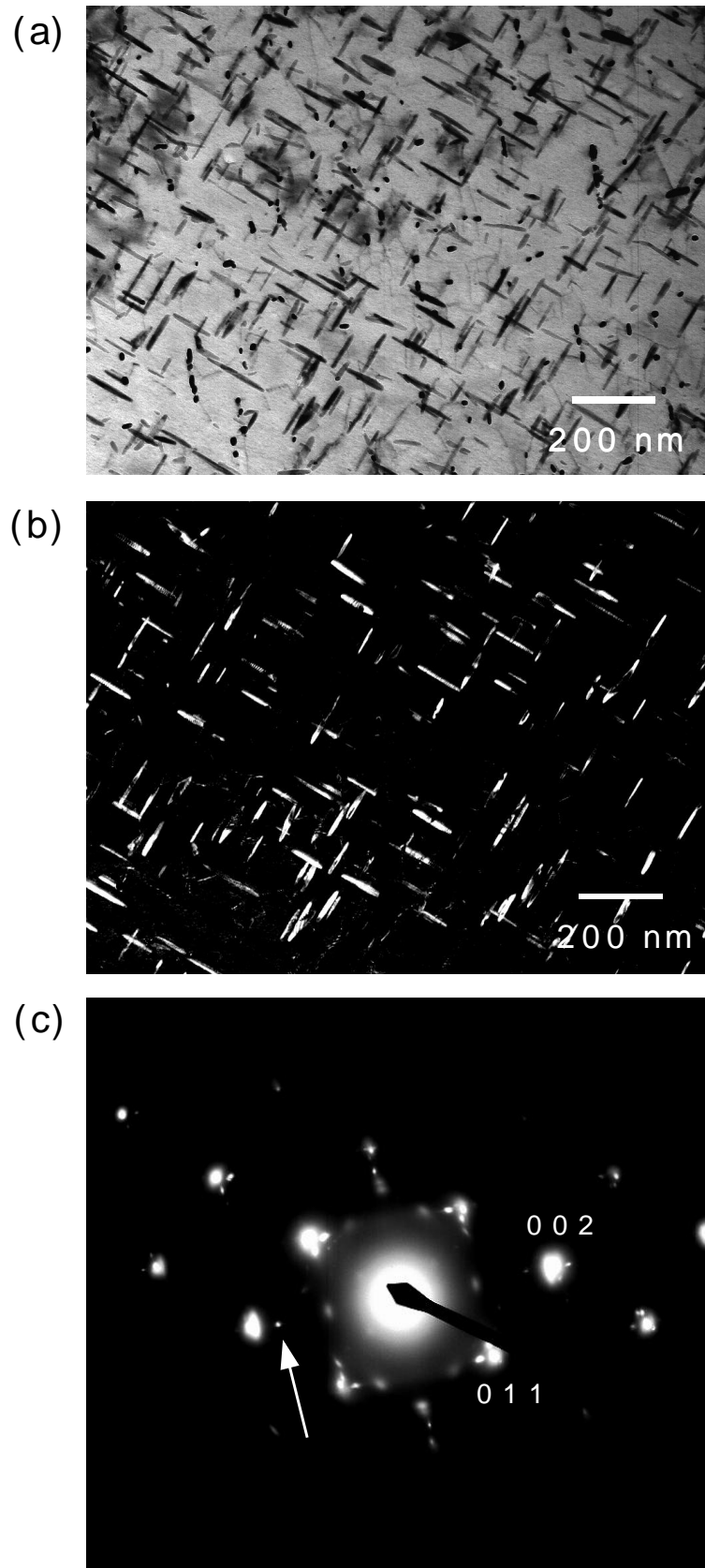


Figure 7.4: TEM observation of a thin-foil from Steel A tempered at 600 °C for 100 h. Zone axis is [100] of ferrite matrix. (a) Bright field image. (b) Dark field image using the carbide diffraction spot indicated by the arrow in (c). The 002 and 011 reflections are from the ferrite.

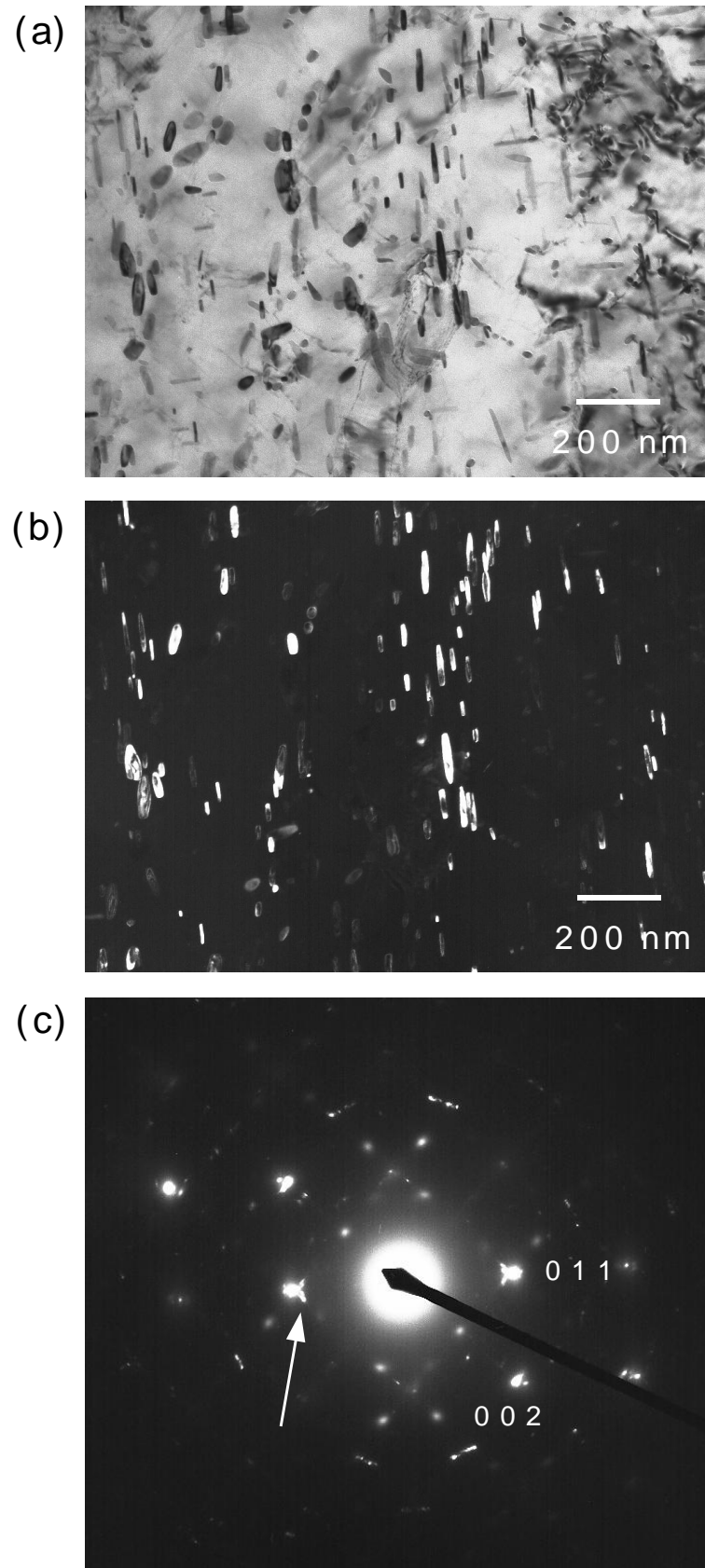


Figure 7.5: TEM observation of a thin-foil from Steel A tempered at 600 °C for 560 h. Zone axis is [100] of ferrite matrix. (a) Bright field image. (b) Dark field image using the carbide diffraction spot indicated by the arrow in (c). The 002 and 011 reflections are from the ferrite.

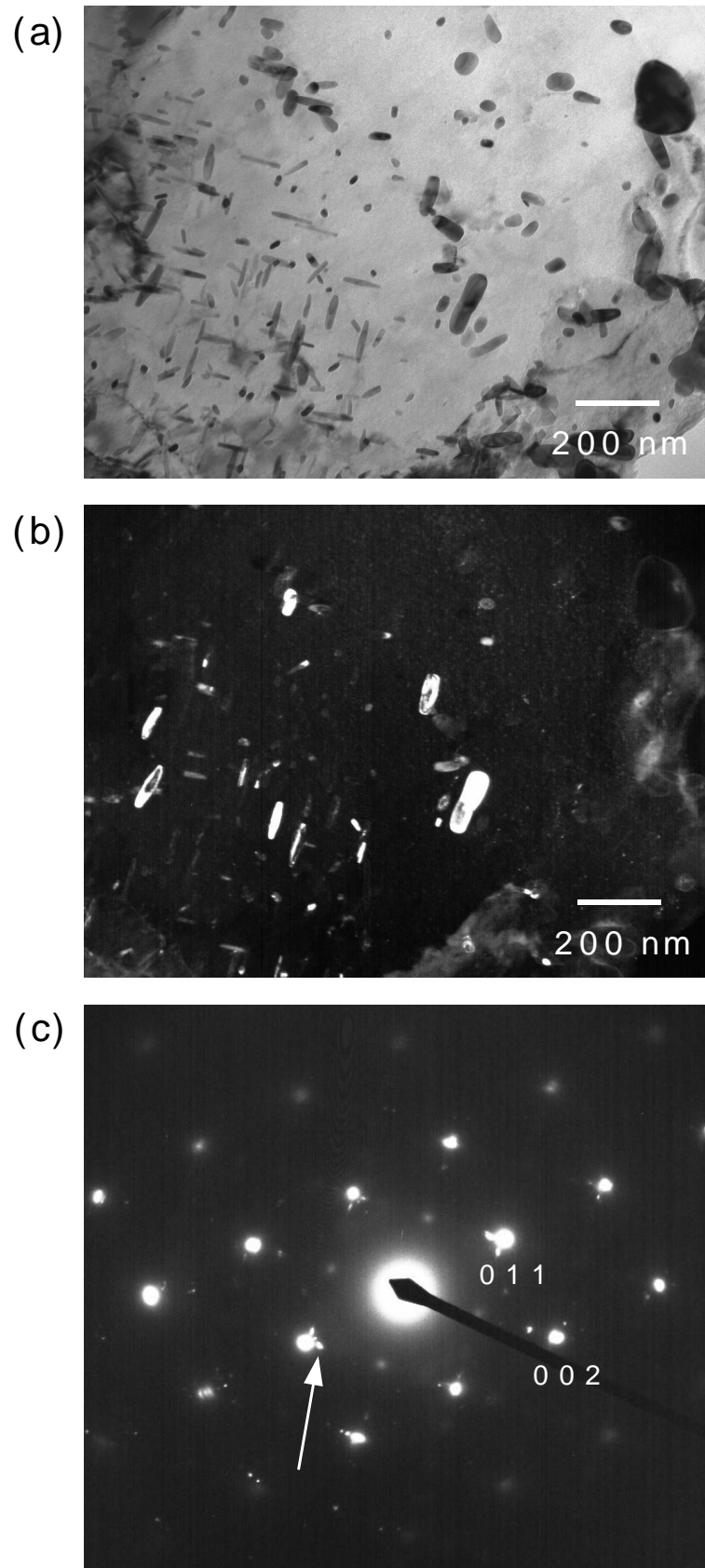


Figure 7.6: TEM observation of a thin-foil from Steel *A* tempered at 600 °C for 1150 h. Zone axis is $[100]$ of ferrite matrix. (a) Bright field image. (b) Dark field image using the carbide diffraction spot indicated by the arrow in (c). The 002 and 011 reflections are from the ferrite.

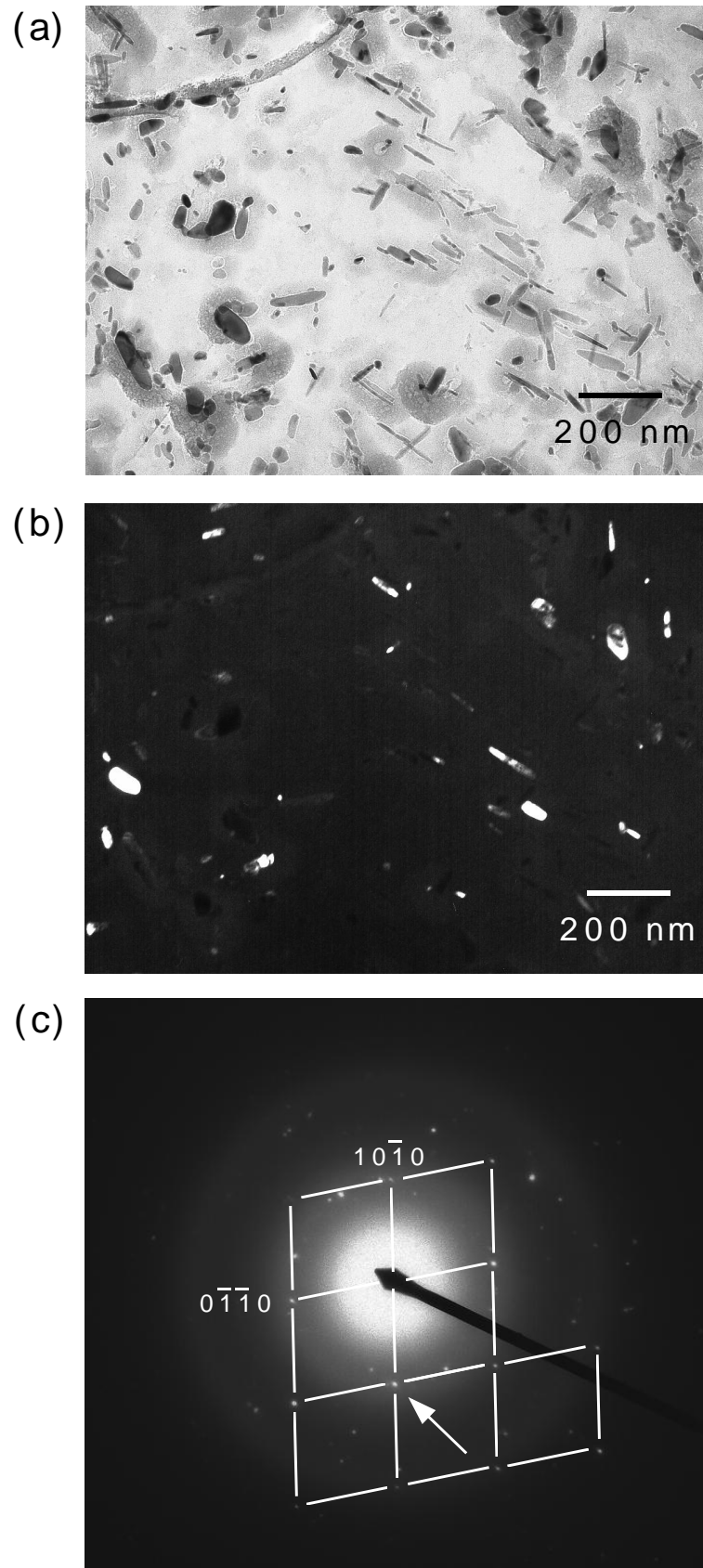


Figure 7.7: TEM observation of carbon replica from Steel A tempered at 600 °C for 560 h. (a) Bright field image. (b) Dark field image using the carbide diffraction spot indicated by the arrow in (c). The $10\bar{1}0$ and $0\bar{1}\bar{1}0$ reflections are from M_2C .

II Cementite

Figures 7.8 - 7.10 show the extraction carbon replica TEM image of Steel *A* tempered for a variety of times. Cementite particles precipitate on the prior-austenite grain boundaries and the martensite lath boundaries. Cementite particles are also evident within the laths. Particles precipitating on the boundaries are spheroidal or plate-shaped and the average thickness is 50 nm. On the other hand, the particles precipitating within the laths are plate-shaped and the average thickness is 20 nm. Cementite in the laths dissolved after 100 h tempering at 600 °C, but it persisted on the grain boundaries.

III Chemical compositions of carbides

The chemical compositions of M_2C and cementite particles were measured using energy dispersive spectroscopy on carbon replica specimens. Figure 7.11 shows the typical X-ray count-energy profiles and the ratio of metallic elements in cementite and M_2C for several tempering times. Experimental data were obtained from at least 5 particles in each sample. In Fig. 7.11, the solid circles represent the average of data from different particles, and the scatter of the data is indicated by error bars. The average atomic ratio of metallic elements in M_2C particles is 0.91Mo:0.06Mn:0.02Fe. M_2C is therefore virtually pure Mo_2C .

IV Foil thickness

A knowledge of the thickness of the foils used for transmission electron microscopy is necessary to estimate the volume fraction of Mo_2C . The thickness was measured using thickness fringes at the grain boundaries. The extinction distances for a two-beam condition are known; it is therefore possible to calculate the thickness of the sample by multiplying the extinction distance by the number of fringes. The thickness of the samples was in this way found to be 80–160 nm.

V Carbide morphology and volume fraction

The carbide size was measured for each sample from at least five different locations, each of which contained over 300 particles. The volume fraction was calculated using the length and diameter of each carbide particle and the foil thickness. The volume fraction, average length, average aspect ratio, number density and number density distribution of the length of Mo_2C particles are shown in Fig. 7.12. In Fig. 7.12, the solid circles represent the average of data from different locations, and the scatter of the data is indicated by error bars. Mo_2C grows at the expense of cementite. It grows in the $\langle 001 \rangle_\alpha$ directions whilst maintaining a needle shape whose average aspect ratio is 9–10 up to 100 h. However, after 100 h tempering, the average aspect ratio decreases, whilst the volume fraction remains constant. This is therefore considered to be an Ostwald ripening stage.

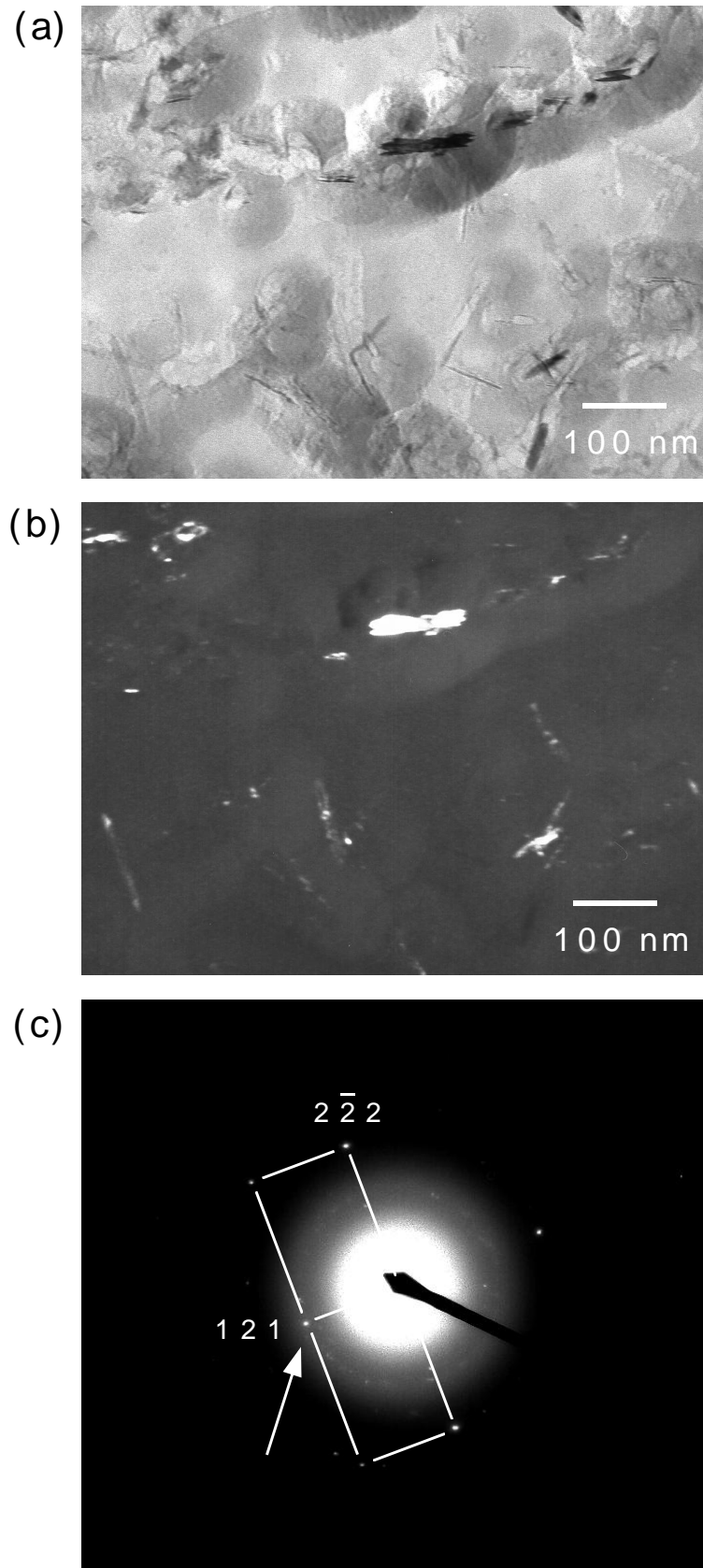


Figure 7.8: TEM observation of carbon replica from Steel A tempered at 600 °C for 0.5 h. (a) Bright field image. (b) Dark-field image using the cementite diffraction spot indicated by the arrow in (c). The $2\bar{2}2$ and 121 reflections are from cementite.

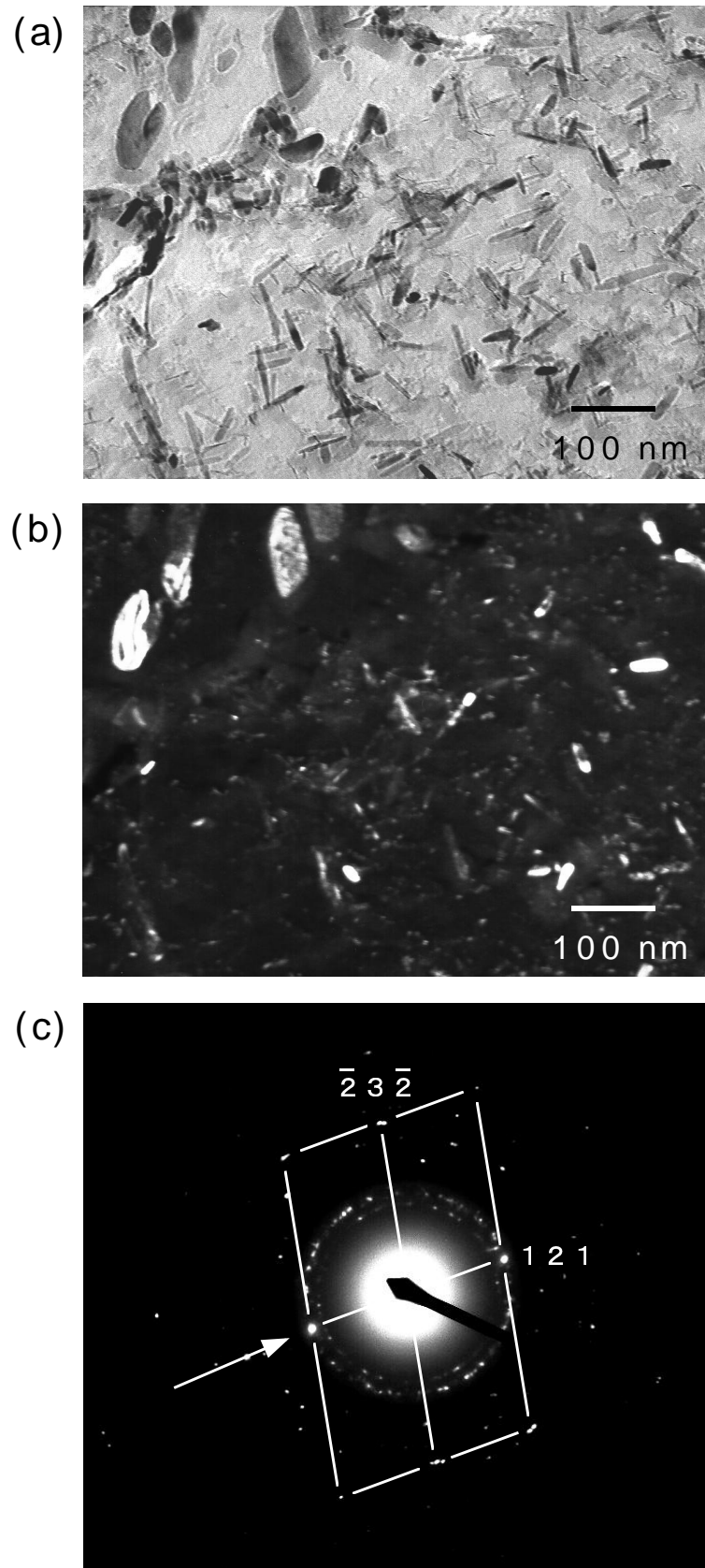


Figure 7.9: TEM observation of carbon replica from Steel A tempered at 600 °C for 10 h. (a) Bright field image. (b) Dark-field image using the cementite diffraction spot indicated by the arrow in (c). The $\bar{2}3\bar{2}$ and 121 reflections are from cementite.

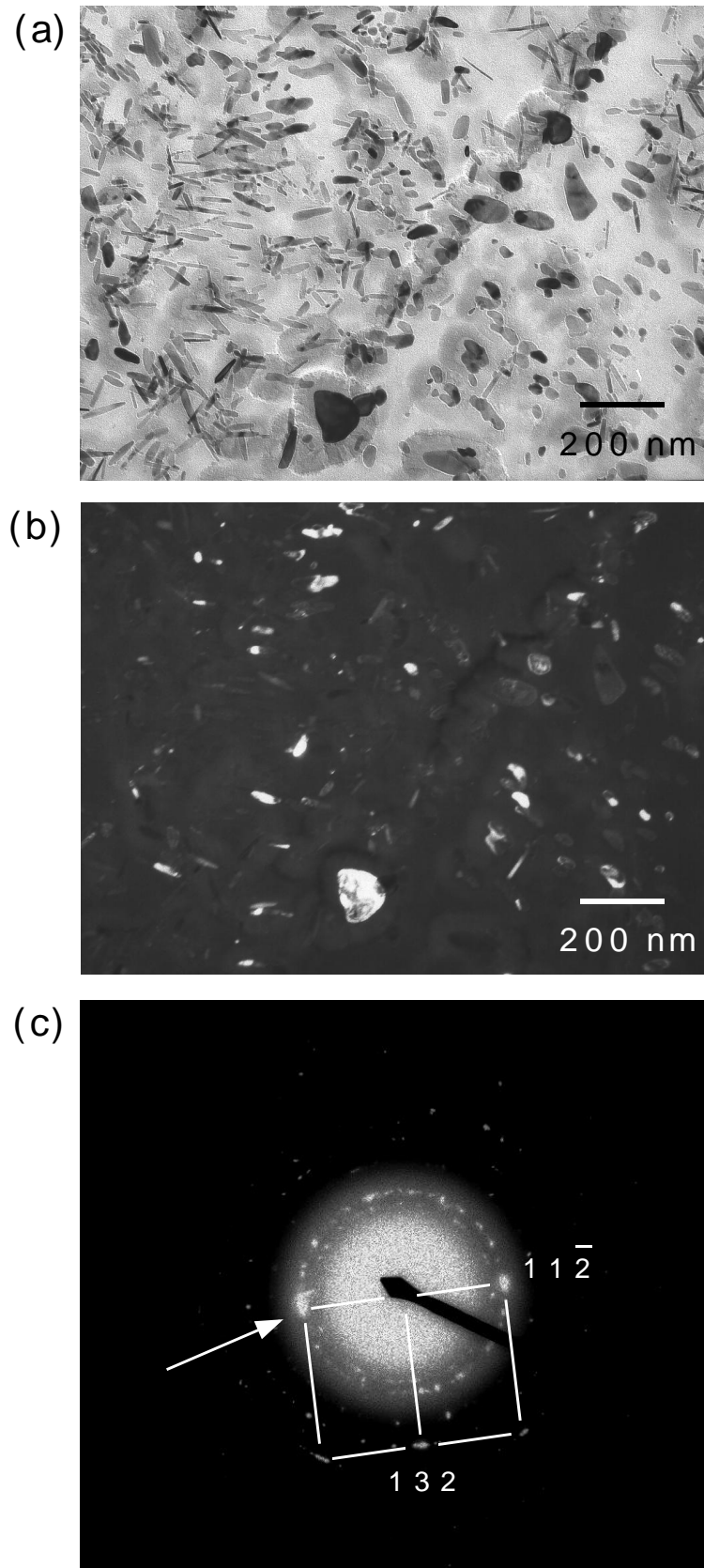


Figure 7.10: TEM observation of carbon replica from Steel A tempered at 600 °C for 100 h. (a) Bright field image. (b) Dark-field image using the cementite diffraction spot indicated by the arrow in (c). The $11\bar{2}$ and 132 reflections are from cementite.

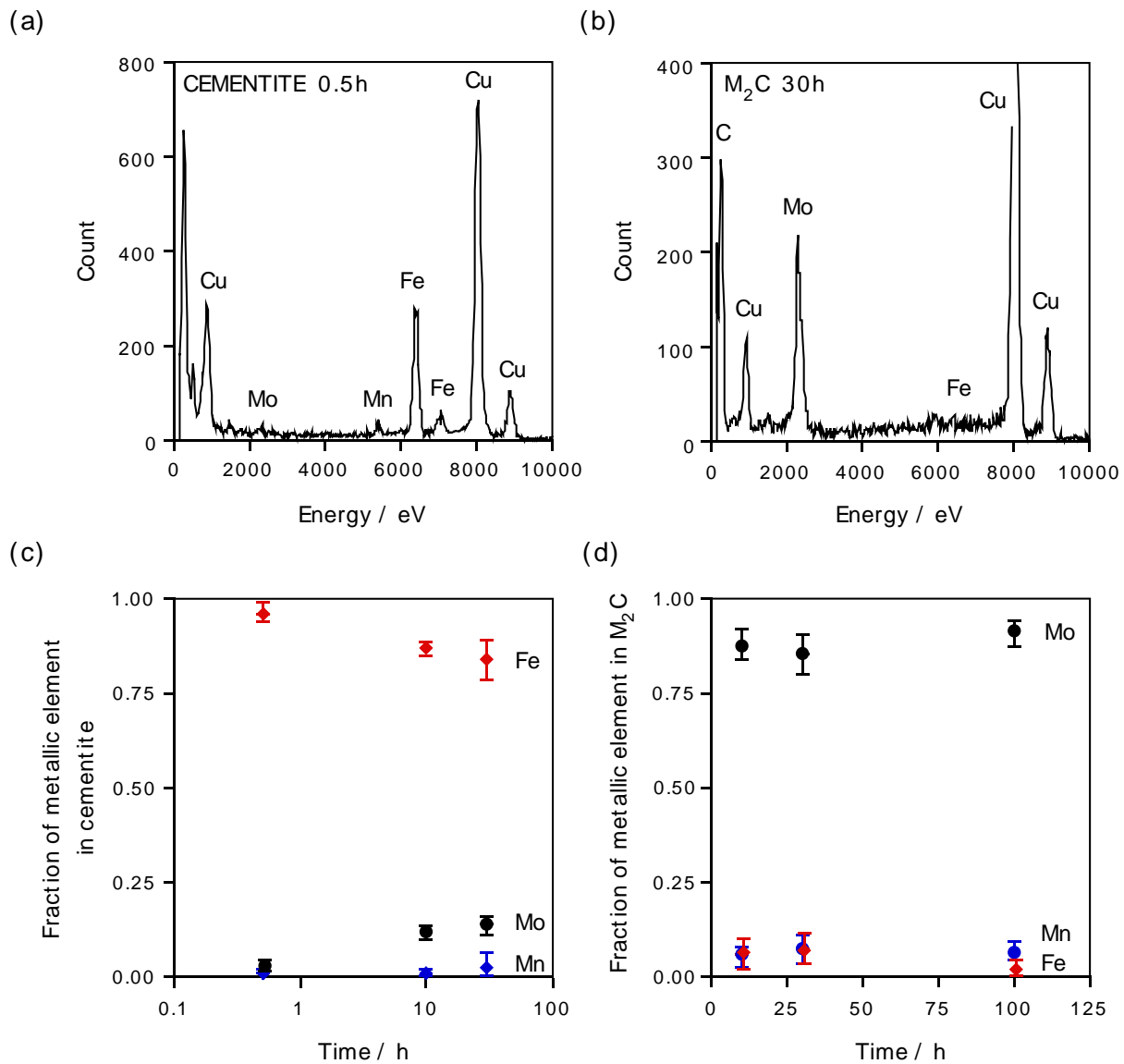


Figure 7.11: XEDS analysis of Steel A tempered at 600 °C. (a) Example of X-ray count-energy profile of cementite, (b) Example of X-ray count-energy profile of M_2C , (c) Relationship between atomic ratio of metallic elements and tempering time for cementite, (d) Relationship between atomic ratio of metallic elements and tempering time for M_2C .

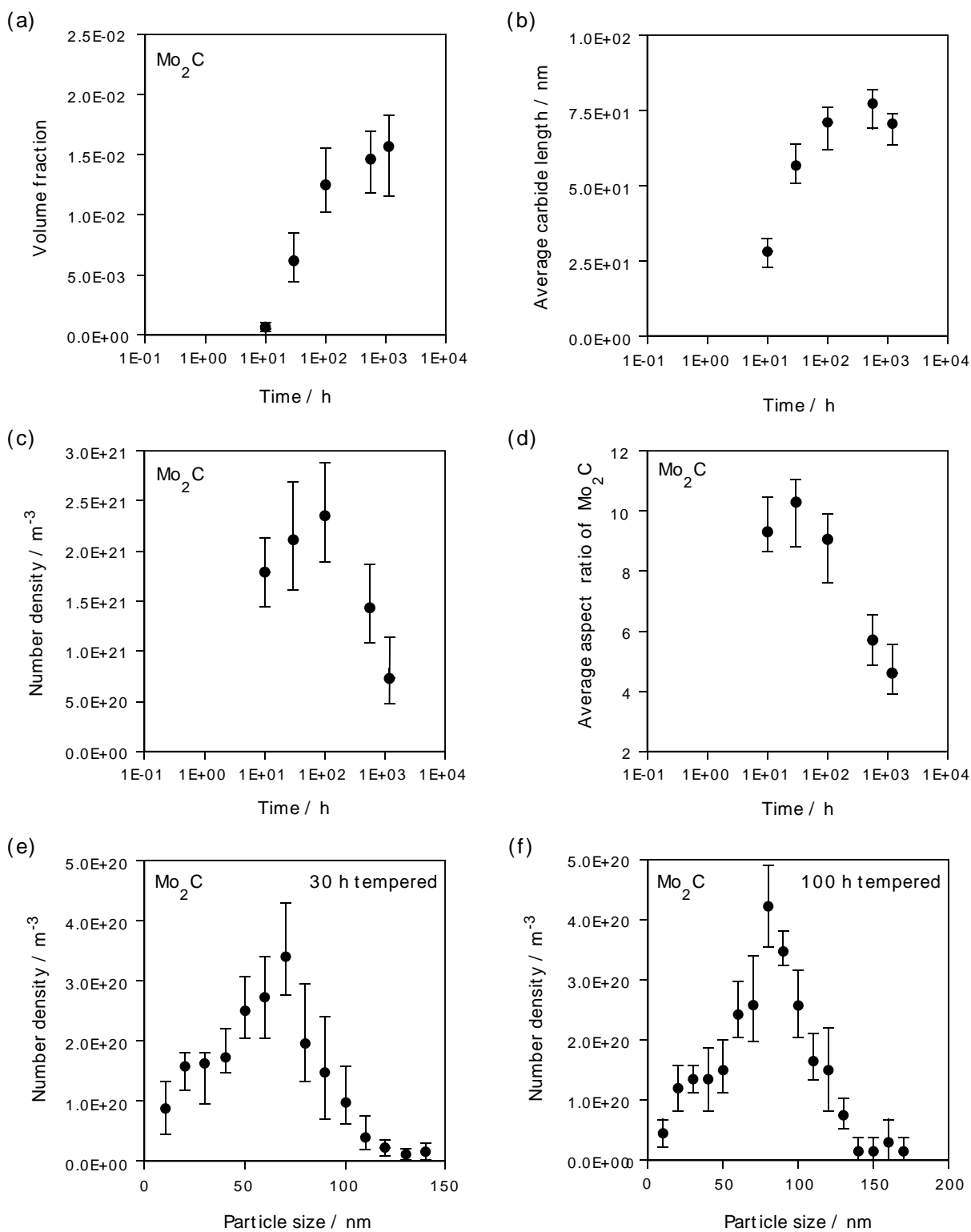


Figure 7.12: Observations of Steel A tempered at 600 °C. (a) Relationship between Mo₂C volume fraction and tempering time. (b) Relationship between average length of Mo₂C particles and tempering time. (c) Relationship between number density of Mo₂C particles and tempering time. (d) Relationship between aspect ratio of Mo₂C particles and tempering time. (e) Number density distribution of length of Mo₂C particles in the steel tempered for 30 h. (f) Number density distribution of length of Mo₂C particles tempered for 100 h.

7.2 Precipitation of alloy carbide with local equilibrium

Carbon is an interstitial solute in iron and hence has a much higher mobility than substitutional solutes or iron. It is natural therefore that iron carbides are the first to form when virgin martensite is tempered. The iron carbides form by a displacive mechanism and hence only the diffusion of carbon is necessary. [14, 15, 16, 17]

The steps following the rapid precipitation of paraequilibrium cementite are complicated because its chemical composition changes towards equilibrium as cementite absorbs molybdenum (enriches) to try to achieve its equilibrium composition. As shown in Fig 7.11 (c), this enrichment was observed in the present work. Cementite, although kinetically favoured, is less stable than many alloy carbides; consequently, while the cementite adapts its chemical composition, molybdenum carbide precipitation commences and eventually leads to the dissolution of the cementite. These processes must all be considered to occur simultaneously in any model.

In the present case, alloy carbide formation involves the diffusion of both molybdenum and carbon, the diffusivities of which are different by many orders of magnitude at the transformation temperature. In order to maintain equilibrium at the transformation interface, the tie-line controlling interface compositions has to be chosen in such a way that the two solutes can keep pace with each other [79]. Another way of expressing this condition is to construct interface-composition (IC) contours on isothermal sections of the ternary phase diagram. All alloys on a single contour transform with the same compositions (same tie-line) at the interface, whilst ensuring that the slow and fast solute-diffusion fluxes are both consistent with the rate at which the interface moves. The IC contour depends on the ratio of the diffusion coefficients of the substitutional solute X and of carbon (D_X/D_C).

Considering this scenario, the precipitation process in a ternary alloy can be illustrated by Fig. 7.13. Point *a* is the overall composition of the alloy, i.e. the composition of the virgin martensite. Point *b* is the matrix composition after paraequilibrium cementite precipitation; this matrix is supersaturated with respect to molybdenum carbide which will precipitate with the interface compositions given by the tie-line *cf*. As it continues to precipitate, the less stable cementite dissolves; this effectively moves *b* in a direction such that the governing tie-line shifts from *cf* towards *ed*. This tie-line shifting [79] ceases when the governing tie-line passes through the average composition *a* and equilibrium is achieved. The cementite acts as a source of carbon.

In Fig. 7.13, to satisfy the mass balances of Mo and C, the interfacial C concentration is assumed to be the same as that of the matrix [79]. Strictly, however, carbon diffusion is affected by other elements. Hillert treated diffusion-controlled growth in a ternary system more rigorously by considering the interatomic effect on diffusion [71]. According to Hillert's theory, the chemical composition of ferrite which is in equilibrium with the carbide can be obtained by the cross point of the ferrite/ferrite + carbide phase boundary curve and the

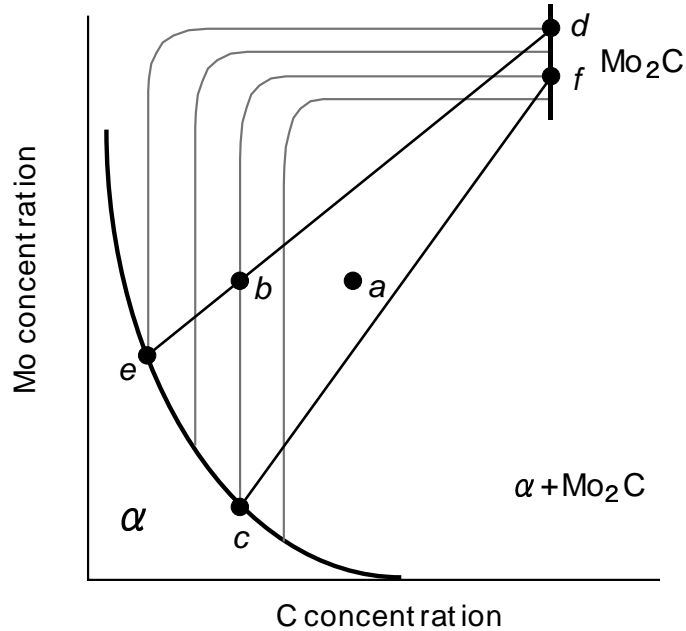


Figure 7.13: Schematic representation of the alloy composition and the tie-lines governing $\alpha/\text{Mo}_2\text{C}$ interface compositions during the precipitation process. Point a is the alloy composition and b is the matrix composition after paraequilibrium cementite precipitation. The points c and f are the ends of the IC contour passing through the point b , and are the $\alpha/\text{Mo}_2\text{C}$ interface compositions.

iso-activity curve of carbon passing through the nominal matrix composition in the ternary phase diagram (the point c' in Fig. 7.14). Later, Coates took into account the interatomic effect on diffusion and came to the same conclusion as Hillert. It is therefore necessary to confirm the iso-activity curve of carbon in a ternary phase diagram to apply Coates' theory represented by Fig. 7.13. If the carbon activity is not affected significantly by Mo, it is possible to apply Fig. 7.13.

Figure 7.15 shows the iso-activity curves in the Fe-C-Mo ternary phase diagram. From these results, it is considered that there could be small deviations (up to about 10 %) of the interfacial carbon concentration by applying Coates' diffusion-controlled growth theory. The assumption in Fig. 7.13 is therefore considered to be valid.

7.3 Growth of particles: capillarity

As presented in section 2.2.3, the most comprehensive theory of diffusion-controlled growth is due to Trivedi [76], following work by Ivantsov [74], in which a needle-shaped particle is represented as a shape-preserving paraboloid of revolution. The curvature is

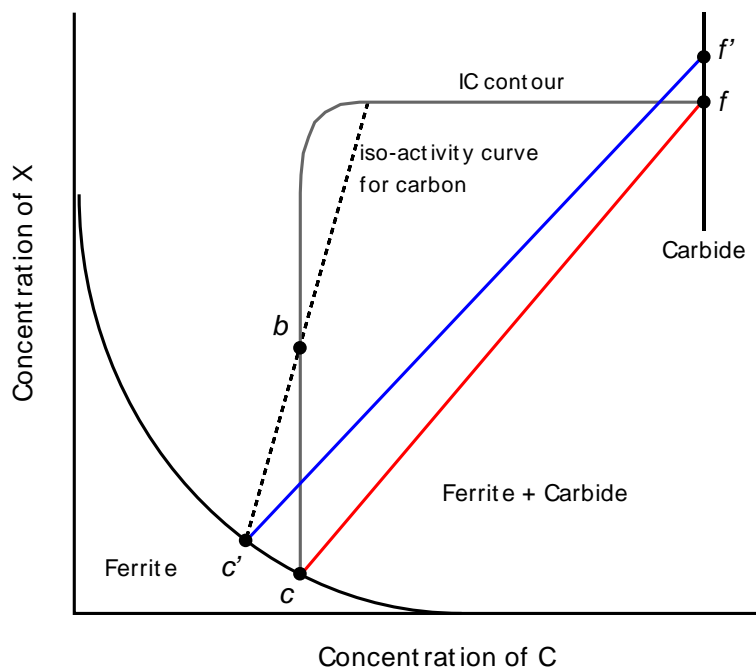


Figure 7.14: Interface compositions with local equilibrium in a Fe-C-X system. Point b is the matrix composition. Interface compositions obtained by Coates' theory are represented by the ends of the tie-line cf . Interface compositions obtained by Hillert's theory, which takes account of the interatomic effect on diffusion, are represented by the ends of the tie-line $c'f'$.

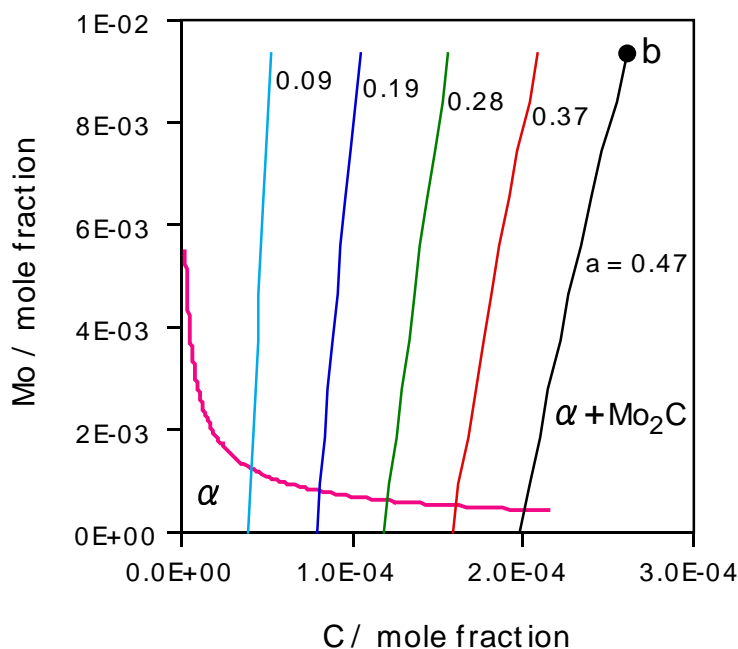


Figure 7.15: Several iso-activity curves for C in the $\alpha + \text{Mo}_2\text{C}$ two-phase field. The values in the figure correspond to the activity of C. The point b represents the ferrite composition after the completion of paraequilibrium precipitation.

not constant across the surface of the needle; Trivedi therefore introduced the functions R_1 and R_2 to account for capillarity and interface kinetics respectively, over the surface of the paraboloid:

$$\Omega = \bar{p} \exp(\bar{p}) E_1(\bar{p}) \left(1 + \frac{v}{v_c} \Omega R_1(\bar{p}) + \frac{r_c}{r^{IC}} \Omega R_2(\bar{p}) \right) \quad (7.1)$$

where Ω is the supersaturation, r^{IC} is the radius of curvature at the tip, r_c is the critical tip radius at which growth ceases, v is the lengthening rate, v_c is the velocity of a flat interface which is completely controlled by the interface processes, \bar{p} is the Péclet number ($\bar{p} = vr^{IC}/2D$) and $E_1(\bar{p})$ represents the exponential integral [75]. $R_1(\bar{p})$, $R_2(\bar{p})$ are:

$$\begin{aligned} R_1(\bar{p}) &= \frac{1}{2\bar{p}} N_1(\bar{p}) - 1 \\ R_2(\bar{p}) &= \frac{1}{4\bar{p}} N_2(\bar{p}) - 1 \end{aligned} \quad (7.2)$$

The values of the functions $N_1(\bar{p})$ and $N_2(\bar{p})$ were obtained numerically by Trivedi; they become 1.4050 and 3.8410, respectively, for small values of supersaturation ($\Omega \ll 1$) [78]. Equation 7.1 gives the general solution for the growth of precipitate needles. The right-hand side is a sum of three terms, of which the first is the result obtained by Ivantsov [74] for the case of the iso-concentrate boundary. The second and third terms are corrections to the Ivantsov solution due to the interface kinetics and capillarity effects respectively.

Equation 7.1 yields the Péclet number as a function of the supersaturation, but a further assumption is needed to obtain a lengthening rate or tip radius. Zener suggested that the particle should adopt a tip radius which gives the maximum growth rate [7]. This maximum growth rate can be obtained by differentiating equation 7.1 with respect to r^{IC} and setting $\frac{\partial v}{\partial r^{IC}} = 0$. The solution of this differential was obtained for large values of Ω ($\Omega \geq 0.2$) [77] and for small values of $\Omega \leq 0.2$ [78]. In the present work, diffusion-controlled growth was assumed; the kinetic term in equation 7.1 was therefore neglected.

7.4 Modelling of needle-shaped carbide growth

7.4.1 Chemical composition and equilibrium phases

Table 7.1 shows the chemical composition of the material under consideration. The steel contains 0.1 wt. % carbon and a stoichiometric quantity of Mo for Mo_2C . Using MT-DATA, the phase fractions and the compositions of the equilibrium carbides for the steel at a variety of temperatures were calculated. The calculations allowed for the potential existence of cementite, M_2C (hcp), M_4C_3 (fcc), M_7C_3 and M_{23}C_6 in addition to ferrite. According to the results, for 600 °C, M_2C (hcp) is the only stable carbide in this steel. The equilibrium composition of M_2C , according to MT-DATA, is 0.57Mo-0.33C-0.09Mn-0.01Fe (mole fraction). The experimental results confirm that Mo_2C is the only stable carbide for the

conditions of the present work. M_2C can therefore be denoted Mo_2C in a Fe-C-Mo ternary system.

7.4.2 Capillarity effect in multicomponent systems

When interfaces are curved, the need to create interfaces affects local equilibrium, an effect which cannot be neglected when dealing with small particles or coarsening reactions. If α and a sphere of β are in contact at a curved interface then the conditions for local equilibrium are [109]:

$$dT^\beta = dT^\alpha = dT \quad (7.3)$$

$$dP^\beta = dP^\alpha + 2\sigma dH \quad (7.4)$$

$$d\mu_1^\beta = d\mu_1^\alpha, \quad d\mu_2^\beta = d\mu_2^\alpha \quad (7.5)$$

Here, T , P , H , σ and μ represent temperature, pressure, curvature of β phase, surface energy, and chemical potential, respectively. If it is assumed that the pressure of the α phase is constant, from equation 7.4, the pressure change of the β phase can be represented as:

$$\Delta P = \int_{P(H=0)}^P dP^\beta = \int_{H=0}^H 2\sigma dH = \frac{2\sigma}{r^{IC}} \quad (7.6)$$

where r^{IC} is the radius of curvature at the tip. Accordingly, if the atomic volume of β is represented as ν^β , the additional Gibbs energy term of β ΔG^β is:

$$\Delta G^\beta = \Delta P \nu^\beta = \frac{2\sigma \nu^\beta}{r^{IC}}. \quad (7.7)$$

The simplest exact method to evaluate the influence of capillarity on the interface composition is to modify the Gibbs energy value of the β phase in the database used by thermodynamic calculation software such as MTDATA. In the case of Mo_2C (hcp, $a=3.0 \text{ \AA}$, $c=4.72 \text{ \AA}$), the atomic volume ν^{Mo_2C} is $1.22 \times 10^{-29} \text{ m}^3$ and the interfacial energy σ can be assumed to be 0.2 J m^{-2} [66]. Accordingly, the additional Gibbs energy would be 2941 J mol^{-1} for $r^{IC} = 10 \text{ \AA}$. The database for the hcp phase (sublattice) was modified to add $1 \times 10^{-6} \text{ J mol}^{-1}$ per 1 Pa pressure increase.

The effect of capillarity on the molybdenum mole fraction of the ferrite in local equilibrium with the carbide ($c_{Mo}^{\alpha Mo_2C}$), evaluated by adding an additional Gibbs energy term in the database used by MTDATA, is shown in Fig. 7.16 as a function of the radius of curvature, for 0.10C-1.60Mo (wt. %) steel.

7.4.3 Overall transformation kinetics

Carbide precipitation during tempering of a Fe-C-Mo steel, which includes the precipitation of Mo_2C and the enrichment and dissolution of cementite, was simulated.

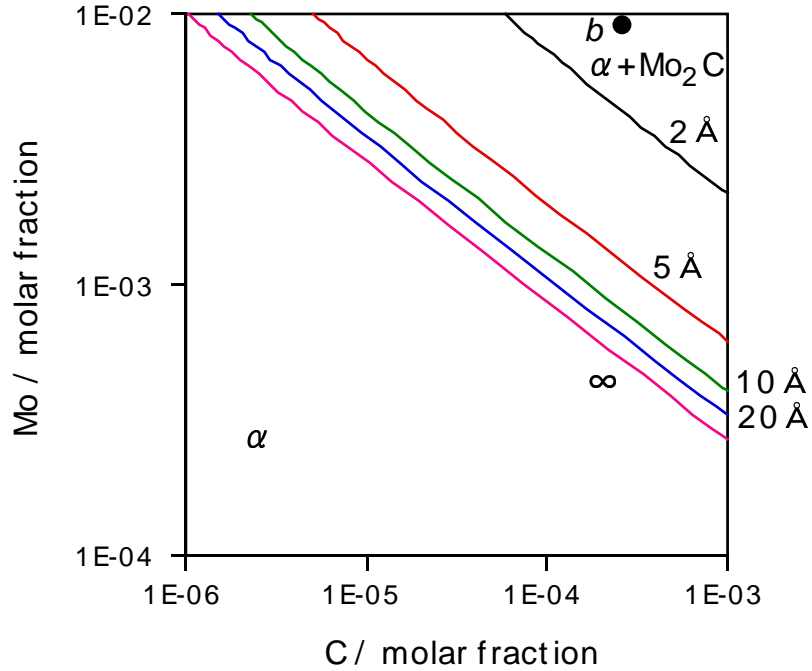


Figure 7.16: Capillarity-corrected composition of ferrite in equilibrium with Mo_2C as a function of the radius of curvature. The point b represents the composition of the ferrite matrix after the completion of paraequilibrium cementite precipitation.

I Enrichment and dissolution of cementite

Cementite was assumed initially to contain the same molybdenum to iron atom ratio as in the average chemical composition. During tempering, molybdenum diffuses into the cementite to enrich it towards equilibrium, and at some stage, the cementite begins to dissolve to give way to the precipitation of the more stable Mo_2C . The volume fraction of cementite can be calculated using the lever rule, assuming that any residual carbon concentration in the ferrite is so small that it can be neglected. The volume fraction of cementite ζ_θ is thus given by [98]:

$$\zeta_\theta = 1.0065 \times \frac{\bar{c}}{c^{\theta\alpha}} \quad \text{with} \quad c^{\theta\alpha} \simeq 0.25 \quad (7.8)$$

by taking account of the difference in ferrite and cementite densities. Transmission electron microscopy indicated an average cementite plate-thickness of about 2×10^{-8} m when the particles were within the ferrite grains and 5×10^{-8} m when they were on the grain boundaries.

The rate of enrichment is given approximately by [96]:

$$c_{\text{Mo}}^{\theta} = \bar{c}_{\text{Mo}} + 4\sqrt{D_{\text{Mo}}t} \frac{(\bar{c}_{\text{Mo}} - c_{\text{Mo}}^{\alpha\theta})}{d_t\sqrt{\pi}} \quad (7.9)$$

where c_{Mo}^{θ} represents the atomic fraction of Mo in cementite, t is the time since cementite formation, d_t is the thickness of the cementite plate, D_{Mo} is the diffusion coefficient of Mo in the matrix (it is assumed that the corresponding diffusivity in the cementite is identical to that in ferrite), $c_{\text{Mo}}^{\alpha\theta}$ is the atomic fraction of Mo in the ferrite which is in equilibrium with the cementite, and \bar{c}_{Mo} is the mean atomic fraction of Mo in the alloy.

The dissolution rate v_{θ} is determined from [94]:

$$v_{\theta} = -\frac{D_{\text{Mo}}}{\bar{d}} \frac{c_{\text{Mo}}^{\alpha\theta} - c_{\text{Mo}}^{\alpha\text{Mo}_2\text{C}}}{c_{\text{Mo}}^{\theta\alpha} - c_{\text{Mo}}^{\alpha\theta}} \quad (7.10)$$

where \bar{d} is the mean diffusion distance between θ and Mo_2C precipitates, given by:

$$\bar{d} = (N^{\theta} + N^{\text{Mo}_2\text{C}})^{-\frac{1}{3}} \quad (7.11)$$

where N^{θ} and $N^{\text{Mo}_2\text{C}}$ are the number densities of θ and Mo_2C particles, respectively.

In addition, dissolution of cementite is restricted in such the way that the carbon concentration in the ferrite matrix (\bar{c}_C) does not exceed the carbon concentration in ferrite which is in equilibrium with cementite ($c_C^{\alpha\theta}$).

II Nucleation of Mo_2C

The nucleation rate is given by:

$$I = N_V \frac{kT}{h} \exp \left\{ \frac{-(G^* + Q^*)}{kT} \right\} \quad (7.12)$$

where N_V is the number density of nucleation sites, Q^* is the activation energy for the transfer of atoms across the interface (approximately equal to the activation energy for diffusion of Mo when the nucleus is coherent), k is the Boltzmann constant and h is the Planck constant [68]. G^* is the activation energy for nucleation:

$$G^* = \frac{16\pi}{3} \frac{\sigma^3}{\Delta G_V^2} \quad (7.13)$$

where ΔG_V is the chemical free energy change per unit volume of nuclei and has a negative value. ΔG_V was calculated using MTDATA as $-1.435 \times 10^9 \text{ J m}^{-3}$. This value is for the beginning of precipitation of Mo_2C , and decreases as precipitation proceeds. The change in the value of ΔG_V is calculated corresponding to the progress of the precipitation reaction using a mean field approximation, i.e. assuming that the solute is uniformly distributed in the matrix. σ is not a true interfacial energy but an effective interfacial energy because equation 7.13 really applies to the homogeneous nucleation, but Mo_2C particles nucleate heterogeneously.

III Diffusion-controlled growth with capillarity

Modelling of growth with local equilibrium at the interface is based on Coates' diffusion-controlled growth theory accounting for the capillarity effect. The critical radius of curvature r_c at which growth ceases was calculated using MTDATA, with a modification to the database of the hcp phase to include a pressure change. The growth rate is the maximum rate obtained using Trivedi's theory, for given values of the carbon concentration in the matrix and the supersaturation Ω of Mo. The growth rate obtained from the values of \bar{p} and the ratio r^{IC}/r_c corresponding to the maximum growth rate satisfies equation 7.1.

IV Ostwald ripening

Coarsening occurs because the total energy of the system is reduced by eliminating interfaces; in practice, large particles grow more rapidly than small particles during precipitation, and large particles grow at the expense of smaller ones during classical coarsening. The average particle size therefore increases with time. Classical coarsening occurs slowly because of the small energies associated with the interfaces compared with the free energy change accompanying precipitation. Ostwald ripening can therefore be assumed to occur after the 'completion' of the precipitation of Mo_2C .

The combination of nucleation and growth gives rise to a distribution of Mo_2C lengths, but for a given supersaturation, they all have the same tip radius. An approximate treatment was adopted, in which coarsening involves the spheroidisation of the needles, assuming that the interfacial energy is isotropic. The spheroidisation is driven by the fact that the additional Gibbs energy by the capillarity effect at the needle tip is greater than on the sides of the needle. A Mo_2C particle can effectively be modelled for coarsening purposes as a cylinder with hemispherical ends. Particle growth and dissolution is then driven by the capillarity effect. The additional Gibbs energy ΔG^β for the hemispherical tip is given by:

$$\Delta G^\beta = \frac{2\sigma\nu^\beta}{r^{IC}} \quad (7.14)$$

and ΔG^β for a cylindrical body is given by:

$$\Delta G^\beta = \frac{\sigma\nu^\beta}{r^{IC}} \quad (7.15)$$

It is then possible to calculate the interfacial mole fraction $c_{\text{Mo},r}^{\alpha\text{Mo}_2\text{C}}$. The concentrations of Mo were therefore calculated separately for the needle tip and for the body, according to the respective curvatures. The growth or dissolution rates at the tip and body were calculated for each particle using these mole fractions, using Zener's theory as:

$$v \simeq \frac{D_{\text{Mo}}}{\bar{d}} \frac{\bar{c}_{\text{Mo}} - c_{\text{Mo},r}^{\alpha\text{Mo}_2\text{C}}}{c_{\text{Mo}_2\text{C}\alpha} - c_{\text{Mo},r}^{\alpha\text{Mo}_2\text{C}}} \quad (7.16)$$

where \bar{d} is the mean diffusion distance between particles; this can be expressed as [94]:

$$\bar{d} = (N^{\text{Mo}_2\text{C}})^{-\frac{1}{3}} \quad (7.17)$$

where $N^{\text{Mo}_2\text{C}}$ is the number density of Mo_2C particles.

Accordingly, particles grow or dissolve as shown in Fig. 7.17.

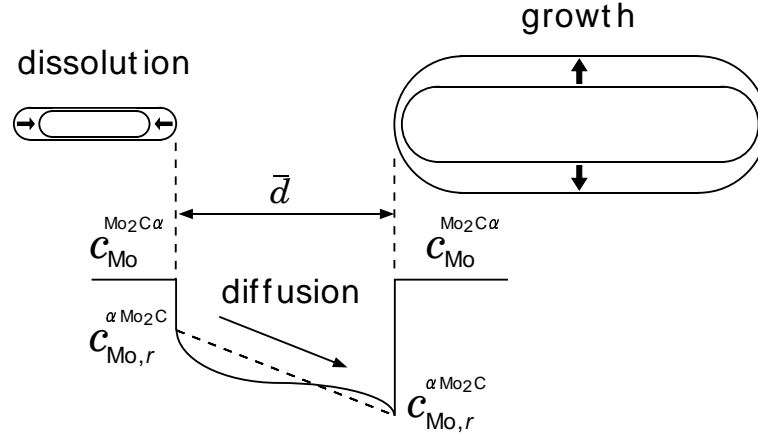


Figure 7.17: Schematic drawing of Ostwald ripening of cylinder-shaped particles.

7.4.4 Inputs and calculations

The precipitation calculations were performed in time steps of 100 s. In each step, the following quantities were calculated: the nucleation rate, nucleus size (the initial size of the particle), growth rate, and the Mo and C mole fraction change in the matrix corresponding to the growth of Mo_2C and the enrichment and dissolution of cementite. The consumption of nucleation sites during the transformation was accounted for in each step. Once the mole fractions of Mo and C in the matrix (\bar{c}_{Mo} and \bar{c}_{C}) had been determined, the corresponding supersaturation of Mo (Ω_{Mo}) and the critical radius r_c could be obtained. By obtaining Ω_{Mo} and r_c , the value of \bar{p} satisfying equation 7.1 could be determined. Finally, the maximum growth rate and tip radius of a Mo_2C particle r^{IC} giving the maximum rate for the corresponding value of \bar{p} were obtained. The volume of each particle was calculated as a paraboloid.

After completion of the precipitation and growth stage, each Mo_2C particle was modelled as a needle, both ends of which were hemispheres, for the Ostwald ripening stage. In this stage, $c_{\text{Mo},r}^{\alpha\text{Mo}_2\text{C}}$ values corresponding to the tip and the body of each needle-shaped particle were calculated, and then the growth (or dissolution) rates at the tip and the body were calculated.

Parameter	condition
Shape of Mo ₂ C	needle
Tempering temperature / °C	600
Interface energy of Mo ₂ C / J m ⁻²	0.2
Driving force for nucleation of Mo ₂ C / J m ⁻³	-1.435 × 10 ⁹
Nucleation site density of Mo ₂ C / m ⁻³	2.46 × 10 ²²
Maximum volume fraction of cementite	1.796 × 10 ⁻²
Maximum volume fraction of Mo ₂ C	1.391 × 10 ⁻²
$c^{\alpha\theta}$ / atomic fraction	8.724 × 10 ⁻³
$c^{\theta\alpha}$ / atomic fraction	4.245 × 10 ⁻²
$c^{\alpha\text{Mo}_2\text{C}}$ / atomic fraction	1.632 × 10 ⁻³
$c^{\text{Mo}_2\text{C}\alpha}$ / atomic fraction	6.556 × 10 ⁻¹
Thickness of cementite in grains / m	2.0 × 10 ⁻⁸
Thickness of cementite on grain boundaries / m	5.0 × 10 ⁻⁸
Diffusion constant of Mo D_{Mo} / m ² s ⁻¹	2.29 × 10 ⁻⁴
Activation energy for Mo diffusion Q_{Mo} / J(mol · K) ⁻¹	2.39 × 10 ⁵

Table 7.2: Calculation parameters for precipitation of carbides in a ternary system (Fe-0.10C-1.60Mo in wt. %).

The parameters used in the calculations are listed in Table 7.2. The nucleation site density was obtained by fitting to experimental data. The Mo₂C/ferrite interface energy [66], and the diffusivity of molybdenum in ferrite [110], were obtained from the literature.

7.5 Results and discussion

Figure 7.18 shows comparisons of the calculations and the observations. Experimental data were obtained from several areas in each sample. In Fig. 7.18, the solid circles represent the average of data from different areas, and the scatter of the data is indicated by error bars. The technique allows the carbide dimensions to be measured to an accuracy of ±1 nm.

After the completion of paraequilibrium cementite precipitation, the concentration of carbon in the matrix is quite low (0.026 at. %, according to MTDATA). Carbon atoms, which are necessary for the precipitation of Mo₂C, are provided by the dissolution of cementite. After the completion of precipitation, Ostwald ripening proceeds with a constant volume fraction of Mo₂C. Figure 7.18 (a) shows such simultaneous Mo₂C precipitation and cementite dissolution behaviour. From the observations and calculations, it can be seen that the volume fraction of Mo₂C increases with time up to 100 h and then remains constant, as shown in Fig. 7.18 (a). It is therefore considered that nucleation and growth stage ends at about 100 h and the Ostwald ripening stage commences after that.

The average length of Mo₂C particles increases during the precipitation and growth stage. During the Ostwald ripening stage, the growth rate (or dissolution rate) at both ends

of a needle is smaller (or larger) than that at the body of a needle because of the capillarity effect. On average, therefore, the length decreases during Ostwald ripening as shown in Fig. 7.18 (b).

The number density of Mo₂C particles with length greater than 5 nm was calculated, as shown in Fig. 7.18 (c), for comparison with observations; Mo₂C particles of size less than 5 nm could not easily be observed using conventional transmission electron microscopy. During the Ostwald ripening stage, the number density of such particles decreases.

The calculated number density distribution of the length of Mo₂C particles is shown in Fig. 7.18 (d) for the tempering time of 30 h. Each point which is placed at the length of X nm represents the number density of particles observed whose length is from (X-5) nm to (X+5) nm.

The calculations in general agree well with the observations. However, there are discrepancies in the number density, and the number-density distribution of the length, of Mo₂C particles. The problem probably lies in the evaluation of nucleation rate. The observations show that even after 100 h tempering, small particles (10–20 nm) exist whereas the calculations predict that nucleation ceases in the relatively early stages of tempering. Nucleation seems to occur more slowly, and persist for a longer period, than implied by the calculations until a relatively late stage of tempering. It is not clear how the nucleation function should be adapted without introducing further unknown parameters such as strain energy.

In the present model, cementite is modelled as a plate, although in practice its morphology is not uniform. To test this assumption, another calculation, in which cementite is modelled as spheres and the capillarity effect is taken into account, was carried out. This predicted that cementite dissolution would be completed 6 h earlier than in the present model. It is therefore considered that, although the detailed morphology of the cementite should affect its dissolution, the difference in time is relatively small compared with that for the alloy carbide reaction.

The growth model used here is based on Trivedi's theory, in which a needle is represented as a paraboloid of revolution. For comparison, a calculation based on Zener's approximation, as adopted by Fujita and Bhadeshia [6], was performed. Even by varying the nucleation site density, it was impossible to fit the results to observations. In particular, the model overestimates the growth rate, as shown in Fig. 7.19.

For the Ostwald ripening stage, Mo₂C particles were modelled as needles with hemispherical ends. Coarsening theory for spheres leads to the following relationship [83, 84]:

$$\bar{r}^3 - r_0^3 = \left(\frac{8\sigma\nu^\beta D_{\text{Mo}} c_{\text{Mo}}^{\alpha\beta}}{9kT} \right) t \quad (7.18)$$

where \bar{r} is the average radius, r_0 is the initial average particle radius and t is time. During Ostwald ripening, the volume fraction of Mo₂C can be assumed to be constant. The number density of Mo₂C can be therefore represented as:

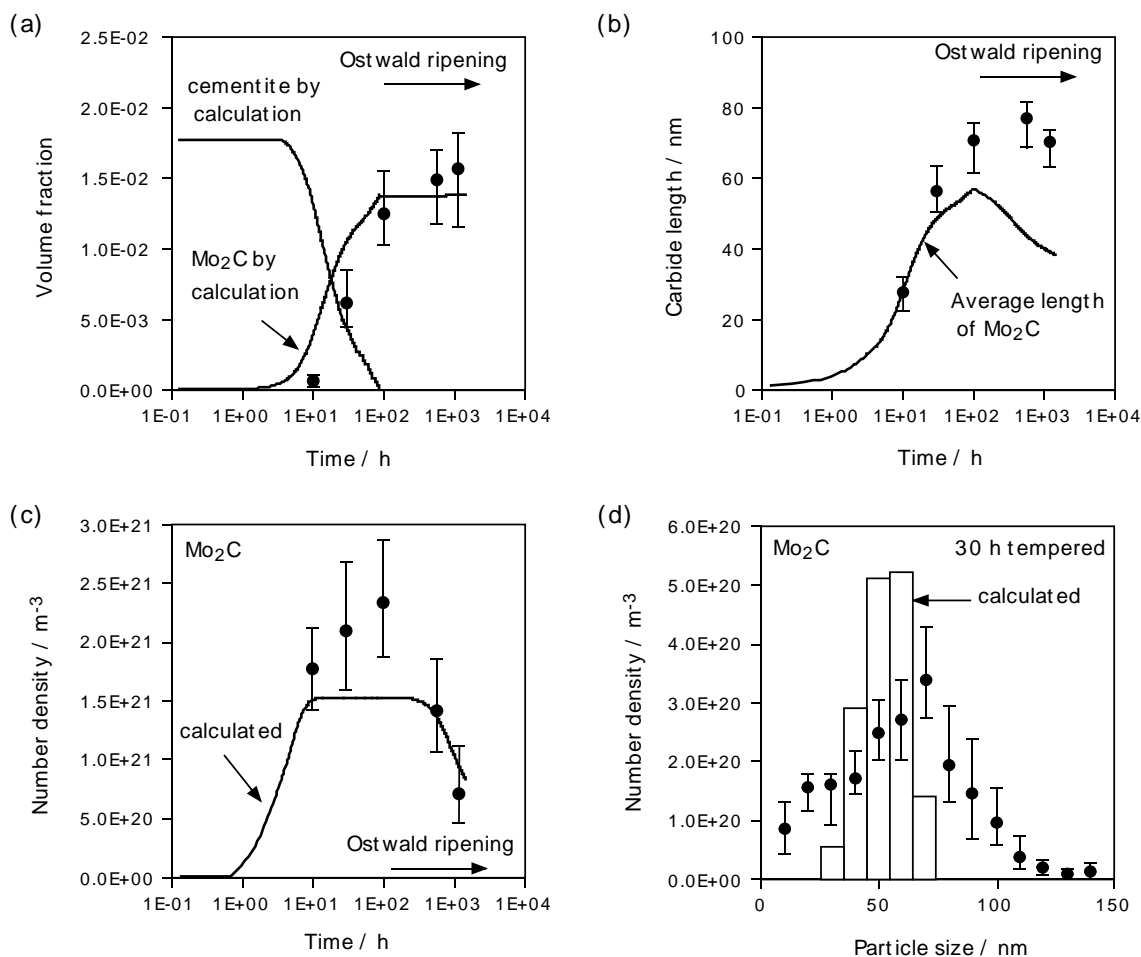


Figure 7.18: Comparisons between calculated curves and observations. (a) Relationship between volume fraction of Mo₂C particles and tempering temperature. (b) Relationship between average length of Mo₂C particles and tempering temperature. (c) Relationship between number density of Mo₂C particles whose size are over 5 nm and tempering temperature. (d) Number density distribution of the length of Mo₂C particles for the 30 h tempered specimen.

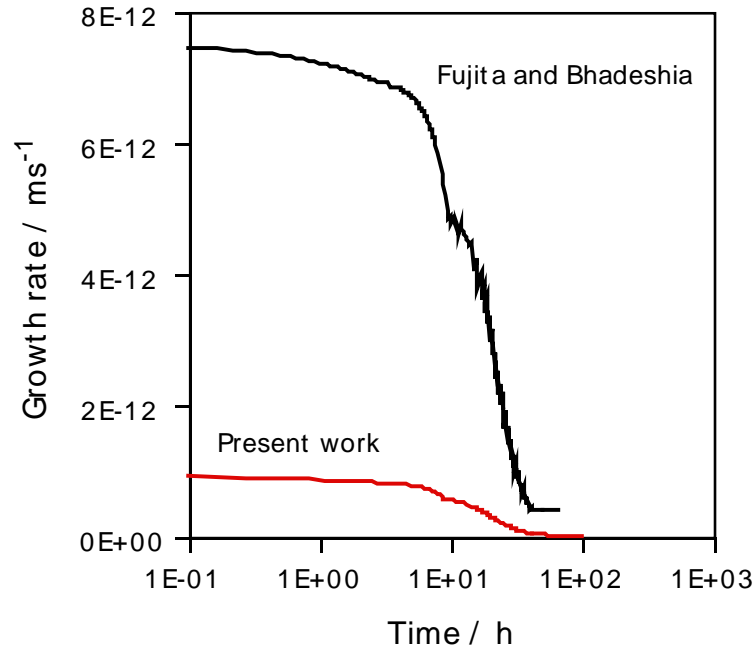


Figure 7.19: Comparisons of the growth rate of Mo_2C particles between Fujita and Bhadeshia model [6] and the present model.

$$N^{\text{Mo}_2\text{C}} = N_0^{\text{Mo}_2\text{C}} \frac{r_0^3}{r_0^3 + \frac{8\sigma\nu^\beta D_{\text{Mo}} c_{\text{Mo}}^{\alpha\beta}}{9kT} t} \quad (7.19)$$

where $N_0^{\text{Mo}_2\text{C}}$ is the initial number density of Mo_2C precipitates when the Ostwald ripening stage starts.

Figure 7.20 shows comparisons of the transition of $N^{\text{Mo}_2\text{C}}$ during Ostwald ripening with Mo_2C particles calculated as needles, as spheres, and using equation 7.19. The calculation assuming a needle shape is identical to that for the Ostwald ripening stage of Fig. 7.18(c). The calculations assuming needle and spherical shapes give similar results, and show a similar tendency to the result of equation 7.19.

7.6 Summary and conclusions

The precipitation and Ostwald ripening behaviour of Mo_2C (needle-shaped) particles during the tempering of a ternary Fe-C-Mo martensitic steel have been characterised and modelled, taking account of local equilibrium, the capillarity effect, and simultaneous cementite enrichment and dissolution.

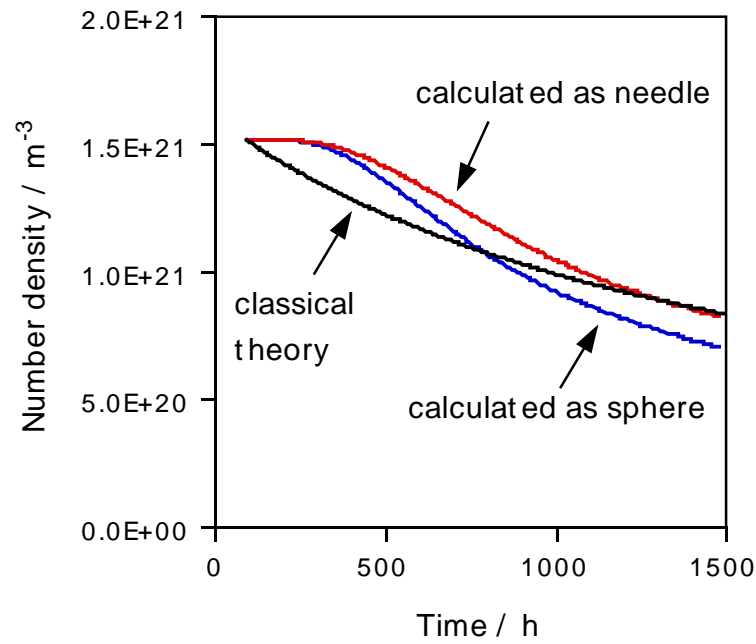


Figure 7.20: Comparisons of the number density of Mo_2C particles calculated as needle-shaped, spherical, and by equation 7.19.

In conclusion, by modelling a Mo_2C particle as a paraboloid and assuming the maximum growth rate, the model has been shown to be capable of estimating the average length, volume fraction, and number density of particles in a manner consistent with experimental observations. The growth rate depends on the supersaturation of Mo (Ω_{Mo}) and the ratio of the solute mole fraction in the matrix $\bar{c}_{\text{Mo}}/\bar{c}_{\text{C}}$ [111].

Chapter 8

Modelling V_4C_3 in a Fe-C-V ternary system

8.1 Experimental work

Experiments were conducted to provide data for model verification. Transmission electron microscopy was used to obtain the necessary data.

8.1.1 Material

Table 8.1 shows the chemical composition of the material designed for the present work. The steel contains 0.1 wt. % carbon and a stoichiometric quantity of vanadium for V_4C_3 . As will be shown later, experimental data and thermodynamic calculations show that in this steel the carbide is virtually pure V_4C_3 with negligible quantities of iron and manganese in the metal sites. Therefore, its precipitation can be modelled as if it occurs in a ternary Fe-V-C system.

	C	Si	Mn	V	Al	N
Steel <i>B</i>	0.10	<0.005	1.99	0.56	0.03	0.0049

Table 8.1: Chemical composition of experimental steel in wt. %.

8.1.2 Transmission electron microscopy

I Vanadium Carbide

Figures 8.1 - 8.6 show thin-foil TEM images of Steel *B* tempered for a variety of times. These pictures were taken from the [100] orientation of the matrix. Figure 8.7 shows the images of the carbon replica from the specimen which was tempered for 100 h at 600 °C. From the diffraction patterns in Fig. 8.7, these plate-shaped precipitates have a face-centred cubic (fcc) structure and are considered to be M_4C_3 , where ‘M’ stands for metal atoms (V,

Fe, Mn); the vanadium-rich carbide is henceforth referred to as M_4C_3 . It is known that M_4C_3 grows on the three equivalent $\{001\}_\alpha$ planes [12]. In Fig. 8.1 - 8.6, the needle-like precipitates are the cross-section images of precipitates growing on the $\{001\}_\alpha$ plane, which is parallel to the observation direction.

II Cementite

Figure 8.8 shows an extraction carbon-replica TEM image of Steel *B* tempered for 0.5 h. Cementite particles precipitate on the prior-austenite grain boundaries and the martensite lath boundaries, and also within the laths. The particles at the boundaries are spherical with an average size of about 50 nm, but those at the laths are plate-shaped with a average thickness of 20 nm.

III Chemical compositions of carbides

The chemical compositions of M_4C_3 and cementite particles were measured using energy dispersive spectroscopy on carbon replica specimens. Figure 8.9 shows typical X-ray count-energy profiles of M_4C_3 and cementite and the atomic ratio of metallic elements for several tempering times. The solid circles represent the average of data from different particles, and the scatter of the data is indicated by error bars. The results shows that M_4C_3 is virtually pure V_4C_3 .

IV Foil Thickness

A knowledge of the thickness of the thin foil is necessary to estimate the volume fraction of V_4C_3 . It was calculated using thickness fringes at the grain boundaries. The extinction distances for a two-beam condition are known; it is therefore possible to calculate the thickness of the sample by multiplying the extinction distance by the number of fringes. The thicknesses of the samples were in this way found to be between 80 and 160 nm.

V Carbide morphology and volume fraction

V_4C_3 grows at the expense of cementite on the $\{001\}_\alpha$ planes, whilst keeping a plate shape whose average aspect ratio is 5 - 6. The carbide size was measured from over 500 particles for each sample. The volume fraction of carbide, average carbide length, number density, aspect ratio and the number density distribution of the length of the particles, are shown in Fig. 8.15. The solid circles represent the average of data from different locations, and the scatter of the data is indicated by error bars.

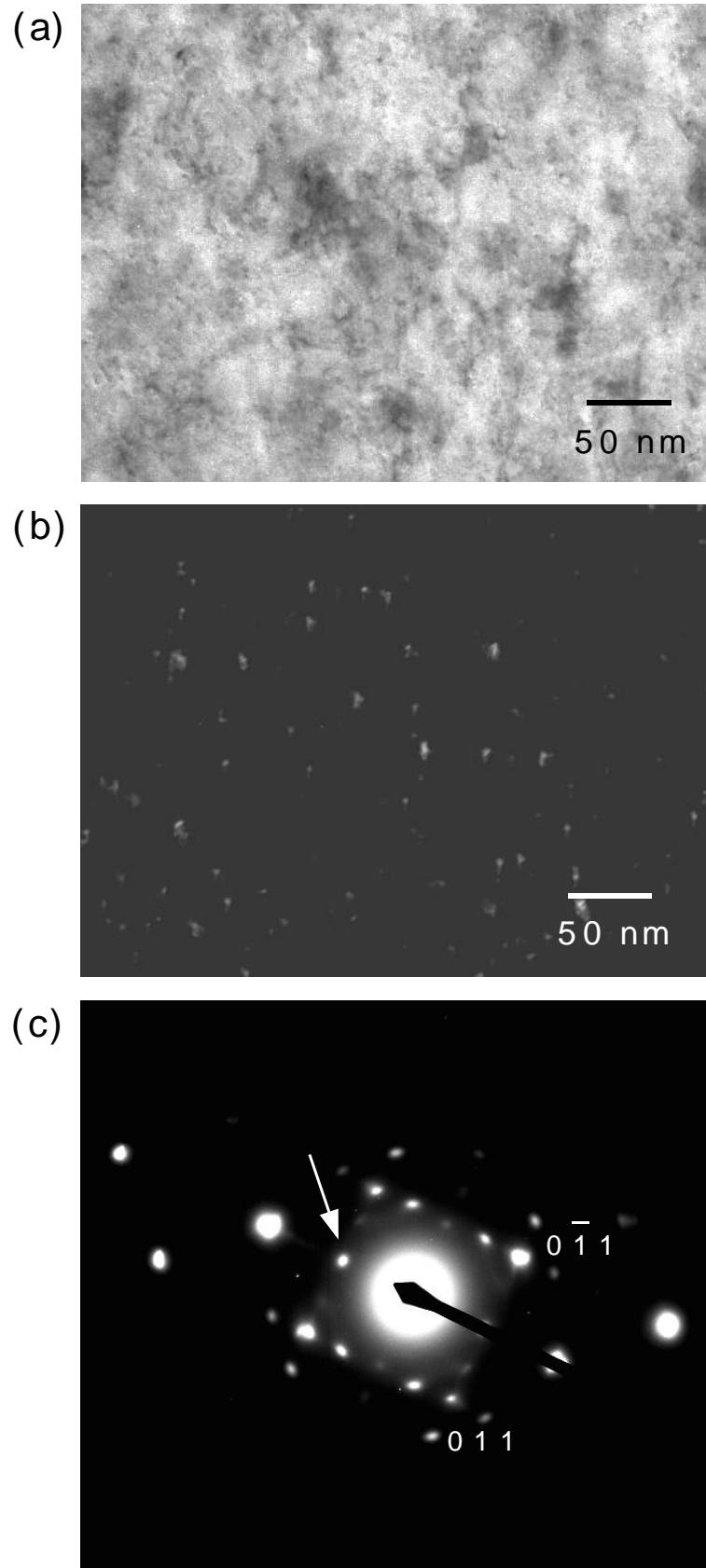


Figure 8.1: TEM observation of a thin-foil from Steel *B* tempered at 600 °C for 0.5 h. Zone axis is [100] of ferrite matrix. (a) Bright field image. (b) Dark field image using the carbide diffraction spot indicated by the arrow in (c). The $0\bar{1}1$ and 011 reflections are from the ferrite.

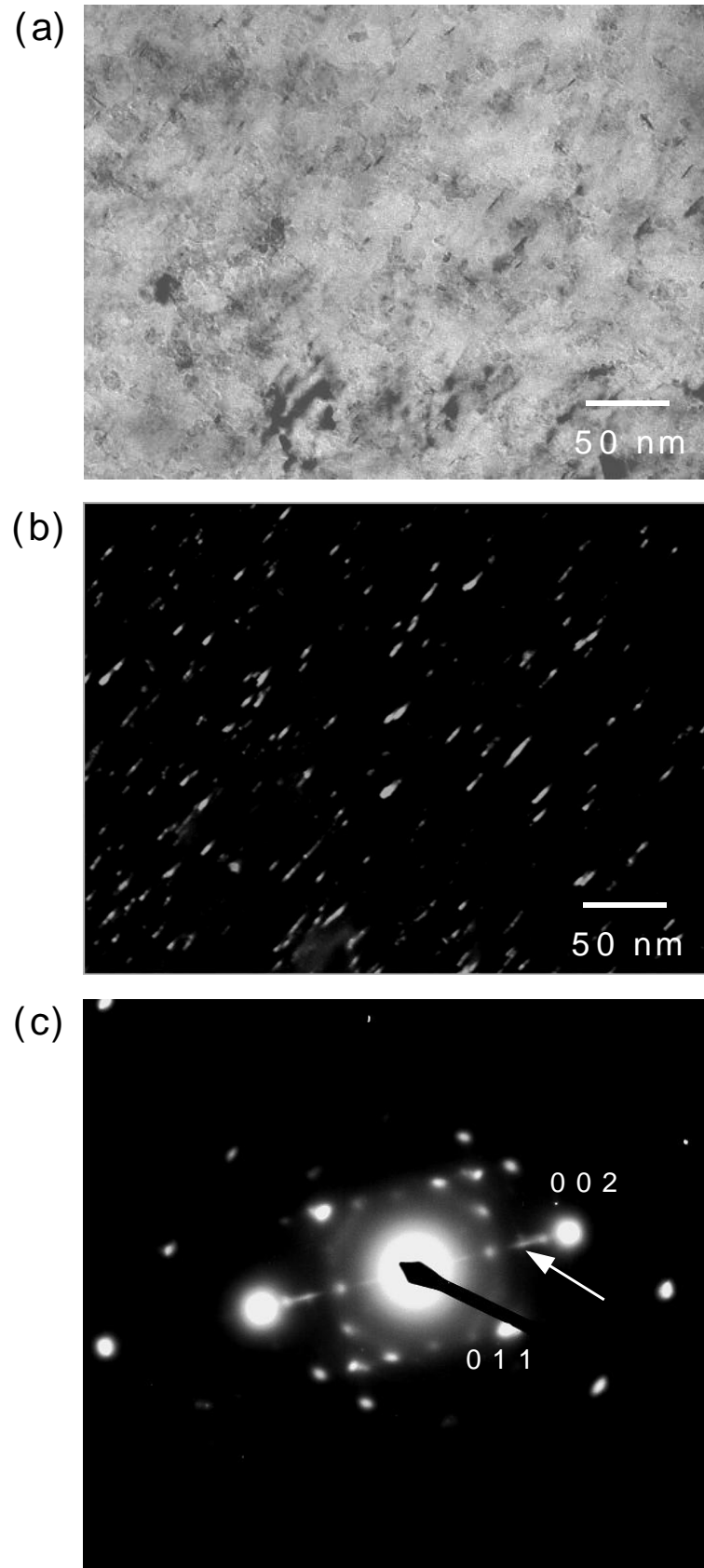


Figure 8.2: TEM observation of a thin-foil from Steel *B* tempered at 600 °C for 10 h. Zone axis is $[100]$ of ferrite matrix. (a) Bright field image. (b) Dark field image using the carbide diffraction spot indicated by the arrow in (c). The 002 and 011 reflections are from the ferrite.

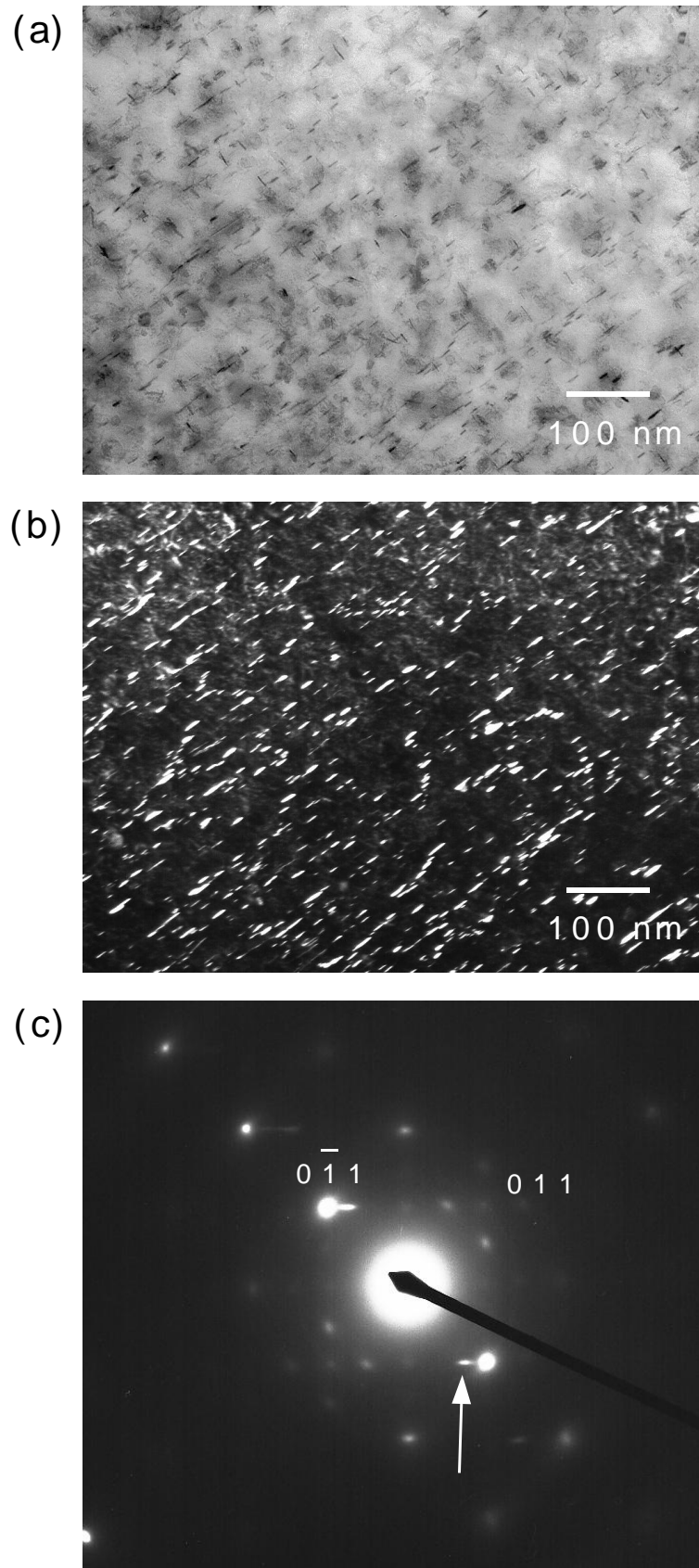


Figure 8.3: TEM observation of a thin-foil from Steel *B* tempered at 600 °C for 30 h. Zone axis is $[100]$ of ferrite matrix. (a) Bright field image. (b) Dark field image using the carbide diffraction spot indicated by the arrow in (c). The $0\bar{1}1$ and 011 reflections are from the ferrite.

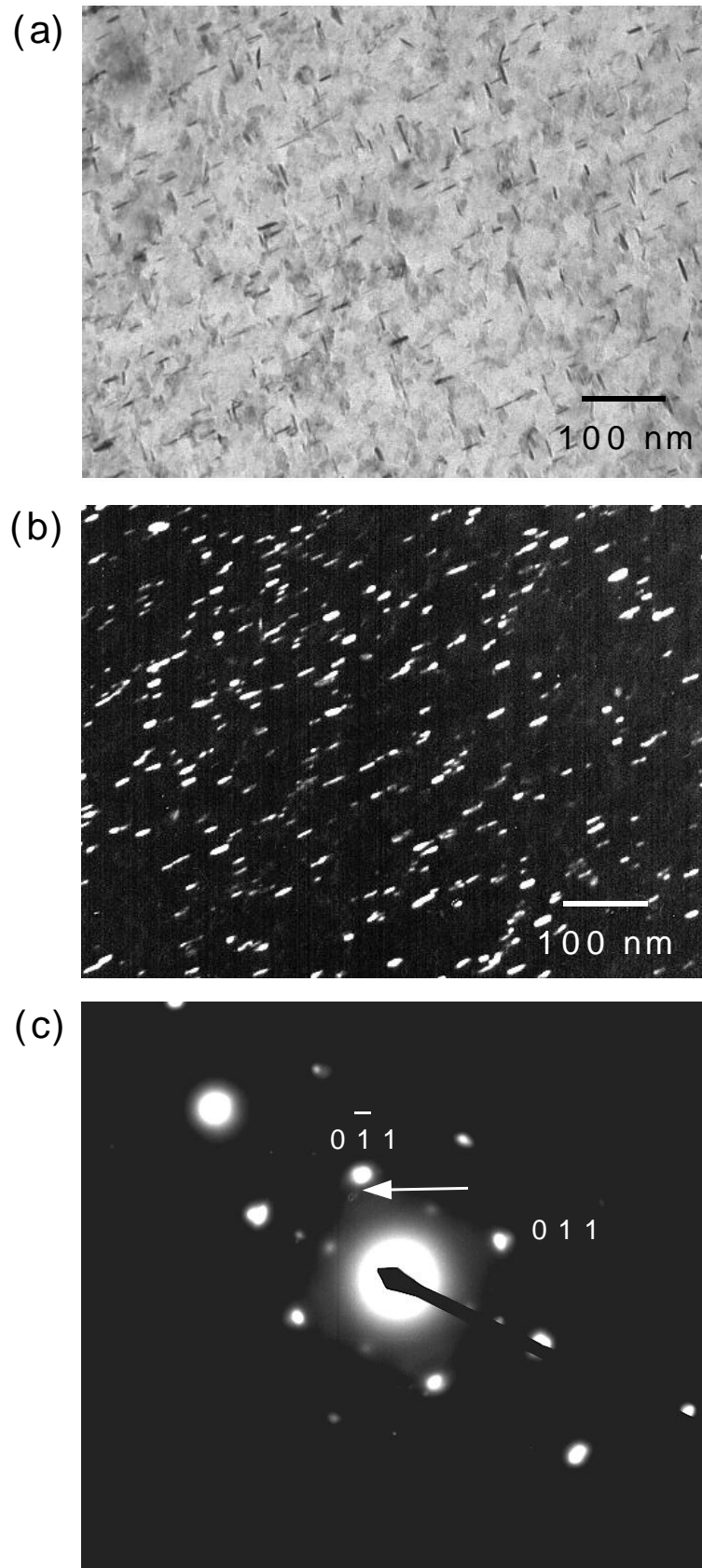


Figure 8.4: TEM observation of a thin-foil from Steel *B* tempered at 600 °C for 100 h. Zone axis is [100] of ferrite matrix. (a) Bright field image. (b) Dark field image using the carbide diffraction spot indicated by the arrow in (c). The $0\bar{1}1$ and 011 reflections are from the ferrite.

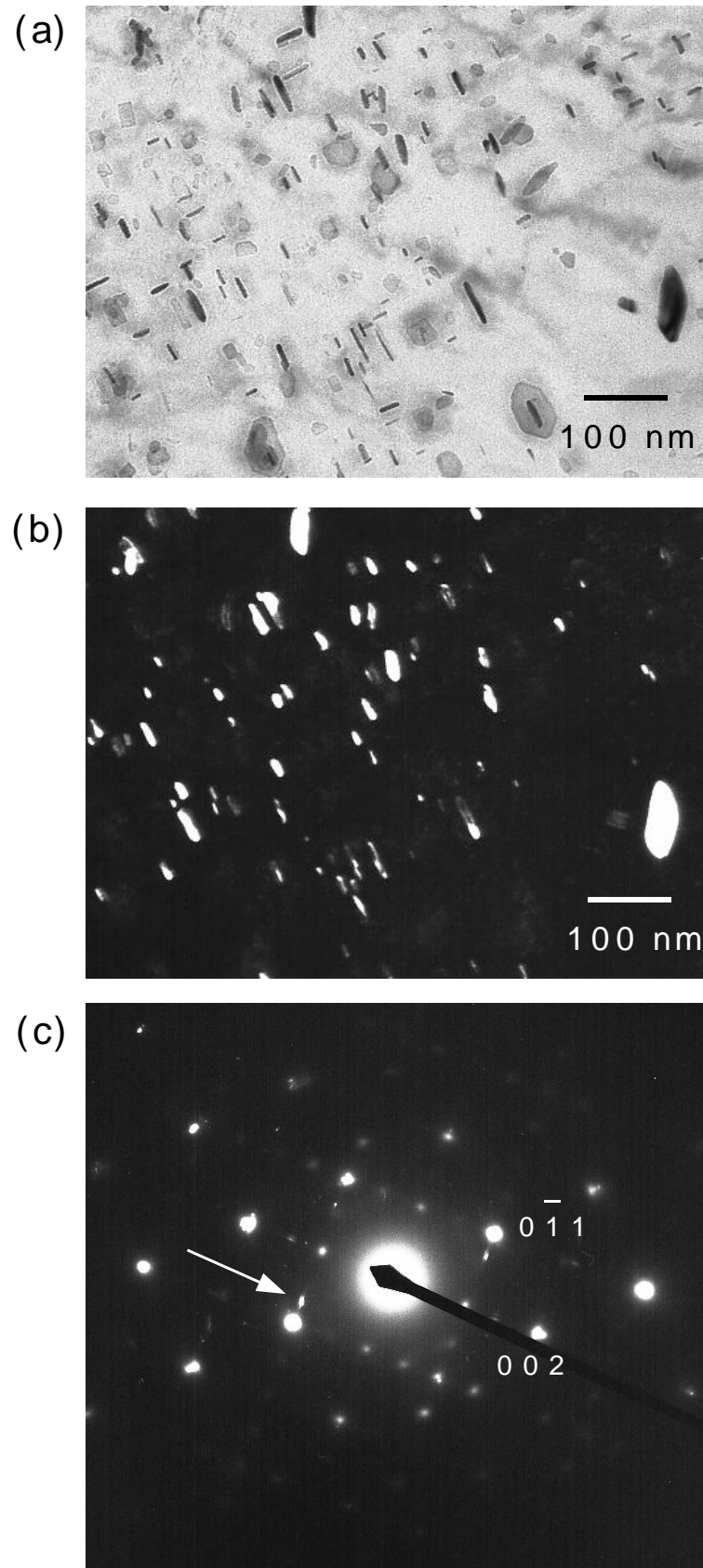


Figure 8.5: TEM observation of a thin-foil from Steel *B* tempered at 600 °C for 560 h. Zone axis is [100] of ferrite matrix. (a) Bright field image. (b) Dark field image using the carbide diffraction spot indicated by the arrow in (c). The 002 and $0\bar{1}1$ reflections are from the ferrite.

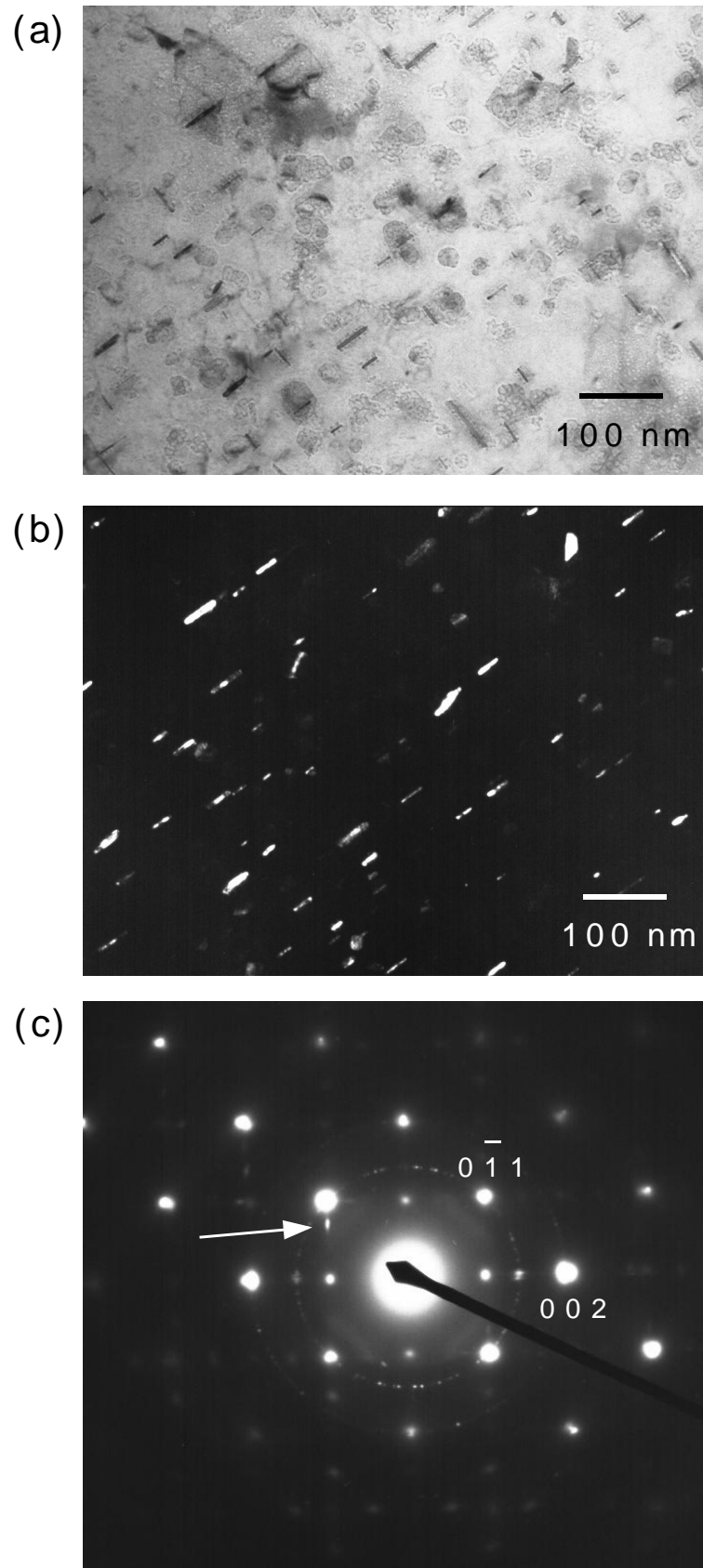


Figure 8.6: TEM observation of a thin-foil from Steel *B* tempered at 600 °C for 1150 h. Zone axis is $[100]$ of ferrite matrix. (a) Bright field image. (b) Dark field image using the carbide diffraction spot indicated by the arrow in (c). The 002 and $0\bar{1}1$ reflections are from the ferrite.

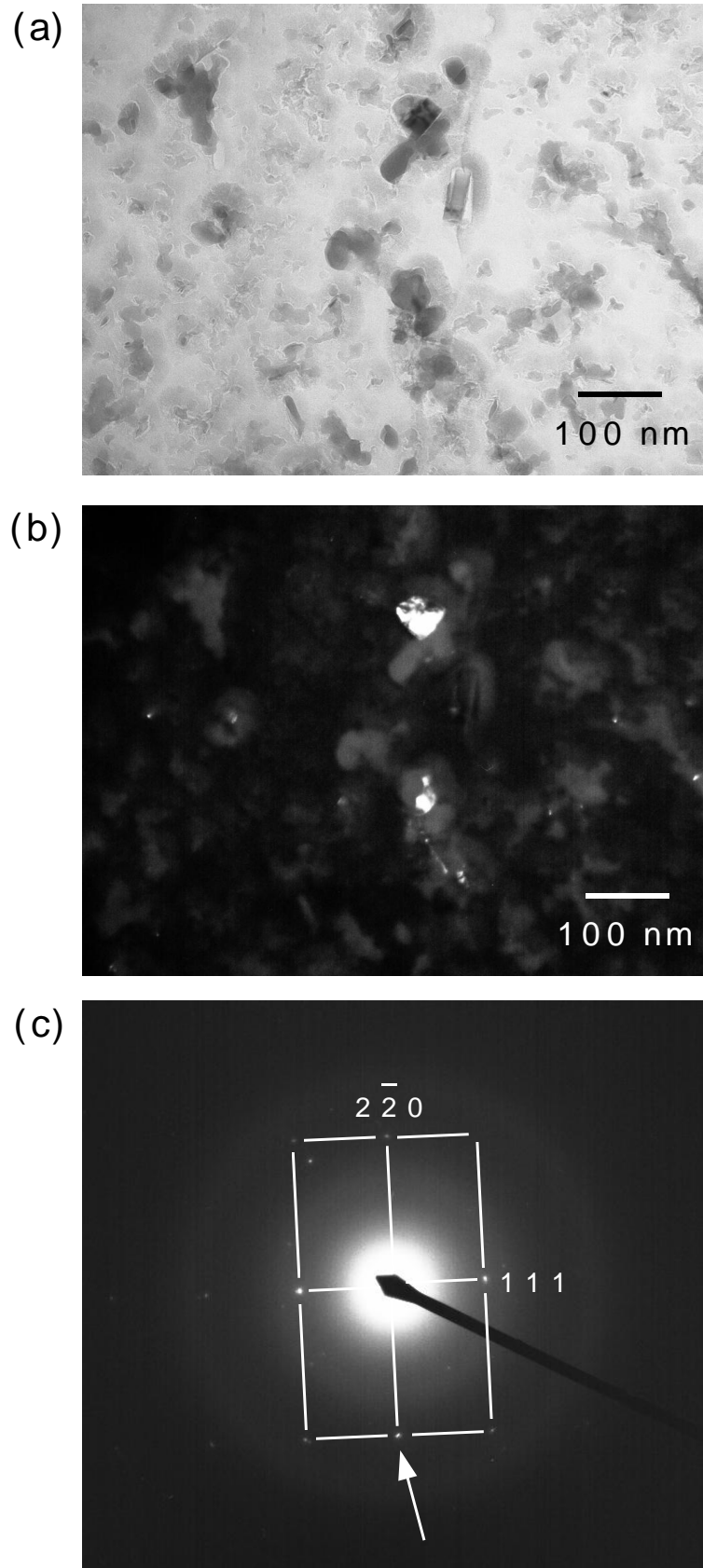


Figure 8.7: TEM observation of carbon replica from Steel *B* tempered at 600 °C for 100 h. (a) Bright field image. (b) Dark field image using the carbide diffraction spot indicated by the arrow in (c). The $2\bar{2}0$ and 111 reflections are from M_4C_3 which has an fcc structure.

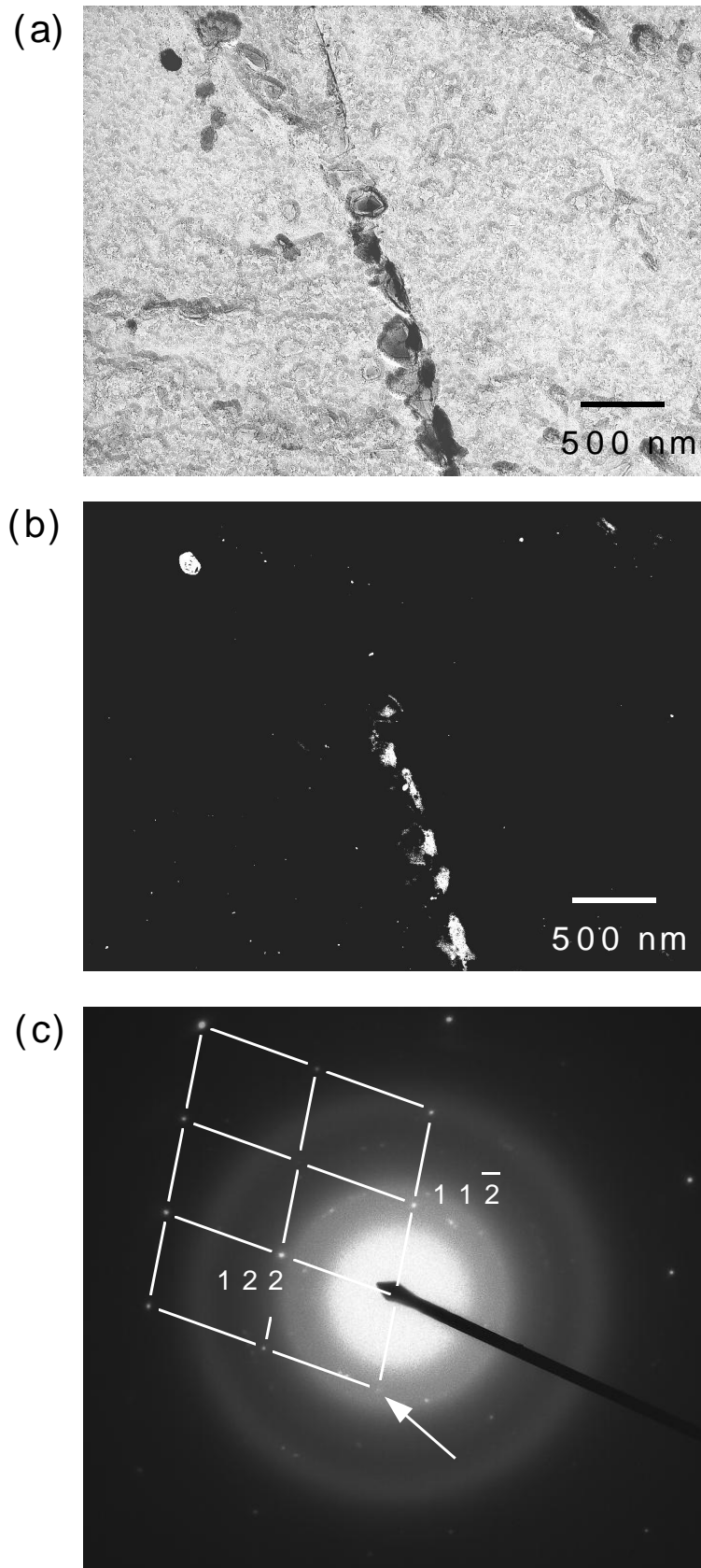


Figure 8.8: TEM observation of carbon replica from Steel *B* tempered at 600 °C for 0.5 h. (a) Bright field image. (b) Dark field image using the cementite diffraction spot indicated by the arrow in (c). The 122 and $11\bar{2}$ reflections are from cementite.

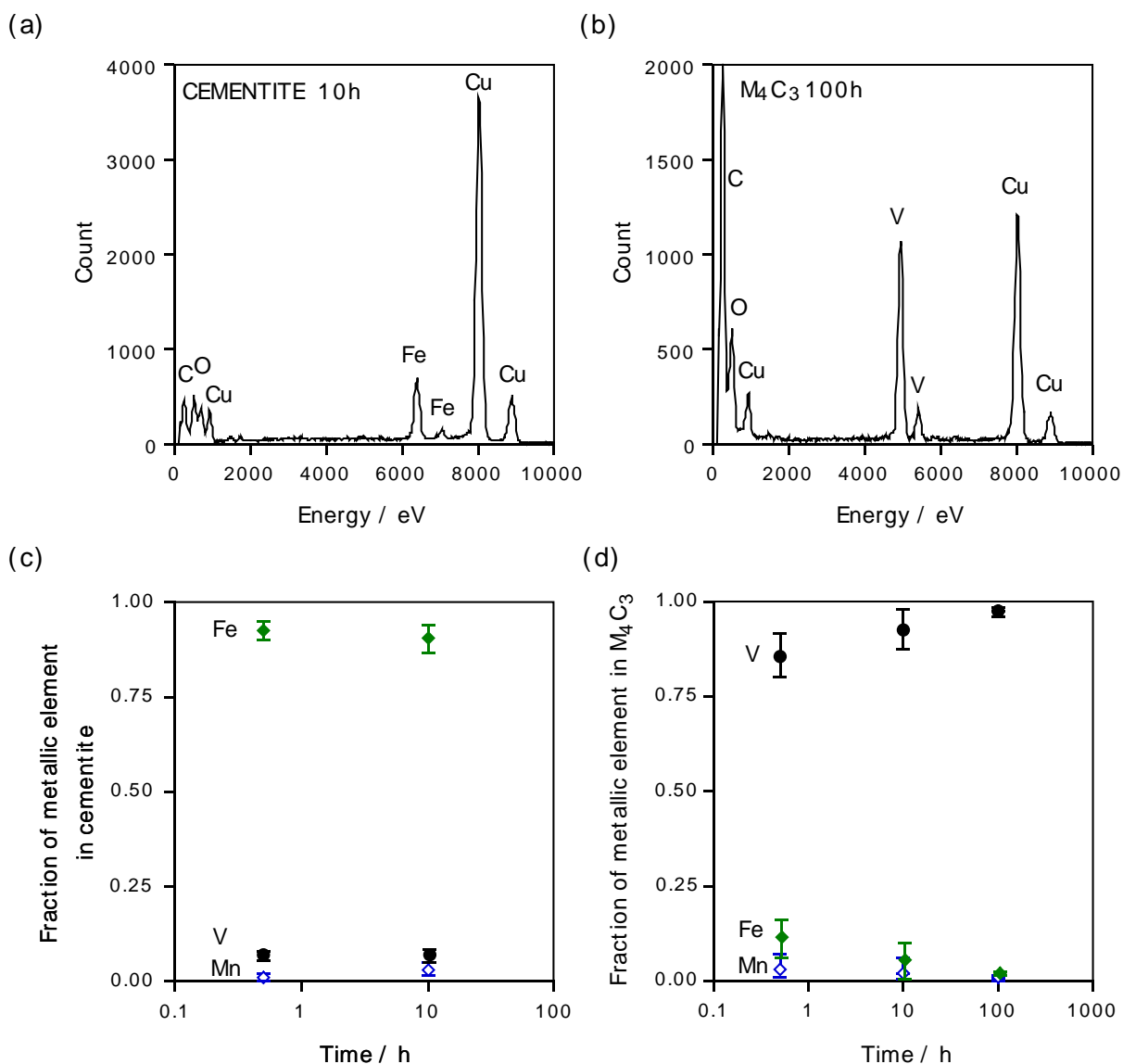


Figure 8.9: XEDS analysis of Steel *B* tempered at 600 °C. (a) Example of X-ray count versus energy profile of cementite, (b) Example of X-ray count-energy profile of M_4C_3 , (c) Relationship between atomic ratio of metallic elements and tempering time for cementite, (d) Relationship between atomic ratio of metallic elements and tempering time for M_4C_3 .

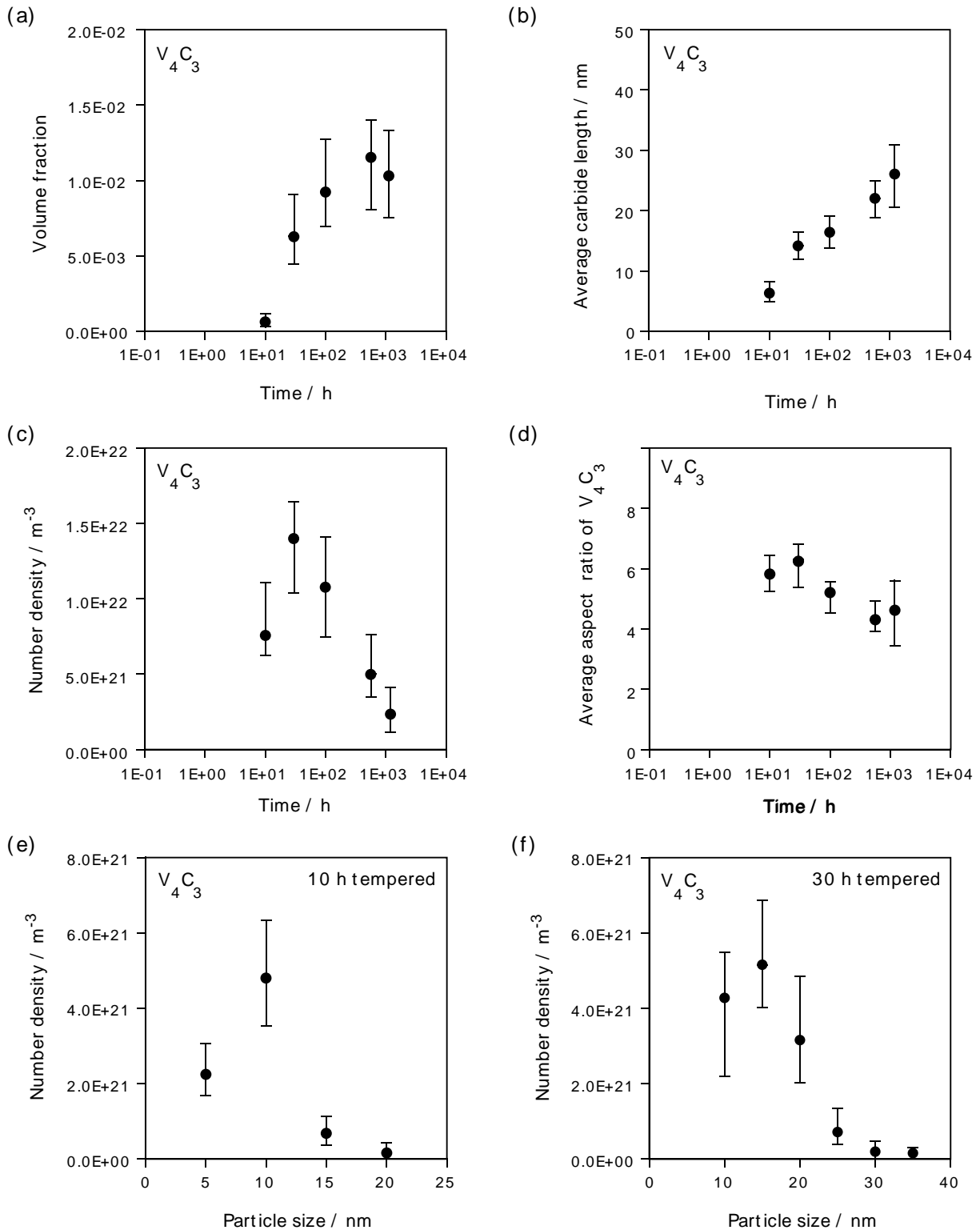


Figure 8.10: Observations of steel *B* tempered at 600 °C. (a) Relationship between the V_4C_3 volume fraction and the tempering time. (b) Relationship between the V_4C_3 length and the tempering time. (c) Relationship between the number density of V_4C_3 particles and the tempering time. (d) Relationship between the V_4C_3 aspect ratio and the tempering time. (e) Number density distribution of the length of V_4C_3 particles in the steel tempered for 10 h. (f) Number density distribution of the length of V_4C_3 particles tempered for 30 h.

8.2 Modelling of plate-shaped carbide growth

8.2.1 Chemical composition and equilibrium phases

Table 8.1 shows the chemical composition of the material under consideration. Using MTDATA, the equilibrium phases and the compositions of the equilibrium carbides for the steel at a variety of temperatures were calculated. The calculations allowed for the potential existence of cementite, M_2C (hcp), M_4C_3 (fcc), M_7C_3 and $M_{23}C_6$ in addition to ferrite. According to the results, for 600 °C, M_4C_3 (fcc) type carbide is the only stable carbide in this steel. The equilibrium composition of M_4C_3 according to MTDATA is 0.529V-0.450C-0.001Mn-0.000Fe-0.019N in atomic fraction. It is therefore denoted V_4C_3 in a Fe-C-V ternary system.

8.2.2 Local equilibrium, multicomponent systems

The concept of local equilibrium has been explained in Chapter 7. V_4C_3 particles precipitate from the matrix after the completion of paraequilibrium cementite precipitation. To satisfy the mass balances of V and C, the interfacial C concentration is assumed to be the same as that of the matrix [79]. However, it is strictly not the C concentration but its activity which should be identical at the ferrite/ V_4C_3 interface and in the matrix far from the interface. The above assumption is not strictly valid if the interaction between C atoms and substitutional atoms is strong, e.g. for the case of C and Cr. Figure 8.11 shows several iso-activity curves in the $\alpha+V_4C_3$ two-phase field. It can be seen that the deviation of the iso-activity curves from the iso-carbon concentration lines (the perpendicular lines) is small, the above approximation is therefore considered to be reasonable.

8.2.3 Capillarity effect, multicomponent systems

From observations made in the present work, V_4C_3 particles have rectangular plate shapes. As will be mentioned later, a plate-shaped particle can be modelled as a parabolic cylinder. If a matrix α and a parabolic cylinder-shaped precipitate of β are in contact at a curved interface then the conditions for local equilibrium are [109]:

$$dT^\beta = dT^\alpha = dT \quad (8.1)$$

$$dP^\beta = dP^\alpha + \sigma dH \quad (8.2)$$

$$d\mu_1^\beta = d\mu_1^\alpha, \quad d\mu_2^\beta = d\mu_2^\alpha \quad (8.3)$$

Here, T , P , H , σ and μ represent temperature, pressure, curvature of β phase, surface energy, and chemical potential, respectively. If it is assumed that the pressure of the α phase is constant, then from equation 8.2, the pressure change of the β phase can be represented as:

$$\Delta P = \int_{P(H=0)}^P dP^\beta = \int_{H=0}^H \sigma dH = \frac{\sigma}{rIC} \quad (8.4)$$

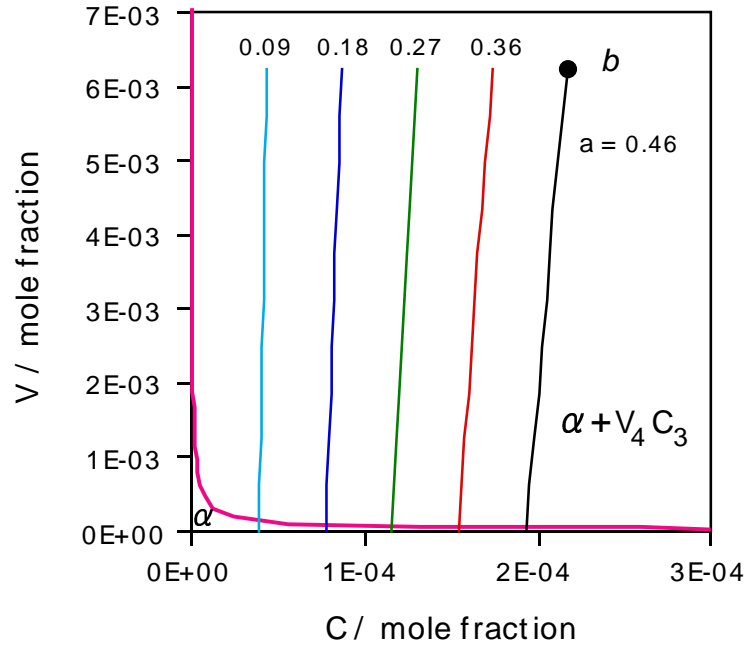


Figure 8.11: Iso-activity curves for C in the $\alpha + V_4C_3$ two-phase field. The numerical values in the figure represent the activity a of C. The point b represents the ferrite composition after the completion of paraequilibrium precipitation.

where r^{IC} is the radius of curvature at the tip. Accordingly, if the atomic volume of β is ν^β , an additional Gibbs energy term ΔG^β for a plate can be represented as:

$$\Delta G^\beta = \Delta P \nu^\beta = \frac{\sigma \nu^\beta}{r^{IC}}. \quad (8.5)$$

The influence of capillarity on the interface composition was evaluated using MTDATA, with a modification to the database of V_4C_3 (fcc) phase to include a pressure change. In the case of V_4C_3 (fcc, lattice parameter $a=4.2 \text{ \AA}$), the atomic volume $\nu^{V_4C_3}$ is $1.06 \times 10^{-29} \text{ m}^3$ and the interfacial energy σ can be assumed to be 0.2 J m^{-2} [66]. Accordingly, the additional Gibbs energy would be 1274 J mol^{-1} for $r^{IC} = 10 \text{ \AA}$. The database for the fcc phase (sublattice) was modified by adding $1 \times 10^{-6} \text{ J mol}^{-1}$ per 1 Pa pressure increase.

The capillarity effect on the interface composition ($c_V^{\alpha V_4C_3}$), which is evaluated by increasing an additional Gibbs energy term in the database of MTDATA, is shown in Fig. 8.12 for several tip radii in 0.1C-0.56V (wt. %) steel.

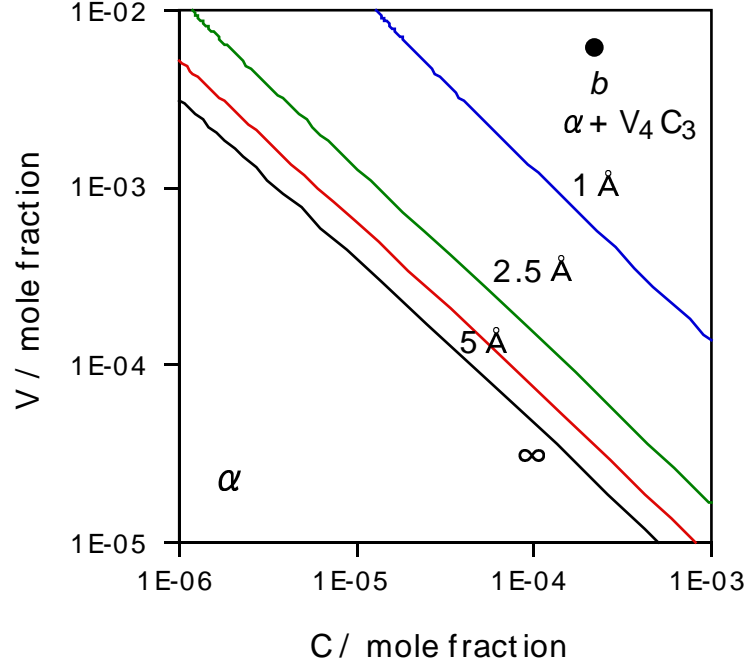


Figure 8.12: Composition of ferrite in equilibrium with V_4C_3 particle for several radius values, taking into account capillarity effect. The point b represents the composition of the ferrite matrix after the completion of paraequilibrium cementite precipitation.

8.2.4 Growth of the particles with capillarity effect

Trivedi has given an exact solution for the diffusion-controlled growth of plates, allowing the composition to vary along the surface assuming that the shape remains that of a parabolic cylinder [77]. In this theory, the capillarity and the interface-kinetics effects are accounted for and it is found that the supersaturation Ω can be represented as:

$$\Omega = \sqrt{\pi\bar{p}} \exp(\bar{p}) \operatorname{erfc}(\sqrt{\bar{p}}) \left(1 + \frac{v}{v_c} \Omega S_1(\bar{p}) + \frac{r_c}{r^{IC}} \Omega S_2(\bar{p}) \right) \quad (8.6)$$

where r^{IC} is the radius of curvature at the tip, r_c is the critical tip radius at which growth ceases, v is the lengthening rate, v_c is the interface-controlled velocity of a flat interface, \bar{p} is the Péclet number ($\bar{p} = vr^{IC}/2D$) and $S_1(\bar{p})$, $S_2(\bar{p})$ are:

$$\begin{aligned} S_1(\bar{p}) &= \frac{1}{2\bar{p}} M_1(\bar{p}) - 1 \\ S_2(\bar{p}) &= \frac{1}{2\bar{p}} M_2(\bar{p}) - 1 \end{aligned} \quad (8.7)$$

The functions $M_1(\bar{p})$ and $M_2(\bar{p})$ were evaluated numerically and they become $2/\pi$ and $4/\pi$ for small values of supersaturation ($\Omega \ll 1$), respectively [78]. Equation 8.6 gives the general solution for the growth of precipitate plates. The right-hand side is a sum of three terms of which the first is the result obtained by Ivantsov [74] for the case of the iso-concentrate boundary. The second and the third terms are corrections to that solution due to the interface kinetics and capillarity effects respectively.

Equation 8.6 does not give a unique value of v or r^{IC} . The maximum growth rate hypothesis is therefore adopted to fix these parameters. The solution of equation 8.6 under the maximum growth rate hypothesis was obtained by Trivedi for large values of Ω ($\Omega \geq 0.2$) [77] and by Rivera-Díaz-del-Castillo for $\Omega \leq 0.2$ [78].

However, equation 8.6 gives huge values of the ratio r^{IC}/r_c at the maximum growth rate for small values of the supersaturation Ω ; for example $r^{IC}/r_c \simeq 10^3$ at $\Omega = 10^{-2}$, $r^{IC}/r_c \simeq 10^4$ at $\Omega = 10^{-3}$ as shown in Fig. 8.13 [78]. The growing front of a particle has a large value of the radius, and the corresponding growth rate is therefore extremely small in the case of low supersaturation, according to equation 8.6. As will be seen later, this is inconsistent with experimental data. An alternative approach was therefore adopted, due to Bolling and Tiller [112]. Their method retains the parabolic shape with an assumed constant concentration at the interface appropriate to the tip radius. This means that if the interface effect can be neglected, the Péclet number is defined by [113]:

$$\Omega = \sqrt{\pi\bar{p}} \exp(\bar{p})\text{erfc}(\sqrt{\bar{p}}) \times \left(1 + \frac{r_c}{r^{IC}} \frac{\Omega}{\sqrt{\pi\bar{p}} \exp(\bar{p})\text{erfc}(\sqrt{\bar{p}})}\right) \quad (8.8)$$

The maximum growth rate can be obtained by differentiating equation 8.8 with respect to r^{IC} and setting $\frac{\partial v}{\partial r^{IC}} = 0$. The relationship between r^{IC}/r_c which gives the maximum growth rate and supersaturation Ω satisfying equation 8.8 is shown in Fig. 8.13.

8.2.5 Overall transformation kinetics

The carbide precipitation sequence during tempering in Fe-C-V steel, which includes the precipitation of V_4C_3 , and the enrichment and dissolution of cementite, was simulated.

I Enrichment and dissolution of cementite

The rate of enrichment of cementite is given approximately by [96]:

$$c_V^\theta = \bar{c}_V + 4\sqrt{D_V t} \frac{(\bar{c}_V - c_V^{\alpha\theta})}{d_t \sqrt{\pi}} \quad (8.9)$$

where c_V^θ represents the atomic fraction of vanadium in cementite, t is the time since cementite formation, d_t is the thickness of the cementite plate, D_V is the diffusion coefficient of vanadium in the matrix (it is assumed that the corresponding diffusivity in the cementite is identical to that in the ferrite), $c_V^{\alpha\theta}$ is the atomic fraction of vanadium in the ferrite which

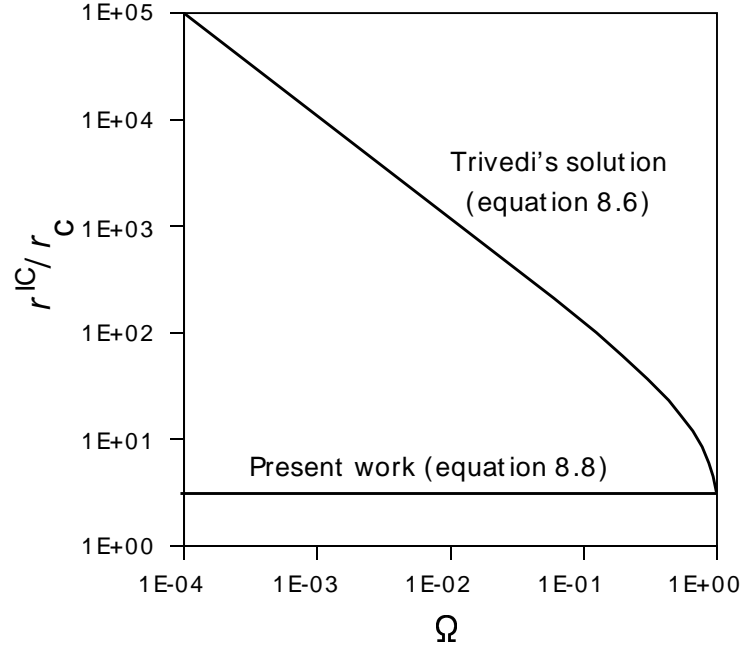


Figure 8.13: Relationship between the supersaturation Ω and the ratio r^{IC}/r_C for the maximum growth rate of plates, as obtained by equations 8.6 [78] and 8.8.

is in equilibrium with the cementite, and \bar{c}_V is the mean atomic fraction of vanadium in the alloy.

It is assumed that cementite dissolves in the manner described by Robson and Bhadeshia [94] so that the dissolution rate v_θ is determined as:

$$v_\theta = -\frac{D_V}{\bar{d}} \frac{c_V^{\alpha\theta} - c_V^{\alpha V_4C_3}}{c_V^{\theta\alpha} - c_V^{\alpha\theta}} \quad (8.10)$$

where \bar{d} is the mean diffusion distance between θ and V_4C_3 precipitates, given by:

$$\bar{d} = (N^\theta + N^{V_4C_3})^{-\frac{1}{3}} \quad (8.11)$$

where N^θ and $N^{V_4C_3}$ are the number densities of θ and V_4C_3 particles respectively.

II Nucleation of V_4C_3

The concept of nucleation has been explained in Chapter 7. The nucleation rate and the activation energy for nucleation are represented by equations 7.12 and 7.13, respectively. The

chemical free energy change per unit volume of nuclei ΔG_V is calculated using MTDATA as $-2.387 \times 10^9 \text{ J m}^{-3}$. This value is for the beginning of precipitation of V_4C_3 and it will decrease as the precipitation proceeds. The change of the value of ΔG_V is calculated corresponding to the progress of the precipitation reaction using a mean field approximation, i.e. assuming that the solute is uniformly distributed in the matrix.

III Diffusion-controlled growth with capillarity

Modelling of the local equilibrium of V_4C_3 precipitation is based on Coates' diffusion-controlled growth theory [79] accounting for the capillarity effect. The critical radius of curvature r_c at which growth ceases was calculated using MTDATA, with a modification to the database of the fcc phase to include a pressure change. The growth rate of particles is the maximum rate, for given values of the carbon concentration in the matrix and the supersaturation Ω of V. The growth rate obtained from the values of \bar{p} and the ratio r^{IC}/r_c corresponding to the maximum growth rate satisfies equation 8.8.

IV Ostwald ripening of particles

The combination of nucleation and growth gives rise to a distribution of V_4C_3 lengths, but for a given supersaturation, they all have the same tip radius. An approximate treatment, in which a V_4C_3 particle is modelled to be a plate of which the periphery is hemicylindrical, was therefore adopted for the Ostwald ripening stage, after the completion of precipitation. The growth (or dissolution) rate can be calculated using Zener's theory as:

$$v \simeq -\frac{D_V}{\bar{d}} \frac{c_V^{\alpha V_4C_3} - c_{V,r}^{\alpha V_4C_3}}{\bar{c}_V - c_{V,r}^{\alpha V_4C_3}} \quad (8.12)$$

where $c_{V,r}^{\alpha V_4C_3}$ is the equilibrium mole fraction of vanadium in ferrite at the hemicylindrical tip of a V_4C_3 particle and \bar{d} is the mean diffusion distance between particles which can be represented as [94]:

$$\bar{d} = (N^\beta)^{-\frac{1}{3}} \quad (8.13)$$

where N^β is the number density of V_4C_3 particles. The interfacial composition at the hemicylindrical tip of the particles can be calculated by an analogous method for the capillarity effect which is explained in section 8.2.3.

During Ostwald ripening, particles should in general become spheroidised to reduce the surface area if the interfacial energy is not orientation dependent. However, the aspect ratio of V_4C_3 particles does not in fact change significantly. These particles are found to grow whilst retaining the plate shape as shown in Fig. 8.1 - 8.6. It is therefore assumed that the shape of the particles is preserved during Ostwald ripening. Accordingly, particles grow or dissolve as shown in Fig. 8.14.

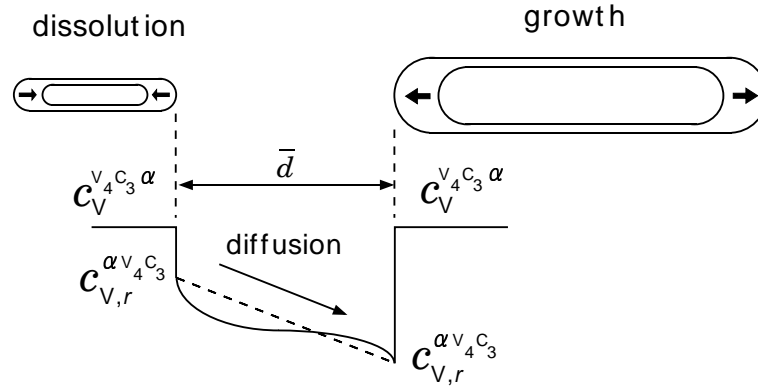


Figure 8.14: Schematic drawing of Ostwald ripening of plate-shaped particles. The aspect ratio of each particle is fixed to be 6.

8.2.6 Inputs and calculations

The precipitation calculations were carried out in time steps of 100 s. In each step, the following quantities were calculated: the nucleation rate, nucleus size (i.e. the initial size of particle growth), the growth rate, and the change in V and C mole fraction in the matrix corresponding to V_4C_3 growth and enrichment and dissolution of cementite. The consumption of nucleation sites during the transformation is accounted for in each step. Once the mole fractions of V and C in the matrix (\bar{c}_V and \bar{c}_C) have been determined, the corresponding supersaturations of V (Ω_V) and the critical radius r_c can be obtained. From the values of Ω_V and r_c , the value of \bar{p} which satisfies equation 8.8 and, finally, the maximum growth rate and the tip radius of a V_4C_3 particle r^{IC} giving the maximum rate for the corresponding value of \bar{p} are obtained. The volume of each particle was calculated as a parabolic cylinder.

After the completion of the precipitation and growth stage, each V_4C_3 particle was modelled as a plate of which the periphery is hemicylindrical for the Ostwald ripening stage. In this stage, the value of $c_{V,r}^{\alpha_{V_4C_3}}$ at the tip of each plate-shaped particle was calculated, and then the growth (or dissolution) rate at the tip was calculated.

The parameters used in the calculations are listed in Table 8.2. The nucleation site density was obtained by fitting to experimental data. The surface energy [66], diffusion constant and activation energy for V diffusion [114] were obtained from the literature.

8.3 Results and discussion

Figure 8.15 shows comparisons between the calculations and experimental observations.

Parameter	condition
Shape	plate
Tempering temperature / °C	600
Surface energy of V_4C_3 / $J m^{-2}$	0.2
Driving force for nucleation of V_4C_3 / $J m^{-3}$	-2.387×10^9
Nucleation site density of V_4C_3 / m^{-3}	1.48×10^{22}
Maximum volume fraction of cementite	1.796×10^{-2}
Maximum volume fraction of V_4C_3	9.66×10^{-3}
$c_V^{\alpha\theta}$ / atomic fraction	4.356×10^{-3}
$c_V^{\theta\alpha}$ / atomic fraction	1.063×10^{-1}
$c_V^{\alpha V_4C_3}$ / atomic fraction	9.620×10^{-4}
$c_V^{V_4C_3\alpha}$ / atomic fraction	5.320×10^{-1}
Thickness of cementite in grains / m	2.0×10^{-8}
Thickness of cementite on grain boundaries / m	5.0×10^{-8}
Diffusion constant of V D_V / m^2s^{-1}	3.05×10^{-4}
Activation energy for V diffusion Q_V / $J mol^{-1}$	2.39×10^5

Table 8.2: The calculation parameters for precipitation of carbides in a ternary system (Fe-0.10C-0.56V in wt. %)

After the completion of paraequilibrium cementite precipitation, the concentration of carbon in the matrix is quite low (0.022 at. %, according to MTDATA). Carbon atoms, which are necessary for the precipitation of V_4C_3 , are provided by the dissolution of cementite. After the completion of precipitation, Ostwald ripening proceeds with a constant volume fraction of V_4C_3 . Figure 8.15 (a) shows such simultaneous V_3C_4 precipitation and cementite dissolution behaviour.

The average length of V_4C_3 particles increases during the precipitation and growth stage. During the Ostwald ripening stage, the aspect ratio of the particles was fixed and the growth rate (or dissolution rate) of each particle was calculated using the tip radius of the edges of a plate. On average, the length therefore increases during Ostwald ripening as shown in Fig. 8.15 (b).

The number density of V_4C_3 particles of length greater than 4 nm was calculated, as shown in Fig. 8.15 (c), for comparison with observation; V_4C_3 particles of size less than 4 nm could not easily be observed using conventional transmission electron microscopy.

The calculated number density distribution of the length of V_4C_3 particles is shown in Fig. 8.15 (d) for a tempering time of 30 h.

The calculations in general agree well with the observations. However, there are discrepancies between calculations and observations for the average length of V_4C_3 particles during Ostwald ripening. It was observed that particles of V_4C_3 kept their shape in the laths, however, they were spheroidised on lath or grain boundaries. Since the observations

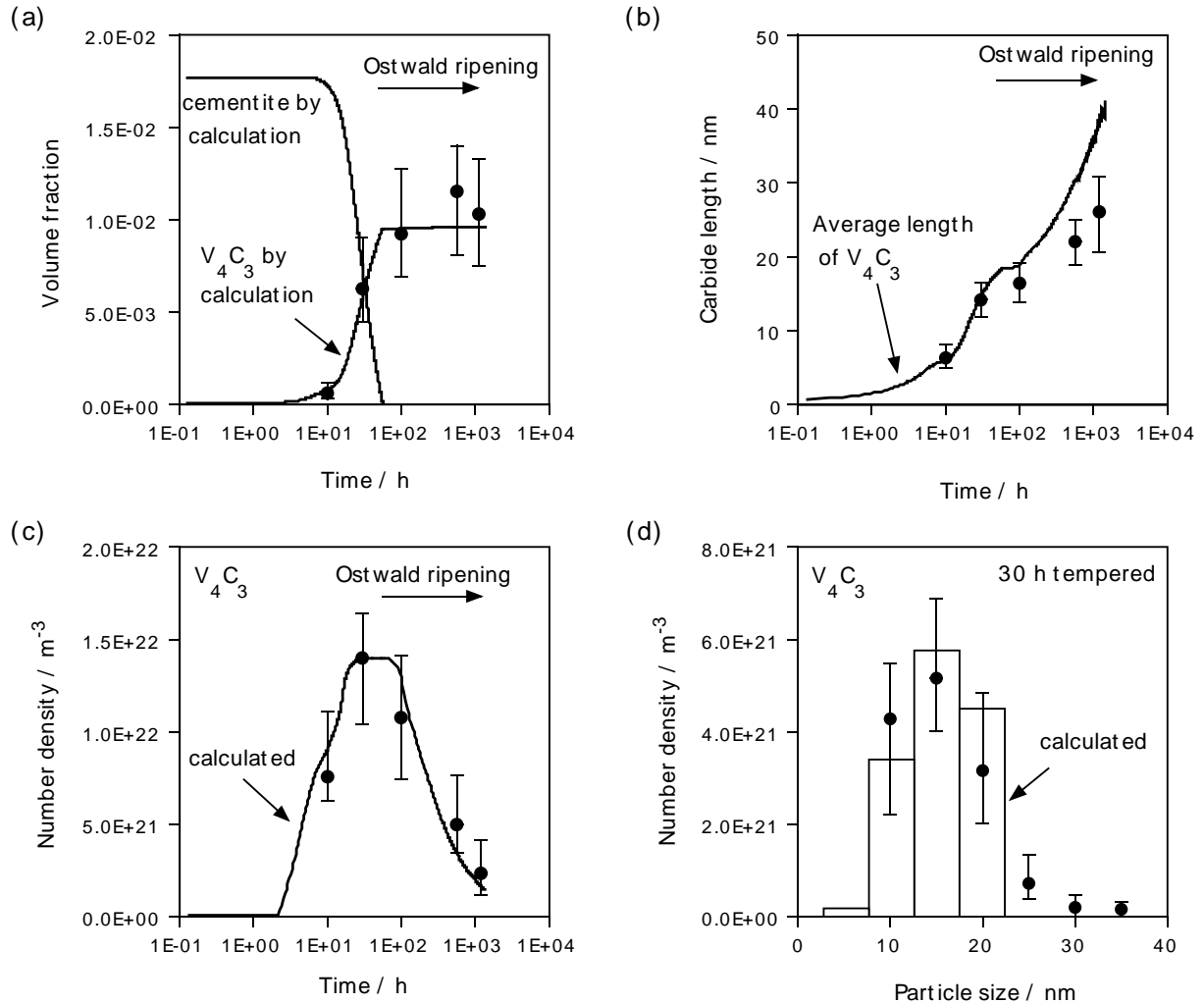


Figure 8.15: Comparisons between calculations and observations. (a) Relationship between volume fraction of V_4C_3 particles and tempering temperature. (b) Relationship between average length of V_4C_3 particles and tempering temperature. (c) Relationship between number density of V_4C_3 particles whose size are over 4 nm and tempering temperature. (d) Number density distribution of the length of V_4C_3 particles for 30 h tempered steel.

contain information on the particles both in the grains and on the grain boundaries, the average length of V_4C_3 particles is smaller than the calculations during Ostwald ripening. The reason why the precipitates retain their shape during coarsening is now discussed.

The orientation relationship between V_4C_3 and the ferrite matrix is reported as [39, 38]:

$$\{100\}_{V_4C_3} // \{100\}_{\alpha}, \langle 001 \rangle_{V_4C_3} // \langle 011 \rangle_{\alpha}$$

V_4C_3 is formed as platelets lying on $\{100\}_{\alpha}$ planes. The configuration of V and Fe atoms in $(100)_{\alpha}$ planes indicates excellent coherency between both lattices (about 2.1 % mismatch). By contrast, the lattice misfit is about 47 % in planes perpendicular to this plane [12]. This is the primary reason that V_4C_3 grows easily as thin plates. In other words, the interfacial energy is orientation-dependent.

For the precipitation and growth stage, Trivedi's theory for the growth of the plate-shaped particles was not adopted; it is not valid because of the large value of r^{IC}/r_c for the small supersaturation. Instead of Trivedi's theory, which allows the composition to vary along the interface of a plane, the composition was assumed to be constant at the interface in the present model. Figure 8.16 shows the comparisons of the calculated average length of particles obtained by Trivedi's theory and the present model, together with experimental data. There is a large discrepancy between the observations and calculations using Trivedi's theory.

For the Ostwald ripening stage, V_4C_3 particles were modelled as plates with hemicylindrical ends. The classical theory of Ostwald ripening, in which the precipitates are modelled as spheres gives the following equation [83, 84]:

$$N^{V_4C_3} = N_0^{V_4C_3} \frac{r_0^3}{r_0^3 + \frac{8\sigma\nu^{\beta} D_V c_V^{\alpha\beta}}{9kT} t} \quad (8.14)$$

where $N_0^{V_4C_3}$ is the initial number density of V_4C_3 particles when the Ostwald ripening stage starts, r_0 is the initial average particle radius, t is time, and D_V is the diffusion coefficient of vanadium in the matrix.

Number densities of V_4C_3 calculated using equation 8.14 were compared with those obtained using the present model assuming either a plate-shaped or a spherical model. As demonstrated by Fig. 8.17, the results are very similar in all three cases.

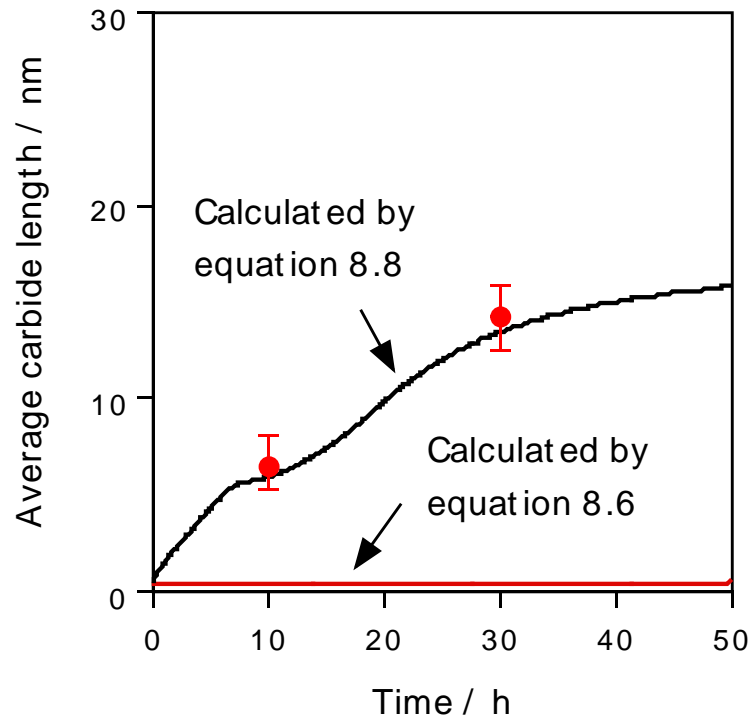


Figure 8.16: Comparisons between the calculated average length of particles obtained using equation 8.6 and the present model (equation 8.8) and observation.

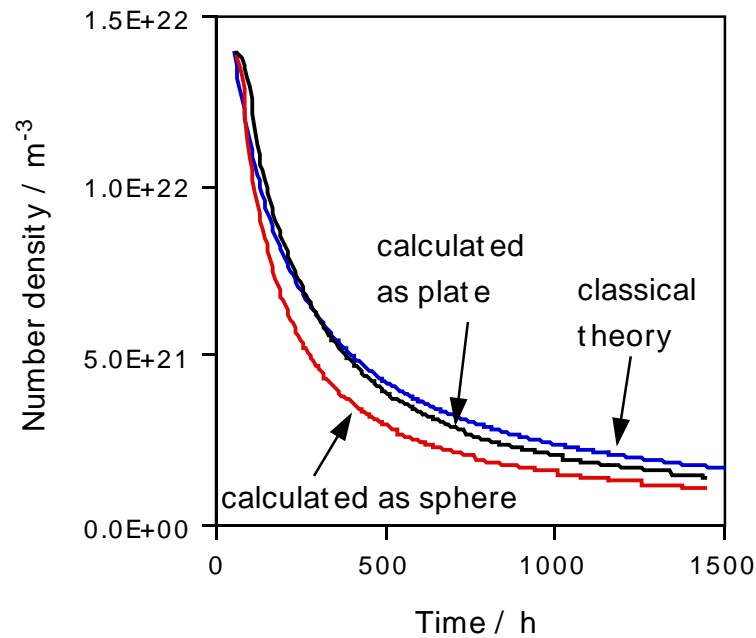


Figure 8.17: Comparisons of the number density of V_4C_3 particles calculated as plate-shaped, spherical and by equation 8.14.

8.4 Summary and conclusions

The precipitation and Ostwald ripening behaviour of V_4C_3 (plate-shaped) particles during the tempering of a ternary Fe-C-V martensitic steel have been characterised and modelled, taking account of local equilibrium, the capillarity effect, and simultaneous cementite enrichment and dissolution.

In conclusion, by modelling a V_4C_3 particle as a parabolic cylinder with a constant concentration of the solute along the surface of the tip, and assuming the maximum growth rate, the model can predict the average length, volume fraction, and number density of particles with good agreement with experimental observations. The growth rate depends on the supersaturation of vanadium (Ω_V) and the ratio of the solute mole fraction in the matrix \bar{c}_V/\bar{c}_C .

Chapter 9

Modelling M_4C_3 in a Fe-C-Mo-V quaternary system

9.1 Experimental work

Experiments were conducted to provide data for model verification. Transmission electron microscopy was used to obtain the necessary data.

9.1.1 Material

Table 9.1 shows the chemical composition of the material designed for the present work. These steels contain 0.1 wt. % carbon. These steels were designed to give different Mo:V ratios in M_4C_3 .

	C	Si	Mn	Mo	V	Al	N
Steel <i>C</i>	0.10	<0.005	2.00	1.59	0.56	0.03	0.0044
Steel <i>D</i>	0.10	<0.005	2.00	0.40	0.56	0.03	0.0040
Steel <i>E</i>	0.10	<0.005	2.00	0.40	0.30	0.03	0.0041

Table 9.1: Chemical composition of experimental steel in wt. %.

9.1.2 TEM observations

I M_4C_3

Figures 9.1 - 9.6 show thin-foil TEM images of Steel *C* tempered for a variety of times. These pictures were taken from the [100] orientation of the matrix. Figure 9.7 shows the images of a carbon replica sample from the specimen which was tempered for 560 h. From the diffraction patterns in Fig. 9.7, these plate-shaped precipitates have a face-centred cubic (fcc) structure and are considered to be M_4C_3 , where ‘M’ stands for metal atoms (V, Mo, Fe, Mn); the vanadium-rich carbide is henceforth referred to as M_4C_3 . It is known that M_4C_3 grows on the three equivalent $\{001\}_\alpha$ planes [12]. In Fig. 9.1 - 9.6, the needle-like precipitates are the

cross-sectioned images of precipitates growing on the $\{001\}_\alpha$ plane, which is parallel to the observation direction. The carbide morphology was characterised from over 500 particles in each sample. Figure 9.8 (a)-(d) shows the volume fraction of carbide, carbide length, number density and aspect ratio plotted against the tempering time. The number density distribution of the length of M_4C_3 particles is also shown for two tempering times in (e) and (f). The solid circles represent the average of data from different locations, and the scatter of the data is indicated by error bars.

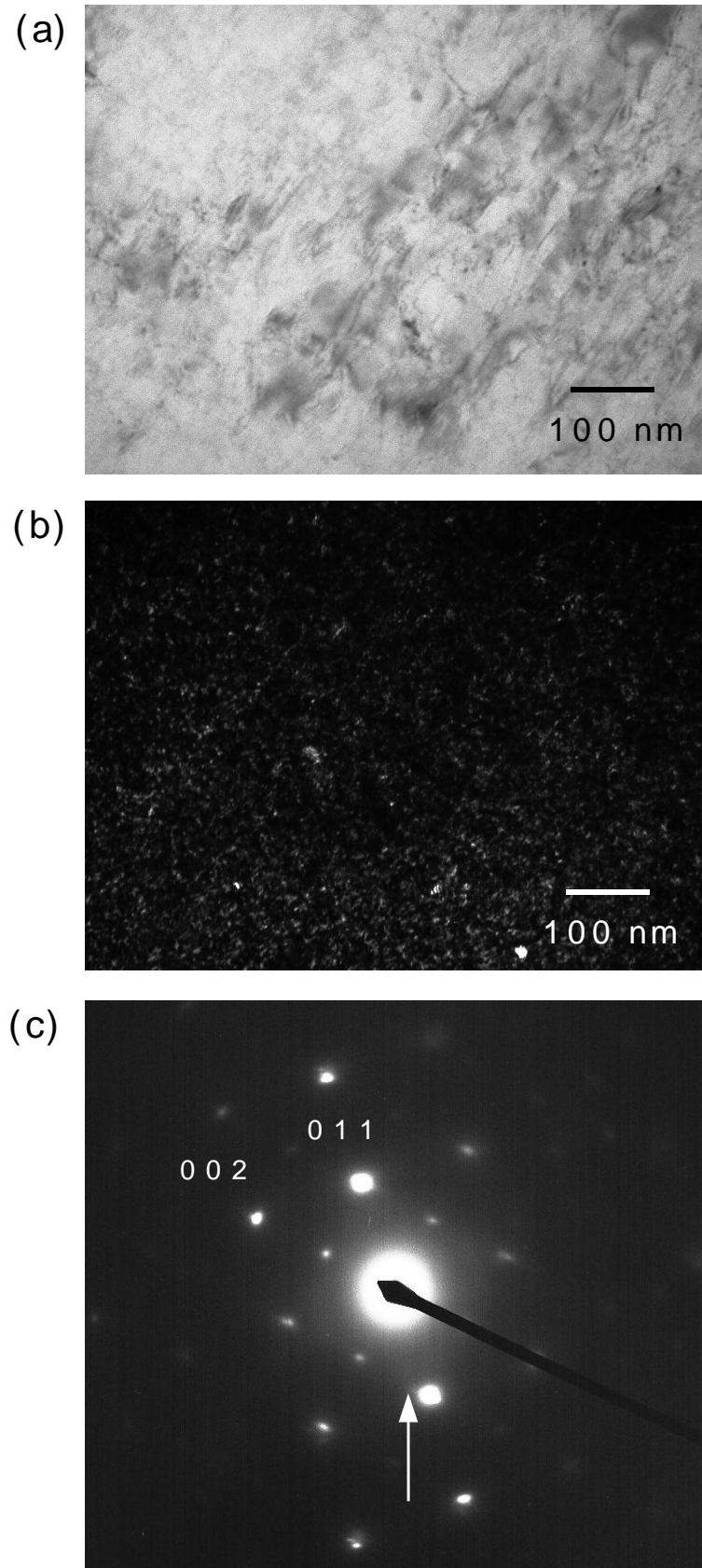


Figure 9.1: TEM observation of a thin-foil from Steel *C* tempered at 600 °C for 0.5 h. Zone axis is [100] of ferrite matrix. (a) Bright field image. (b) Dark field image using the carbide diffraction spot indicated by the arrow in (c). The 002 and 011 reflections are from the ferrite.

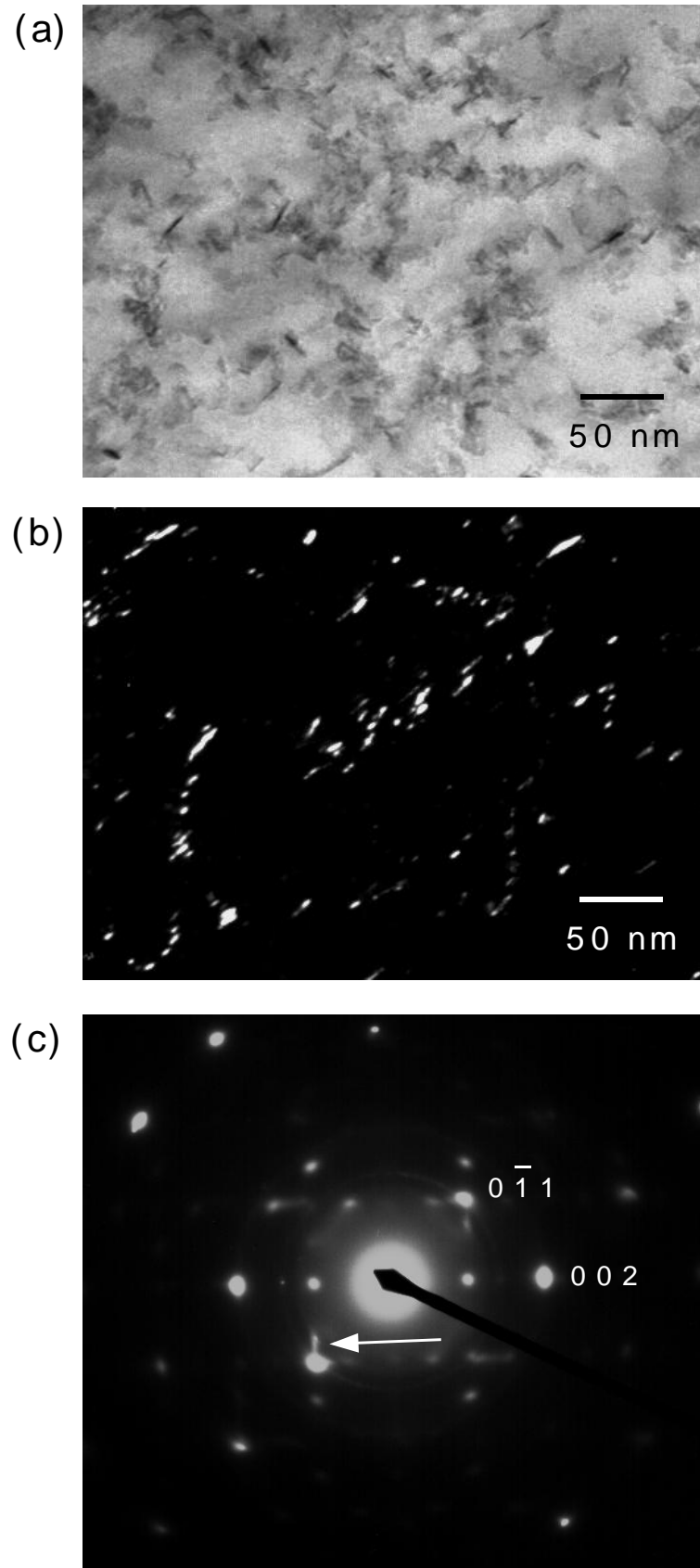


Figure 9.2: TEM observation of a thin-foil from Steel *C* tempered at 600 °C for 10 h. Zone axis is [100] of ferrite matrix. (a) Bright field image. (b) Dark field image using the carbide diffraction spot indicated by the arrow in (c). The 002 and $0\bar{1}1$ reflections are from the ferrite.

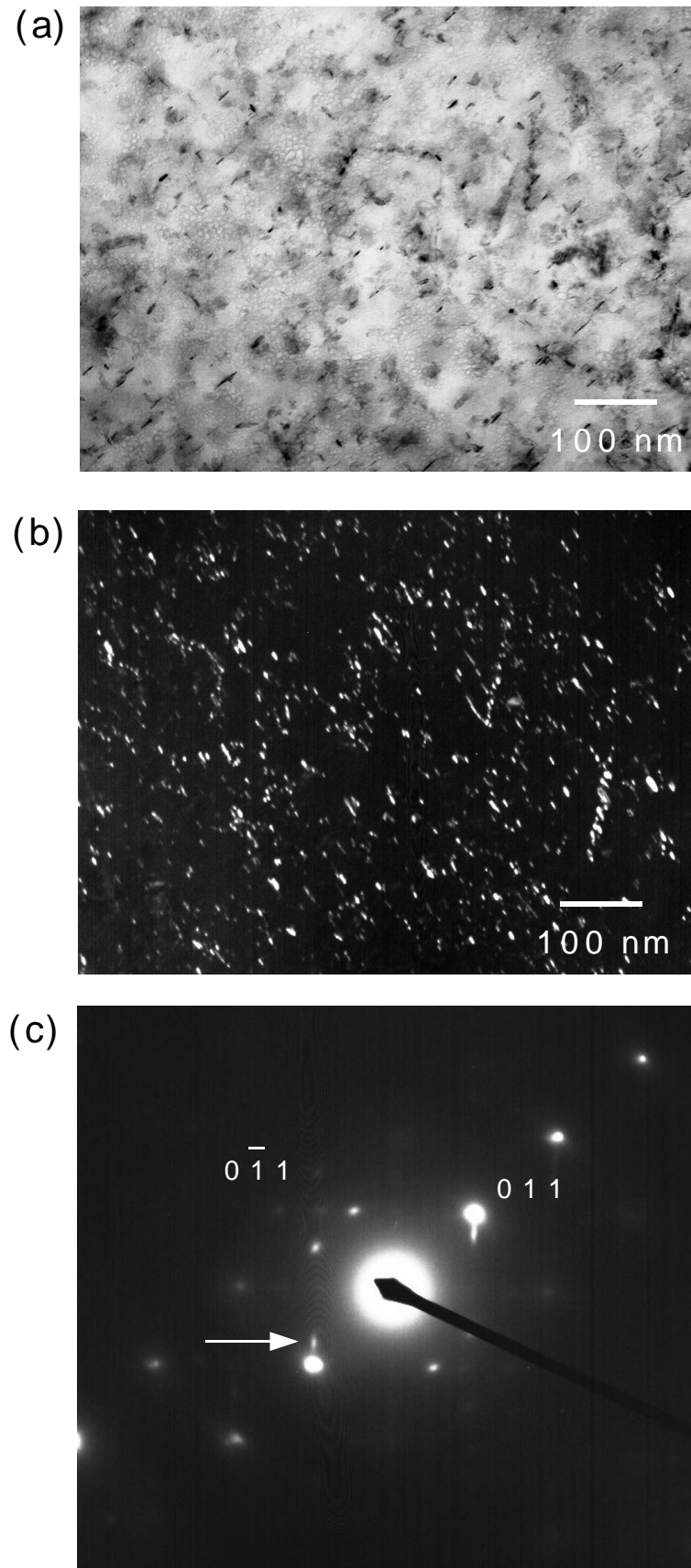


Figure 9.3: TEM observation of a thin-foil from Steel *C* tempered at 600 °C for 30 h. Zone axis is [100] of ferrite matrix. (a) Bright field image. (b) Dark field image using the carbide diffraction spot indicated by the arrow in (c). The $0\bar{1}1$ and 011 reflections are from the ferrite.

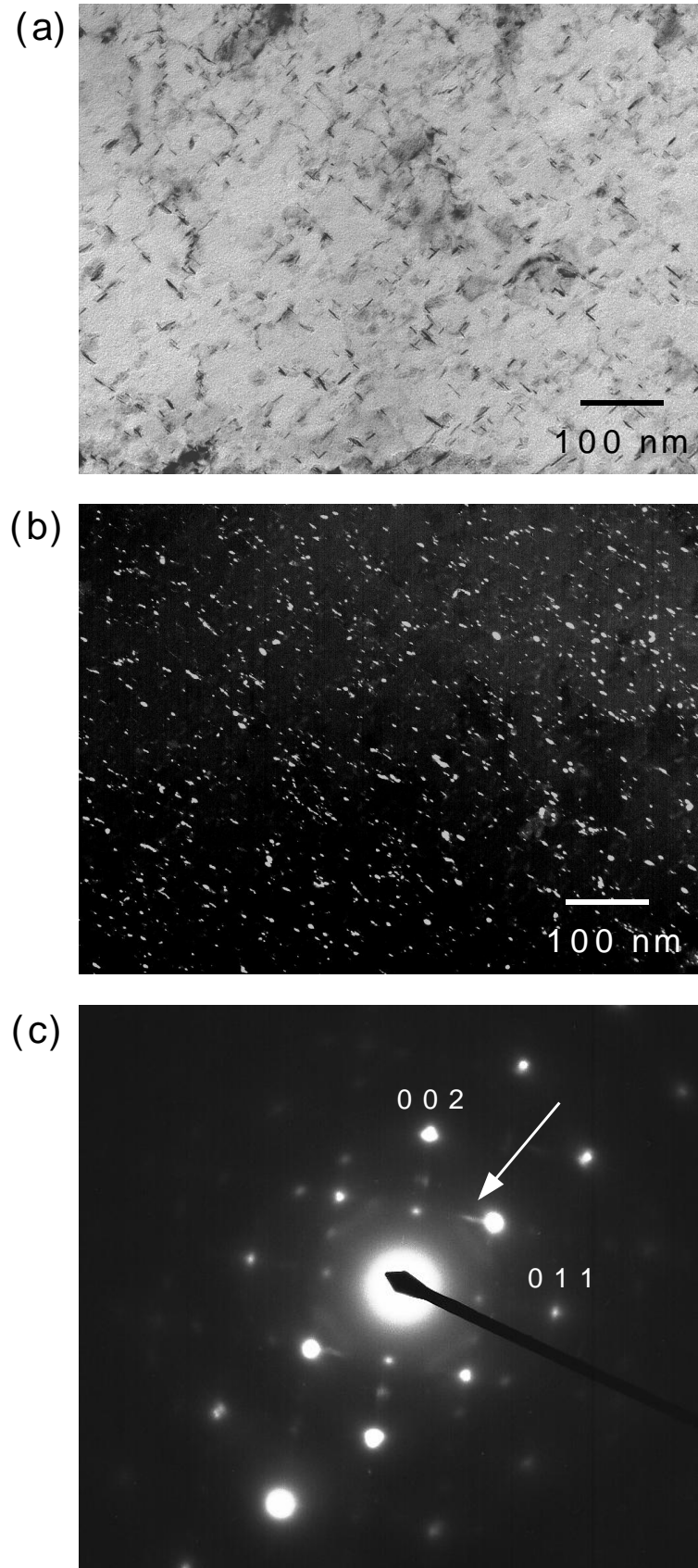


Figure 9.4: TEM observation of a thin-foil from Steel *C* tempered at 600 °C for 100 h. Zone axis is [100] of ferrite matrix. (a) Bright field image. (b) Dark field image using the carbide diffraction spot indicated by the arrow in (c). The 002 and 011 reflections are from the ferrite.

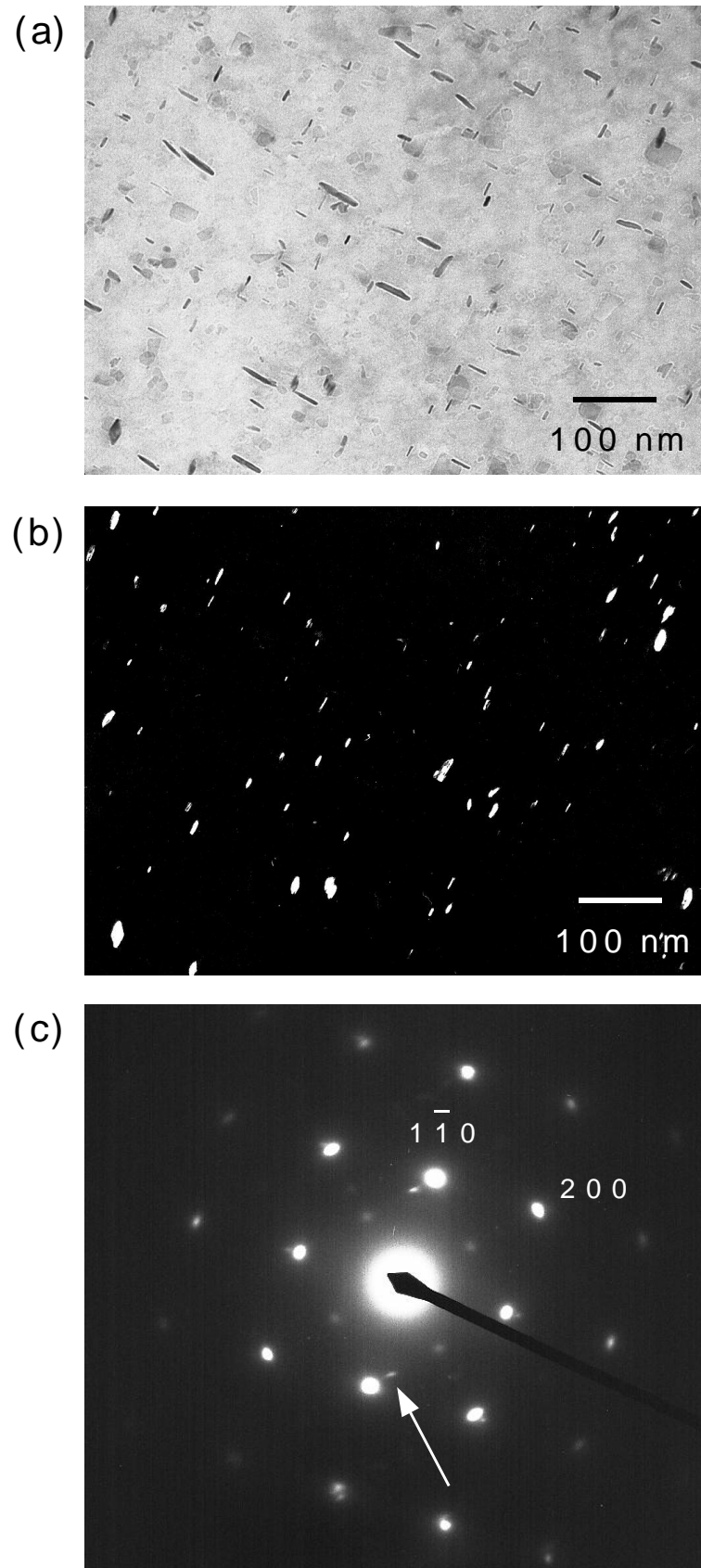


Figure 9.5: TEM observation of a thin-foil from Steel *C* tempered at 600 °C for 560 h. Zone axis is [100] of ferrite matrix. (a) Bright field image. (b) Dark field image using the carbide diffraction spot indicated by the arrow in (c). The 200 and 011 reflections are from the ferrite.

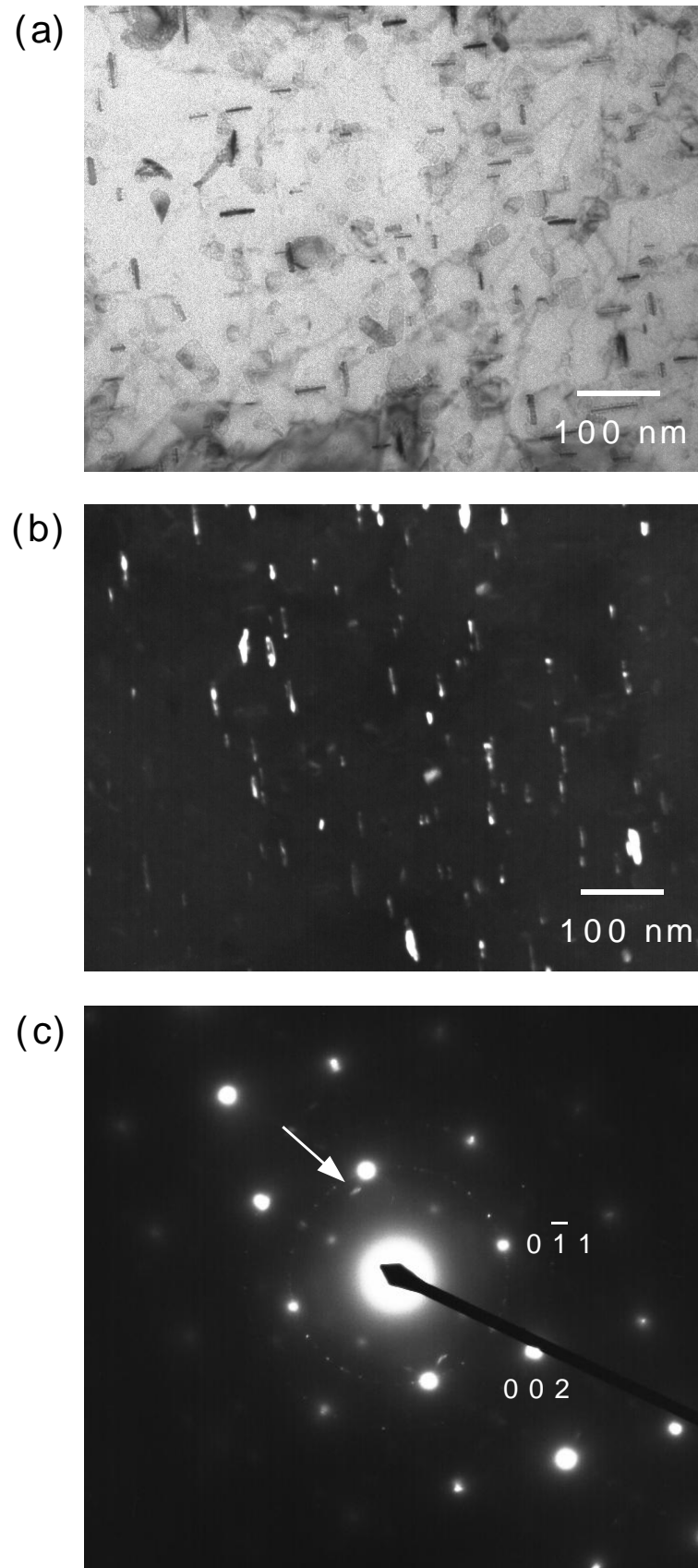


Figure 9.6: TEM observation of a thin-foil from Steel *C* tempered at 600 °C for 1150 h. Zone axis is $[100]$ of ferrite matrix. (a) Bright field image. (b) Dark field image using the carbide diffraction spot indicated by the arrow in (c). The 002 and $0\bar{1}1$ reflections are from the ferrite.

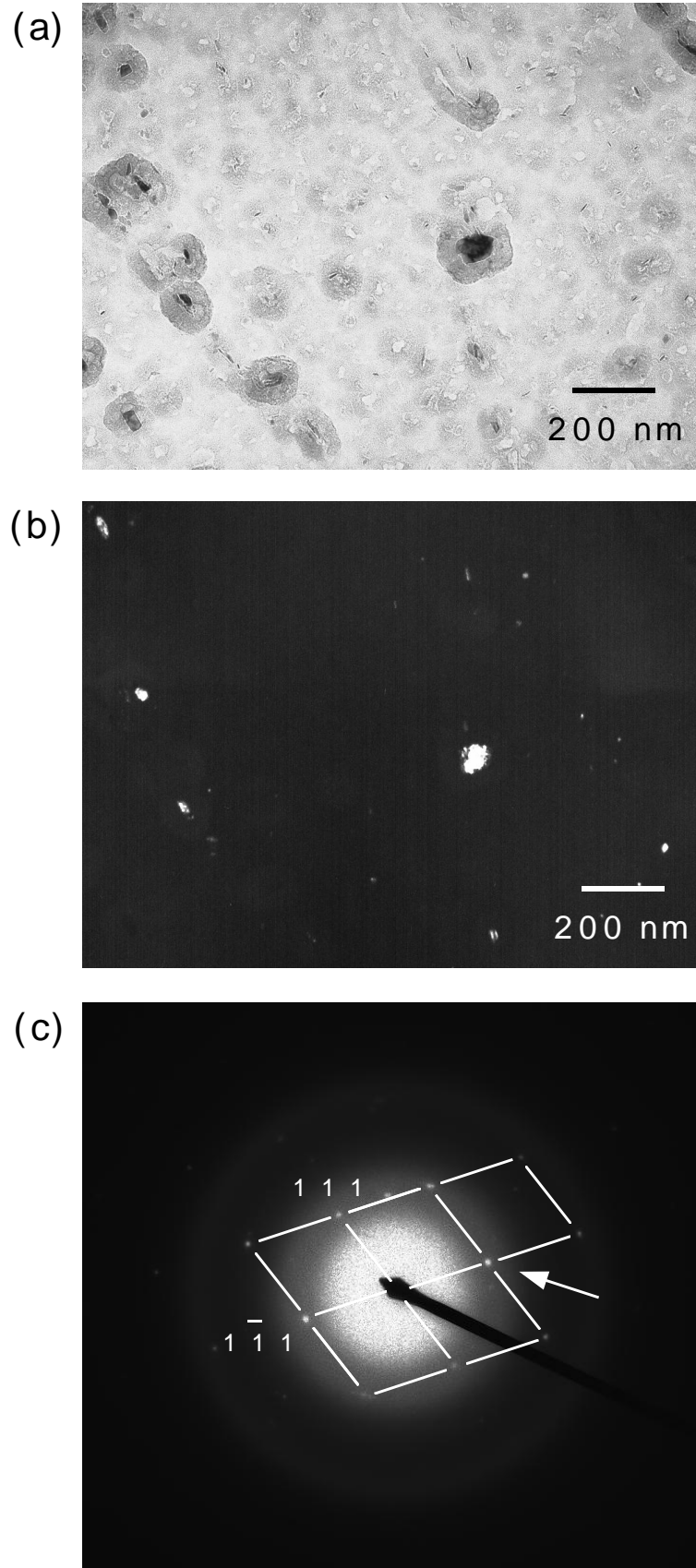


Figure 9.7: TEM observation of carbon replica from Steel *C* tempered at 600 °C for 560 h. (a) Bright field image. (b) Dark field image using the diffraction spot indicated by the arrow in (c). These particles are fcc structure with the lattice parameter of 4.2 Å.

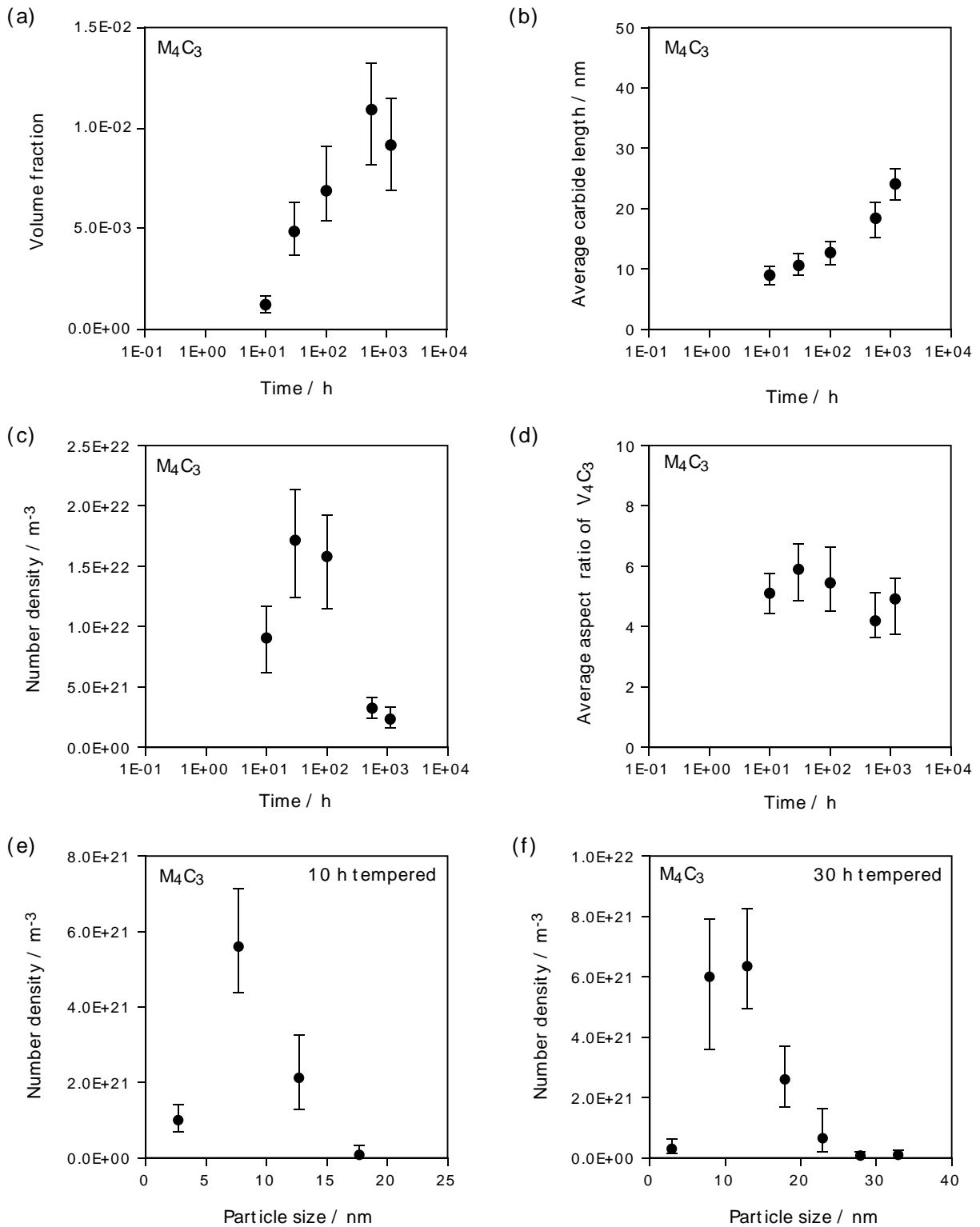


Figure 9.8: Observations of steel *C* tempered at 600 °C. (a) Relationship between the M_4C_3 volume fraction and the tempering time. (b) Relationship between the M_4C_3 length and the tempering time. (c) Relationship between the number density of M_4C_3 particles and the tempering time. (d) Relationship between the M_4C_3 aspect ratio and the tempering time. (e) Number density distribution of the length of M_4C_3 particles in the steel tempered for 10 h. (f) Number density distribution of the length of M_4C_3 particles tempered for 30 h.

Figures 9.9 - 9.11 show thin-foil TEM images of Steel *D* tempered for a variety of times. These pictures were taken from the [100] orientation of the matrix. In Fig. 9.9 - 9.11, the needle-like precipitates are the cross-sectioned images of precipitates growing on the $\{001\}_\alpha$ plane, which is parallel to the observation direction. The carbide morphology was characterised from over 500 particles in each sample. Figure 9.12 shows the volume fraction of carbide, carbide length and number density plotted against the tempering time. The number density distribution of the length of M_4C_3 particles is also shown. The solid circles represent the average of data from different locations, and the scatter of the data is indicated by error bars.

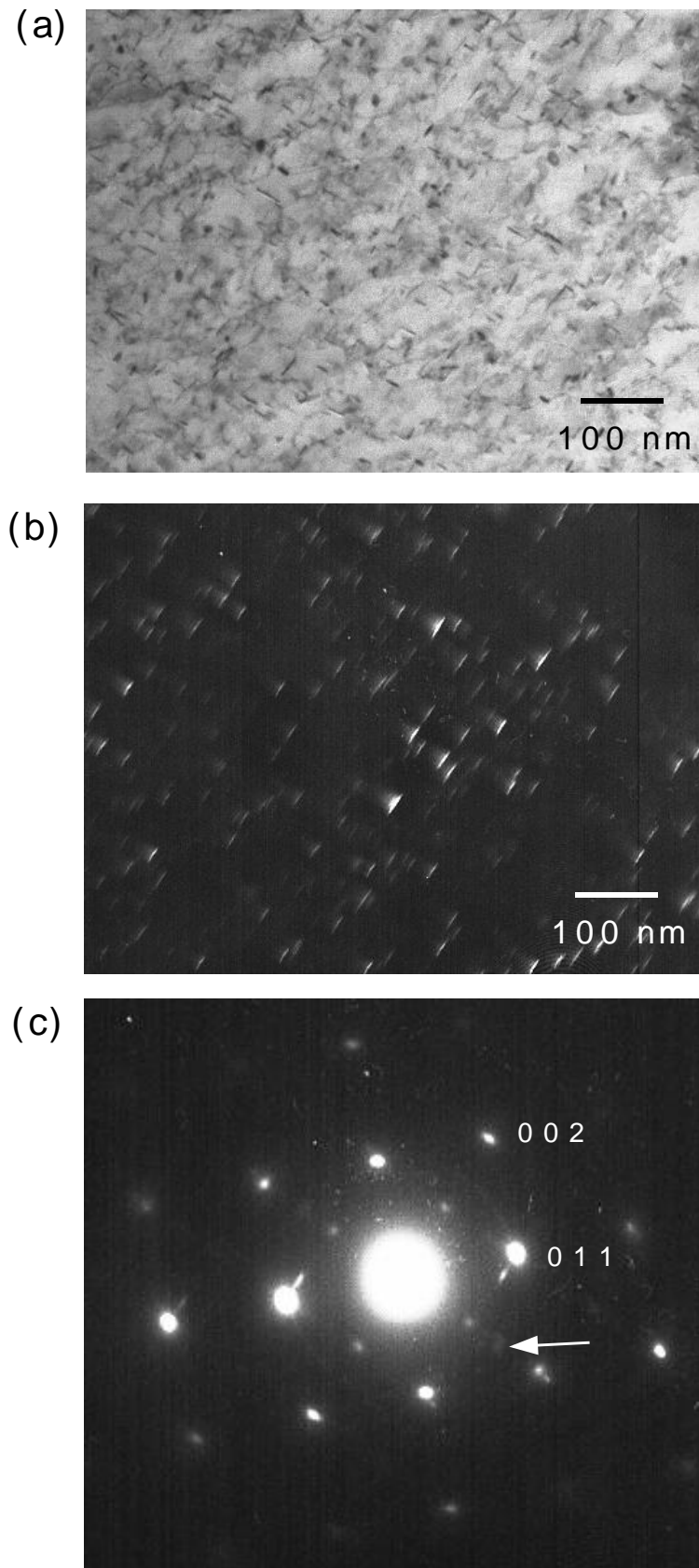


Figure 9.9: TEM observation of a thin-foil from Steel *D* tempered at 600 °C for 10 h. Zone axis is [100] of ferrite matrix. (a) Bright field image. (b) Dark field image using the carbide diffraction spot indicated by the arrow in (c). The 002 and 011 reflections are from the ferrite.

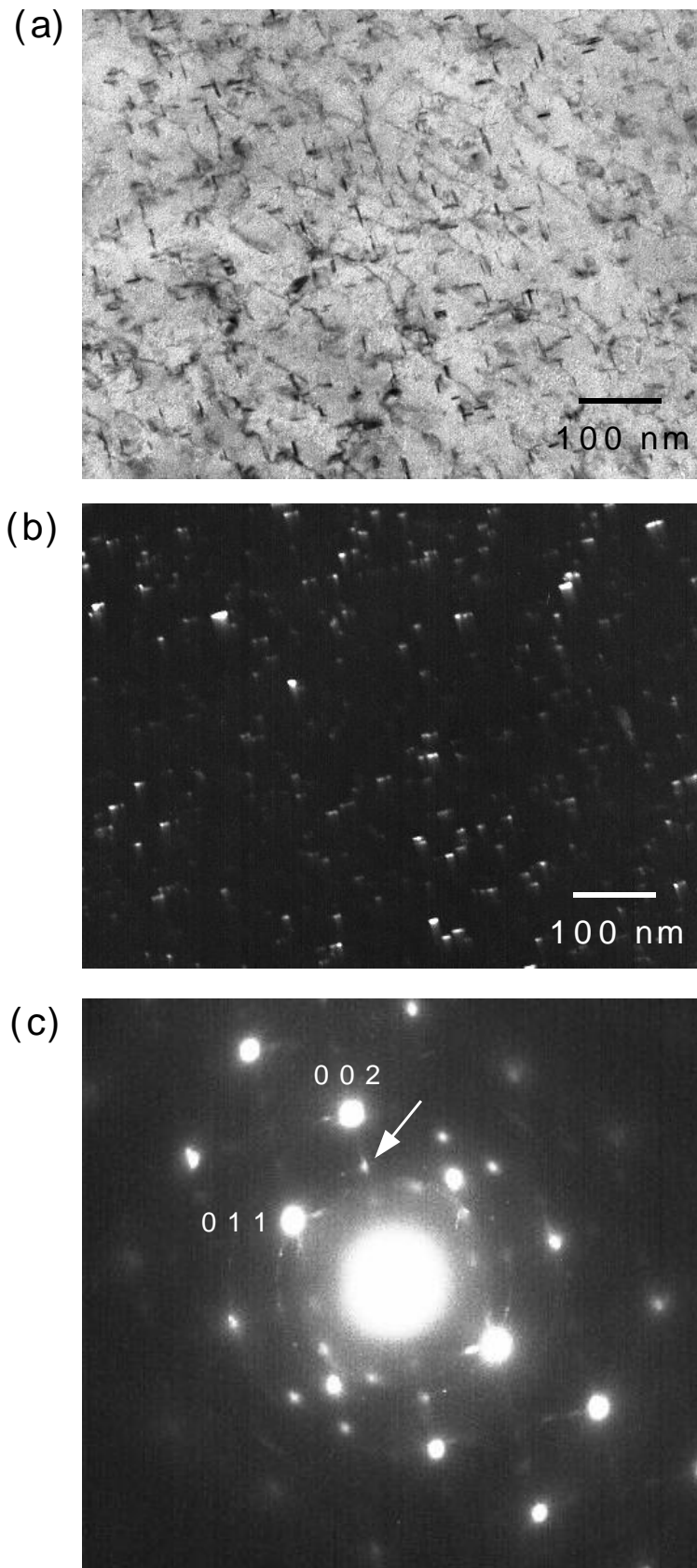


Figure 9.10: TEM observation of a thin-foil from Steel *D* tempered at 600 °C for 20 h. Zone axis is [100] of ferrite matrix. (a) Bright field image. (b) Dark field image using the carbide diffraction spot indicated by the arrow in (c). The 002 and 011 reflections are from the ferrite.

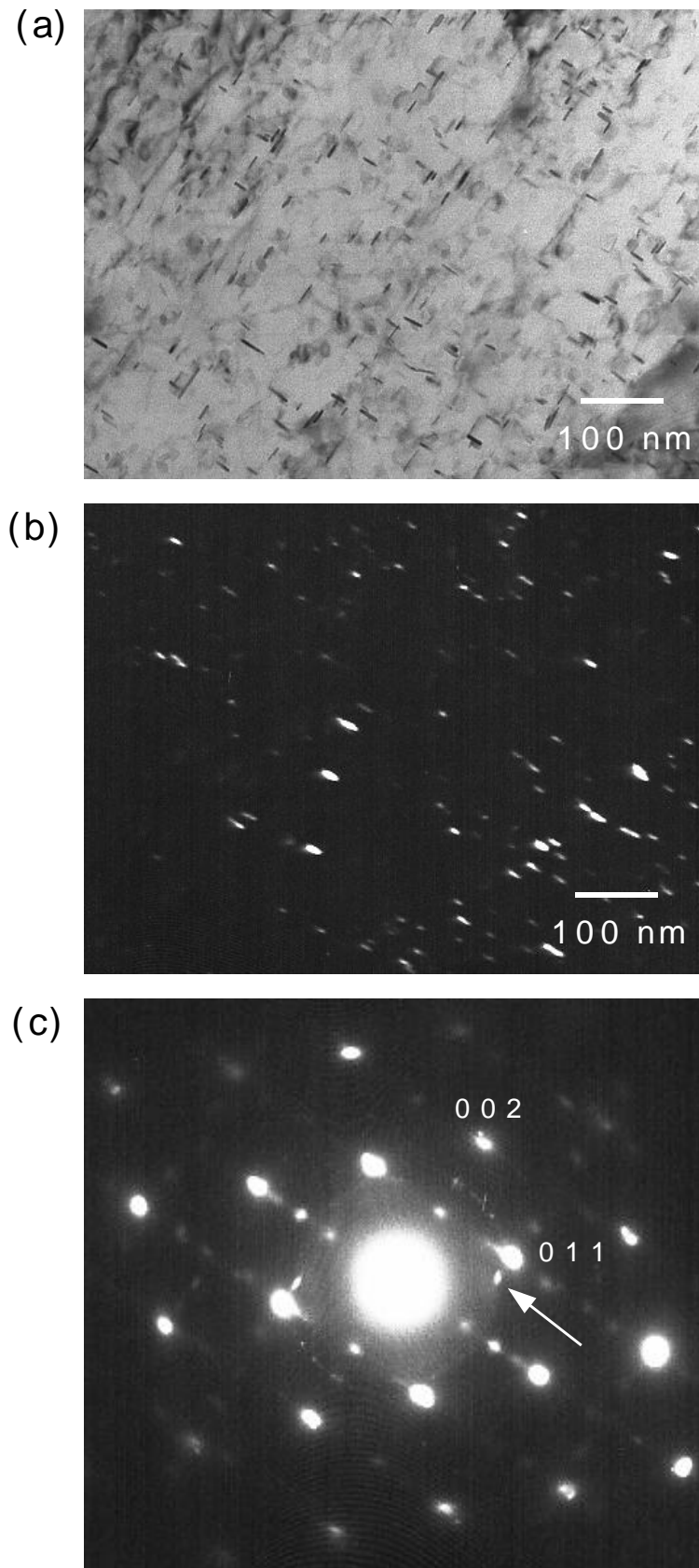


Figure 9.11: TEM observation of a thin-foil from Steel *D* tempered at 600 °C for 30 h. Zone axis is [100] of ferrite matrix. (a) Bright field image. (b) Dark field image using the carbide diffraction spot indicated by the arrow in (c). The 002 and 011 reflections are from the ferrite.

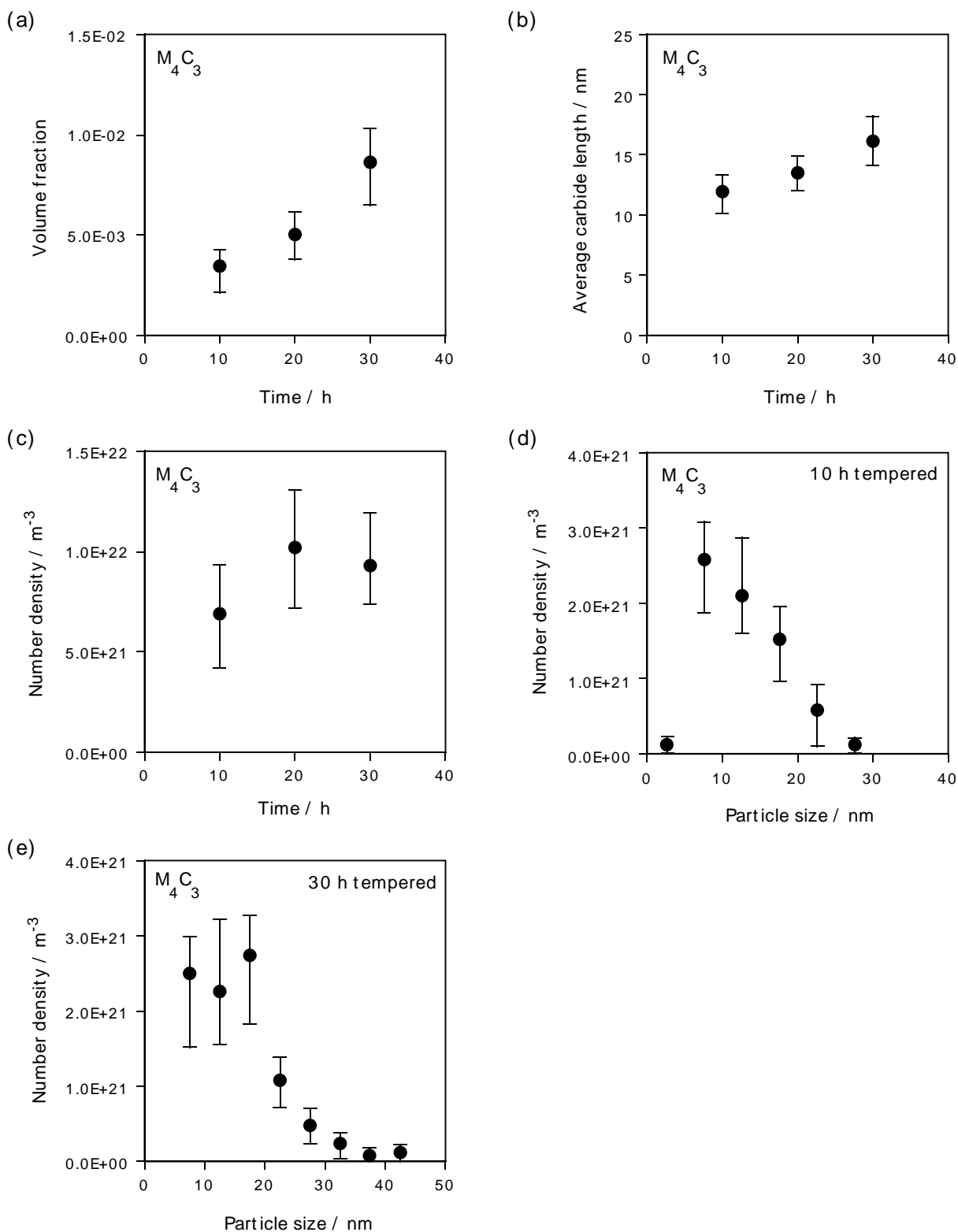


Figure 9.12: Observations of steel *D* tempered at 600 °C. (a) Relationship between the M_4C_3 volume fraction and the tempering time. (b) Relationship between the M_4C_3 length and the tempering time. (c) Relationship between the number density of M_4C_3 particles and the tempering time. (d) Number density distribution of the length of M_4C_3 particles in the steel tempered for 10 h. (e) Number density distribution of the length of M_4C_3 particles tempered for 30 h.

Figures 9.13 - 9.15 show thin-foil TEM images of Steel E tempered for a variety of times. These pictures were taken from the $[100]$ orientation of the matrix. In Fig. 9.13 - 9.15, the needle-like precipitates are the cross-sectioned images of precipitates growing on the $\{001\}_\alpha$ plane, which is parallel to the observation direction. The carbide morphology was characterised from over 500 particles in each sample. Figure 9.16 shows the volume fraction of carbide, carbide length and number density plotted against the tempering time. The number density distribution of the length of M_4C_3 particles is also shown. The solid circles represent the average of data from different locations, and the scatter of the data is indicated by error bars.

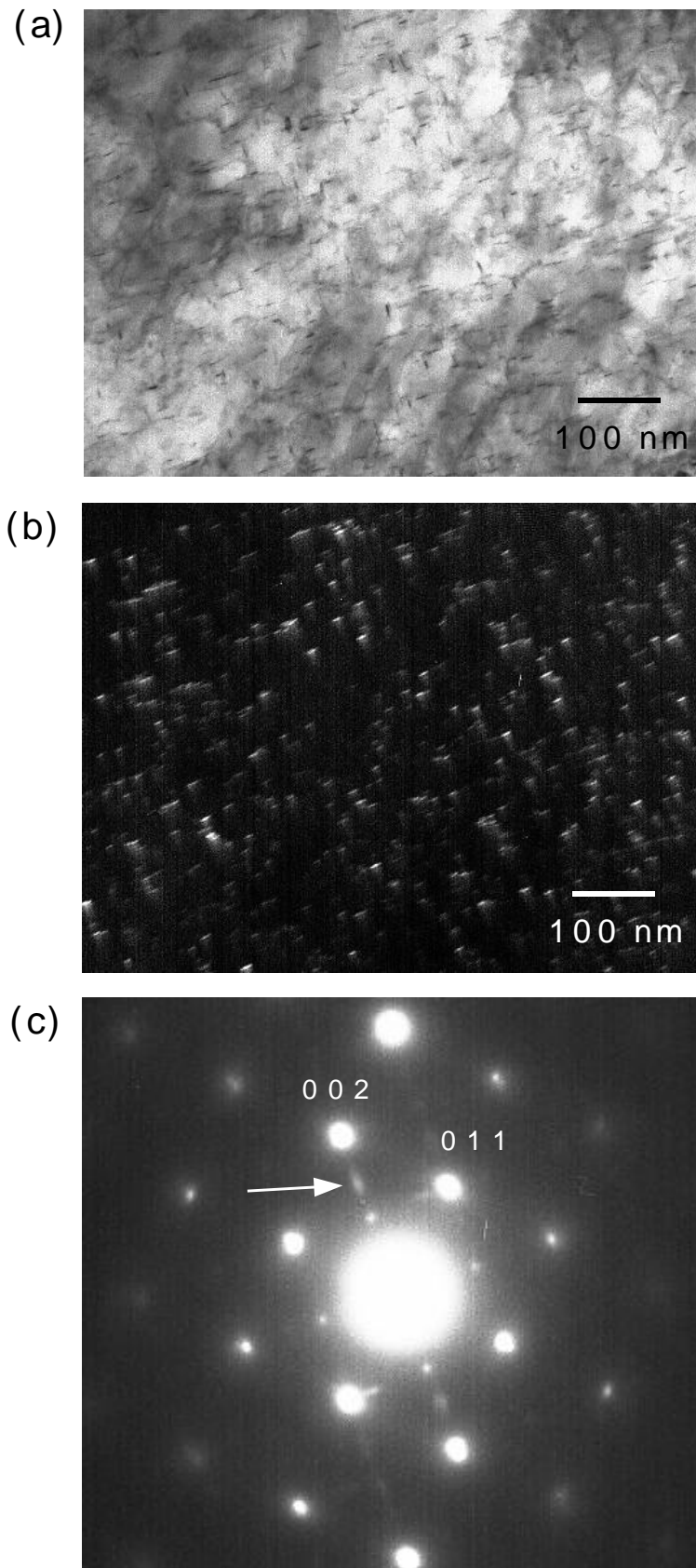


Figure 9.13: TEM observation of a thin-foil from Steel *E* tempered at 600 °C for 10 h. Zone axis is [100] of ferrite matrix. (a) Bright field image. (b) Dark field image using the carbide diffraction spot indicated by the arrow in (c). The 002 and 011 reflections are from the ferrite.

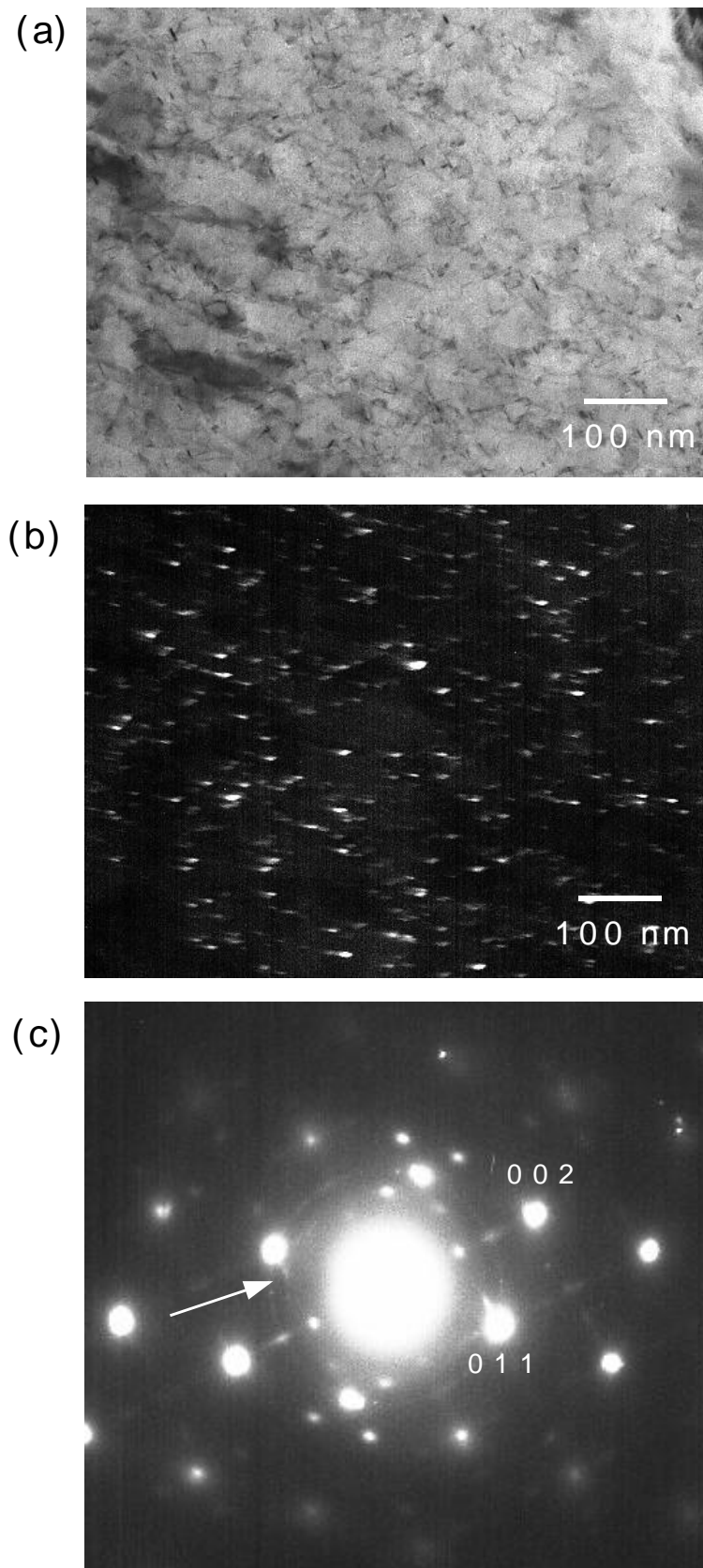


Figure 9.14: TEM observation of a thin-foil from Steel *E* tempered at 600 °C for 20 h. Zone axis is [001] of ferrite matrix. (a) Bright field image. (b) Dark field image using the carbide diffraction spot indicated by the arrow in (c). The 002 and 011 reflections are from the ferrite.

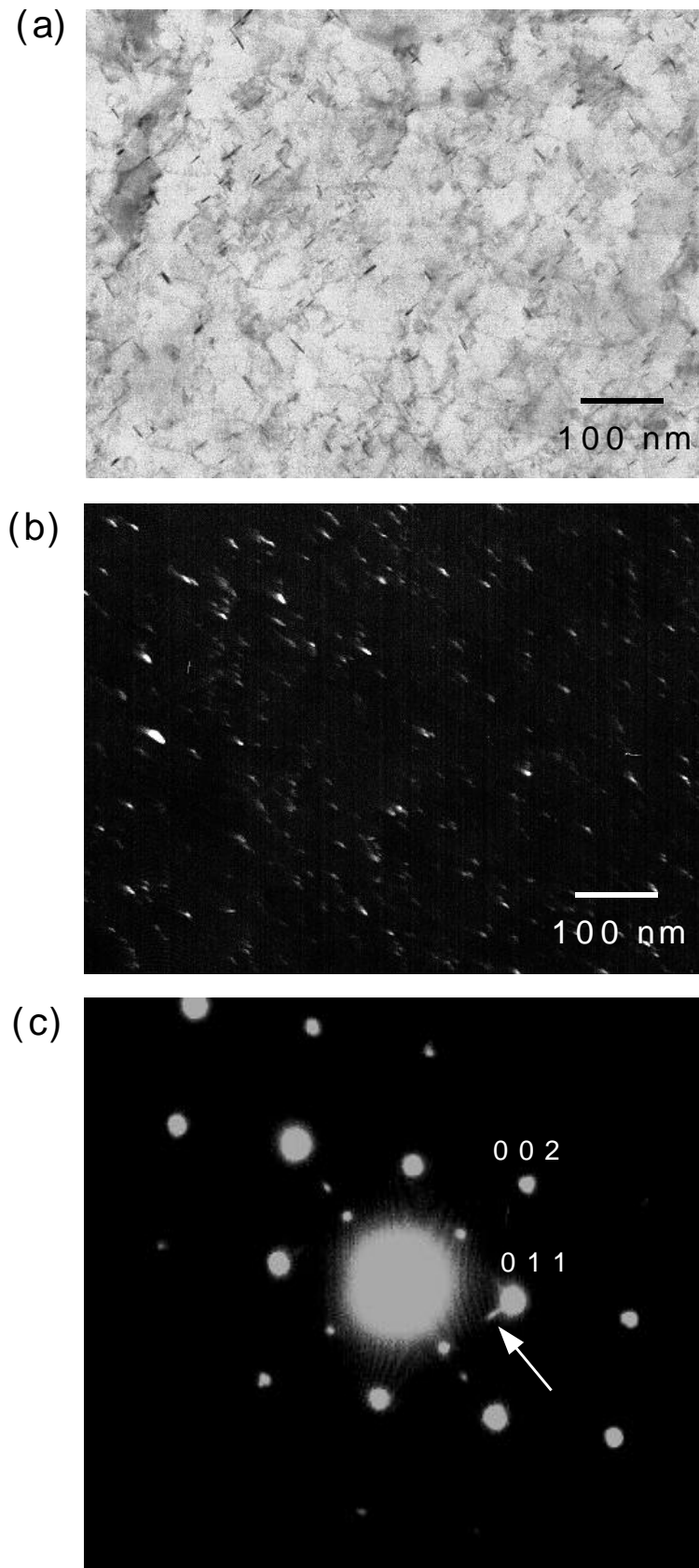


Figure 9.15: TEM observation of a thin-foil from Steel *E* tempered at 600 °C for 30 h. Zone axis is [001] of ferrite matrix. (a) Bright field image. (b) Dark field image using the carbide diffraction spot indicated by the arrow in (c). The 002 and 011 reflections are from the ferrite.

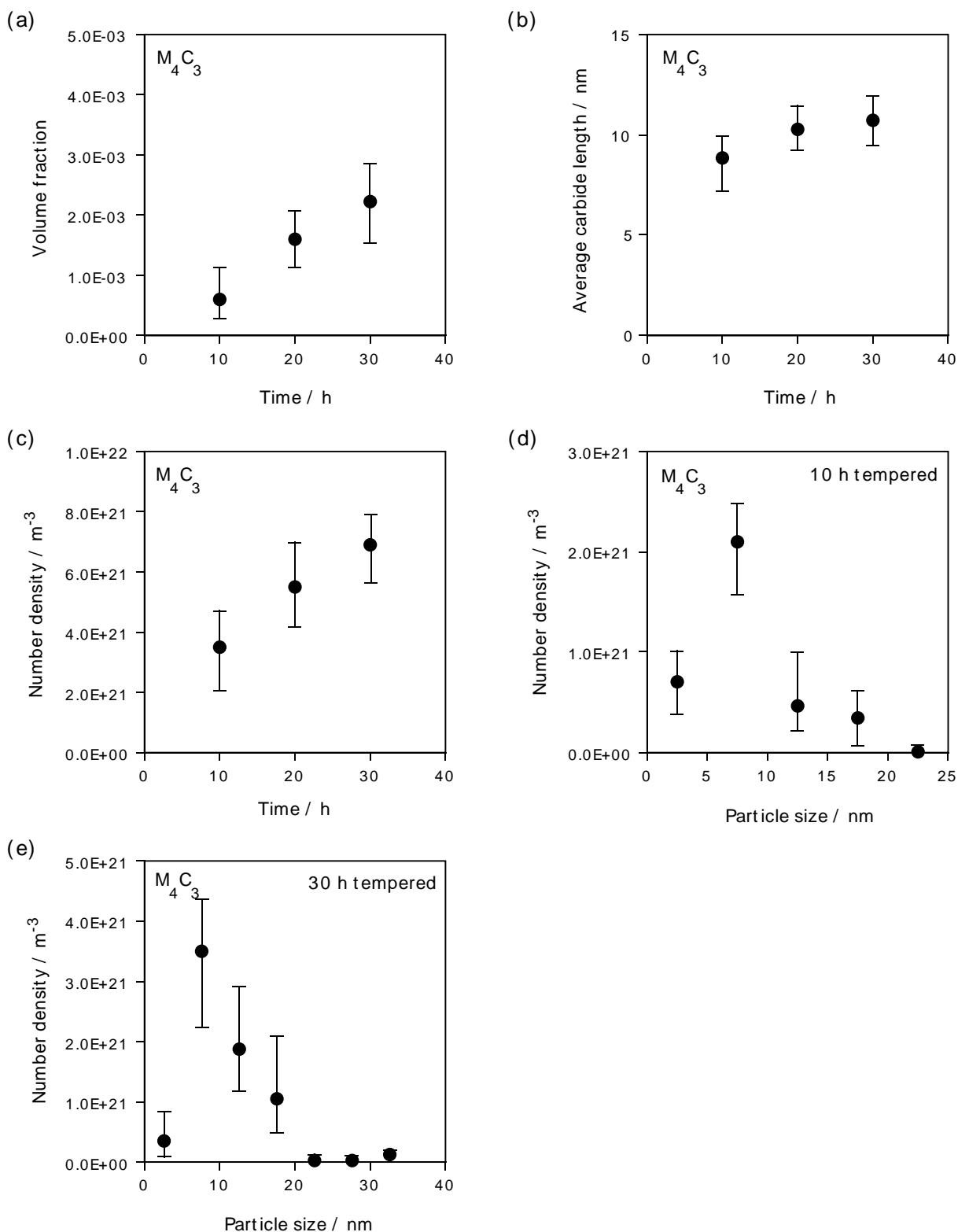


Figure 9.16: Observations of steel *E* tempered at 600 °C. (a) Relationship between the M_4C_3 volume fraction and the tempering time. (b) Relationship between the M_4C_3 length and the tempering time. (c) Relationship between the number density of M_4C_3 particles and the tempering time. (d) Number density distribution of the length of M_4C_3 particles in the steel tempered for 10 h. (e) Number density distribution of the length of M_4C_3 particles tempered for 30 h.

II Chemical compositions of carbides

The chemical compositions of M_4C_3 particles were measured using energy dispersive spectroscopy using carbon replica specimens. The atomic fractions of metallic elements in the carbides are plotted against tempering time for Steel *C* in Fig. 9.17. According to these results, the precipitates are $(V,Mo)_4C_3$, and the Mo/V ratio changes with tempering time. Figure 9.18 shows the Mo/V ratio of M_4C_3 particles in Steels *D* and *E*. XEDS analysis was performed on at least 5 particles for each specimen. The circles represent the average and the error bars show the scatter of data.

III Foil Thickness

The thickness of the thin foil was calculated using thickness fringes at the grain boundaries. The extinction distances for a two-beam condition are known; it is therefore possible to calculate the thickness of the sample by multiplying the extinction distance by the number of fringes. The thicknesses of the samples were in this way found to be between 80 and 160 nm.

9.2 Modelling of plate-shaped carbide growth

9.2.1 Chemical composition and equilibrium phases

Table 9.1 shows the chemical composition of the material under consideration. Using MTDATA, the equilibrium phases and the compositions of the equilibrium carbides for each steel at a variety of temperatures were calculated. In the calculation, cementite, hcp (M_2C), fcc (M_4C_3), M_7C_3 , $M_{23}C_6$ and M_6C were chosen as probable carbides. According to the results for 600 °C, M_4C_3 (fcc) type and M_6C type carbides are stable carbides in these steels. The equilibrium atomic fraction of M_4C_3 according to MTDATA is 0.438C-0.440V-0.104Mo-0.000Mn-0.000Fe-0.017N and M_6C is 0.143C-0.048V-0.500Mo-0.000Mn-0.310Fe-0.000N. However, M_6C was not observed using TEM in the experimental part of the present work. Only cementite and M_4C_3 were therefore considered in the calculations.

9.2.2 Capillarity effect in multicomponent systems

The concept of the capillarity effect for a parabolic cylinder-shaped precipitate has been explained by equations 8.1 - 8.5 in Chapter 8.

The capillarity effect on the interface composition was evaluated by increasing an additional Gibbs energy term in the database of MTDATA. In the case of M_4C_3 (fcc, the lattice parameter $a=4.2$ Å), the atomic volume $\nu^{M_4C_3}$ is 1.06×10^{-29} m³ and interfacial energy σ can be assumed to be 0.2 Jm⁻² [66], and accordingly, the additional Gibbs energy would be 1274 J/mol for $r^{IC} = 10$ Å. The database for the fcc phase (sublattice) was modified to add 1×10^{-6} J mol⁻¹ per 1 Pa pressure increase.

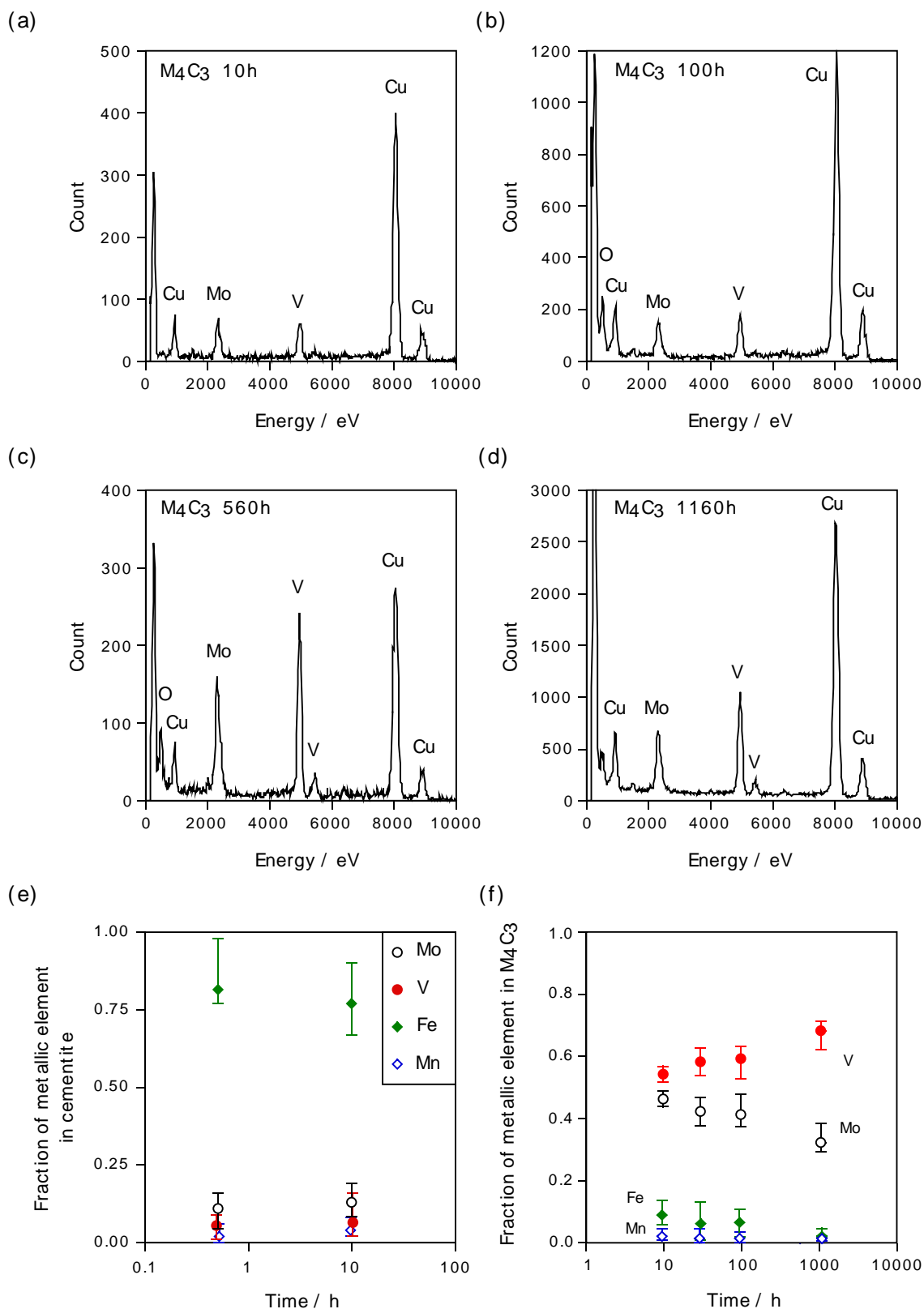


Figure 9.17: XEDS analysis of Steel *C* tempered at 600 °C. X-ray count-energy profile of M_4C_3 tempered for (a) 10 h, (b) 100 h, (c) 560 h and (d) 1150 h. (e) Relationship between atomic fraction of metallic elements in cementite and tempering time, (f) Relationship between atomic fraction of metallic elements in M_4C_3 and tempering time.

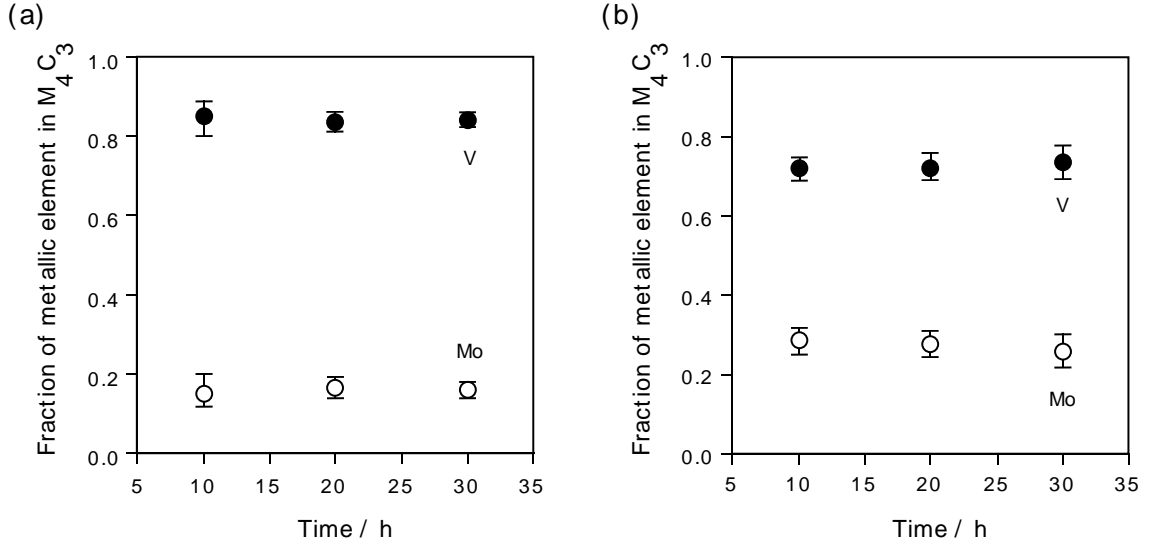


Figure 9.18: XEDS analysis of M_4C_3 particles in (a) Steel *D* and (b) Steel *E* tempered at 600 °C.

9.2.3 Precipitation of the alloy carbide with local equilibrium and capillarity effect

Observations indicated that M_4C_3 carbide grows in the form of plates, which is therefore the shape assumed for the calculations which follow.

M_4C_3 particles precipitate from the matrix after the completion of paraequilibrium cementite precipitation. We assume that they grow with local equilibrium at the interface. The basic concepts of growth with local equilibrium and the capillarity effect have been explained in Chapter 7. However, the circumstances are now more complicated due to the mass-balance of each component at the interface. The Péclet numbers \bar{p} for Mo and V are represented as:

$$\begin{aligned}\bar{p}_{Mo} &= \frac{vr^{IC}}{2D_{Mo}} \\ \bar{p}_V &= \frac{vr^{IC}}{2D_V}\end{aligned}\tag{9.1}$$

where D_{Mo} and D_V are diffusion coefficients of Mo and V respectively in ferrite. v is the growth rate of a particle and r^{IC} is the curvature radius of the tip of a particle. Both v and r^{IC} are unique for a particle. It follows that:

$$\bar{p}_{\text{Mo}} D_{\text{Mo}} = \bar{p}_{\text{V}} D_{\text{V}} \quad (9.2)$$

Trivedi has given an exact solution for the diffusion problem which allows the composition to vary along the interface of a plate but assumes that the shape remains that of a parabolic cylinder [77]. However, Trivedi's solution is limited to large values of supersaturation, as presented in Chapter 8 [115]. Instead of Trivedi's theory which allows the composition to vary along the interface of a plane, an alternative approach due to Bolling and Tiller [112] was therefore adopted. Their method retains the parabolic shape with an assumed constant concentration at the interface appropriate to the tip radius. This means that if the interface effect can be neglected, the Péclet numbers \bar{p}_{Mo} and \bar{p}_{V} must satisfy the following relations simultaneously [113]:

$$\Omega_{\text{Mo}} = \sqrt{\pi \bar{p}_{\text{Mo}}} \exp(\bar{p}_{\text{Mo}}) \text{erfc}(\sqrt{\bar{p}_{\text{Mo}}}) \times \left(1 + \frac{r_c}{r^{IC}} \frac{\Omega_{\text{Mo}}}{\sqrt{\pi \bar{p}_{\text{Mo}}} \exp(\bar{p}_{\text{Mo}}) \text{erfc}(\sqrt{\bar{p}_{\text{Mo}}})} \right) \quad (9.3)$$

$$\Omega_{\text{V}} = \sqrt{\pi \bar{p}_{\text{V}}} \exp(\bar{p}_{\text{V}}) \text{erfc}(\sqrt{\bar{p}_{\text{V}}}) \times \left(1 + \frac{r_c}{r^{IC}} \frac{\Omega_{\text{V}}}{\sqrt{\pi \bar{p}_{\text{V}}} \exp(\bar{p}_{\text{V}}) \text{erfc}(\sqrt{\bar{p}_{\text{V}}})} \right) \quad (9.4)$$

where Ω_{Mo} is the supersaturation of Mo, Ω_{V} is the supersaturation of V and r_c is the critical tip radius at which growth ceases.

With local equilibrium [79] in a multicomponent system, $c_{\text{C}}^{\alpha\beta}$, the carbon concentration of ferrite at the ferrite/carbide interface can be approximated to that of the matrix. Figure 9.19 shows a schematic diagram of the matrix composition b from which M_4C_3 particles precipitate, interfacial ferrite composition c and M_4C_3 composition f which is in equilibrium with ferrite whose composition is the point c . The point a represents the alloy composition from which paraequilibrium cementite precipitates. The points e and d are the ends of the tie-line which passes through b and denote respectively the composition of ferrite which is in equilibrium with carbide, and the corresponding composition of carbide. Since it is assumed that $D_{\text{Mo}} \ll D_{\text{C}}$ and $D_{\text{V}} \ll D_{\text{C}}$, the ferrite composition at the interface should be on the ferrite solubility curve (blue curve on the plane B) which is the intersection between the α/α +carbide interface (curved plane A) and the constant carbon concentration plane B which passes through the point b .

For a given value of r^{IC} , the ferrite solubility curve on the plane B is decided uniquely. The point c can be any point on the ferrite solubility curve. The point f is another end of the tie-line passing through the point c and represents the carbide composition. There is an unlimited choice of tie-lines, but only one tie-line can satisfy equations 9.3 and 9.4 simultaneously. The values of \bar{p}_{Mo} and \bar{p}_{V} which satisfy equation 9.2 can be therefore decided for a given value of r^{IC} . The corresponding growth rate v can be obtained from equation 9.1. Since v depends on r^{IC} , the maximum growth rate v_{max} can be obtained by calculating the growth rate v for each value of r^{IC} , as shown in Fig. 9.20.

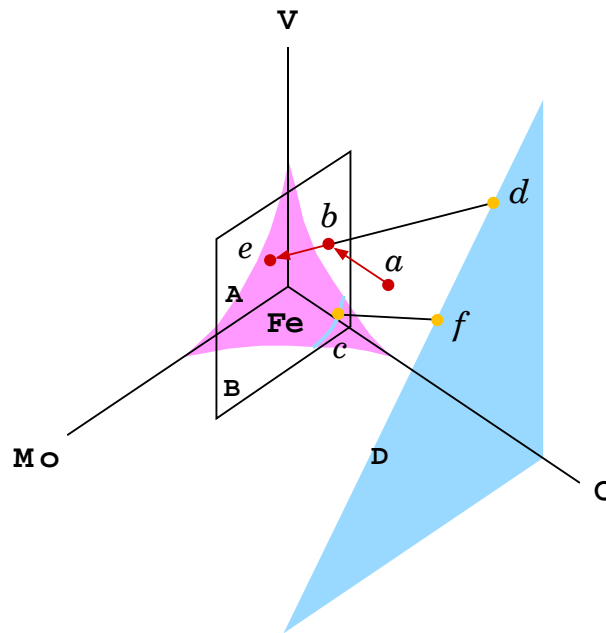


Figure 9.19: Schematic drawing of the tie-line in the Fe-C-Mo-V system. The plane *A* is the ferrite solubility plane which is the interface between the ferrite phase field and ferrite + carbide two-phase field. The plane *B* passing through the point *b* is iso-carbon concentration plane. The points on the plane *D* represent the carbide concentration. The point *c* can be any point on the intersection (shown as the blue curve) between the plane *A* and plane *B*. However, only one point can satisfy equation 9.3 and 9.4 simultaneously.

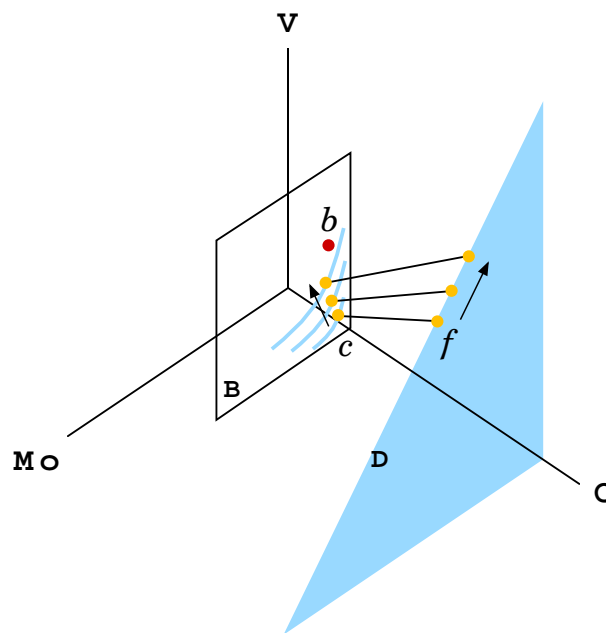


Figure 9.20: Schematic drawing for tie-line shifting due to the capillarity effect in Fe-C-Mo-V system. The ferrite solubility curves (shown as the blue curves) on the iso-carbon plane *B* depend on the tip radius r^{IC} of a particle.

Figure 9.21 shows an example of the growth rates concerning Mo diffusion and V diffusion in the case in which the chemical composition of the matrix from which M_4C_3 precipitates is 0.0002C-0.9Mo-0.6V (at. %). These curves are almost identical, and thus the growth rate could be obtained uniquely. The rate reaches a peak at intermediate tip radius. If the Zener's maximum growth rate hypothesis can be adopted, the growth rate and the tip radius of a particle can therefore be obtained uniquely for a given matrix composition.

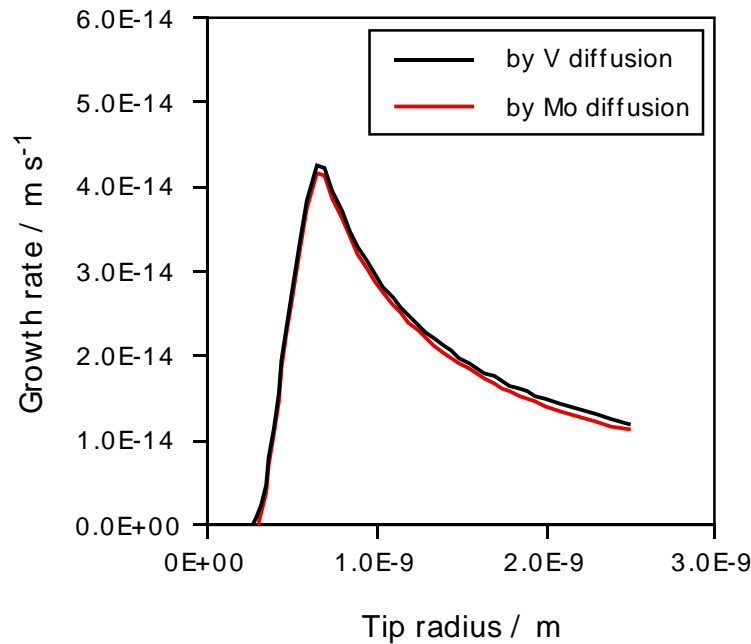


Figure 9.21: Relationship between the tip radius of a particle r^{IC} and its growth rate. The chemical composition of the matrix (point b in Fig. 9.19) is $\bar{c}_{Mo} = 0.9$ at. %, $\bar{c}_V = 0.6$ at. % and $\bar{c}_C = 0.0002$ at. %.

9.2.4 Overall transformation kinetics

The carbide reaction during tempering in Fe-C-Mo-V steel was simulated. This includes the precipitation of M_4C_3 and the enrichment and dissolution of cementite.

I Enrichment and dissolution of cementite

The rates of enrichment of molybdenum and vanadium are given approximately by equations 7.9 and 8.9 respectively.

It is assumed that cementite dissolves in the manner described by Robson and Bhadeshia [94]. However, they treated ternary systems. An assumption has therefore been adopted for this work, that the concentration gradient of the slowest diffuser dominates the dissolution

of cementite in quaternary systems. In Fe-C-Mo-V systems, molybdenum is the slowest diffuser; the dissolution rate is therefore represented by equation 7.10, where \bar{d} is the mean diffusion distance between θ and M_4C_3 precipitates, given by:

$$\bar{d} = (N^\theta + N^{M_4C_3})^{-\frac{1}{3}} \quad (9.5)$$

where N^θ and $N^{M_4C_3}$ are the number densities of θ and M_4C_3 particles respectively.

II Nucleation of M_4C_3

The nucleation rate and the activation energy for nucleation are represented by equations 7.12 and 7.13, respectively. The chemical free energy change per unit volume of nuclei ΔG_V is calculated as $-2.440 \times 10^9 \text{ J m}^{-3}$. This value is for the beginning of precipitation of M_4C_3 and it will decrease as the precipitation proceeds. The change of the value of ΔG_V is calculated corresponding to the progress of the precipitation reaction using a mean field approximation, i.e. assuming that the solute is uniformly distributed in the matrix.

III Diffusion-controlled growth with capillarity effect

Modelling of the local equilibrium of M_4C_3 precipitation is based on Coates' diffusion-controlled growth theory [79] accounting for the capillarity effect. The critical radius of curvature r_c at which growth ceases was calculated using MTDATA, with a modification to the database of the fcc phase to include a pressure change. The growth rate of particles is the maximum rate, for given values of the carbon concentration in the matrix and the supersaturation Ω of V and Mo. The growth rate obtained from the values of p_V , p_{Mo} and the ratio r^{IC}/r_c corresponding to the maximum growth rate satisfies equation 9.3 and 9.4, as shown in section 9.2.3.

IV Ostwald ripening of particles

The combination of nucleation and growth gives rise to a distribution of M_4C_3 lengths, but for a given supersaturation, they all have the same tip radius. An approximate treatment, in which a M_4C_3 particle is modelled to be a plate of which the periphery is hemicylindrical, was therefore adopted for the Ostwald ripening stage, after the completion of precipitation. The growth (or dissolution) rate can be calculated using Zener's theory as:

$$v \simeq -\frac{D_M}{\bar{d}} \frac{c_M^{M_4C_3\alpha} - c_{M,r}^{\alpha M_4C_3}}{\bar{c}_M - c_{M,r}^{\alpha M_4C_3}} \quad (9.6)$$

where $c_{M,r}^{\alpha M_4C_3}$ is the equilibrium mole fraction of solute M in ferrite at the hemicylindrical tip of a M_4C_3 particle and \bar{d} is the mean diffusion distance between particles which can be represented as [94]:

$$\bar{d} = (N^\beta)^{-\frac{1}{3}} \quad (9.7)$$

where N^β is the number density of M_4C_3 particles.

Modelling of Ostwald ripening in a quaternary system still presents the same difficulty as that of precipitation and growth process: satisfaction of the mass-balance of Mo and V. However, adopting Zener's maximum growth rate hypothesis and using the same approach described in Figures 9.19 and 9.20, we can obtain unique growth or dissolution rates for each size of M_4C_3 particle.

During Ostwald ripening, particles in which the interfacial energy is orientation-independent should become spheroidised to reduce the surface area. However, the observations indicate that after the completion of the precipitation of M_4C_3 , the aspect ratio of M_4C_3 particles within the grains did not change greatly. These particles were found to grow whilst keeping the plate shape, as shown in Figures 9.1 - 9.6. It is therefore assumed that the shape of particles was preserved during Ostwald ripening, as shown in Fig. 9.22.

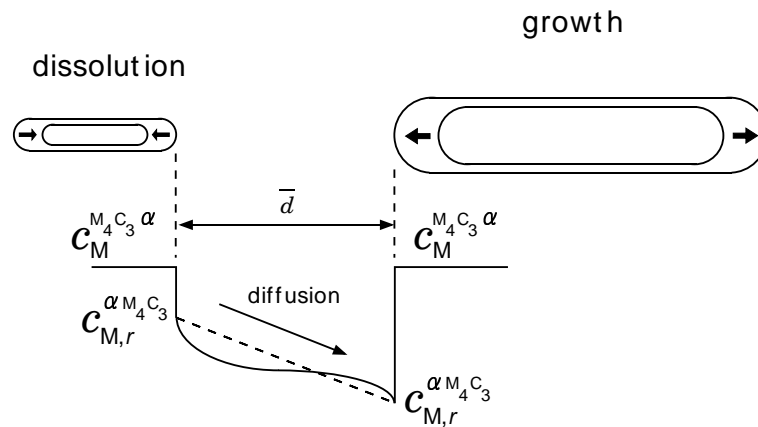


Figure 9.22: Schematic drawing of Ostwald ripening of plate-shaped particles. The aspect ratio of each particle is fixed to be 6.

9.2.5 Inputs and calculations

For the precipitation and growth stages, the calculations were performed in steps of 50 s. In each step, the following quantities were calculated: the nucleation rate, nucleus size (which is the initial size of particle growth), the growth rate and the mole fraction change of Mo, V and C in the matrix. This last corresponds to the growth of M_4C_3 and the enrichment and dissolution of cementite. The consumption of nucleation sites during the transformation is accounted for in each step. Once the mole fractions of Mo, V and C in the matrix (\bar{c}_{Mo} , \bar{c}_V and \bar{c}_C) have been determined, the corresponding supersaturation of Mo and V (Ω_{Mo} and Ω_V) and the critical radius r_c can be obtained. Using Ω_{Mo} , Ω_V and r_c , the value of

Parameter	Steel <i>C</i>	Steel <i>D</i>	Steel <i>E</i>
Shape	plate	plate	plate
Tempering temperature / °C	600	600	600
Surface energy of M_4C_3 / $J\ m^{-2}$	0.2	0.2	0.2
Driving force for nucleation / $J\ m^{-3}$	-2.440×10^9	-2.430×10^9	-2.140×10^9
Nucleation site density / m^{-3}	1.48×10^{22}	1.48×10^{22}	1.48×10^{22}
Maximum volume fraction of cementite	1.796×10^{-2}	1.796×10^{-2}	1.796×10^{-2}
Maximum volume fraction of M_4C_3	9.73×10^{-3}	9.73×10^{-3}	9.53×10^{-3}
$c_V^{\alpha\theta}$ / atomic fraction	4.491×10^{-3}	4.360×10^{-3}	2.146×10^{-3}
$c_{Mo}^{\alpha\theta}$ / atomic fraction	8.905×10^{-3}	2.227×10^{-3}	2.205×10^{-3}
$c_V^{\theta\alpha}$ / atomic fraction	1.009×10^{-1}	1.035×10^{-1}	6.425×10^{-2}
$c_{Mo}^{\theta\alpha}$ / atomic fraction	2.907×10^{-2}	7.420×10^{-3}	8.643×10^{-3}
$c_V^{\alpha M_4C_3}$ / atomic fraction	1.845×10^{-3}	1.289×10^{-3}	2.900×10^{-5}
$c_{Mo}^{\alpha M_4C_3}$ / atomic fraction	8.174×10^{-3}	1.785×10^{-3}	6.567×10^{-4}
$c_V^{M_4C_3\alpha}$ / atomic fraction	4.313×10^{-1}	4.826×10^{-1}	3.411×10^{-1}
$c_{Mo}^{M_4C_3\alpha}$ / atomic fraction	1.152×10^{-1}	5.527×10^{-2}	1.754×10^{-1}
Thickness of cementite in grains / m	2.0×10^{-8}	2.0×10^{-8}	2.0×10^{-8}
Thickness of cementite on grain boundaries / m	5.0×10^{-8}	5.0×10^{-8}	5.0×10^{-8}
Diffusion constant of V D_V / $m^2\ s^{-1}$	3.05×10^{-4}	3.05×10^{-4}	3.05×10^{-4}
Diffusion constant of V D_{Mo} / $m^2\ s^{-1}$	2.29×10^{-4}	2.29×10^{-4}	2.29×10^{-4}
Activation energy for V diffusion Q_V / $J\ mol^{-1}$	2.39×10^5	2.39×10^5	2.39×10^5
Activation energy for Mo diffusion Q_{Mo} / $J\ mol^{-1}$	2.39×10^5	2.39×10^5	2.39×10^5

Table 9.2: Calculation parameters for precipitation of carbides in Steel *C*, *D* and *E*.

p_{Mo} and p_V satisfying equation 9.3 and 9.4, and, finally, the maximum growth rate and the corresponding tip radius of a M_4C_3 particle r^{IC} can be determined. The volume of each particle was calculated as a parabolic cylinder.

After the completion of the precipitation and growth stage, each M_4C_3 particle was modelled as a plate of which the periphery is hemicylindrical for the Ostwald ripening stage. In this stage, the values of $c_{Mo,r}^{\alpha M_4C_3}$ and $c_{V,r}^{\alpha M_4C_3}$ at the tip of each plate-shaped particle were calculated, and then the growth (or dissolution) rate at the tip was calculated.

The calculation parameters for precipitation and dissolution of carbides in Steels *C*, *D* and *E* are listed in Table 9.2. The nucleation site density and the surface energy were obtained by fitting. The diffusion constant and the activation energy for diffusion of Mo and V were obtained from the literature [110, 114].

9.3 Results and discussion

Figure 9.23 shows comparisons between the calculations and the observations of Steel *C*.

After the completion of paraequilibrium cementite precipitation, the concentration of

carbon in the matrix is quite low (0.027 at. %, according to MTDATA). Carbon atoms, which are necessary for the precipitation of M_4C_3 , are provided by the dissolution of cementite. Figure 9.23 (a) shows such simultaneous M_4C_3 precipitation and cementite dissolution behaviour.

The average length of M_4C_3 particles increases during the precipitation and growth states. During the Ostwald ripening stage, the aspect ratio of the particles was fixed by the assumptions made in the calculations. The growth rate (or dissolving rate) of each particle was calculated using the tip radius at the edges of the plate. On average, the length increases during Ostwald ripening as shown in Fig. 9.23 (b).

The number density of M_4C_3 particles whose length was over 4 nm was calculated in Fig. 9.23 (c) for comparison with observation; M_4C_3 particles of size less than 4 nm could not easily be observed using conventional transmission electron microscopy.

The calculated and observed chemical compositions of M_4C_3 particles for several tempering times are shown in Fig. 9.23 (d). To satisfy the mass-balance between Mo and V, a change in the carbide composition is predicted.

The growth rates of M_4C_3 particles by diffusion of Mo and V atoms must be identical since the interface must be unique. Figure 9.24 shows the relationship between the calculated growth rates determined by diffusion of Mo and V. They are almost identical and it is therefore considered that the mass-balance of Mo and V at the interface was satisfied in the present model.

The calculations in general agree well with the observations. However, there are discrepancies between calculations and observations for the chemical composition of M_4C_3 particles. The reasons will be discussed.

According to the calculation using MTDATA, the fraction of Mo amongst metallic elements in equilibrium M_4C_3 should be 0.21 in Steel *C*. However, Steel *C* contains a larger amount of Mo than V. The Mo mole fraction at the interface $c_{Mo}^{M_4C_3\alpha}$ should therefore be higher than the equilibrium mole fraction to keep pace with V diffusion during growth. The calculated chemical compositions attains the equilibrium composition at the end of the growth stage, as shown in Fig. 9.23 (d). During the Ostwald ripening stage which follows the growth stage, the chemical composition of M_4C_3 is close to equilibrium as shown in Fig. 9.23 (d). However, observations show that the composition of M_4C_3 is not the equilibrium composition at a tempering time of 100 h, at which stage growth is complete. Equilibrium is reached during the Ostwald ripening stage. In the calculation, the diffusion of molybdenum and vanadium atoms in M_4C_3 is ignored; the chemical composition of M_4C_3 particles is assumed to be identical to the interface composition. It is considered that the discrepancies between calculation and experiment are caused by the neglect of the diffusion within M_4C_3 particles in the calculations.

For the precipitation and growth stage, Trivedi's theory for the growth of the plate-shaped particles was not adopted, since it causes difficulties because of the large value of

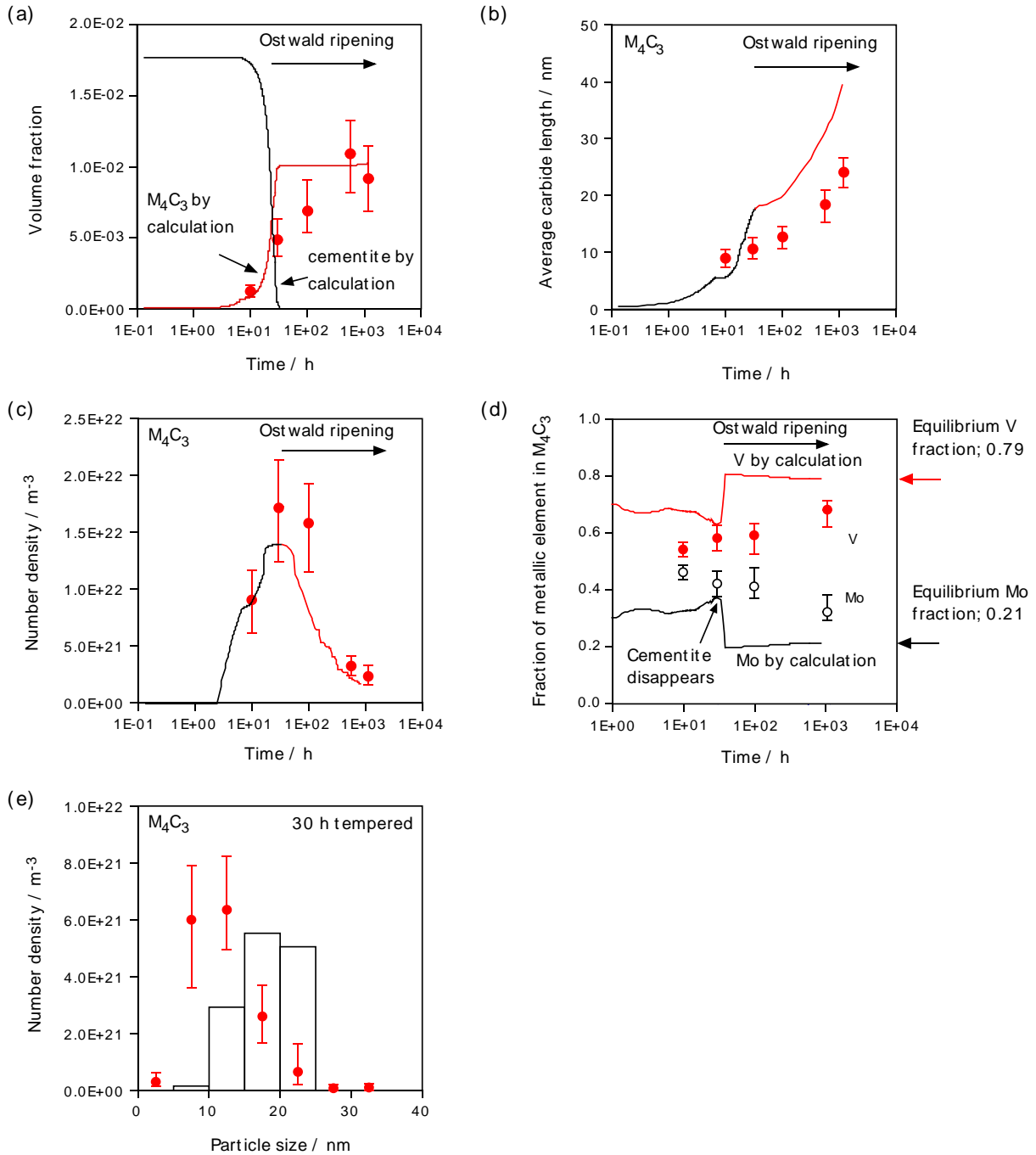


Figure 9.23: Comparisons between calculations and observations of Steel C. (a) Relationship between volume fraction of M_4C_3 particles and tempering time. (b) Relationship between average length of M_4C_3 particles and tempering time. (c) Relationship between number density of M_4C_3 particles whose size is over 4 nm and tempering time. (d) Relationship between chemical composition of M_4C_3 particles and tempering time. (e) Number density distribution of the length of M_4C_3 particles for 30 h tempered steel.

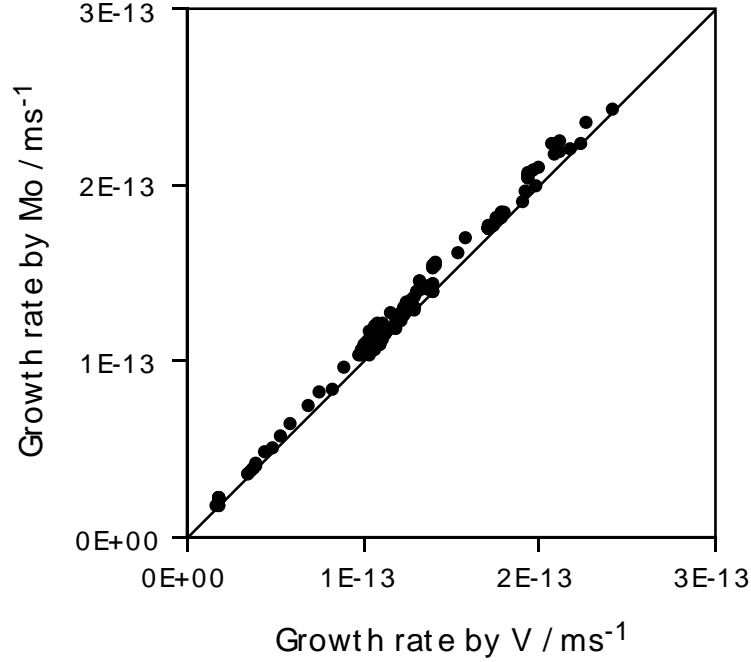


Figure 9.24: Comparisons between the calculated growth rate by diffusion of Mo atoms and V atoms.

r^{IC}/r_c for a small supersaturation. Instead of Trivedi's theory, which allows the composition to vary along the interface of a plate, the composition was assumed to be constant at the interface in the present model, as presented in the Chapter 8.

For the Ostwald ripening stage, M_4C_3 particles were modelled as plates with hemicylindrical ends. According to the classical theory of Ostwald ripening, in which the precipitates are modelled as spheres, the following equation is obtained [83, 84]:

$$N^{M_4C_3} = N_0^{M_4C_3} \frac{r_0^3}{r_0^3 + \frac{8\sigma\nu^\beta D_X c_X^{\alpha\beta}}{9kT} t} \quad (9.8)$$

where $N_0^{M_4C_3}$ is the initial number density of M_4C_3 particles when Ostwald ripening stage starts and r_0 is the initial average particle radius, t is time, and D_X is the diffusion coefficient of element X in the matrix.

Figure 9.25 shows comparisons of the transient of $N^{M_4C_3}$ during Ostwald ripening calculated using the classical theory (equation 9.8) for the diffusion of Mo and V, and using the present model, with the particles modelled as plates and as spheres. The calculation in which M_4C_3 is modelled as plates is the same as that for the Ostwald ripening stage in Fig. 9.23 (c). The calculations using the plate and spherical morphology give similar results,

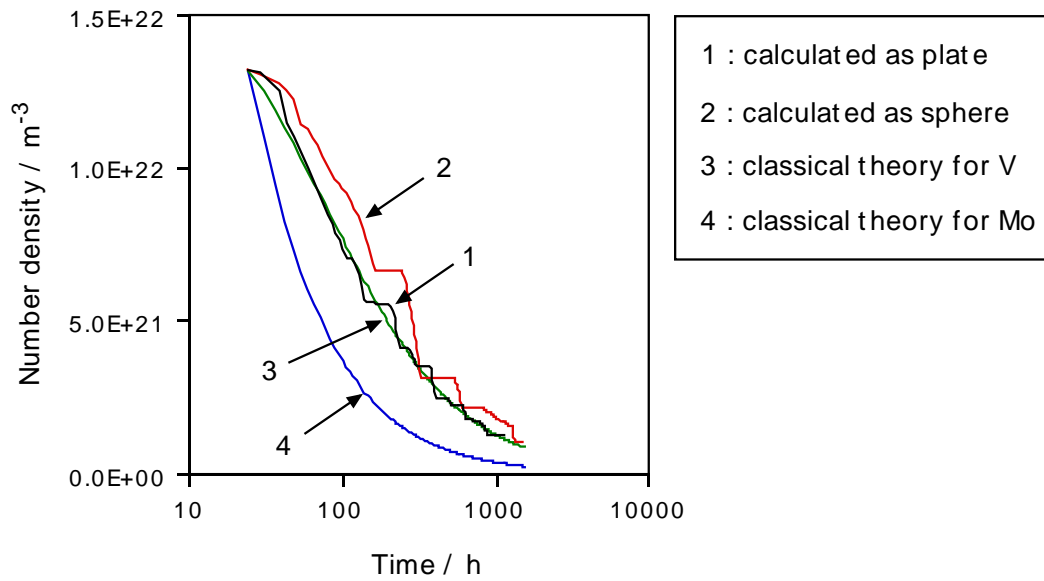


Figure 9.25: Comparisons of the number density of M_4C_3 particles calculated as plate-shaped, spherical and by equation 9.8.

and show a very similar tendency to the result from equation 9.8 for the diffusion of V atoms. However, the corresponding result for molybdenum diffusion deviates from the others. It is therefore difficult to predict the Ostwald ripening behaviour using equation 9.8 in quaternary systems.

Figures 9.26 and 9.27 show comparisons of calculations using present model for plate-shaped particles and observations for Steel *D* and *E*. The calculations in general agree well with the observations. According to the calculations, the growth rate of M_4C_3 in Steel *E* is smaller than those in Steels *C* and *D*. It is considered that the reason for this is that in Steel *E*, which contains 0.30 wt. % vanadium which is the primary metallic element in M_4C_3 , the supersaturation of V (Ω_V) for M_4C_3 is smaller than those in Steels *C* and *D*, which contain 0.56 wt. % vanadium. For example, Fig. 9.28 shows the relationship between the values of supersaturation and Péclet number which satisfy equation 9.4 for $r^{IC}/r_c = 3$. The Péclet number, which is proportional to the growth rate for a fixed tip radius r^{IC} , increases with the supersaturation. It is therefore considered that because of the relatively low supersaturation of V in Steel *E*, the growth rate of M_4C_3 particles is smaller. This tendency was verified by observations; comparing Figures 9.12 and 9.16, the average particle length is smaller in Steel *E* than Steel *D*.

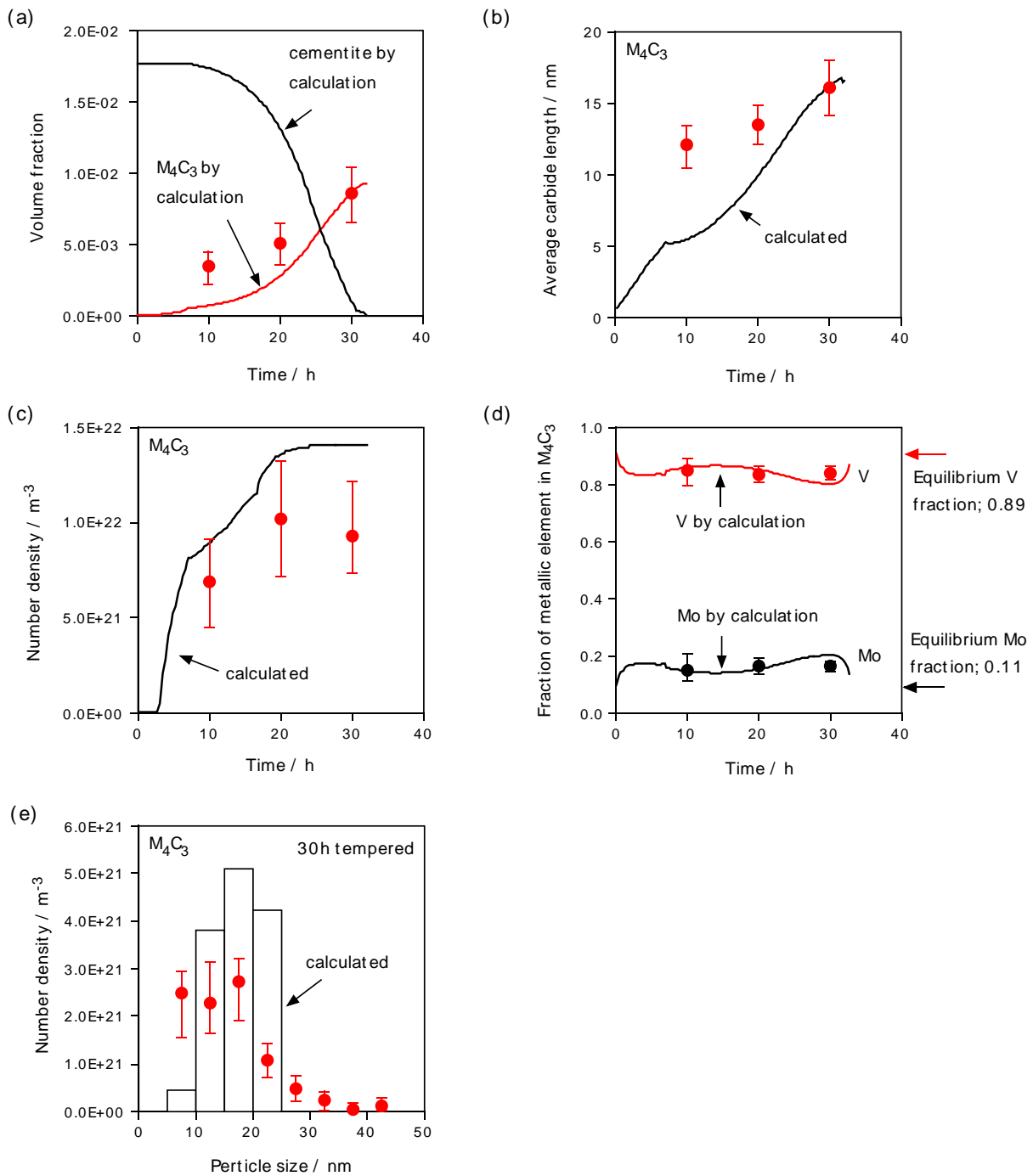


Figure 9.26: Comparisons between calculations and observations for Steel *D*. (a) Relationship between volume fraction of M_4C_3 particles and tempering time. (b) Relationship between average length of M_4C_3 particles and tempering time. (c) Relationship between number density of M_4C_3 particles whose size are over 4 nm and tempering time. (d) Relationship between chemical composition of M_4C_3 particles and tempering time. (e) Number density distribution of the length of M_4C_3 particles for 30 h tempered steel.

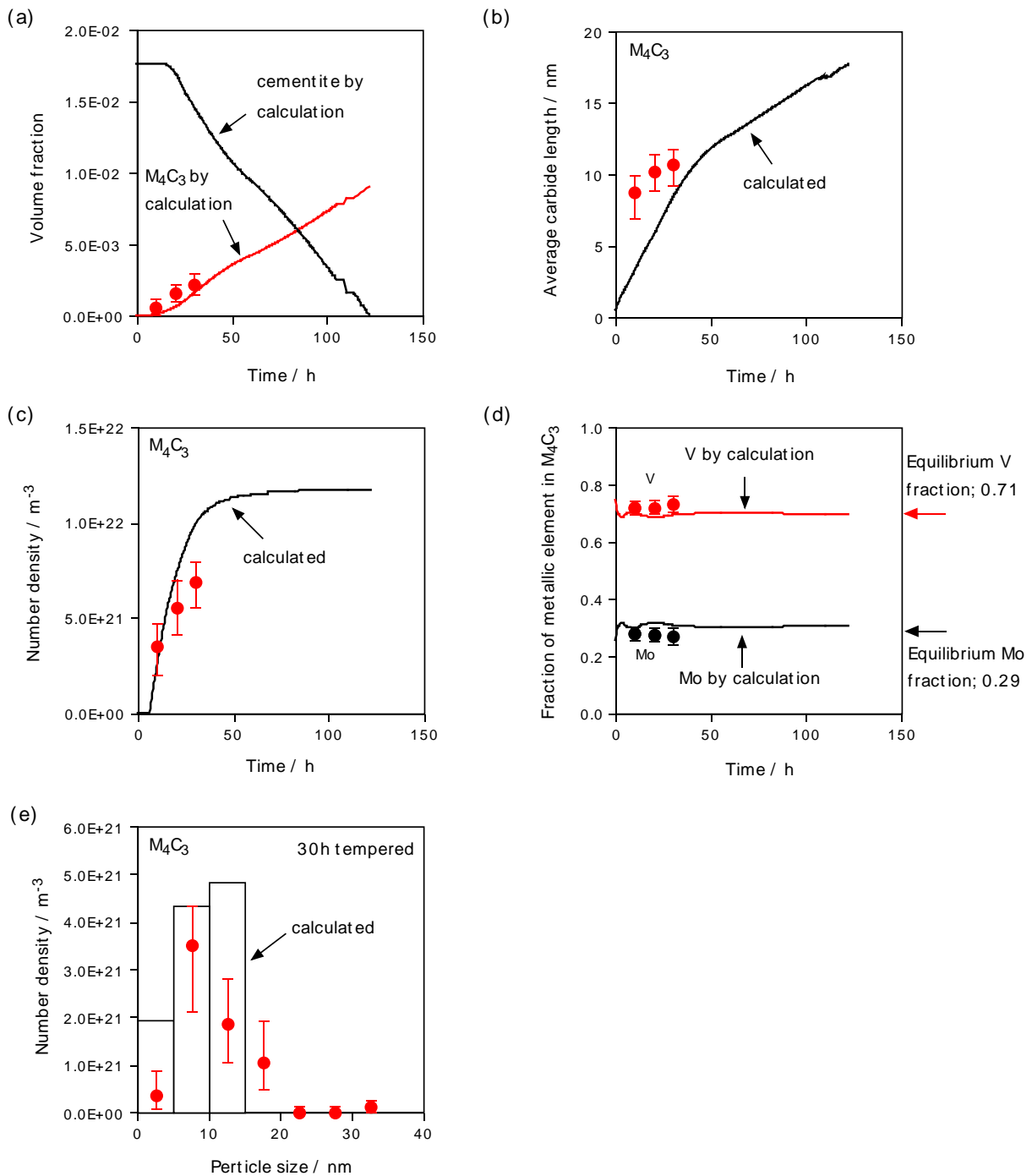


Figure 9.27: Comparisons between calculations and observations for Steel E. (a) Relationship between volume fraction of M₄C₃ particles and tempering time. (b) Relationship between average length of M₄C₃ particles and tempering time. (c) Relationship between number density of M₄C₃ particles whose size are over 4 nm and tempering time. (d) Relationship between chemical composition of M₄C₃ particles and tempering time. (e) Number density distribution of the length of M₄C₃ particles for 30 h tempered steel.

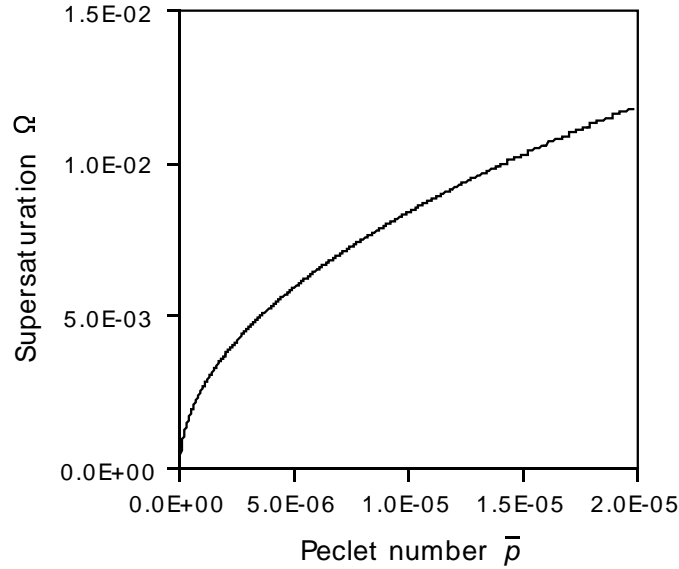


Figure 9.28: Relationship between supersaturation and Péclet number which satisfy equation 9.4 in the case of $r^{IC}/r_c = 3$.

9.4 Summary and conclusions

The precipitation and Ostwald ripening behaviour of M_4C_3 (plate-shaped) particles during the tempering of a quaternary Fe-C-Mo-V martensitic steel have been characterised and modelled, taking account of local equilibrium, the capillarity effect and simultaneous cementite enrichment and dissolution.

In conclusion, by modelling a M_4C_3 particle as a parabolic cylinder with a constant solute concentration along the surface of the tip, and assuming a maximum growth rate, the model can predict the average length, volume fraction, and number density of particles with good agreement with observations. The growth rate depends on the supersaturation of V (Ω_V) and Mo (Ω_{Mo}) and the ratio of the solute concentration in the matrix: \bar{c}_V/\bar{c}_C and \bar{c}_{Mo}/\bar{c}_C .

Chapter 10

Hydrogen trapping behaviour

10.1 Introduction

Hydrogen introduced into steels causes a deterioration in the mechanical properties and unpredictable fracture. There are several types of hydrogen trapping sites in steels, as mentioned in Chapter 1. Hydrogen trapped at octahedral sites in ferrite lattices, dislocations, and grain boundaries is called diffusible hydrogen, since it can diffuse and be evolved from steels at room temperature. It is reported that it is diffusible hydrogen which causes hydrogen embrittlement [47, 62, 63]. Diffusible hydrogen can be analysed through programmed temperature analysis using a gas chromatograph or mass spectrometry [62, 63]. There have been attempts to improve the hydrogen embrittlement resistance of steels, for example by reducing the concentrations of impurities such as sulfur and phosphorus. Hydrogen trapping by some carbides is one of the most efficient methods of improving the hydrogen embrittlement resistance [1, 2, 62, 63]. Martensitic steels in which M_4C_3 particles precipitate during tempering show high hydrogen trapping capacity [2, 63]. However, the dominant factors for trapping capacity, for example particle size and the chemical composition of particles, have not been examined in detail. The purpose of this chapter is to clarify the factors which make M_4C_3 particles effective for hydrogen trapping and to determine the compositions and heat treatment conditions necessary to obtain steels with excellent hydrogen trapping capacity.

10.2 Discussion

In Fig. 6.4, the hydrogen evolution peak temperatures were 120 °C for Steel *A* and 180 °C for Steels *B*, *D* and *E*. The evolution rate curve of Steel *C* seems to have two peaks at 180 °C and 250 °C. From TEM observations, it is considered that the 120 °C peak represents hydrogen trapped by Mo_2C and the 180 °C peak is from hydrogen trapped by M_4C_3 . However, the trapping site corresponding to the 250 °C peak has not been identified.

Figure 10.1 (a) shows the relationships between the hydrogen trapping capacity and tempering time, for Steel *B* - *E*. The relationships between the interfacial area of M_4C_3 particles, the volume fraction of M_4C_3 and the interfacial area of M_4C_3 particles less than

10 nm, and tempering time are shown in Fig. 10.1 (b), (c) and (d), respectively. The lattice misfit between M_4C_3 and ferrite is about 2.1 %, and it is therefore considered that M_4C_3 can grow up to 10 nm on $\{100\}_\alpha$ planes without introducing a misfit dislocation. The coherent interfacial area, measured as the sum of the surface area of M_4C_3 particles whose length is less than 10 nm, is shown in Fig. 10.1 (d). The coherent M_4C_3 /ferrite interface and the chemical Mo/V molar ratio in M_4C_3 particles seem to dominate the hydrogen trapping capacity. In the present work, steel with high hydrogen trapping capacity can be obtained by increasing the Mo/V molar ratio up to 0.85 in M_4C_3 particles and tempering to give an average length of M_4C_3 particles of 10 nm.

Hydrogen trapping is believed to be caused by chemical or physical interactions. Vanadium is known to form hydrides, and the chemical interaction between vanadium and hydrogen must therefore be strong. However, chemical interactions cannot explain the carbide size dependence of the hydrogen trapping capacity, since the trapping capacity shows a maximum at the tempering time for which the average length of M_4C_3 particles is about 10 nm. It seems that interface coherency, or, in other words, elastic interaction, plays an important role in the hydrogen trapping phenomenon.

Although it has not been verified in the present work, the precise trapping site, for example the carbide plane or edge, must be examined to clarify the hydrogen trapping mechanism.

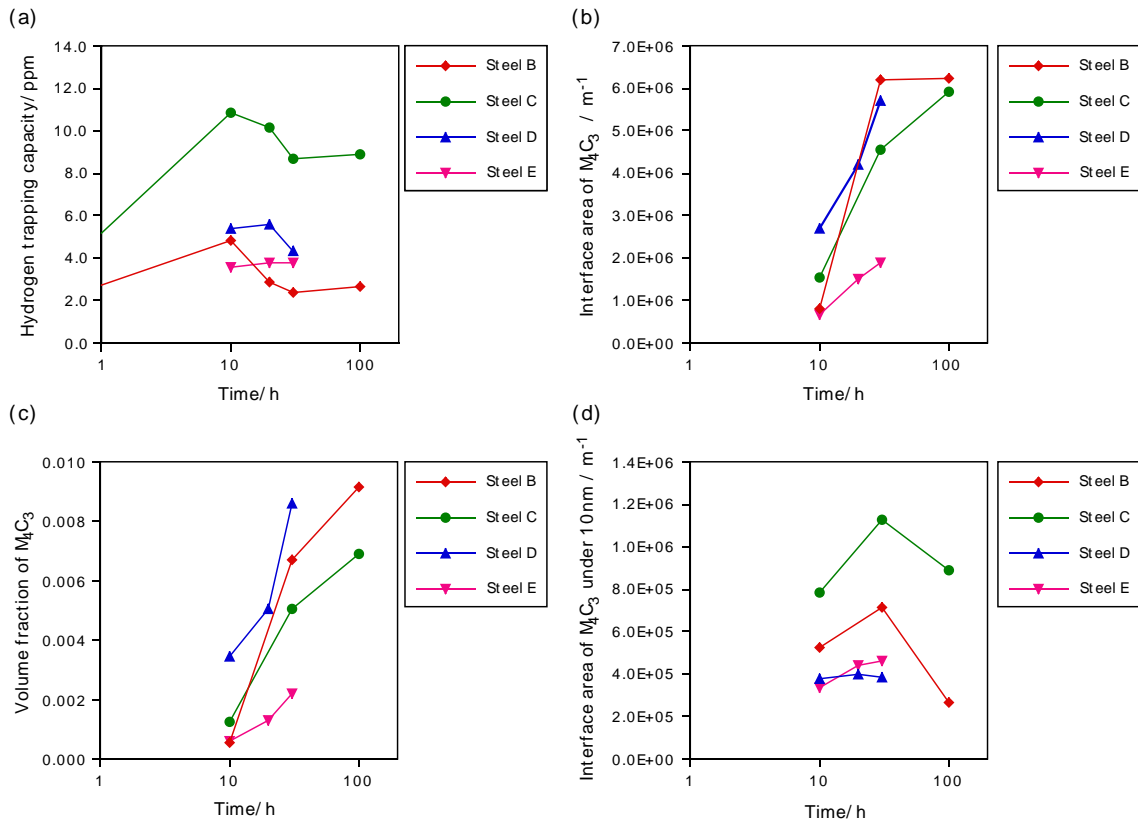


Figure 10.1: Relationships between the following quantities and tempering time at 600 °C: (a) hydrogen trapping capacity, (b) interfacial area of M_4C_3 particles, (c) volume fraction of M_4C_3 particles, (d) interfacial area of M_4C_3 particles less than 10 nm in length. Data were obtained by observations.

Chapter 11

Conclusions and suggestions for further work

The precipitation and Ostwald ripening behaviour of Mo_2C (needle-shaped) particles in a Fe-C-Mo ternary system, V_4C_3 (plate-shaped) particles in a Fe-C-V ternary system and M_4C_3 (plate-shaped) particles in a Fe-C-Mo-V quaternary system during the tempering of martensitic steels has been characterised and modelled, taking account of local equilibrium, the capillarity effect, and simultaneous cementite enrichment and dissolution.

For Mo_2C particles, by modelling a particle as a paraboloid and adopting Trivedi's solution for the diffusion problem, which allows the composition to vary along the interface of a paraboloid but assumes that the shape is preserved, and assuming a maximum growth rate, the model can predict the average length, volume fraction, and number density of particles with good agreement with observations. The growth rate depends on the supersaturation of molybdenum (Ω_{Mo}) and the ratio of the solute mole fraction in the matrix $\bar{c}_{\text{Mo}}/\bar{c}_{\text{C}}$.

For V_4C_3 or M_4C_3 , by modelling a particle as a parabolic cylinder with a constant concentration of solute along the surface of the tip, and assuming the maximum growth rate, the model can predict the average length, volume fraction, and number density of particles with good agreement with observations. The growth rate depends on the supersaturation of vanadium (Ω_{V}) and the ratio of the solute mole fraction in the matrix $\bar{c}_{\text{V}}/\bar{c}_{\text{C}}$.

The hydrogen trapping capacity of these carbides has been investigated. The amount of trapped hydrogen per unit volume of carbide is largest for M_4C_3 , whose atomic ratio of metallic elements is 0.52V:0.45Mo:0.02Fe:0.01Mn. Experimental data showed that the hydrogen trapping capacity of each steel tested was a maximum when the average size of carbide particles was the value to which carbides can grow while maintaining coherency with the ferrite matrix. This shows that the coherent interface between carbide and matrix plays an important role for hydrogen trapping phenomena.

The following problems could be investigated further to improve the precision of the predictions:

-
1. Dislocation recovery: this factor is believed to affect the nucleation site density and the nucleation rate.
 2. Pipe diffusion: this factor is believed to affect the growth rate of carbide particles, especially in the early stage of tempering.
 3. Coherency and the coherent strain at the carbide/matrix interface: this factor may affect the morphology of carbide particles and the hydrogen trapping capacity.

Chapter 12

Appendix - Computer program

12.1 Program for nucleation and growth of needle-shaped precipitate : Mo_2C

12.1.1 Provenance of Source Code

Shingo Yamasaki,
Phase Transformations Group,
Department of Materials Science and Metallurgy,
University of Cambridge,
Cambridge, U. K.

12.1.2 Purpose

To calculate the kinetics of carbides precipitating under diffusion-controlled growth and capillarity effect, with particular reference to the needle-shaped carbides in Fe-C-Mo steel. In the calculations, the first carbide is assumed to be cementite.

12.1.3 Specification

This is a self-contained program

12.1.4 Description

The program reads thermodynamic data from a pre-established database. It then calculates the evolution of volume fractions, average size, chemical composition and number density of Mo_2C particles.

12.1.5 References

S. Yamasaki and H. K. D. H. Bhadeshia : *Materials Science and Technology* 19(2003) pp. 723-731

12.1.6 Parameters

I Input parameters

I - Integer

Carbide which should be calculated (1:cementite, 2: Mo_2C 3: M_4C_3)

II - Integer

Alloy element (1:Mo, 2:V)

CXB - double precision

Mean concentration of carbon in alloy

XB(II) - double precision

Mean concentration of II in alloy (mole fraction)

CXA(I) - double precision

Carbon concentration in ferrite in equilibrium with carbide I (mole fraction)

SFEN(I) - double precision

Surface energy of the growing interface of Mo_2C particles (J m^{-2})

NAD(I) - double precision

Nucleation site density factors of carbide I

CTYPE(I) - double precision

Morphology for carbide I (1=Needle shaped, 2=Disc shaped)

DS(I) - integer

Species assumed to be controlling dissolution of cementite (1=Mo, 2=V)

VMAX(I) - double precision

Maximum volume fraction of carbide I

VEQ(I) - double precision

Equilibrium volume fraction of carbide I

DG(I) - double precision

Driving force for forming carbide (J)

VDIV(I) - double precision

Maximum volume fraction of carbide I (for driving force)

XC(II,I) - double precision

Mole fraction of II in carbide I in equilibrium with ferrite matrix

XA(II,I) - double precision

Mole fraction of II in ferrite in equilibrium with carbide I

DT - double precision

Time step for calculation (sec)

TK - double precision

Absolute temperature (K)

CC - double precision

Carbon concentration of an alloy in wt. %

DR - double precision

Ratio of cementite particles at grain boundary:intergranular

DTHI - double precision

Thickness of cementite particles at grain boundaries

THI - double precision

Thickness of cementite particles in grains

II Output parameter

TINST - double precision
Time in second
SZMAX - double precision
Maximum half length of Mo_2C particles
MSZEX - double precision
Average half length of Mo_2C particles
V(1) - double precision
Volume fraction of cementite
VE(I) - double precision
Volume fraction of carbide I
GRT(I) - double precision
Growth rate of carbide I (m/s)
NR(I) - double precision
Nucleation rate of carbide I (m/s)
ONXCM - double precision
Mole fraction of Mo in cementite

12.1.7 Error Indicators

None

12.1.8 Accuracy

No information supplied

12.1.9 Further Comments

The program is set to read the following input data files:

multi01Mo_2input.d ;
ternaryMon.txt.

and to write the results to the following output data files:

multi01Mo_output.d ;
multi01Mo_xbinst.d ;
multi01Mo_ro.d ;
ternaryMon.d ;
ostwald_Mo_para.d.

12.1.10 Examples

An example for cementite and Mo_2C precipitation in a quaternary Fe-0.1C-1.60Mo wt. % steel tempered at 600 °C

I Program data

Parameter	Data	comment
CXB	0.0046623D0	mean carbon concentration
XB(1)	0.0093390D0	mean Mo concentration
XB(2)	0.0000000D0	mean V concentration
CXA(1)	0.0001049D0	C concentration in α equilibrium with θ
SFEN(1)	0.0D0	interfacial energy of cementite
NAD(1)	1.0D0	site density factor of cementite
CTYPE(1)	0	phase type of cementite
DS(1)	1	species controlling diffusion (1=Mo, 2=V)
VMAX(1)	1.75961D-2	maximum volume fraction of cementite
VEQ(1)	1.75961D-2	equilibrium volume fraction of cementite
DG(1)	-1.07D2	driving force for forming cementite
VDIV(I)	1.75961D-2	maximum volume fraction of cementite
XC(1,1)	0.0424479D0	equilibrium Mo concentration in cementite
XA(1,1)	0.0087239D0	Mo concentration in α equilibrium with cementite
XC(2,1)	0.0000000D0	equilibrium V concentration in cementite
XA(2,1)	0.0000000D0	equilibrium V concentration in α
CXA(2)	0.0000260D0	C concentration in α equilibrium with M_2C
SFEN(2)	0.2D0	interfacial energy of M_2C
NAD(2)	20.0D0	site density factor of M_2C
CTYPE(2)	1	phase type of M_2C (1=needle, 2=spherical)
DS(2)	1	species controlling diffusion (1=Mo, 2=V)
VMAX(2)	1.39120D-2	maximum volume fraction of M_2C
VEQ(2)	1.39120D-2	equilibrium volume fraction of M_2C
DG(2)	-1.98D2	driving force for forming M_2C
VDIV(2)	1.39120D-2	maximum volume fraction of M_2C
XC(1,2)	0.5556297D0	equilibrium Mo concentration in M_2C
XA(1,2)	0.0016320D0	Mo concentration in α equilibrium with M_2C
XC(2,2)	0.0000000D0	equilibrium V concentration in M_2C
XA(2,2)	0.0000000D0	V concentration in α equilibrium with M_2C
DT	100.0D	time step
TK	873.0D0	absolute temperature
CC	0.10D0	carbon concentration in wt. %
DR	0.9	ratio of cementite at boundary:intergranular
DTHI	5.0D-8	grain boundary cementite thickness
THI	2.0D-8	intergranular cementite thickness

II Program results

Time / h	Volume fraction of cementite	Volume fraction of Mo_2C	Particle length of Mo_2C / m	Number density of Mo_2C / m^{-3}
5.56E-01	1.76E-02	3.17E-06	2.32E-09	1.77E+20
1.94E+00	1.76E-02	9.15E-05	6.45E-09	6.13E+20
3.06E+00	1.76E-02	2.95E-04	9.46E-09	9.11E+20
5.00E+00	1.71E-02	8.77E-04	1.38E-08	1.28E+21
1.00E+01	1.35E-02	3.54E-03	2.73E-08	1.51E+21
1.50E+01	9.91E-03	6.23E-03	3.70E-08	1.51E+21
2.00E+01	7.30E-03	8.12E-03	4.26E-08	1.51E+21
2.50E+01	5.68E-03	9.38E-03	4.59E-08	1.51E+21
3.00E+01	4.39E-03	1.02E-02	4.80E-08	1.51E+21
3.50E+01	3.83E-03	1.08E-02	4.94E-08	1.51E+21
4.00E+01	3.25E-03	1.12E-02	5.04E-08	1.51E+21
4.50E+01	2.65E-03	1.16E-02	5.12E-08	1.51E+21
5.00E+01	2.34E-03	1.18E-02	5.17E-08	1.51E+21
5.50E+01	2.03E-03	1.20E-02	5.22E-08	1.51E+21
6.00E+01	1.71E-03	1.23E-02	5.27E-08	1.51E+21
6.50E+01	1.40E-03	1.25E-02	5.32E-08	1.51E+21
7.00E+01	1.09E-03	1.27E-02	5.37E-08	1.51E+21
7.50E+01	7.81E-04	1.29E-02	5.43E-08	1.51E+21
8.00E+01	4.70E-04	1.32E-02	5.48E-08	1.51E+21
8.50E+01	2.94E-04	1.34E-02	5.52E-08	1.51E+21
9.00E+01	1.10E-04	1.36E-02	5.56E-08	1.51E+21
9.10E+01	5.79E-05	1.36E-02	5.57E-08	1.51E+21
9.21E+01	5.45E-06	1.37E-02	5.58E-08	1.51E+21
9.78E+01	0.00E+00	1.36E-02	5.66E-08	1.51E+21
1.03E+02	0.00E+00	1.37E-02	5.65E-08	1.51E+21
2.03E+02	0.00E+00	1.38E-02	5.28E-08	1.51E+21
3.03E+02	0.00E+00	1.38E-02	4.94E-08	1.51E+21
4.03E+02	0.00E+00	1.38E-02	4.67E-08	1.51E+21
5.03E+02	0.00E+00	1.38E-02	4.47E-08	1.51E+21
6.03E+02	0.00E+00	1.38E-02	4.32E-08	1.50E+21
7.03E+02	0.00E+00	1.38E-02	4.19E-08	1.47E+21
8.03E+02	0.00E+00	1.38E-02	4.11E-08	1.43E+21
9.03E+02	0.00E+00	1.38E-02	4.04E-08	1.38E+21
1.00E+03	0.00E+00	1.38E-02	3.99E-08	1.34E+21
1.10E+03	0.00E+00	1.38E-02	3.94E-08	1.29E+21
1.20E+03	0.00E+00	1.38E-02	3.90E-08	1.25E+21
1.30E+03	0.00E+00	1.38E-02	3.85E-08	1.21E+21
1.40E+03	0.00E+00	1.38E-02	3.81E-08	1.17E+21
1.48E+03	0.00E+00	1.38E-02	3.78E-08	1.13E+21

12.2 Program for nucleation and growth of needle-shaped precipitate : V_4C_3

12.2.1 Provenance of Source Code

Shingo Yamasaki,
Phase Transformations Group,
Department of Materials Science and Metallurgy,
University of Cambridge,
Cambridge, U. K.

12.2.2 Purpose

To calculate the kinetics of carbides precipitating under diffusion-controlled growth and capillarity effect, with particular reference to the needle-shaped carbides in Fe-C-V steel. In the calculations, the first carbide is assumed to be cementite.

12.2.3 Specification

This is a self-contained program

12.2.4 Description

The program reads thermodynamic data from a pre-established database. It then calculates the evolution of volume fractions, average size, chemical composition and number density of V_4C_3 particles.

12.2.5 References

S. Yamasaki and H. K. D. H. Bhadeshia : *Materials Science and Technology* 19(2003) pp. 1335-1343

12.2.6 Parameters

I Input parameters

I - Integer

Carbide which should be calculated (1:cementite, 2: V_4C_3 , 3: Mo_2C)

II - Integer

Alloy element (1:V, 2:Mo)

CXB - double precision

Mean concentration of carbon in alloy

XB(II) - double precision

Mean concentration of II in alloy (mole fraction)

CXA(I) - double precision

Carbon concentration in ferrite in equilibrium with carbide I (mole fraction)

SFEN(I) - double precision

Surface energy of the growing interface of V_4C_3 particles ($J\ m^{-2}$)

NAD(I) - double precision

Nucleation site density factors of carbide I

CTYPE(I) - double precision
Morphology for carbide I (1=Disc shaped, 2=Needle shaped)

DS(I) - integer
Species assumed to be controlling dissolution of cementite (1=V, 2=Mo)

VMAX(I) - double precision
Maximum volume fraction of carbide I

VEQ(I) - double precision
Equilibrium volume fraction of carbide I

DG(I) - double precision
Driving force for forming carbide (J)

VDIV(I) - double precision
Maximum volume fraction of carbide I (for driving force)

XC(II,I) - double precision
Mole fraction of II in carbide I in equilibrium with ferrite matrix

XA(II,I) - double precision
Mole fraction of II in ferrite in equilibrium with carbide I

DT - double precision
Time step for calculation (sec)

TK - double precision
Absolute temperature (K)

CC - double precision
Carbon concentration of an alloy in wt. %

DR - double precision
Ratio of cementite particles at grain boundary:intergranular

DTHI - double precision
Thickness of cementite particles at grain boundaries

THI - double precision
Thickness of cementite particles in grains

II Output parameter

TINST - double precision
Time in second

SZMAX - double precision
Maximum half length of V_4C_3 particles

MSZEX - double precision
Average half length of V_4C_3 particles

V(1) - double precision
Volume fraction of cementite

VE(I) - double precision
Volume fraction of carbide I

GRT(I) - double precision
Growth rate of carbide I (m/s)

NR(I) - double precision
Nucleation rate of carbide I (m/s)

ONXCM - double precision
Mole fraction of V in cementite

12.2.7 Error Indicators

None

12.2.8 Accuracy

No information supplied

12.2.9 Further Comments

The program is set to read the following input data files:

multi01V_2input.d ;
ternaryV.txt.

and to write the results to the following output data files:

multi01V_output.d ;
multi01V_xbinst.d ;
multi01V_ro.d ;
ternaryV.d ;
ostwald_V_para.d.

12.2.10 Examples

An example for cementite and V_4C_3 precipitation in a quaternary Fe-0.1C-0.56V wt. % steel tempered at 600 °C

I Program data

Parameter	Data	comment
CXB	0.0046287D0	mean carbon concentration
XB(1)	0.0062207D0	mean V concentration
XB(2)	0.0000000D0	mean Mo concentration
CXA(1)	0.0000578D0	C concentration in α equilibrium with θ
SFEN(1)	0.0D0	interfacial energy of cementite
NAD(1)	1.0D0	site density factor of cementite
CTYPE(1)	0	phase type of cementite
DS(1)	1	species controlling diffusion (1=V, 2=Mo)
VMAX(1)	1.7624358D-2	maximum volume fraction of cementite
VEQ(1)	1.7624358D-2	equilibrium volume fraction of cementite
DG(1)	-1.07D2	driving force for forming cementite
VDIV(I)	1.7624358D-2	maximum volume fraction of cementite
XC(1,1)	0.1063089D0	equilibrium V concentration in cementite
XA(1,1)	0.0043562D0	V concentration in α equilibrium with cementite
XC(2,1)	0.0000000D0	equilibrium Mo concentration in cementite
XA(2,1)	0.0000000D0	equilibrium Mo concentration in α
CXA(2)	0.0000340D0	C concentration in α equilibrium with M_2C
SFEN(2)	0.2D0	interfacial energy of V_4C_3
NAD(2)	0.3D0	site density factor of V_4C_3
CTYPE(2)	1	phase type of V_4C_3 (1=plate, 2=needle)
DS(2)	1	species controlling diffusion (1=V, 2=Mo)
VMAX(2)	0.966D-2	maximum volume fraction of V_4C_3
VEQ(2)	0.966D-2	equilibrium volume fraction of V_4C_3
DG(2)	-1.98D2	driving force for forming V_4C_3
VDIV(2)	0.966D-2	maximum volume fraction of V_4C_3
XC(1,2)	0.5320034D0	equilibrium Mo concentration in V_4C_3
XA(1,2)	0.0009620D0	V concentration in α equilibrium with V_4C_3
XC(2,2)	0.0000000D0	equilibrium Mo concentration in V_4C_3
XA(2,2)	0.0000000D0	Mo concentration in α equilibrium with V_4C_3
DT	100.0D	time step
TK	873.0D0	absolute temperature
CC	0.10D0	carbon concentration in wt. %
DR	0.9	ratio of cementite at boundary:intergranular
DTHI	5.0D-8	grain boundary cementite thickness
THI	2.0D-8	intergranular cementite thickness

II Program results

Time / h	Volume fraction of cementite	Volume fraction of V_4C_3	Particle length of V_4C_3 / m	Number density of V_4C_3 / m^{-3}
2.08E+00	1.76E-02	2.36E-05	2.13E-09	5.64E+21
4.03E+00	1.76E-02	1.21E-04	3.46E-09	8.55E+21
5.97E+00	1.76E-02	3.13E-04	4.72E-09	1.04E+22
8.06E+00	1.75E-02	5.13E-04	5.46E-09	1.16E+22
1.00E+01	1.73E-02	6.45E-04	5.79E-09	1.24E+22
1.21E+01	1.69E-02	8.36E-04	6.34E-09	1.30E+22
1.40E+01	1.64E-02	1.09E-03	7.06E-09	1.34E+22
1.60E+01	1.57E-02	1.43E-03	7.95E-09	1.36E+22
1.81E+01	1.46E-02	1.92E-03	9.06E-09	1.38E+22
2.00E+01	1.35E-02	2.47E-03	1.01E-08	1.38E+22
2.21E+01	1.23E-02	3.09E-03	1.12E-08	1.39E+22
2.40E+01	1.12E-02	3.66E-03	1.21E-08	1.39E+22
2.60E+01	1.01E-02	4.22E-03	1.28E-08	1.39E+22
2.81E+01	9.04E-03	4.79E-03	1.36E-08	1.39E+22
3.00E+01	8.03E-03	5.29E-03	1.42E-08	1.39E+22
3.21E+01	7.08E-03	5.79E-03	1.47E-08	1.39E+22
3.40E+01	6.28E-03	6.21E-03	1.52E-08	1.39E+22
3.60E+01	5.48E-03	6.60E-03	1.56E-08	1.39E+22
3.81E+01	4.76E-03	6.98E-03	1.60E-08	1.39E+22
4.00E+01	4.14E-03	7.31E-03	1.63E-08	1.39E+22
4.21E+01	3.49E-03	7.64E-03	1.66E-08	1.39E+22
4.40E+01	2.96E-03	7.91E-03	1.69E-08	1.39E+22
4.60E+01	2.50E-03	8.17E-03	1.71E-08	1.39E+22
4.81E+01	2.01E-03	8.41E-03	1.73E-08	1.39E+22
5.00E+01	1.59E-03	8.63E-03	1.75E-08	1.39E+22
5.21E+01	1.17E-03	8.84E-03	1.77E-08	1.39E+22
5.40E+01	8.24E-04	9.02E-03	1.78E-08	1.39E+22
5.60E+01	4.70E-04	9.19E-03	1.80E-08	1.39E+22
5.81E+01	1.89E-04	9.36E-03	1.81E-08	1.39E+22
6.49E+01	0.00E+00	9.35E-03	1.83E-08	1.39E+22
7.04E+01	0.00E+00	9.35E-03	1.83E-08	1.39E+22
1.04E+02	0.00E+00	9.35E-03	1.85E-08	1.29E+22
1.93E+02	0.00E+00	9.41E-03	2.16E-08	8.64E+21
2.98E+02	0.00E+00	9.46E-03	2.42E-08	6.24E+21
3.98E+02	0.00E+00	9.49E-03	2.62E-08	4.86E+21
4.98E+02	0.00E+00	9.52E-03	2.83E-08	3.91E+21
5.98E+02	0.00E+00	9.54E-03	3.01E-08	3.35E+21
6.98E+02	0.00E+00	9.56E-03	3.17E-08	2.82E+21
7.98E+02	0.00E+00	9.57E-03	3.29E-08	2.50E+21
8.98E+02	0.00E+00	9.59E-03	3.39E-08	2.25E+21
1.00E+03	0.00E+00	9.60E-03	3.55E-08	1.99E+21
1.10E+03	0.00E+00	9.61E-03	3.67E-08	1.82E+21

12.3 Program for nucleation and growth of plate-shaped precipitate : M_4C_3

12.3.1 Provenance of Source Code

Shingo Yamasaki,
Phase Transformations Group,
Department of Materials Science and Metallurgy,
University of Cambridge,
Cambridge, U. K.

12.3.2 Purpose

To calculate the kinetics of carbides precipitating under diffusion-controlled growth and capillarity effect, with particular reference to the plate-shaped carbides in Fe-C-Mo-V steel. In the calculations, the first carbide is assumed to be cementite.

12.3.3 Specification

This is a self-contained program

12.3.4 Description

The program reads thermodynamic data from a pre-established database. It then calculates the evolution of volume fractions, average size, chemical composition and number density of M_4C_3 particles.

12.3.5 References

- S. Yamasaki and H. K. D. H. Bhadeshia : *Materials Science and Technology* 19(2003) pp. 723-731
- S. Yamasaki and H. K. D. H. Bhadeshia : *Materials Science and Technology* 19(2003) pp. 1335-1343

12.3.6 Parameters

I Input parameters

I - Integer

Carbide which should be calculated (1:cementite, 2: M_4C_3 , 3: M_2C)

II - Integer

Alloy element (1:Mo, 2:V)

CXB - double precision

Mean concentration of carbon in alloy

XB(II) - double precision

Mean concentration of II in alloy (mole fraction)

CXA(I) - double precision

Carbon concentration in ferrite in equilibrium with carbide I (mole fraction)

SFEN(I) - double precision

Surface energy of the growing interface of M_4C_3 particles ($J\ m^{-2}$)

NAD(I) - double precision

Nucleation site density factors of carbide I

CTYPE(I) - double precision

Morphology for carbide I (1=Disc shaped, 2=Needle shaped)

DS(I) - integer

Species assumed to be controlling dissolution of cementite (1=Mo, 2=V)

VMAX(I) - double precision

Maximum volume fraction of carbide I

VEQ(I) - double precision

Equilibrium volume fraction of carbide I

DG(I) - double precision

Driving force for formation of carbide (J)

VDIV(I) - double precision

Maximum volume fraction of carbide I (for driving force)

XC(II,I) - double precision

Mole fraction of II in carbide I in equilibrium with ferrite matrix

XA(II,I) - double precision

Mole fraction of II in ferrite in equilibrium with carbide I

DT - double precision

Time step for calculation (sec)

TK - double precision

Absolute temperature (K)

CC - double precision

Carbon concentration of alloy in wt. %

DR - double precision

Ratio of cementite particles at grain boundary:intergranular

DTHI - double precision

Thickness of cementite particles at grain boundaries

THI - double precision

Thickness of cementite particles in grains

II Output parameter

TINST - double precision
Time in second

SZMAX - double precision
Maximum half length of M_4C_3 particles

MSZEX - double precision
Average half length of M_4C_3 particles

V(1) - double precision
Volume fraction of cementite

VE(I) - double precision
Volume fraction of carbide I

GRT(I) - double precision
Growth rate of carbide I (m/s)

NR(I) - double precision
Nucleation rate of carbide I (m/s)

ONXCV - double precision
Mole fraction of V in cementite

ONXCM - double precision
Mole fraction of Mo in cementite

XCINST(1,I) - double precision
Mole fraction of Mo in carbide I

XCINST(2,I) - double precision
Mole fraction of V in carbide I

12.3.7 Error Indicators

None

12.3.8 Accuracy

No information supplied

12.3.9 Further Comments

The program is set to read the following input data files:

multi01MoV_5input.d ;
quaternary_data001aa.txt ;
quaternary_data002aa.txt ;
quaternary_data005aa.txt ;
quaternary_data010aa.txt ;
quaternary_data020aa.txt ;
quaternary_data034aa.txt ;
quaternary_data067aa.txt ;
quaternary_data133aa.txt ;
quaternary_data199aa.txt ;
quaternary_data266aa.txt ;
quaternary_data001cc.txt ;

and to write the results to the following output data files:

multi01MoV_V_output.d ;
 multi01MoV_V_xbinst.d ;
 multi01MoV_V_ostwald.d ;
 multi01MoV_V_PARA.d ;
 quaternary.d.

12.3.10 Examples

An example for cementite and M_4C_3 precipitation in a quaternary Fe-0.1C-1.60Mo-0.56V wt. % steel tempered at 600 °C

I Program data

Parameter	Data	comment
CXB	0.0046595D0	mean carbon concentration
XB(1)	0.0092740D0	mean Mo concentration
XB(2)	0.0062621D0	mean V concentration
CXA(1)	0.0000672D0	C concentration in α equilibrium with θ
SFEN(1)	0.0D0	interfacial energy of cementite
NAD(1)	1.0D0	site density factor of cementite
CTYPE(1)	0	phase type of cementite
DS(1)	2	species controlling diffusion (1=Mo, 2=V)
VMAX(1)	1.7624358D-2	maximum volume fraction of cementite
VEQ(1)	1.7624358D-2	equilibrium volume fraction of cementite
DG(1)	-1.12D2	driving force for forming cementite
VDIV(1)	1.7624358D-2	maximum volume fraction of cementite
XC(1,1)	0.0290715D0	equilibrium Mo concentration in cementite
XA(1,1)	0.0089045D0	Mo concentration in α equilibrium with cementite
XC(2,1)	0.1008791D0	equilibrium V concentration in cementite
XA(2,1)	0.0044911D0	equilibrium V concentration in α
CXA(2)	0.0000014D0	C concentration in α equilibrium with M_4C_3
SFEN(2)	0.2D0	interfacial energy of M_4C_3
NAD(2)	12.0D0	site density factor of M_4C_3
CTYPE(2)	1	phase type of M_4C_3 (1=plate, 2=needle)
DS(2)	2	species controlling diffusion (1=Mo, 2=V)
VMAX(2)	0.961D-2	maximum volume fraction of M_4C_3
VEQ(2)	0.961D-2	equilibrium volume fraction of M_4C_3
DG(2)	-2.61D2	driving force for forming M_4C_3
VDIV(2)	0.961D-2	maximum volume fraction of M_4C_3
XC(1,2)	0.1152479D0	equilibrium Mo concentration in M_4C_3
XA(1,2)	0.0081739D0	Mo concentration in α equilibrium with M_4C_3
XC(2,2)	0.4313452D0	equilibrium V concentration in M_4C_3
XA(2,2)	0.0018450D0	V concentration in α equilibrium with M_4C_3
DT	100.0D	time step
TK	873.0D0	absolute temperature
CC	0.10D0	carbon concentration in wt. %
DR	0.9	ratio of cementite at boundary:intergranular
DTHI	5.0D-8	grain boundary cementite thickness
THI	2.0D-8	intergranular cementite thickness

II Program results

Time / h	Volume fraction of cementite	Volume fraction of M_4C_3	Particle length of M_4C_3 / m	Mole fraction of V in M_4C_3	Mole fraction of Mo in M_4C_3
1.39E-01	1.76E-02	2.13E-08	4.29E-10	3.19E-01	1.11E-01
6.94E-01	1.76E-02	7.25E-07	8.77E-10	3.45E-01	1.40E-01
1.25E+00	1.76E-02	3.60E-06	1.32E-09	3.36E-01	1.47E-01
2.36E+00	1.76E-02	2.35E-05	2.30E-09	3.39E-01	1.66E-01
2.92E+00	1.76E-02	4.35E-05	2.77E-09	3.39E-01	1.68E-01
3.47E+00	1.76E-02	7.28E-05	3.22E-09	3.41E-01	1.67E-01
4.03E+00	1.76E-02	1.10E-04	3.68E-09	3.44E-01	1.65E-01
4.58E+00	1.76E-02	1.57E-04	4.13E-09	3.46E-01	1.65E-01
5.69E+00	1.76E-02	2.74E-04	4.89E-09	3.51E-01	1.61E-01
6.81E+00	1.76E-02	4.65E-04	5.65E-09	3.55E-01	1.59E-01
7.36E+00	1.74E-02	6.68E-04	5.98E-09	3.66E-01	1.54E-01
8.47E+00	1.70E-02	8.63E-04	6.20E-09	3.74E-01	1.49E-01
9.03E+00	1.68E-02	9.75E-04	6.49E-09	3.77E-01	1.49E-01
1.01E+01	1.62E-02	1.30E-03	7.59E-09	3.81E-01	1.47E-01
1.13E+01	1.55E-02	1.72E-03	8.83E-09	3.84E-01	1.46E-01
1.24E+01	1.44E-02	2.29E-03	1.01E-08	3.86E-01	1.45E-01
1.29E+01	1.38E-02	2.64E-03	1.07E-08	3.87E-01	1.45E-01
1.35E+01	1.30E-02	3.05E-03	1.09E-08	3.88E-01	1.44E-01
1.40E+01	1.21E-02	3.39E-03	1.11E-08	3.87E-01	1.46E-01
1.46E+01	1.13E-02	3.73E-03	1.15E-08	3.83E-01	1.49E-01
1.51E+01	1.05E-02	4.10E-03	1.20E-08	3.79E-01	1.52E-01
1.57E+01	9.82E-03	4.47E-03	1.25E-08	3.76E-01	1.54E-01
1.63E+01	9.13E-03	4.84E-03	1.29E-08	3.73E-01	1.56E-01
1.68E+01	8.37E-03	5.24E-03	1.34E-08	3.70E-01	1.59E-01
1.74E+01	7.54E-03	5.67E-03	1.38E-08	3.67E-01	1.61E-01
1.79E+01	6.72E-03	6.10E-03	1.43E-08	3.64E-01	1.63E-01
1.85E+01	5.93E-03	6.52E-03	1.47E-08	3.62E-01	1.65E-01
1.90E+01	5.08E-03	6.97E-03	1.51E-08	3.59E-01	1.68E-01
1.96E+01	4.21E-03	7.43E-03	1.55E-08	3.57E-01	1.70E-01
2.07E+01	2.36E-03	8.39E-03	1.64E-08	3.52E-01	1.74E-01
2.18E+01	7.10E-04	9.24E-03	1.68E-08	3.48E-01	1.78E-01
2.29E+01	1.27E-04	9.70E-03	1.74E-08	3.45E-01	1.79E-01
5.00E+01	0.00E+00	9.71E-03	1.78E-08	4.39E-01	1.07E-01
1.00E+02	0.00E+00	9.73E-03	1.99E-08	4.37E-01	1.09E-01
2.00E+02	0.00E+00	9.75E-03	2.44E-08	4.34E-01	1.11E-01
3.00E+02	0.00E+00	9.79E-03	2.52E-08	4.33E-01	1.13E-01
4.00E+02	0.00E+00	9.93E-03	2.93E-08	4.32E-01	1.14E-01
5.00E+02	0.00E+00	9.98E-03	2.93E-08	4.32E-01	1.14E-01
6.00E+02	0.00E+00	1.00E-02	3.22E-08	4.32E-01	1.14E-01
7.00E+02	0.00E+00	1.01E-02	3.35E-08	4.31E-01	1.15E-01
8.00E+02	0.00E+00	1.01E-02	3.37E-08	4.31E-01	1.15E-01

Bibliography

- [1] N. Ibaraki, A. Inada, M. Shimotsusa, T. Nakayama, T. Iwata and M. Nagao: *Kobelco Technol. Rev.* (1998), pp. 21–25.
- [2] S. Yamasaki, M. Kubota and T. Tarui: *Nippon Steel Technical Report*, **80** (1999), pp. 50–55.
- [3] T. Kushida, N. Kuratomi, T. Kudoh, H. Matsumoto, T. Tsumura and F. Nakasato: *Tetsu-to-Hagane*, **82** (1996), pp. 297–302.
- [4] J. D. Robson: “Modelling of precipitation in power plant steels”: *Ph. D. Thesis, University of Cambridge*, U. K. (1996).
- [5] N. Fujita: “Modelling carbide precipitation in alloy steels”: *Ph. D. Thesis, University of Cambridge*, U. K. (2000).
- [6] N. Fujita and H. K. D. H. Bhadeshia: *Mater. Sci. and Technol.*, **15** (1999), pp. 627–634.
- [7] C. Zener: *Trans. AIME*, **167** (1946), pp. 550–595.
- [8] L. J. E. Hofer, E. M. Cohn and W. C. Peebles: *J. Amer. Chem. Soc.*, **71** (1949), pp. 189–195.
- [9] K. H. Jack: *J. Iron and Steel Inst.*, **169** (1951), pp. 26–36.
- [10] A. K. Seal and R. W. K. Honeycombe: *J. Iron and Steel Inst.*, **188** (1958), pp. 343–350.
- [11] M. Tanino and K. Aoki: *Trans. Iron and Steel Inst. Japan*, **8** (1968), pp. 337–345.
- [12] M. Tanino: “Precipitation behavior of alloy carbides relating to transformation and hot deformation”: *Proc. Int. Conf. Phys. Metall. Thermoch. Process Steels Other Met.*, vol. 1, Montreal (1988), pp. 70–79.
- [13] A. Hultgren: *Trans. ASM*, **39** (1968), pp. 915–1005.
- [14] H. K. D. H. Bhadeshia: “Bainite in steels (2nd edition)”, London, UK: IOM Communications Ltd (2001), p. 63.
- [15] S. S. Babu, K. Hono and T. Sakurai: **67** (1993), pp. 321–327.
- [16] R. C. Thomson and M. K. Miller: **87/88** (1995), pp. 185–193.
- [17] R. C. Thomson and M. K. Miller: *Acta Metall.*, **46** (1998), pp. 2203–2213.

-
- [18] R. C. Thomson and H. K. D. H. Bhadeshia: *Mater. Sci. and Technol.*, **10** (1994), pp. 193–203.
- [19] H. K. D. H. Bhadeshia: “Bainite in steels (2nd edition)”, London, UK: IOM Communications Ltd (2001), p. 130.
- [20] W. Pitsch and A. Schrader: *Arch. Eisenhüttenw.*, **29** (1958), pp. 715–721.
- [21] D. Raynor, J. A. Whiteman and R. W. K. Honeycombe: *J. Iron and Steel Inst.*, **204** (1966), pp. 349–354.
- [22] R. G. Baker and J. Nutting: *J. Iron and Steel Inst.*, **192** (1959), pp. 257–268.
- [23] R. G. Baker and J. Nutting: *ISI Special Report*, **64** (1959), pp. 1–10.
- [24] J. Janovec, A. Vyrostkva and M. Svoboda: *Metall. Trans. A*, **25** (1994), pp. 267–275.
- [25] J. H. Woodhead and A. G. Quarrell: *J. Iron and Steel Inst.*, **203** (1965), pp. 605–620.
- [26] J. Pilling and N. Ridley: *Metall. Trans. A*, **13A** (1982), pp. 557–563.
- [27] B. A. Senior: *Mater. Sci. and Eng. A*, **119** (1989), pp. L5–L7.
- [28] K. J. Irvine and F. B. Pickering: *J. Iron and Steel Inst.*, **195** (1960), pp. 137–153.
- [29] K. J. Kurzydowski and W. Zielinski: *Metal Sci.*, **18** (1984), pp. 223–224.
- [30] K. Kuo: *J. Iron and Steel Inst.*, **176** (1956), pp. 258–268.
- [31] D. J. Dyson, S. R. Keown, D. Raynor and J. A. Whiteman: *Acta Metall.*, **14** (1966), pp. 867–875.
- [32] T. Sato, N. Nishizawa and Tamaki: *J. Japan Inst. Met.*, **24** (1960), pp. 395–399.
- [33] M. Tanino, T. Nishida and K. Aoki: *J. Japan Inst. Met.*, **30** (1966), pp. 894–895.
- [34] R. Uemori and M. Tanino: *J. Japan Inst. Met.*, **55** (1991), pp. 141–150.
- [35] J. Dubois, T. Epicier, C. Esnouf and G. Fantozzi: *Acta Metall.*, **36** (1988), pp. 1891–1901.
- [36] T. Epicier, J. Dubois, C. Esnouf and G. Fantozzi: *Acta Metall.*, **36** (1988), pp. 1903–1921.
- [37] D. J. Dyson and K. W. Andrews: *J. Iron and Steel Inst.*, **202** (1964), pp. 325–329.
- [38] E. Tekin and P. M. Kelly: *J. Iron and Steel Inst.*, **203** (1965), pp. 715–720.
- [39] R. G. Baker and J. Nutting: “”: *ISI Special Report*, No. 64 (1959), p. 1.
- [40] K. W. Andrews, D. J. Dyson and S. R. Keown: “Interpretation of electron diffraction patterns”, London: Hilger and Watts (1967).
- [41] H. Okada: “Proc. Int. Conf. SCC and HE of Iron base Alloys, NACE-5”: *NACE* (1977), p. 124.

-
- [42] H. Bennek, H. Schenk and H. Muller: *Stahl und Eisen*, **55** (1935), p. 321.
- [43] A. Sieverts: *Z. Phys. Chem.*, **60** (1907), pp. 129–201.
- [44] A. Sieverts, W. Krumbhaar and E. Jurisch: *ibid*, **154** (1911), p. 591.
- [45] M. Smialowski: “Hydrogen in steel”, Warszawa: Pergamon press (1962), p. 389.
- [46] K. Horikawa: *Tetsu-to-Hagane*, **54** (1968), p. 610.
- [47] N. Yurioka: *International Mater. Rev.*, **35** (1990), pp. 217–250.
- [48] C. D. Beachem: *Metall. Trans.*, **3** (1972), pp. 437–451.
- [49] W. W. Gerberich, R. A. Oriani, M. J. Lii, X. Chen and T. Foecke: *Phil. Mag.*, **63A** (1991), pp. 363–376.
- [50] A. R. Troiano: *Trans. ASM*, **52** (1960), pp. 54–80.
- [51] S. P. Lynch: *Acta Metall.*, **36** (1988), pp. 2639–2661.
- [52] I. M. Robertson, T. Tanabe, W. Wei, F. Heubaumsnd and H. K. Birnbaum: *Scripta Metall.*, **18** (1984), pp. 841–846.
- [53] H. G. Lee and J. Y. Lee: *Acta Metall.*, **32** (1984), pp. 131–136.
- [54] A. J. Kunnick and H. H. Johnson: *Metall. Trans. A*, **6A** (1975), pp. 1087–1091.
- [55] W. Y. Choo and J. Y. Lee: *Metall. Trans. A*, **13A** (1982), pp. 135–140.
- [56] W. Y. Choo and J. Y. Lee: *Metall. Trans. A*, **14A** (1983), pp. 1299–1305.
- [57] A. Turnbull, M. W. Carroll and D. H. Ferriss: *Acta Metall.*, **37** (1989), pp. 2039–2046.
- [58] K. Ono and M. Meshii: *Acta Metall. mater.*, **40** (1992), pp. 1357–1364.
- [59] G. W. Hong and J. Y. Lee: *J. Mater. Sci.*, **18** (1983), pp. 271–277.
- [60] W. M. Robertson and A. W. Thompson: *Metall. Trans. A*, **11A** (1980), pp. 553–557.
- [61] I. K. Pokhodnya and V. I. Shvachko: *Metall. Trans. A*, **22** (1997), pp. 285–289.
- [62] S. Yamasaki and T. Takahashi: *Tetsu-to-Hagane*, **83** (1997), pp. 454–459.
- [63] T. Tarui and S. Yamasaki: *Tetsu-to-Hagane*, **88** (2002), pp. 612–619.
- [64] H. Saito, K. Miyazawa and M. Mori: *J. Japan Inst. Met.*, **62** (1998), pp. 215–223.
- [65] F. R. N. Nabarro: *Proc. Phys. Soc.*, **52** (1940), pp. 90–104.
- [66] D. A. Porter and K. E. Easterling: “Phase transformations in metals and alloys (2nd edition)”, London: Chapman and Hall (1992), p. 147.
- [67] M. Volmer and A. Weber: *Z. Phys. Chem.*, **119** (1926), pp. 277–301.
- [68] J. W. Christian: “The theory of transformations in metals and alloys (2nd edition), part I”, Oxford: Pergamon Press (1975), p. 441.
-

-
- [69] C. Zener: *J. Appl. Phys.*, **20** (1949), pp. 950–953.
- [70] J. W. Christian: “The theory of transformations in metals and alloys (2nd edition), part I”, Oxford: Pergamon Press (1975), p. 180.
- [71] M. Hillert: *Jernkontorets Annaler*, **141** (1957), pp. 757–789.
- [72] J. W. Christian: “The theory of transformations in metals and alloys (2nd edition), part I”, Oxford: Pergamon Press (1975), p. 497.
- [73] G. Horvay and J. W. Cahn: *Acta Metall.*, **9** (1961), pp. 695–705.
- [74] G. P. Ivantsov: *Dolk. Akad. Nauk. SSSR*, **58** (1947), pp. 567–569.
- [75] M. Abramowitz: “Handbook of mathematical functions”, New York: Wiley (1965).
- [76] R. Trivedi: *Acta Metall.*, **18** (1970), pp. 287–295.
- [77] R. Trivedi: *Metall. Trans.*, **1** (1970), pp. 921–927.
- [78] P. E. J. Rivera and H. K. D. H. Bhadeshia: *Mater. Sci. and Technol.*, **17** (2000), pp. 25–29.
- [79] D. E. Coates: *Metall. Trans.*, **3** (1972), pp. 1203–1212.
- [80] D. E. Coates: *Metall. Trans.*, **4** (1973), pp. 1077–1086.
- [81] M. Hillert: “The mechanism of phase transformations in crystalline solids”, London: Inst. of Metals (1969).
- [82] R. T. DeHoff: “Diffusion controlled growth in polycomponent systems”: *Solid-Solid Phase Transformations '81* (1981), pp. 503–518.
- [83] I. M. Lifshitz and V. V. Slyozov: *J. Phys. Chem. Solids*, **19** (1961), pp. 35–50.
- [84] R. Wagner and R. Kampmann: “Homogeneous second phase precipitation”: *Materials Science and Technology*, vol. 5, Weinheim: VCH (1991), pp. 213–303.
- [85] W. J. Liu and J. J. Jonas: *Metall. Trans.*, **20A** (1989), pp. 689–697.
- [86] S. Aakamatsu, T. Senuma and M. Hasebe: *ISIJ International*, **32** (1992), pp. 275–282.
- [87] S. Okaguchi and T. Hashimoto: *ISIJ International*, **32** (1992), pp. 283–290.
- [88] S. P. Keown and W. G. Wilson: “Thermomechanical Processing of Microalloyed Austenite, ed. by A. J. DeArdo, G. A. Ratz and P. L. Wray”: *AIME*, Penn., U. S. (1982), p. 343.
- [89] A. Bon, J. R. Vernis and C. Rossard: *Metal Sci.*, **9** (1975), pp. 36–40.
- [90] Y. Saito, C. Shiga and T. Enami: “Proc. Int. Conf. On Physical Metallurgy of Thermomechanical Processing of steel and Other Metals”: Japan (1988).
- [91] A. N. Kolmogorov: *Bulletin de L'Academie des Sciences de L'URSS*, **3** (1937), pp. 355–359.
-

-
- [92] W. A. Johnson and R. F. Mehl: *Transaction of the American Institute of Mining and Metallurgical Engineering*, **135** (1939), pp. 416–458.
- [93] M. Avrami: *J. Chemical Physics*, **7** (1939), pp. 1103–1112.
- [94] J. D. Robson and H. K. D. H. Bhadeshia: *Mater. Sci. and Technol.*, **13** (1997), pp. 631–639.
- [95] J. D. Robson and H. K. D. H. Bhadeshia: *Mater. Sci. and Technol.*, **13** (1997), pp. 640–644.
- [96] H. K. D. H. Bhadeshia: *Mater. Sci. and Technol.*, **5** (1989), pp. 131–137.
- [97] R. C. Thomson and H. K. D. H. Bhadeshia: *Mater. Sci. and Technol.*, **10** (1994), pp. 205–208.
- [98] M. Takahashi and H. K. D. H. Bhadeshia: *Mater. Sci. and Technol.*, **6** (1990), pp. 592–603.
- [99] D. Venugopalan and J. S. Kirkaldy: “Hardenability Concepts with Applications to Steel”: *AIME conference*, New York, U. S. (1978).
- [100] S. M. Hodson: “MTDATA-Metallurgical and Thermochemical Databank, National Physical Laboratory”: *MTDATA-Metallurgical and Thermochemical Databank, National Physical Laboratory*, Teddington, U. K. (1989).
- [101] J. Yu: *Metall. Trans. A*, **20A** (1989), pp. 1561–1564.
- [102] P. M. Kerry and J. Nutting: *J. Iron and Steel Inst.* (1959), pp. 246–248.
- [103] D. B. Williams and C. B. Carter: “Transmission electron microscopy”, New York: Kluwer Academic / Plenum Publishers (1996), p. 150.
- [104] D. B. Williams and C. B. Carter: “Transmission electron microscopy”, New York: Kluwer Academic / Plenum Publishers (1996), p. 13.
- [105] S. Zhang and J. Jin: “Computation of special functions”, New York: Wiley (1996).
- [106] H. Asahi, D. Hirakami and S. Yamasaki: *ISIJ International*, **43** (2002), pp. 527–533.
- [107] W. Y. Choo and J. Y. Lee: *J. Mater. Sci.*, **17** (1982), pp. 1930–1938.
- [108] G. W. Hong and J. A. Lee: *J. Mater. Sci.*, **18** (1983), pp. 271–277.
- [109] R. T. Dehoff: “Thermodynamics in materials science”, New York: McGraw-Hill (1993), p. 378.
- [110] C. P. Heijwegen and G. D. Rieck: *Acta Metall.*, **22** (1974), pp. 1268–1281.
- [111] S. Yamasaki and H. K. D. H. Bhadeshia: *Mater. Sci. and Technol.*, **19** (2003), pp. 723–731.
- [112] G. F. Bolling and W. A. Tiller: *J. Appl. Phys.*, **32** (1961), pp. 2587–2605.

- [113] J. W. Christian: “The theory of transformations in metals and alloys (2nd edition), part I”, Oxford: Pergamon Press (1975), p. 498.
- [114] A. W. Bowen and G. M. Leak: *Metall. Trans.*, **1** (1970), pp. 1695–1700.
- [115] S. Yamasaki and H. K. D. H. Bhadeshia: *Mater. Sci. and Technol.*, **19** (2003), pp. 1335–1343.